MECHANICAL AND ACOUSTICAL PROPERTIES OF SANDSTONES AND SHALES

A DISSERTATION
SUBMITTED TO THE DEPARTMENT OF GEOPHYSICS
AND THE COMMITTEE ON GRADUATE STUDIES
OF STANFORD UNIVERSITY
IN PARTIAL FULFILLMENT OF THE REQUIREMENTS
FOR THE DEGREE OF
DOCTOR OF PHILOSOPHY

By
Diane Linda Jizba
March 1991

Abstract

The determination of in situ rock-mechanical properties such as static moduli and shear strength is essential in a variety of reservoir production and engineering tasks that include hydraulic fracturing, estimation of recoverable reserves, prediction of well-bore stability and subsidence. Because of the technical difficulties in directly measuring these properties in situ, mechanical properties may be estimated indirectly through the use of velocities provided we understand the relationships between acoustical and mechanical properties of rocks. This dissertation presents new results on acoustical and mechanical properties of sandstones and the influence of petrography, petrophysical properties, and stress.

Measurements of velocity, static moduli, and strength were obtained on a set of tight gas sandstones and shales. Petrographic studies reveal the existence of three main classes of lithology; sandstones, shaley sandstones and shales, based on clay content and quartz cement. A model for cementation suggests how textural features (distribution of porosity, clay mineral content, and quartz cement) may originate and affect petrophysical measurements as well as velocity and mechanical properties.

Results from petrographic analysis are used to explain the relationships between static and dynamic moduli. In my data set I find that static moduli are lower than dynamic moduli. This discrepancy arises from strain-amplitude differences between mechanical and acoustical measurements and the discrepancy is strongly related to both lithology and confining pressure. In shales, the ratio of dynamic to static moduli is rather insensitive to confining pressure. In contrast, sandstones exhibit strong dependence of the ratio of dynamic to static moduli on confining pressure. This behavior may be attributed to the differing sensitivity of static and dynamic moduli to cracks. For saturated rocks, in addition to strain amplitude, the discrepancy depends on frequency. A model is proposed to estimate the effect of frequency on elastic properties of rocks quantifying the effects of local flow at different measurement frequencies. The model results explain the measured total P and S wave dispersion for a variety of saturated rocks.

The influence of petrography and petrophysical properties is also observed in confined uniaxial compressive strength data where two regimes can be identified: (1) In sandstones (clay volume fractions less than 17 percent), strength τ is strongly dependent on confining pressure σ and porosity ϕ, following a relation of the form $\tau = \tau_0(\phi_c - \phi)\sigma^n$. (2) In shaley sandstones and shales (clay volume fractions greater than 17 percent), strength is sensitive to confining pressure and weakly sensitive to clay content C, following a relation of the form $\tau = \tau_0(1 - aC) + \mu\sigma$. A correlation is also observed between velocity and strength which depends on confining pressure and lithology.

The last section of this dissertation deals with overpressuring of source rocks and its relationship to mechanical properties. Results from modeling indicate that during hydrocarbon maturation, overpressuring is inevitable in all but the most compliant pore geometries. A consequence is the development of fractured source/reservoir rocks.

Acknowledgments

I wish to thank members of the Stanford Rock and Borehole Project (SRB) for their financial support. The Gas Research Institute funded the experimental work on strength and static and dynamic moduli. Thanks are extended to the companies involved in various aspects of this contracted experimental work: CER corporation, New England Research, Science Applications International Corporation, Core Laboratories, and the Bureau of Economic Geology in Austin, Texas.

During the course of my stay at Stanford, I have benefited greatly from interaction with many individuals.

I express sincerest gratitude to Amos Nur for sharing his insights and interests, and for providing me with financial support. This thesis has benefited greatly from contributed discussions and ideas of Gary Mavko, Richard Nolen-Hoeksema, and Dominique Marion. Thanks also go to Norm Sleep and Simon Klemperer for useful comments as members of my dissertation committee. I am grateful to Rosemary Knight who introduced me initially to the Stanford Rock Physics Project, and to Margaret Muir for her resourcefulness and kindness. It has been an enjoyable experience to be part of this research group. I am grateful to all of the former and present SRB students for their support, stimulating discussions, and continuing friendship.

Finally, I wish to thank my parents and sisters for their motivation and encouragement throughout the course of this thesis.

Contents

List of Tables

List of Figures

Chapter 1

Introduction

Rock mechanical properties that include elastic moduli, pore compressibility, and rock strength are important in a number of reservoir production, engineering, and rock mechanics problems. In reservoir engineering, pore compressibilities are needed to calculate compaction and subsidence. This is a critical factor to consider in design of platforms and well casing. In reservoir production, the use of hydraulic fracture to stimulate oil and gas production requires knowledge of the in situ stress state and rock strength, both of which influence the design of the fracture itself in terms of determination of adequate barriers to fracture growth and prediction of fracture geometry. In rock mechanics, rock strength is needed to determine stability of the rock around the borehole in order to determine proper mud weight, when to set casing, or to gravel pack a formation.

There are several ways to get at these parameters. In situ tests such as hydraulic fracturing can be performed, providing a direct measurement of the least horizontal stress for use in hydraulic fracture design. Laboratory measurements provide a direct measurement of any mechanical property required. The drawback of both techniques is cost, hence the number and availability of measurements is often limited. In addition, with laboratory measurements there tends to be sampling bias towards more highly consolidated rocks, and reconstruction of in situ conditions is not always achieved. An alternative is to determine the mechanical properties indirectly using methods based on propagation of P and S-waves. The advantage of using acoustic logging or seismic surveys is that they are performed on a fairly routine basis, and provide dense measurement coverage at in situ conditions. When combined with density, the acoustic logging tool provides a measurement of dynamic moduli. However, in order to use velocities towards this purpose the relationship between dynamic, static moduli and strength must be understood.

It has long been recognized that a discrepancy exists between static moduli obtained by measuring strain of the rock and dynamic moduli obtained using wave propagation, with the dynamic moduli being invariably greater than static. Existing theories attribute the origin of this discrepancy to measurement scale (Lin and Heuze, 1986); strain amplitude (Winkler and Nur, 1982); and/or frequency. Laboratory investigations have usually concentrated on examining only a few rocks in detail. Pressure dependence and the discrepancy between static and dynamic moduli has been attributed to the presence of micro-cracks (Simmons and Brace, 1965; King, 1983). Experimental observations in support of this concept have shown that as cracks close up with confining pressure, the static moduli approach dynamic ones (Cheng and Johnston, 1981). However, little work has been done on investigating systematically the influence of variables encountered in reservoirs on the ratio of static to dynamic moduli.

All of the above mentioned rock mechanical properties are tied to lithology. Petrography is an important consideration because the deformational properties and textural features of the rock are related. Clay for example, has a marked impact on rock properties. When logging in a shaley environment the effect of clay must be accounted for and corrections made to measurements of electrical conductivity (Waxman and Smits, 1968; Clavier et al., 1977; Johnston, 1987), permeability (Heron, 1987; Neasham, 1977), and velocities (Tosaya and Nur, 1984; Kowallis et al., 1984; Han et al., 1986; Johnston,1987).

Petrography is also an important consideration when trying to extend measurements at the well-bore laterally and correlate geologic facies. In the absence of seismic data, geological information is often the only tool that is used to try to extrapolate data of physical properties obtained at the well laterally into the field. It is hence advantageous to be able to predict variability of physical properties using sedimentological input such as age, depositional environment, degree of cementation, and rock composition.

The objective of this thesis is to investigate the relations between velocity, static moduli, strength, and rock properties. This thesis is organized as follows:

Chapter 2 is aimed at trying to understand the physical meaning behind relationships between physical properties and the influence of clay and cement. Using a simple model for cementation the effect of clay content and cementation on porosity, permeability, and velocity in sandstones and shales is investigated. The model is relevant to sediments initially deposited in a deltaic environment. Results are compared to tight gas sandstone data in order to understand qualitatively the trends observed in core data. This modeling approach might be useful in estimating how physical properties may extrapolate laterally (with diagenesis and composition) and vertically (with age, composition and diagenesis) in a sedimentary sequence.

In chapter 3 the relation between dynamic and static moduli in a suite of East Texas tight gas sandstones and shales is investigated experimentally. In investigating this data set it is found that the relation between static and dynamic moduli is dictated by (1) lithology and (2) confining pressure. In shales, the ratio of dynamic to static moduli is rather insensitive to confining pressure. In contrast, sandstones exhibit strong dependence of the ratio of dynamic to static moduli on confining pressure. This behavior may be attributed to the differing sensitivity of dynamic and static moduli to cracks. For fluid saturated rocks, the discrepancy between static and dynamic is a function of frequency and strain amplitude. A model that estimates the effect of frequency on velocity when combined with Biot's theory, explains the measured total P- and S-wave dispersion in fully water-saturated granite and a variety of sandstones.

In chapter 4 the relation between strength, velocity, porosity, clay content, and confining pressure is investigated using data from uniaxial confined compression measurements on tight gas sandstones and shales. An area-of-contact model is proposed to describe how measured stresses in a rock may be related to intrinsic rock properties, and consequently how we might expect dependence of rock strength on these rock properties to arise. Data indicate that shear strength in the sandstones investigated is influenced by porosity and confining pressure. In shales, strength is more weakly dependent on confining pressure and clay content. The relation between strength and velocity is also examined.

In chapter 5 the consequence that hydrocarbon maturation has on fluid overpressuring is considered. Overpressuring of a source rock depends on the phase change that takes place during kerogen maturation and on pore compressibility. In typical low-permeability source rocks, the process of kerogen maturation can be considered to be a closed system mechanically. Consequently in a given source rock, overpressuring will be controlled by the pore compressibility. It is found that overpressuring is inevitable in all but the most compliant pore geometries. A consequence is the development of fractured source/reservoir rocks.

Chapter 6 contains listings of test data on static and dynamic bulk moduli (Chapter 3) and uniaxial compressive strength (Chapter 4).

References

Cheng, C.H., and Johnston, D.H., 1981, Dynamic and static moduli, Geophys. Res. Let., **8**(1), 39-42.

Clavier, C., Coates, G., and Dumanoir, 1977, The theoretical and experimental bases for the 'Dual Water' model for the interpretation of shaly sands: Presented at the 52nd Ann. Fall Tech. Conf. of Soc. Pet. Eng. Denver.

Han, D., Nur, A., and Morgan, D., 1986, Effect of porosity and clay content on wave velocity in sandstones: Geophysics, **51**, 2093-2107.

Johnston, D. H., 1987, Physical properties of shale at temperature and pressure: Geophysics, **52**, 1391-1401.

Heron, M. M., 1987, Estimating the intrinsic permeability of clastic sediments from geochemical data: Presented at the Soc. Prof. Well-log Anal. Mtg., paper HH.

King, M.S., 1983, Static and dynamic elastic properties of rocks from the Canadian Shield, Int. J. Rock Mech. Min. Sci. & Geomech. Abstr., **20**, 237-241.

Kowallis, B. Jones, L. E. A., and Wang H. F., 1984, Velocity-porosity-clay content; systematics of poorly consolidated sandstones: J. Geophys. Res., **89**, 10355-10364.

Lin, W., and Heuze, F.E., 1986, In-situ dynamic moduli of Mesaverde rocks, compared to static and dynamic laboratory moduli, 27th U.S. Symposium on Rock Mechanics: Key to Energy Production.

Montmayeur, H., and Graves, R.M., 1986, Prediction of static elastic/mechanical properties of consolidated and unconsolidated sands from acoustic measurements: Correlations, paper SPE 15644 presented at the Annual Technical Conference, New Orleans, October 5-8.

Neasham, J. W., 1977, The morphology of dispersed clay in sandstones and its effect on sandstone shaliness, pore space and fluid flow properties: 52nd Annual Fall Technical Conference and Exhibition of the Society of Petroleum Engineers of AIME, Denver, SPE paper 6858.

Simmons, G., and Brace, W. F., 1965, Comparison of static and dynamic measurements of compressibility of rocks: J. Geophys. Res., 70, 5649-5656.

Tosaya, C., and Nur, A., 1982, Effect of the diagenesis of clays on compressional velocity in rocks: Geophys. Res. Let., **9**, 5-8.

Winkler, K.W., and Nur, A., 1982, Seismic attenuation: Effects of pore fluids and frictional sliding, Geophysics, **47**, 1-15.

Waxman, M. H., and Smits, L. J. M., 1968, Electrical conductivities in oil-bearing shaly sands: Soc. Pet. Engrs. J., **8**, 107-122.

Chapter 2

Physical Properties of Tight Gas Sandstones and Shales

Abstract

Three main classes of lithology are observed from petrographic analyses of a suite of East Texas tight gas sandstones: Sandstones with low clay content and high amounts of quartz cement; shaley sandstones with variable amounts of authigenic clay, detrital clay, and secondary porosity; and shales with high amounts of detrital clay in which sand grains are suspended. We propose to explain the tight gas sandstone petrography with a diagenetic model in which: (1) fluid flow is the driving mechanism for cementation and feldspar alteration, and (2) fluid flow is limited by clay. From model results we identify two regimes that match both petrographic description and laboratory measured rock properties: (1) In sandstones and shaley sandstones, cement volume fraction is inversely proportional to clay content. The effect of increasing cement is to decrease porosity and is mostly effective at low clay content (between zero and 10 - 20 percent). This leads to an overall increase in porosity and permeability, and a decrease in velocity with increasing clay content, as rocks with higher clay content are less cemented. (2) In shales, the amount of cement is strongly reduced.

2.1 Introduction

Clay content is recognized as being an important variable in controlling the physical properties of reservoir rocks. The influence of clay has been investigated extensively in electrical (Waxman and Smits, 1968; Clavier et al., 1977; Johnston, 1987; Givens, 1988), transport (Heron, 1987; Neasham, 1977), and elastic properties (Tosaya and Nur, 1984; Kowallis et al., 1984; Han et al., 1986; Johnston, 1987). In addition, we find that cement may be an important parameter in controlling storage and transport properties (Morris et al., 1979; Wood, 1989) and elastic properties (Galloway, 1979).

In this chapter we analyze the relationships between physical properties and the influence of clay and cement in tight gas sandstones using a set of core data. Our approach is to use physical models in order to gain a better understanding of the physical mechanisms behind the data.

We begin with a simple sand/clay mixture model which allows us to estimate porosity, permeability, and velocity as a function of clay content. By making some simple assumptions about fluid diffusion in a rock mass, we try to simulate how the addition of cement and alteration of feldspars causes changes in porosity, permeability, and velocity away from the initial model. Finally, we compare the simulation to tight gas sandstone data.

2.2 Samples and Petrography

Tight gas sandstone and shale data from 88 cores were provided by the Gas Research Institute (GRI). The cores are from seven of GRI's cooperative wells in the Travis Peak Formation in East Texas (Dutton and Finley, 1986), at depths ranging from 6,000 to 10,000 feet. Helium porosity of the samples ranges from .8 to 20 percent and clay content ranges from 0 to 63 percent by volume. Clay content was determined from thin-section point count. Laboratory measurements include fully water-saturated ultrasonic compressional V_p and shear V_s velocity, porosity, and gas permeability as a function of confining pressure.

The samples consist of low-permeability, fine-grained sandstones, siltstones, and mudstones. Sediments were deposited initially as a complex of delta lobes that prograded over a broad continental shelf and were later reworked by fluvial processes as depositional centers shifted location (Dutton, 1987; Dutton and Finley, 1986). Sandstones in the Travis Peak are fine grained quartz arenites and feldspathic sandstones of average composition $Q_{95}F_{3.8}R_{1.2}$ (quartz 95 %, feldspar 3.8 %, and rock fragments 1.2 %). Much of the original porosity in the sandstones has been reduced by quartz overgrowth cementation. Partial dissolution of feldspars has produced authigenic clays (illite and chlorite) and created secondary porosity. Siltstones and mudstones in the Travis Peak Formation contain detrital clay matrix composed of illite and chlorite as identified from x-ray diffraction (Dutton, 1987).

From the petrographic descriptions we observe three main classes of lithology (Figure 2.1) which we distinguish based on the mineral constituents (quartz and feldspar are predominant framework constituents, detrital clay is the predominant matrix constituent) and their arrangement as load-bearing phases in the rock (based on thin-section photomicrographs and deformational rock properties). Approximate divisions between these lithologies are based on total clay volume fraction, C: (A) The sandstone lithology contains low amounts of clay. Quartz and feldspar grains are well-cemented by quartz overgrowths and form the load-bearing frame of the rock. Total clay volume fraction ranges from approximately 0 to 17 percent. (B) The shaley sandstone lithology contains variable amounts of quartz cement, authigenic clay, detrital clay, and secondary porosity. Both clay and quartz are load-bearing. Total clay volume fraction ranges from approximately 17 to 38 percent. (C) The shale lithology (includes sandy shales) contains quartz and feldspar grains which are suspended in a detrital clay or carbonate matrix with very little cement. The clay or carbonate matrix is load-bearing. Total clay volume fractions are greater than

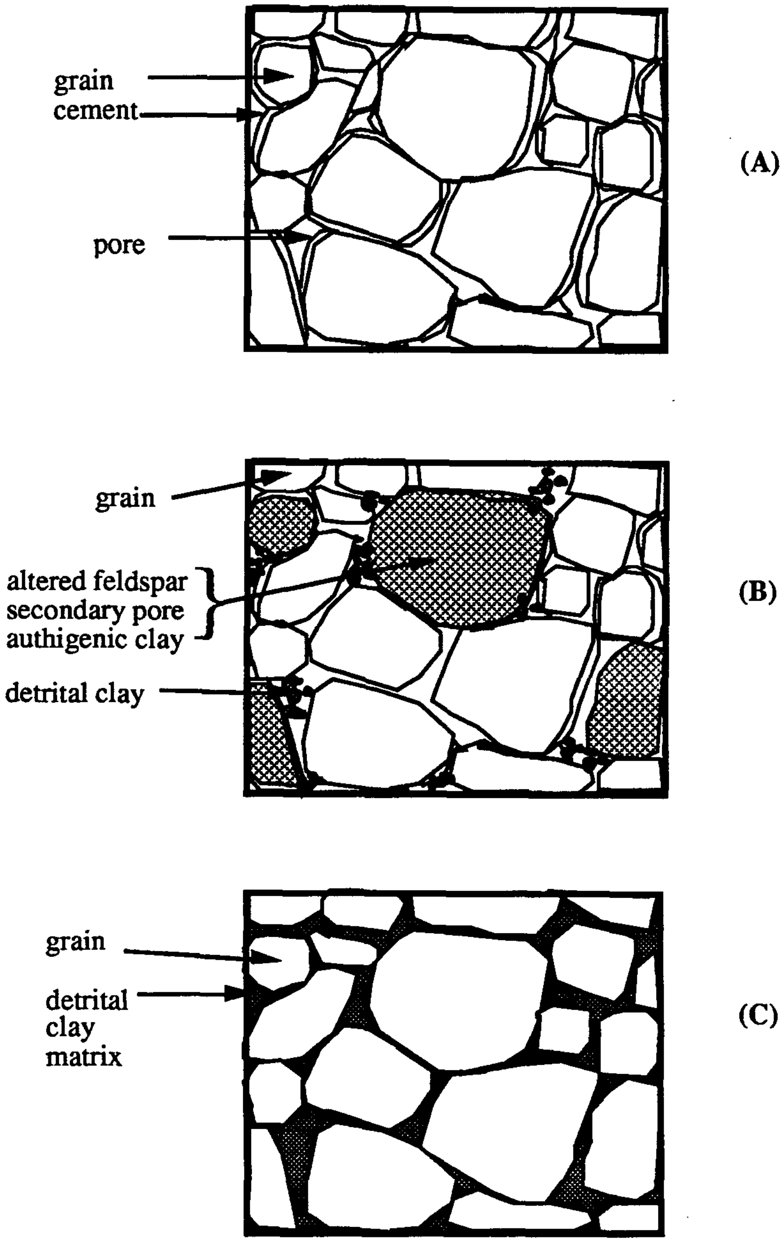

Figure 2.1: Three main types of lithology found in tight gas sandstones. Approximate divisions are based on clay volume fraction: Sandstones ($0 < C < .17$), shaley sandstones, ($.17 \leq C \leq .38$), and sandy shales and shales, ($C > .38$), where C is the clay volume fraction.

approximately 38 percent.

Figures 2.2 - 2.4 are photo-micrograph examples of the three lithologies. In Figure 2.2 we see an example of the sandstone lithology. Detrital quartz grains are cemented extensively by quartz overgrowths. Figure 2.3 is an example of a shaley sandstone that contains detrital clay filling the pore space. Figure 2.4 shows an example of a sandy shale containing 55 percent clay. Notice how the quartz grains are suspended in the clay matrix.

From the petrographic data we note that an apparent inverse relation exists between quartz cement and clay content (Figure 2.5) (ankerite, an iron rich carbonate, occludes pore space in the same manner as detrital clay and is therefore included in the clay fraction). We observe that quartz cement decreases approximately linearly from 25-35 percent when no clay is present to zero at 30-40 percent clay volume fraction. We will try to explain how this observation might arise in section 2.4.

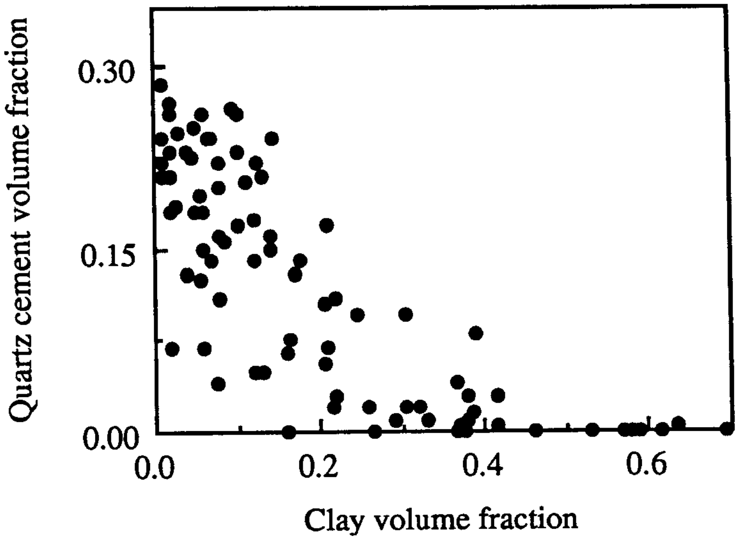

Figure 2.5: Quartz cement volume fraction vs. clay data from thin-section point-count analysis. Data show an overall decrease of quartz cement with increasing clay content suggesting that clay is a limiting factor for cementation.

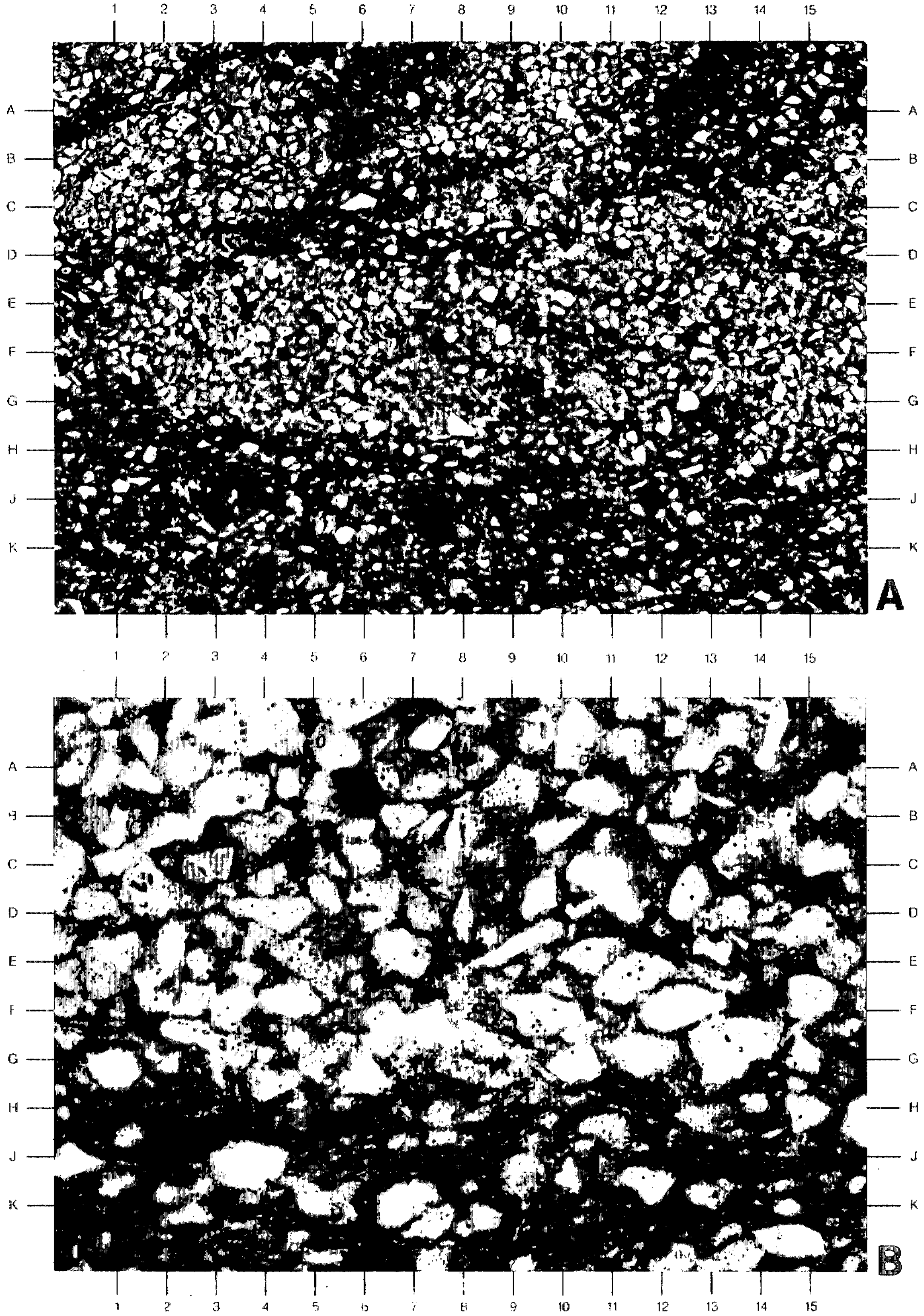

Figure 2.2: Photomicrograph of a clean sandstone containing abundant quartz overgrowths. Sample is from the Prairie Mast A 1 well at a depth of 9980.5 feet. A detailed description is found on the following page.

Travis Peak Formation
A.T. Mast A-1 Well
Prairie Producing
Nacogdoches County, Texas

Depth: 9980.5 Feet

Plate A

ROCK TYPE: Sandstone
ROCK NAME (FOLK, 1982): Quartzarenite
FRAMEWORK GRAINS: Monocrystalline quartz (B-C1-2, E12, J7-8)
ACCESSORY GRAINS: Rutile (locally concentrated; black; above A6-7, E15, K12, E2)
MATRIX: Detrital clay rims define the edge of quartz grains throughout the view (brown; A-B6, E11-12)
CEMENTS: Quartz overgrowth cement (D9-10, C3, H7-8)
PORE TYPES: Fracture pores are present in other areas of the thin section
POROSITY NETWORK: Poorly developed, moderately well interconnected
RESERVOIR QUALITY: Poor
COMMENTS: In fractured areas of the sample, sheared rock material is present.
MAGNIFICATION: 31X, plane-polarized light

Plate B

This high-magnification emphasizes the great extent of quartz overgrowth (D2, A-B14-15, J7) cementation. Detrital clay rims on quartz grains display a yellow-green birefringence (J3, D1, B9-10). A zircon grain can be seen at G8. (125X, cross-polarized light)

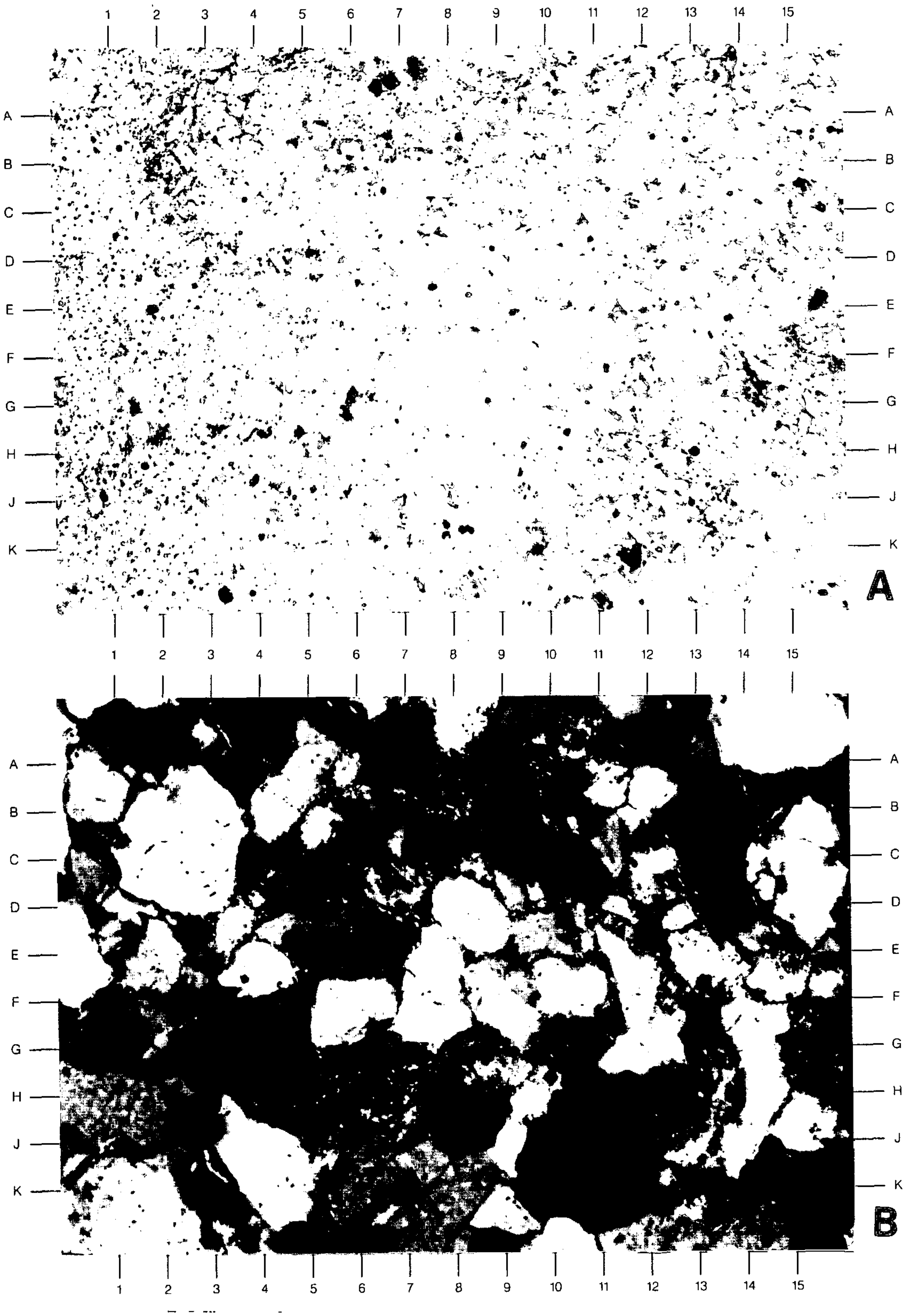

Figure 2.3: Photomicrograph of a shaley sandstone containing detrital clay. Sample is from the Sam Hughes 1 well at a depth of 7057 feet. A detailed description is found on the following page.

Travis Peak Formation
Sam Hughes 1 Well
Clayton Williams Jr.
Panola County, Texas

Depth: 7057.5 Feet

Plate A

ROCK TYPE: Siltstone
ROCK NAME (FOLK, 1982): Sublitharenite
FRAMEWORK GRAINS: Monocrystalline quartz (D2, E7, H13)
ACCESSORY GRAINS: Muscovite (F-G4), rutile (black; C-D10-11)
MATRIX: Detrital clay is visible throughout the view
PORE TYPES: Micropores associated with detrital clay, fracture pore from B1-B6
POROSITY NETWORK: Poorly developed, poorly interconnected
RESERVOIR QUALITY: Poor
MAGNIFICATION: 31X, plane-polarized light

Plate B

This view of a coarse grained, well sorted siltstone highlights brownish detrital clay occupying interstitial areas. Residual organic material can be observed as black particles throughout the view (above A11-12, E9, E6, G7). (125X, plane-polarized light)

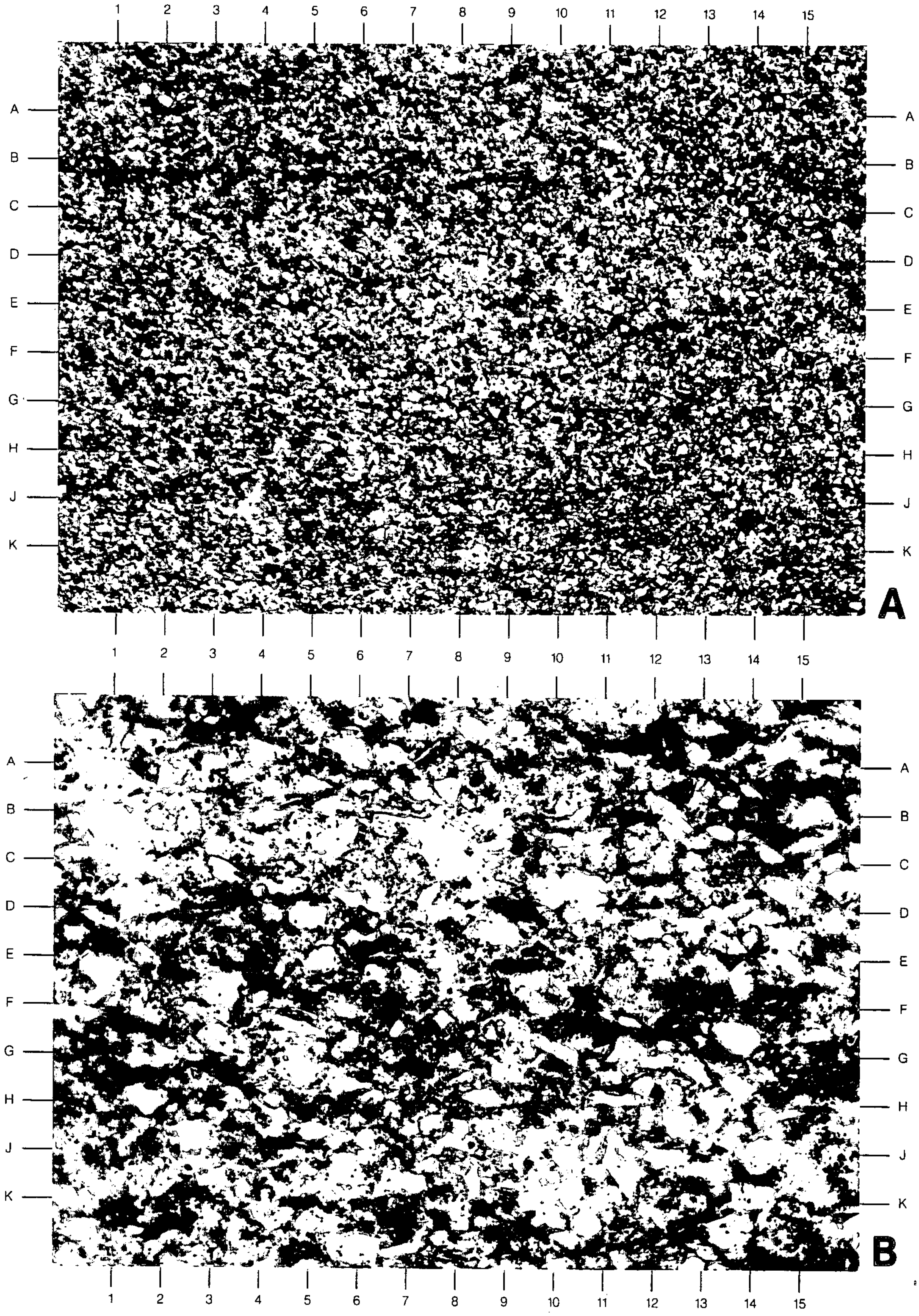

Figure 2.4: Photomicrograph of a shale. Note the quartz grains that are suspended in a clay matrix. Sample is from the B. F. Phillips well at a depth of 8227.5 feet. A detailed description is found on the following page.

Travis Peak Formation
B.F. Phillips 1 Well
ARCO Oil & Gas
Smith County, Texas

Depth: 8227.5 Feet

Plate A

ROCK TYPE: Silty Mudstone
ROCK NAME (FOLK, 1982): Not applicable
DETRITAL CONSTITUENTS: Detrital clay (brown; distributed throughout view), monocrystalline quartz (C1, K5-6, E11), chert (G10-11, E4-5)
AUTHIGENIC CONSTITUENTS: Ankerite (stained blue; F9-10)
PORE TYPES: Fracture pores occur in other areas of the sample
POROSITY NETWORK: Poorly developed, poorly interconnected
RESERVOIR QUALITY: Poor
COMMENTS: Silty mud areas are intermixed with muddy silt areas
MAGNIFICATION: 31X, plane-polarized light

Plate B

The highlight of this high-magnification photomicrograph is the presence of brownish detrital clay throughout interstitial areas of silt. Crystals of dolomite (C3, B1-2, F9) and ankerite (blue-stained; F4, C-D15) are scattered through the view. (125X, plane-polarized light)

2.3 Initial model

Consider a sequence of unconsolidated fluvial and deltaic sediments as the initial model. These sediments are modeled as a sand/detrital-clay sequence. The sandstone end-member is a water-saturated loose packing of sand grains. The shale end-member is a clay-water suspension. At intermediate clay concentrations, detrital clay fills the pore space (domain of shaley sand) until the sand pore space becomes filled completely; at higher clay concentrations sand grains become suspended in a clay matrix (sandy shale and shale). Storage, elastic, and transport properties of the above described rock sequence have been modeled by Marion (1990) and are used as our initial model.

2.3.1 Porosity

Equations for porosity corresponding to this initial model are given by

$$\phi = \phi_s - C\,(1-\phi_c) \qquad C \leq \phi_s \tag{2.1}$$

$$\phi = C\,\phi_c \qquad C > \phi_s \tag{2.2}$$

where ϕ_s is the porosity of the clay free sand, ϕ_c is micro-porosity of the detrital clay, and C is the volume fraction of detrital clay.

2.3.2 Permeability

Permeability is estimated using the Kozeny-Carman equation (Carman, 1956):

$$k = \frac{\phi^3}{k_o\, T^2\, S^2} \tag{2.3}$$

where k, T, ϕ, and S are the permeability, tortuosity, porosity, and specific surface area (surface area per unit bulk volume) respectively, and k_o is an empirical constant found to be equal to 2.5 (Carman, 1956). Tortuosity, T, and specific surface area, S, of the sand-clay composite are expressed as (Marion, 1990)

$$T = T_s\left[1 + \frac{C}{\phi_s}(T_c - 1)\right] \quad C \leq \phi_s \tag{2.4}$$

$$T = T_c\left[1 + \frac{T_s - 1}{\phi_s - 1}(C - 1)\right] \quad C > \phi_s \tag{2.5}$$

$$S = S_s + CS_c \quad C \leq \phi_s \tag{2.6}$$

$$S = S_s\frac{1 - C}{1 - \phi_s} + CS_c \quad C > \phi_s \tag{2.7}$$

where T_s, T_c, S_s, S_c, and C, are tortuosity of the clean sandstone, micro-tortuosity of the detrital clay, surface area to volume ratio of the clean sand, surface area to volume ratio of the clay, and clay volume fraction respectively. The surface-area-to-volume ratio of the sandstone is expected to be proportional to the sand porosity and can be approximated by $3(1 - \phi_s)/r$ for sphere-shaped grains, where r is the average sand-grain radius.

2.3.3 Velocity

In an isotropic elastic material, the compressional V_p and shear V_s velocities are given by

$$V_p = \sqrt{\frac{K + (4/3)G}{\rho}} \tag{2.8}$$

$$V_s = \sqrt{\frac{G}{\rho}} \tag{2.9}$$

where K, G, and ρ are the bulk modulus, shear modulus, and bulk density of the fluid-saturated sediment. These quantities are computed for the sand-clay mixture as follows.

Sand and shaley sands, $C \leq \phi_s$: In sandstones and shaley sandstones we estimate the fluid-saturated bulk and shear moduli using the Bound Averaging Method (Marion and Nur, 1991). This method uses theoretical upper and lower bounds (eg. Voigt (1928) and Reuss (1929), Hashin-Shtrikman (1963)) for the mineral/pore-fluid two-phase composite. The idea behind this method is that the elastic moduli of a fluid-saturated rock can be expressed as a weighted arithmetic average between the two bounds, using the same arithmetic average regardless of the fluid saturant. Bulk and shear modulus of the fluid saturated rock are expressed as:

$$K = K^- + (K_{fr} - K_{fr}{}^-)\left(\frac{K^+ - K^-}{K_{fr}{}^+ - K_{fr}{}^-}\right) \tag{2.10}$$

$$G = G^- + (G_{fr} - G_{fr}{}^-)\left(\frac{G^+ - G^-}{G_{fr}{}^+ - G_{fr}{}^-}\right) \tag{2.11}$$

where K_{fr} is the measured bulk modulus of the dry sand frame. $K_{fr}{}^+$ and $K_{fr}{}^-$ are the dry elastic moduli computed using theoretical upper and lower bounds respectively. K^+ and K^- are the fluid-saturated elastic moduli computed using theoretical upper and lower bounds respectively (Marion and Nur, 1991). To estimate these quantities we use the Voigt (1928) and Reuss (1929) bounds here, expressed using a power law relation of the constituent moduli:

$$K_{fr}{}^+ = ((1 - \phi_s)K_q{}^p + \phi_s K_a{}^p)^{1/p}, \quad p = 1 \tag{2.12}$$

$$K_{fr}{}^- = ((1 - \phi_s)K_q{}^p + \phi_s K_a{}^p)^{1/p}, \quad p = -1 \tag{2.13}$$

$$K^+ = ((1 - \phi_s)K_q{}^p + \phi_s K_{fl}{}^p)^{1/p}, \quad p = 1 \tag{2.14}$$

$$K^- = ((1 - \phi_s)K_q{}^p + \phi_s K_{fl}{}^p)^{1/p}, \quad p = -1 \tag{2.15}$$

where K_q, K_a, K_{fl}, and ϕ_s are the bulk modulus of quartz, bulk modulus of air, bulk modulus of the water-clay suspension, and sand porosity. p is the coefficient used in the power average, equal to 1 and -1 for the upper and lower bounds respectively. Parameters required to compute shear modulus are similar.

As clay is dispersed within the pore space, clay is considered to be part of the fluid phase. Bulk and shear modulus of the clay-water composite fluid, K_{fl} and G_{fl} in equations (2.14) and (2.15), are estimated using a power law average of the constituent moduli in the form:

$$K_{fl} = (C{K_c}^p \;+\; (1-C){K_w}^p)^{1/p} \tag{2.16}$$

$$G_{fl} = (C{G_c}^p \;+\; (1-C){G_w}^p)^{1/p} \tag{2.17}$$

where K_c, G_c, K_w, and G_w the bulk and shear modulus of the clay mineral, and bulk and shear moduli of water respectively. The power, p, used in averaging here is taken equal to .8 to reproduce the trend of experimental data on pure kaolinite (Yin et al., 1988). This power of .8 used in averaging indicates that the kaolinite mineral phase is predominantly load-bearing.

Saturated bulk density is given by

$$\rho = (1-\phi_s)\rho_q \;+\; C(1-\phi_c)\rho_c + (\phi_s - C(1-\phi_c))\rho_w \tag{2.18}$$

where ρ_q, ρ_c, ρ_w, are the density of quartz grains, clay mineral, and water respectively.

Sandy shales and shales $C \leq \phi_s$: In sandy shales and shales, we consider that quartz grains are completely suspended in the clay matrix. Bulk and shear modulus are described a power law of the constituent moduli using a power of $p = -1$. This is also known as the Reuss (1929) or an isostress average:

$$K = ((1-C){K_q}^p \;+\; C{K_{fl}}^p)^{1/p}, \quad p=-1 \tag{2.19}$$

$$G = ((1-C){G_q}^p \; + \; C{G_{fl}}^p)^{1/p}, \qquad p = -1 \tag{2.20}$$

where K_{fl} and G_{fl} are from equations (2.15) and (2.16). Bulk density is expressed as

$$\rho = (1-C)\rho_q \; + \; C(1-\phi_c)\rho_c + C\phi_c\rho_w \tag{2.21}$$

where ρ_q, ρ_c, ρ_w, are the density of quartz grains, clay mineral, and water respectively.

Table 2.1

Mineral and Fluid Properties	K (GPa)	G (GPa)	Density, ρ (g/cm^3)
Quartz	38	44	2.65
Clay (excludes micro-porosity)	25	10	2.75
Water	2	0	1.0

Bulk Properties	K (GPa)	G (GPa)	Porosity, ϕ (%)	Tortuosity, T	Surface area, S (m^2/g)
Sand	1.8[1]	1.7[1]	36	1.5	.014
Shale	eq.(2.19)	eq.(2.20)	10-2[2]	8	2

[1] Ottawa sand from Domenico (1977).

[2] Porosity of the shale, ϕ_c, varies linearly from 10 % at $C = \phi_s$ to 2 % at $C = 1$.

The initial model described above and shown in Figure 2.6, is calculated with the input parameters listed in Table 2.1. The values listed are reasonable estimates for quartz and clay mineral constituents. We find however, that to describe the shales from the Travis Peak Formation, we need to consider variable shale porosity, ϕ_c, that decreases with increasing clay content (suggesting that shale is compacted more at higher clay fractions). We also find that to describe the permeability of the shales using the Kozeny-Carman equation, we need to use a value of specific surface area for clay (2 m^2/g) that is lower than the expected range of surface areas (10-500 m^2/g)

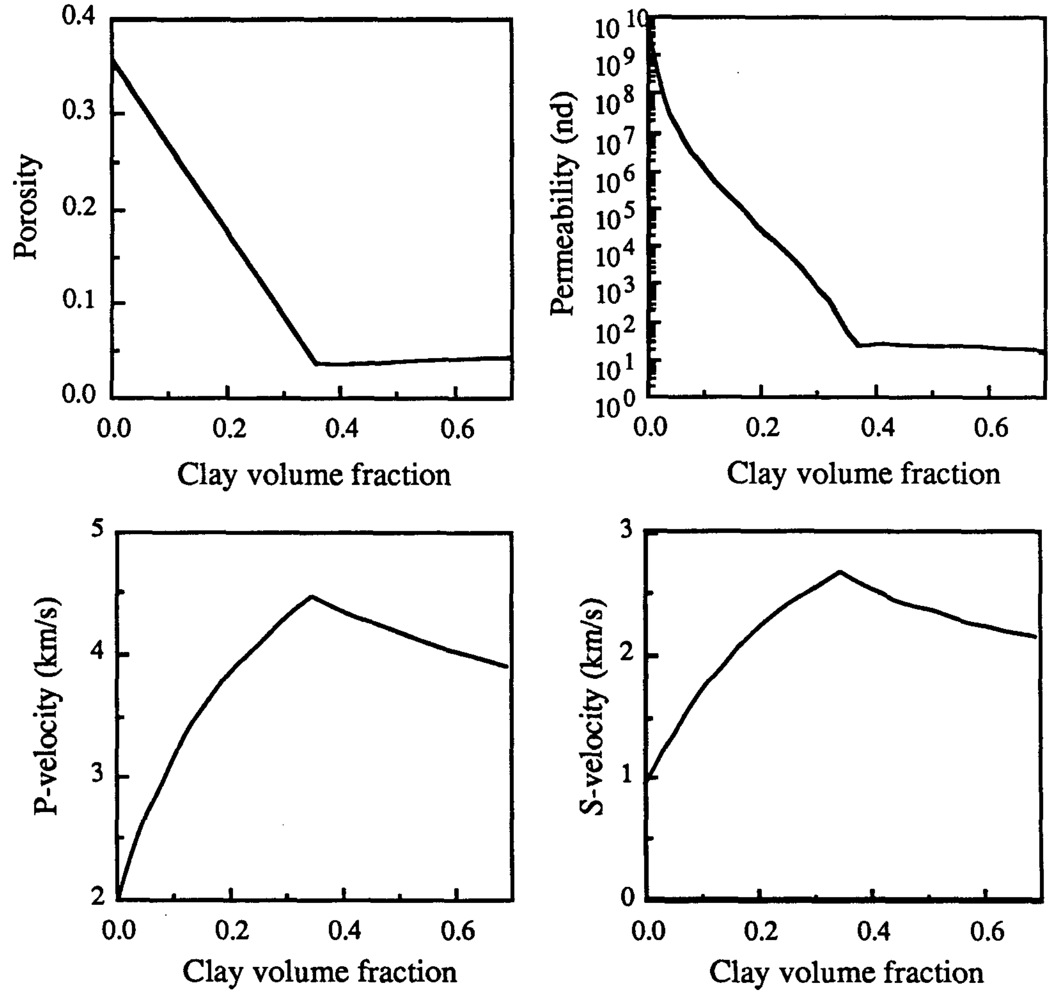

Figure 2.6: Initial model of sand/detrital-clay sequence before cementation. For clay volume fractions less than ϕ_s=36 percent, clay only partially fills the pore space and causes porosity and permeability to decrease with increasing clay. For clay volume fractions greater than ϕ_s=36 percent, quartz grains are suspended in clay matrix. Permeability and porosity remain low and P- and S- velocities decrease slightly with increasing clay content.

(Knight, 1986) of pure clays. This may suggest that the Kozeny-Carman equation may not describe very well the behavior of shales or that effective specific surface area that affects gas permeability in these shales is lower.

2.4 Quartz cementation

The effect of quartz cementation on reducing porosity in sandstones has been documented through modeling (Blatt, 1979; Berner, 1980; Wood, 1989; Bjørlykke,1979) and in petrographic studies (Heald, 1966; Hayes, 1979). We wish to examine the influence that clay content may have on the diagenetic process of quartz cementation. Rather than investigating one rock type, we examine a full spectrum of sedimentary rocks corresponding to a sand/detrital-clay sequence. To simulate the effect of quartz cementation and its effect on porosity, permeability, and velocity, we use Darcy's law and the initial permeability model for the sand/detrital-clay sequence.

The volumetric flow rate of fluid through the pore space is computed using Darcy's Law:

$$Q_w = \frac{kA}{\mu}\frac{dP}{dx} \tag{2.22}$$

where Q_w, k, μ, A, and $\frac{dP}{dx}$ are the volumetric flow rate, permeability, fluid viscosity, cross-sectional area, and pressure gradient respectively.

In order for quartz to precipitate as cement we assume that two conditions exist: First, the pore fluid must have an excess concentration of silica. This may occur when pore fluid that is initially saturated with silica changes equilibrium conditions of temperature, pH, and/or pore pressure. The symbol E_q is used to denote the excess silica concentration that will be deposited (usually expressed in ppm). The volume of excess cement that flows across the surface with area, A, over time Δt is, $V_{ex(\Delta t)} = Q_w \Delta t E_q$. Second, we assume that quartz overgrowths precipitate as a continuous mineral phase. Hence, we consider that quartz precipitates in the pore space which is not occluded by clay. In sandstone and shaley sandstones, this pore space is equal to $\phi_s - C$. In our model for shales, clay occludes all available pore space. Consequently, we will only treat the case of sandstones and shaley sandstones.

In this analysis, we consider that all the excess silica in solution precipitates, so the volume fraction of quartz that gets deposited, $V_{q(\Delta t)}$, is equal to the total excess volume fraction of quartz in solution, $V_{q(\Delta t)} = V_{ex(\Delta t)}$. This silica that precipitates as quartz cement is proportional to the amount of fluid that flows through the pore space:

$$V_{q(\Delta t)} = E_q \, V_{w(\Delta t)} \tag{2.23}$$

where, $V_{q(\Delta t)}$, the volume fraction of quartz cement at any time must not exceed the free pore space available. E_q is the excess concentration of silica in solution that deposits.

If we consider that mineral gets deposited in a volume of rock, V, the volume fraction of fluid, $V_{w(\Delta t)}$, that flows through the pore space during a period of time, Δt, is

$$V_{w(\Delta t)} = \frac{Q_w \Delta t}{V} \tag{2.24}$$

Equation 2.23 can also be expressed using equation 2.22 and 2.24 as

$$V_{q(\Delta t)} = E_q \, \frac{\Delta t}{V} \, (\frac{kA}{\mu} \frac{dP}{dx}) \tag{2.25}$$

We assume that $\frac{dP}{dx}$ in equation 2.25 is constant. This is a reasonable assumption for a homogeneous medium. From equation 2.25 we see that the volume fraction of quartz cement deposited during a time interval, Δt, depends on permeability. As cementation proceeds, porosity, permeability, and the rate of flow decrease causing the rate of cementation to decrease in turn. Initially, there is no quartz cement. We numerically simulate the cementation process stepping through time:

$$V_{q(t+\Delta t)} = V_{q(t)} + V_{q(\Delta t)} \tag{2.26}$$

With each time increment, a new value of porosity, permeability and cement volume fraction are computed. The total volume of quartz cement that deposits in a given time interval must not exceed the available porosity. An outline of the procedure and computer programs used are given in Appendix B.

Figure 2.7 shows quartz cement volume fraction as a function of dimensionless time computed using the initial sand/detrital-clay model and the input parameters listed in Table 2.2. Note how the cementation rate decreases with increasing diagenesis, indicating that the process of cementation is self limiting: Increasing cement reduces the permeability, which in turn limits the flow that supplies additional cement.

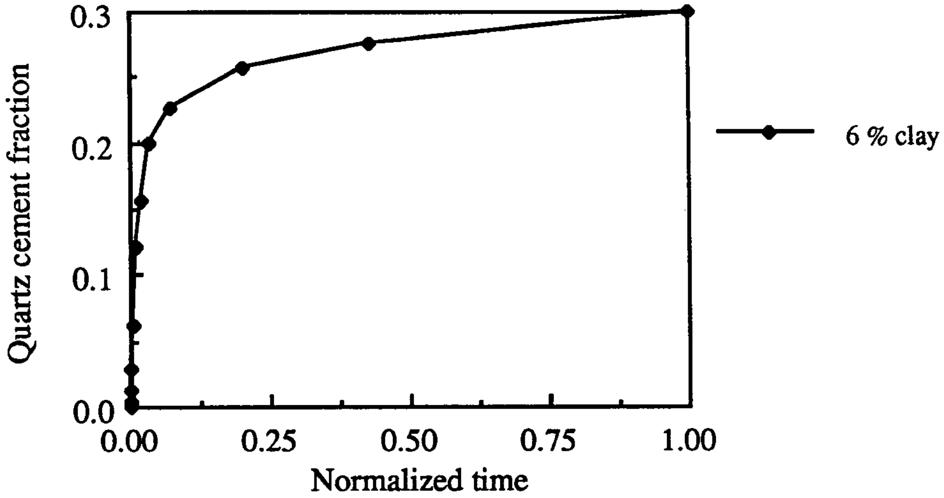

Figure 2.7: Model results for quartz cement fraction vs. normalized time indicate that cementation is a self-limiting process. The example shown here is for a sandstone containing 6 % clay.

In addition, we expect that an increase in the amount of clay will decrease permeability and therefore decrease the amount of fluid flow and cementation. This is suggested in the petrography data (Figure 2.5) where quartz cement is inversely proportional to clay content. Our simulation results (Figure 2.8) show the same trend which is a nearly linear decrease in cement volume fraction with increasing clay content. Three stages of diagenesis are shown (corresponding to .3, 6, and 100 million years at fixed E_q =10 ppm). We note that quartz cement depends linearly on time and cementation efficiency=E_q. Hence, time and efficiency are interchangeable and the curves shown in Figure 2.8 could correspond equally to cement vs. clay at a fixed time and variable rates of cementation efficiency (E_q = .03, .6, and 10 ppm at 100 million years).

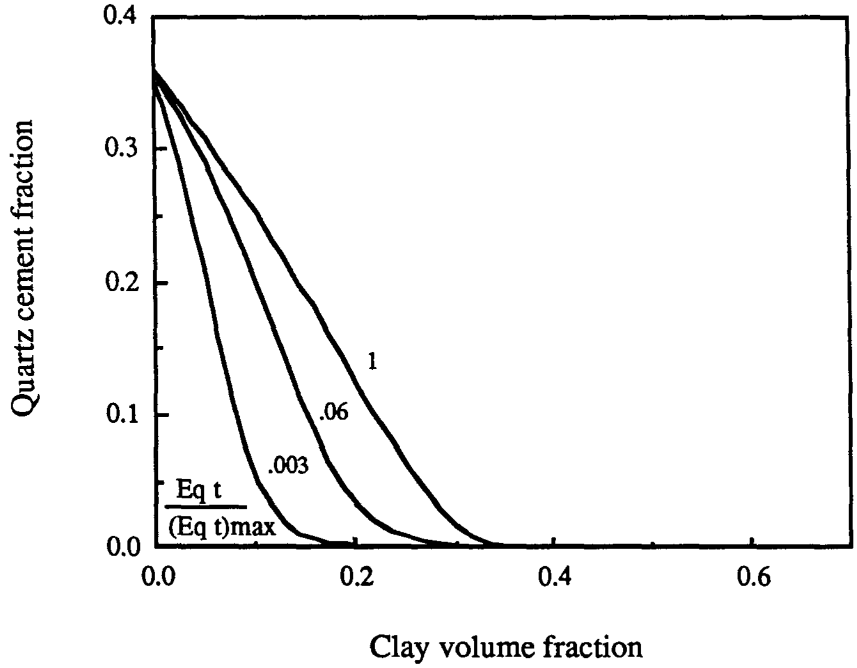

Figure 2.8: Simulation results for the relation between quartz cement and clay content at various degrees of diagenesis. The model agrees qualitatively with the data (Figure 2.5) showing a decrease in cement with increase in clay content. For a given clay content, cement increases with diagenesis as more fluid flows through the rock. Curves represent increasing degrees of diagenesis indicated by the normalized product of cementation efficiency and elapsed time.

In our simulation, we have predicted how variability in quartz cement vs. clay content data may arise during diagenesis as a function of time and cementation efficiency. We note that variability of cement volume fraction may be caused by other factors. One possibility is barriers to fluid flow that would change pressure gradients locally. Variability in the temperature gradient of upwhelling fluids that cool may also cause the concentration of excess silica in solution to vary. We now examine how quartz cementation affects porosity, permeability, and velocity.

Table 2.2

Distance fluid travels is 680 m/yr.
$Q_w = 2 \text{ x } 10^7 \text{ m}^3/\text{s}$, in sandstone of 100 md permeability
$V = 1 \text{ cm}^3$
$E_q = 10$ ppm
$\eta = 2 \text{ x } 10^{-4}$ Pa s

2.4.1 Effect on porosity

During a time interval, Δt, the amount of porosity reduced by quartz overgrowth is equal to the volume fraction of quartz cement deposited, $\Delta\phi_{(\Delta t)} = V_{q(\Delta t)}$. If we assume that the initial porosity is given by equation (2.1), then we can simulate the porosity reduction process by stepping through time:

$$\phi_{(t+\Delta t)} = \phi_{(t)} - V_{q(\Delta t)} \tag{2.27}$$

where $V_{q(\Delta t)}$ from equation 2.25 is input at each successive time increment.

Figure 2.9 shows the influence of cementation and clay content on porosity computed using input parameters listed in Table 2.2. Three stages of diagenesis are shown (corresponding to .3, 6, and 100 million years at fixed E_q =10 ppm). Notice that at low clay volume fractions that initial permeability is highest (Figure 2.6) and porosity changes most from the initial model. Thus, quartz cementation dramatically reduces porosity in low-clay, high-permeability rocks whereas it has little effect on shaley sandstones. Hence, from porosity vs. clay curves (Figure 2.9), we expect to see a large amount of variability of porosity data in sandstones and shaley sandstones (0 to 20-30 % clay) with a global increase of porosity with increasing clay, followed by a decrease of porosity with increasing clay until the shale domain (30-40 % clay) is reached.

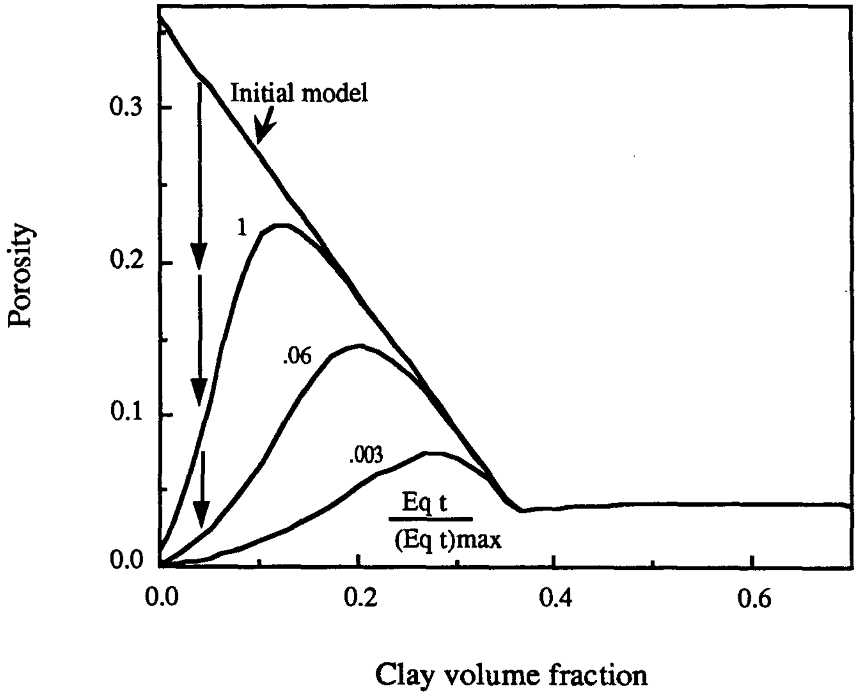

Figure 2.9: Effect of quartz cement on porosity. Cement acts to decrease porosity and is mostly effective at low clay content (between 0 and 10-20 %). This leads to an overall increase in porosity with increasing clay. Curves represent increasing degrees of diagenesis indicated by the normalized product of cementation efficiency and elapsed time.

2.4.2 Effect on permeability

The effect of cementation on permeability appears mostly through the reduction of porosity due to cementation. Initial permeability (equation 2.3) and permeability at $t + \Delta t$ is estimated using the Kozeny-Carman equation

$$k_{(t+\Delta t)} = \frac{\phi_{(t+\Delta t)}{}^3}{k_o \, T^2_{(t+\Delta t)} \, S^2_{(t+\Delta t)}} \tag{2.28}$$

where k, T, ϕ, and S are the permeability, tortuosity, porosity, and specific surface area (surface area per unit bulk volume) respectively, and k_o is an empirical constant set equal to 2.5 (Carman, 1956). At each successive time increment, porosity is input from equation (2.27), and surface area, and tortuosity are recomputed (see Appendix

B for detailed procedure).

Permeability is computed using the initial sand/detrital clay model and the input parameters listed in Table 2.1. Using the Kozeny-Carman equation we find that the decrease in permeability with cementation is proportional to porosity cubed. Hence, the permeability vs. clay content curve during diagenesis mimics the porosity vs. clay content curve as shown in Figure 2.10. Permeability is reduced primarily in the sandstones, and is changed only slightly in shaley sandstones. Note the potential for scatter of permeability vs. clay data as a function cementation in sandstones and shaley sandstones. We also note that the decrease in quartz cement with increasing clay content leads to a slight increase of permeability with increasing clay in sandstones.

2.4.3 Effect on velocity

To compute the effect of cementation on P- and S-velocity we use coefficients from the regression equations (Table 3.3) discussed in Chapter 3 to describe the effect of quartz cementation on bulk and shear frame moduli. Quartz cement acts to increase frame bulk and shear modulus and to increase bulk density. Initial values of the dry bulk and shear frame moduli are for uncemented sand (Table 2.1). At $t + \Delta t$ dry bulk and shear frame moduli are calculated using

$$K_{fr(t+\Delta t)} = K_{fr(t)} + V_{q(\Delta t)} 73.5 \tag{2.29}$$

$$G_{fr(t+\Delta t)} = G_{fr(t)} + V_{q(\Delta t)} 87.5 \tag{2.30}$$

$$\rho_{(t+\Delta t)} = \rho_{\Delta t} + V_{q(\Delta t)} \rho_q \tag{2.31}$$

where the coefficients in equations 2.29 and 2.30 in GPa represent the empirical increase in stiffness of dry frame moduli with increase in quartz cement. Having these new values of $K_{fr(t+\Delta t)}$, $G_{fr(t+\Delta t)}$, $\phi_{s(t+\Delta t)}$, and $\rho_{(t+\Delta t)}$, we compute the saturated moduli using the Bound Averaging method (Marion and Nur, 1991) as described in section 2.3.3.

Using the initial model and quartz cement computed using the parameters listed in Table 2.2, we obtain the relationships between P- and S-velocity and clay at various degrees of diagenesis. The effect of cementation is to increase frame stiffness in sandstones and shaley sandstones (from zero to 10-30 percent clay). Hence, velocity increases dramatically from the initial model at low clay concentrations and increases less in shaley sandstones. This results in the curves shown in Figure 2.11 with a net decrease in velocity with increasing clay primarily due to more extensive cementation of the cleaner sandstones.

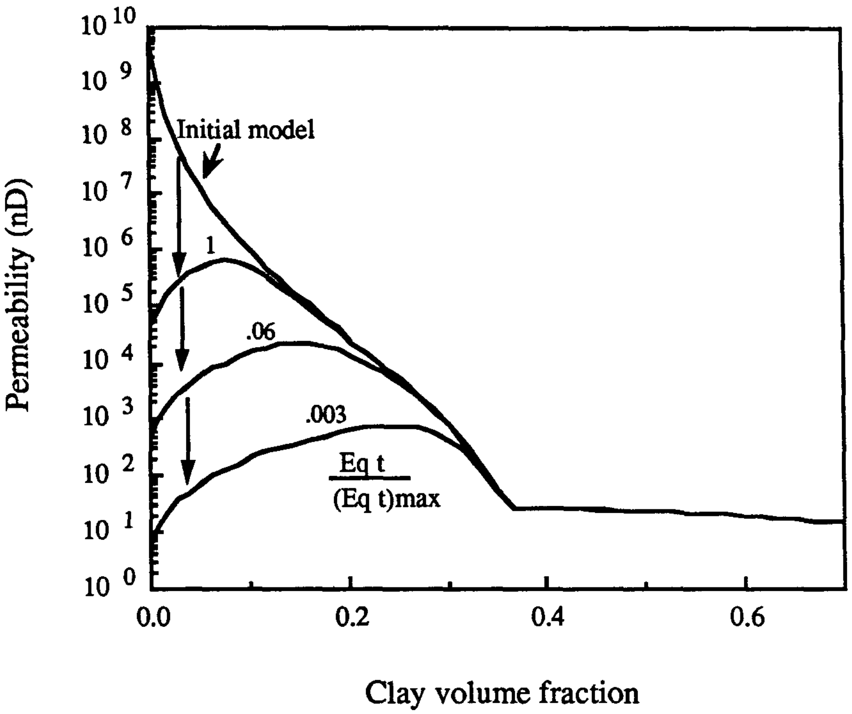

Figure 2.10: Effect of cementation on permeability. Cement acts to decrease permeability and is mostly effective at low clay (between 0 and 10-20 %). In sandstones, this leads to a slight increase in porosity with increasing clay. Curves represent increasing degrees of diagenesis indicated by the normalized product of cementation efficiency and elapsed time.

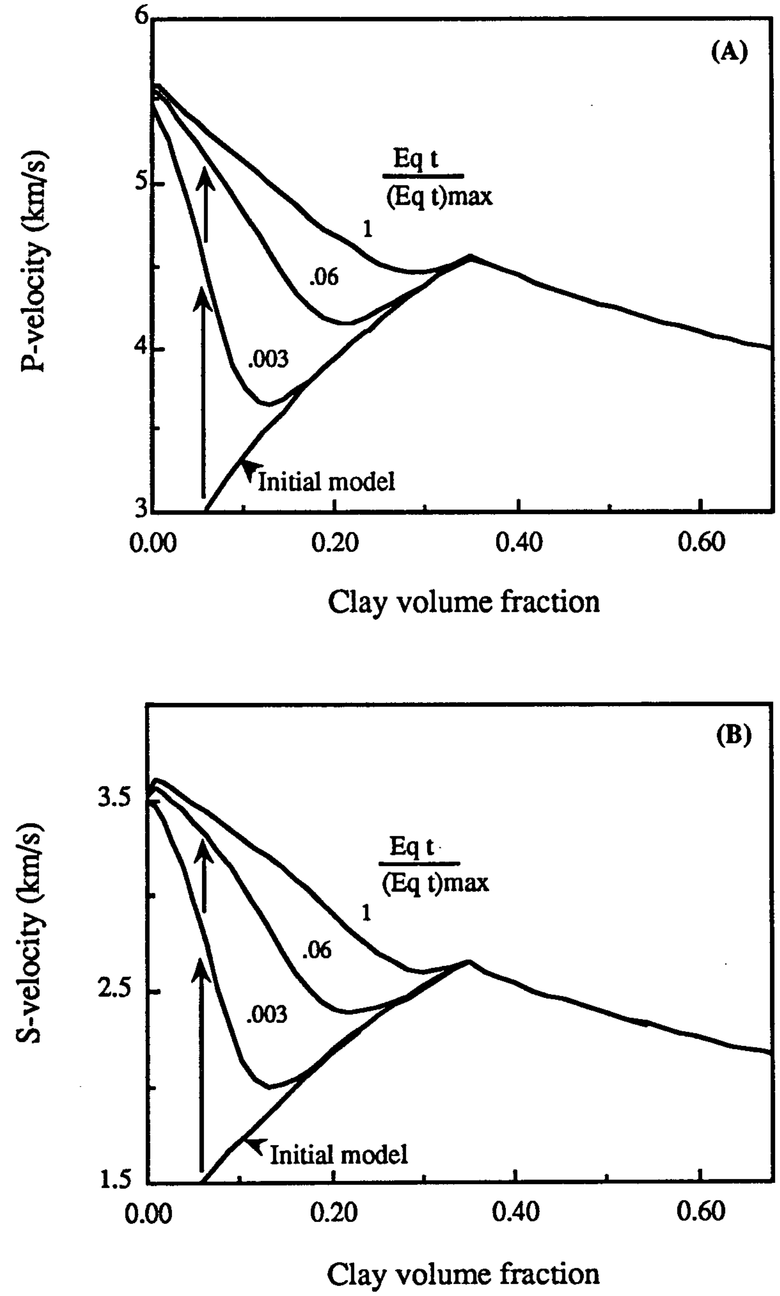

Figure 2.11: Effect of cementation on velocity. Cementation occurs selectively in cleaner sandstones and results in an overall decrease in P-and S-velocity with increasing clay. Curves represent increasing degrees of diagenesis indicated by the normalized product of cementation efficiency and elapsed time.

2.5 Feldspar alteration

We observe from petrography data the presence of altered feldspars in tight gas sandstones. These are generally observed in sandstones and shaley sandstones, with clay less than 30-40 percent. We propose to simulate the effect of clay on fluid flow and on feldspar alteration and examine how it impacts porosity, permeability, and velocity. We treat the process of feldspar alteration in a separate, but similar way to that of quartz cementation.

We start with an initial feldspar content (9 % estimated in samples from Travis Peak (Dutton, 1987)). During burial, diagenesis occurs. Feldspar becomes unstable and is altered under appropriate pressure, temperature, and pore-fluid composition conditions (Bjørlykke, 1988). As with the case of quartz cementation (equation 2.24), we consider that the quantity of feldspar that dissolves is proportional to the amount of fluid, $V_{w(\Delta t)}$, that flows through the pore space

$$V_{fsp(\Delta t)} = E_{fsp}\, V_{w(\Delta t)} \tag{2.32}$$

where $V_{fsp(\Delta t)}$ is the volume fraction of altered feldspar and E_{fsp} is the coefficient that describes the volume of feldspar that alters per unit volume of pore-fluid. Combining equations 2.22, 2.24, and 2.32 we may write the volume fraction of altered feldspar, $V_{fsp(\Delta t)}$, (analogous to equation 2.25) as

$$V_{fsp(\Delta t)} = E_{fsp}\, \frac{\Delta t}{V}\, (\frac{kA}{\mu}\frac{dP}{dx}) \tag{2.33}$$

2.5.1 Effect on porosity

We assume that the alteration of feldspars produces authigenic clay and leaves a residual secondary porosity. Initially we set, $V_{fsp(t=0)}= 9$ % , $V_{Aut(t=0)}=0$, and $\phi_{sec(t=0)}=0$, where $V_{Aut(t=0)}$ and $\phi_{sec(t)}$ are the volume fraction of authigenic clay and secondary porosity respectively. At time, $t+\Delta t$, the decrease in feldspar content due to feldspar alteration causes a corresponding increase in authigenic clay and secondary porosity.

$$V_{fsp(t+\Delta t)} = V_{fsp(t)} - V_{fsp(\Delta t)} \tag{2.34}$$

$$V_{Aut(t+\Delta t)} = V_{Aut(t)} + V_{fsp(\Delta t)} \tag{2.35}$$

$$\phi_{sec(t+\Delta t)} = \phi_{sec(t)} + V_{fsp(\Delta t)}\phi_{aut} \tag{2.36}$$

where V_{Aut}, is the volume fraction of authigenic clay (includes its micro-porosity; classified as framework cement in thin-section point count), ϕ_{sec} is the secondary porosity created by feldspar dissolution, and ϕ_{aut} is the micro-porosity of the authigenic clay (we estimate this at 40 %). The creation of secondary porosity and authigenic clay lead to this increase in the total clay volume fraction and porosity respectively

$$\phi_{(t+\Delta t)} = \phi_{(t)} + \phi_{sec(\Delta t)} \tag{2.37}$$

$$C(t+\Delta t) = C_{(t)} + V_{Aut(t)} \tag{2.38}$$

In computing the effect of feldspar alteration on porosity we use the same input parameters used in the quartz cementation model with the additional parameter, E_{fsp}, that describes the efficiency of feldspar dissolution (Table 2.3). The model is computed for the case where quartz overgrowth cementation and feldspar dissolution are concurrent.

Results in Figure 2.12 show the effect of alteration of all the feldspar in the clay free sandstone into authigenic clay and secondary porosity. The dashed line shows the initial cemented sand/detrital-clay sequence. The effect of feldspar alteration (solid curve) is to shift the initial model toward higher clay content and higher porosity.

Table 2.3

Distance fluid travels is 680 m/yr.
Q_w = 2 x 10^7 m^3/s, in sandstone of 100 md permeability
$V = 1$ cm^3
$E_q = 10$ ppm
$E_{fsp} = 3$ ppm
$\eta = 2 \times 10^{-4}$ (Pa s)

Note for instance, how the point (C=0, ϕ=.04) is shifted to (C=.10, ϕ=.08). As with cementation, feldspar alteration occurs predominantly in high permeability rocks having clay content between 0 and 20-30 percent.

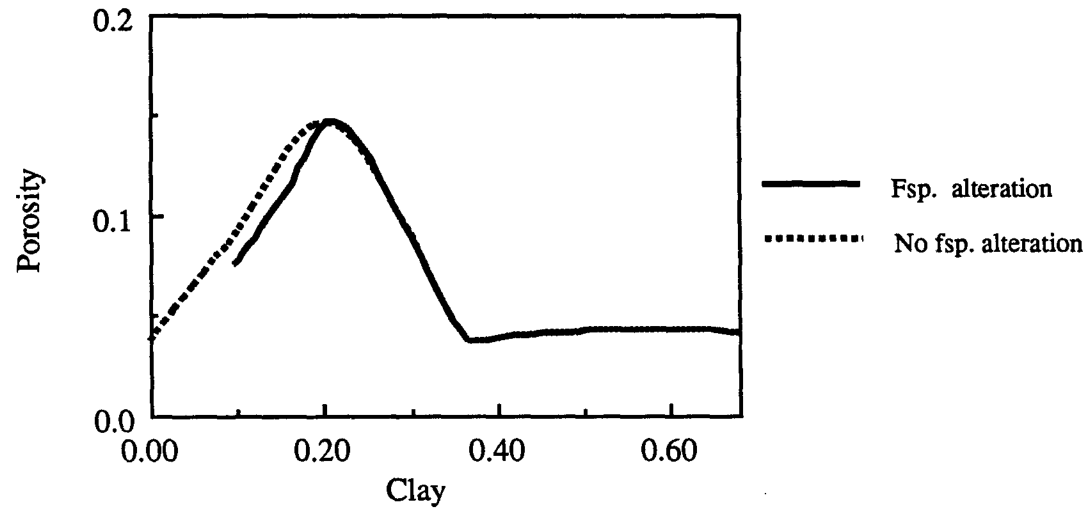

Figure 2.12: Effect of feldspar alteration on porosity. Feldspar alteration into authigenic clay leads to an increase in effective porosity and a decrease in clay content from the initial cemented state. Feldspar alteration has observable effects mostly in non-shale rocks.

2.5.2 Effect on permeability and velocity

The effect of feldspar dissolution is mostly an effect of porosity that reinforces the effect of cementation; causing an increase in permeability and a decrease in P- and S-velocity in the clay content range of sandstones and shaley sandstones, $C < \phi_s$.

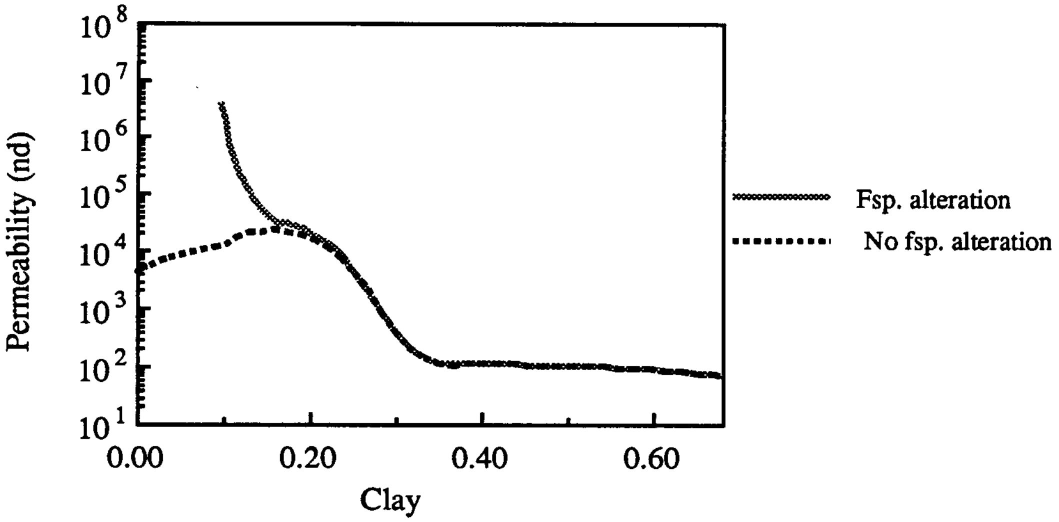

Figure 2.13: Effect of feldspar alteration on permeability. The alteration of feldspar into porous clay leads to an increase in permeability for sandstones from the cemented state.

2.6 Tight gas sandstone porosity, permeability, and velocity data

In this section we show how the combination of petrographic description and our diagenetic model can help to interpret the trends observed in the tight gas sandstone data. A first look at the data in Figures 2.14 - 2.17 shows that (1) the range of variability of porosity, permeability, and P- and S-velocity data is considerable, and

(2) direct correlation of these properties with clay content is not obvious. Using our model, we identify three zones.

In sandstones (clay volume fraction ranging from 0 to 17-20 percent), the competing effects of cementation and clay lead to an increase in porosity, and decrease in velocity for both P and S, with increasing clay content. The effect of feldspar alteration reinforces this trend of cementation. For permeability, the effect of cementation would lead to an increase in permeability with clay content. However, the effect of feldspar alteration may smear this effect or reverse the trend.

In shaley sandstones (clay volume fraction ranging from 17-20 to 36-40 percent), the presence of clay prevents cementation and feldspar alteration, and the trend of the initial model is unchanged. In shaley sandstones we observe a decrease in porosity due to in-filling clay and a decrease in permeability. We can see a slight increase in P-velocity (more easily seen in bulk modulus).

In shales (clay volume fraction greater than 36-40 percent), few data are available. These data tend to exhibit porosity, permeability, and velocity that are fairly constant with clay content (the initial sand/detrital-clay model).

To compare in more detail the predictions with the initial model we show the relation between computed initial porosity (equal to the measured porosity plus cement minus porosity associated with authigenic clay) versus clay volume fraction (Figure 2.17). We include ankerite as part of the clay fraction here because it affects storage properties, occluding pore space, in the same manner as detrital clay. This plot should indicate the trend of porosity vs. clay content of the initial model (Figure 2.6). We observe a decrease in porosity with increasing clay that follows the trend of the initial sand-detrital clay model (Figure 2.6), with some uncertainty that can be related to both assumptions in the model used (initial sand porosity value, cementation due to quartz overgrowths vs. pressure solution) and accuracy of cement clay content determination from thin-section point count.

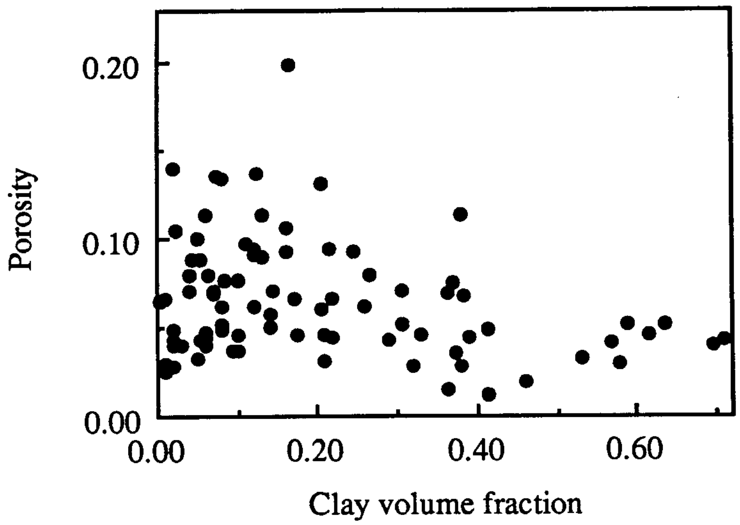

Figure 2.14: Porosity data vs. clay content. Compare the overall trend of the data with simulation results in Figure 2.9. Ankerite is included in the clay fraction.

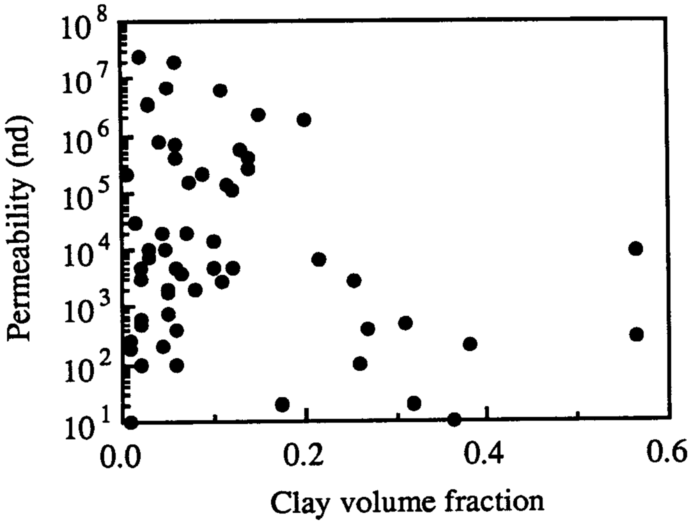

Figure 2.15: Permeability data vs. clay content. Compare the overall trend of the data with simulation results in Figure 2.10.

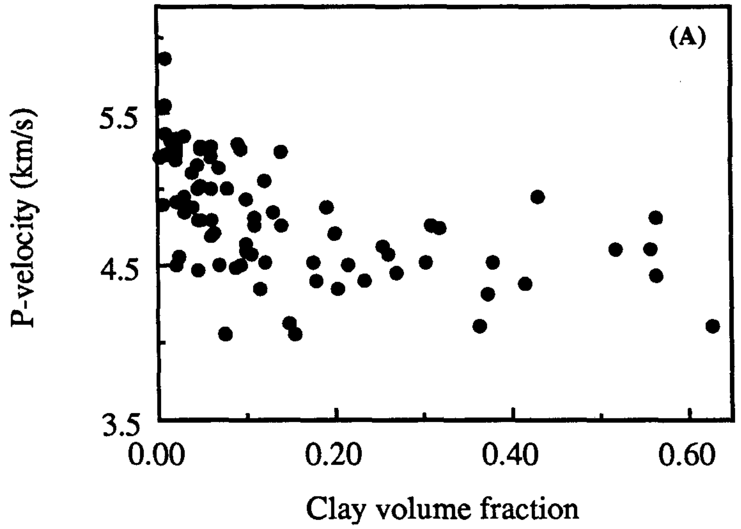

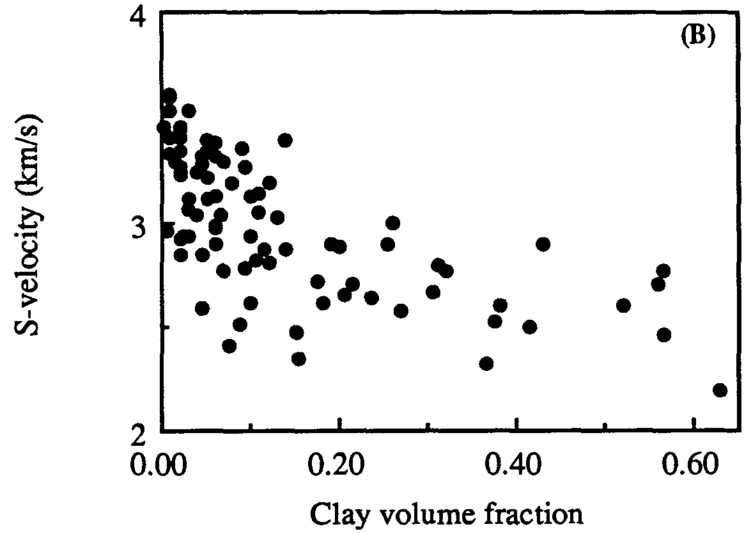

Figure 2.16: P and S- velocity data vs. clay content. Comparing the data to simulation results in Figure 2.11, we suggest that quartz cementation strongly influences P and S- velocity in these tight gas sandstones (approximate clay volume fraction ranging from 0 to 17-20 percent).

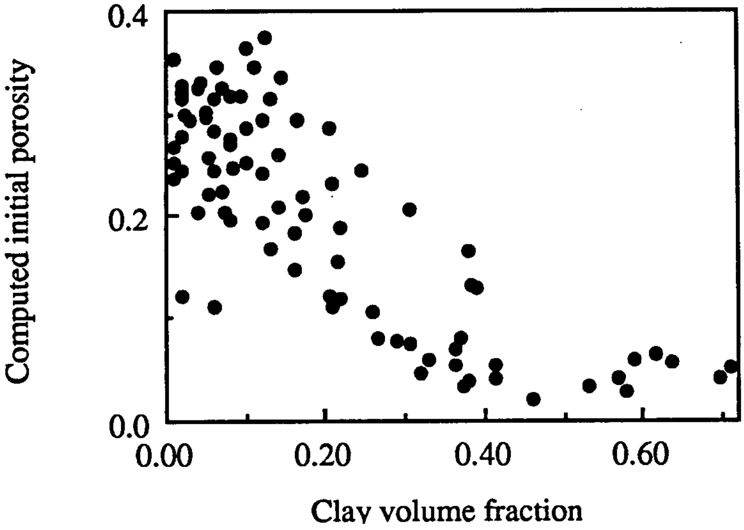

Figure 2.17: Initial porosity computed from data (initial porosity = measured porosity + quartz cement + .4(authigenic clay)). Clay fraction plotted includes ankerite.

2.7 Conclusion

We proposed a simple model for diagenesis of tight gas sandstones. Using a sand/clay sequence as the initial model, it was found that the behavior of physical properties over a wide range of clay content could be related to diagenetic processes such as quartz cementation and feldspar alteration. The effect of quartz cementation is to reduce porosity, permeability, and to increase velocity in sandstones and shaley sandstones. Feldspar alteration also occurs in low clay content rocks and its effect is to increase porosity, permeability, and clay content, and to decrease velocity.

These results will be used to explain observations and model static and mechanical properties of tight gas sandstones and their relationship to the petrography, clay, and cement.

References

Berner, R. A., 1980, Early Diagenesis: New Jersey, Princeton University press, 241 pp.

Bjørlykke, K., 1979, Cementation of sandstones: J.Sediment. Petrol., **49** , 1358-1359.

Bjørlykke, K., 1988, Sandstone diagenesis in relation to preservation, destruction and creation of porosity. In: G. V. Chilingarian and K. H. Wolf (eds.) Developments in Sedimentology, **41**, Elsevier, Amsterdam, 591 pp.

Blatt, 1979, Diagenetic processes in sandstones, in P. A. Scholle and Schluger, P. R. (eds.) Aspects of Diagenesis, Society of Economic Paleontologists and Mineralogists Special Publication, **26**, 141-148.

Carman, P., C., 1956, Flow of gasses through porous media: New York Academic Press.

Chilingarian, G. V., and Wolf, K. H., (eds.), 1975, Compaction of coarse-grained sediments I, Elsevier, Amsterdam, 552 pp.

Clavier, C., Coates, G., and Dumanoir, 1977, The theoretical and experimental bases for the 'Dual Water' model for the interpretation of shaly sands: Presented at the 52nd Ann. Fall Tech. Conf. of Soc. Pet. Eng. Denver.

Domenico, S. N., 1977, Elastic properties of unconsolidated porous sand reservoirs: Geophysics, **42**, 1339-1368.

Dutton, S. P., and Finley, R. J., 1986, Depositional and diagenetic controls on reservoir quality in tight sandstones of the Travis Peak (Hosston) Formation, East Texas: SPE, Paper 15220, presented at the 1986 Soc. Petr. Engr. Unconventional Gas Technology Symposium, Louisville, KY, May 18-21, 1986.

Dutton, S. P., 1987, Diagenesis and burial history of the lower Cretaceous Travis Peak Formation, East Texas: controls on permeability in a tight gas sandstones: Bureau of Economic Geology, Gas Research Institute topical report.

Galloway, W. E., 1979, Diagenetic control of reservoir quality in arc-derived sandstones: implications for petroleum exploration, in P. A. Scholle and Schluger, P. R. (eds.) Aspects of Diagenesis, Society of Economic Paleontologists and Mineralogists Special Publication, **26**, 251-262.

Gassmann, F., 1951, Elastic waves through a packing of spheres: Geophysics, **16**, 673-685.

Givens, W. W., 1988, A dual-porosity surface, and matrix electrical conduction model for low-contrast resistivity sandstones: Presented at the Soc. Prof. Well-log Anal. Ann. Mtg., paper E.

Han, D., Nur, A., and Morgan, D., 1986, Effect of porosity and clay content on wave velocity in sandstones: Geophysics, **51**, 2093-2107.

Hashin Z., and Shtrikman, S., 1963, A variational approach to the elastic behavior of multiphase materials: J. Mech. Phys. Solid, **11**, 127-140.

Hayes, J. B., 1979, Sandstone diagenesis - the hole truth, in P. A. Scholle and Schluger, P. R. (eds.) Aspects of Diagenesis, Aspects of Diagenesis, Society of Economic Paleontologists and Mineralogists Special Publication, **26**, 127-139.

Heald, M. T., and Renton, J. J., 1966, Experimental study of sandstone cementation: Jour. Sed. Petrology., **36**, 977-991.

Heron, M. M., 1987, Estimating the intrinsic permeability of clastic sediments from geochemical data: Presented at the Soc. Prof. Well-log Anal. Mtg., paper HH.

Johnston, D. H., 1987, Physical properties of shale at temperature and pressure: Geophysics, **52**, 1391-1401.

Kowallis, B. Jones, L. E. A., and Wang H. F., 1984, Velocity-porosity-clay content; systematics of poorly consolidated sandstones: J. Geophys. Res., **89**, 10355-10364.

Knight, R., 1986, Mineralogy, Petrology, and Geochemistry of clay minerals, class notes, Stanford University.

Marion, D. P., 1990, Acoustical, mechanical, and transport properties of sediments and granular materials: Ph.D. thesis, Stanford University.

Marion, D. P., and Nur, A., 1991, Pore-filling material and its effect on velocity in rocks: submitted to Geophysics.

Morris, R. C., Proctor, K. E., and Koch, M. R., 1979, Petrology and diagenesis of deep-water sandstones, Ouachita mountains, Arkansas and Oklahoma, in P. A. Scholle and Schluger, P. R. (eds.) Aspects of Diagenesis, Aspects of Diagenesis, Society of Economic Paleontologists and Mineralogists Special Publication, **26**, 263-279.

Neasham, J. W., 1977, The morphology of dispersed clay in sandstones and its effect on sandstone shaliness, pore space and fluid flow properties: 52nd Annual Fall Technical Conference and Exhibition of the Society of Petroleum Engineers of AIME, Denver, SPE paper 6858.

Reuss, A., 1929, Berechnung der fliessgrense von mischkristallen auf grund der plastizitatsbedingung fur einkristalle: Zeitschrift fur Angewandte Mathematik und Mechanik, **9**, 49-58.

Thomas, E. C., and Stieber, S. J., 1975, The distribution of shale and its effect on porosity: Presented at the Soc. Prof. Well-log Anal. Ann. Mtg., paper T.

Tosaya, C., and Nur, A., 1982, Effect of the diagenesis of clays on compressional velocity in rocks: Geophys. Res. Let., **9**, 5-8.

Voigt, W., 1928, Lehrbuch der Kristallphysik, Teubner, Leipzig.

Watt, J. P., Davies, G. F., and O'Connell, R. J., 1976, The elastic properties of composite materials: Rev. Geophys. and Space Phys., **14**(4) 541-563.

Waxman, M. H., and Smits, L. J. M., 1968, Electrical conductivities in oil-bearing shaly sands: Soc. Pet. Engrs. J., **8**, 107-122.

Wood, J. R., 1989, Modeling the effect of compaction and precipitation/dissolution on porosity, in Hutcheon, I. E. (ed.), Short Course in Burial Diagenesis, Min. Assoc. of Canada, **15**, 311-347.

Yin, H., Han, D., and Nur, A., 1988, Study of velocities and compaction on sand-clay mixtures (graphs of the experiment results): Stanford Rock Physics Project Report, Stanford University, **33**, 265-302.

References for data from GRI cooperative wells

Core Laboratories, 1987, Special Analysis Report: Werner-Sawmill No. 5, Marshall Exploration Co.

Core Laboratories, 1988, Special Analysis Core Report, Staged Field Experiment No. 2, S.A. Holditch Associates. File: SCAL-308-87220.

David K. Davies and Associates, Inc., 1985, Fluid Sensitivity Evaluation of the 8188 to 8394.9 Foot Travis Peak Interval, Arco B.F. Phillips No. 1 Well, Smith County, Texas.

David K. Davies and Associates, Inc., 1985, Fluid Sensitivity Evaluation Three Travis Peak Sand Zones, Ashland S.F.O.T. No. 1 Well, Nacogdoches County, Texas.

David K. Davies and Associates, Inc., 1985, Fluid Sensitivity Evaluation Three Travis Peak Sand Zones, Prairie Producing Mast No. A-1 Well, Nacogdoches County, Texas.

Petrophysical Services, Inc., 1984, Gas Research Institute Tight Gas Sand Core Analysis, Sam Hughes No. 1, Revision Level: 2. *GRI contract No. 5083-211-0813.*

Petrophysical Services, Inc., 1985, Gas Research Institute Tight Gas Sand Core Analysis, B.F. Phillips No. 1, Revision Level: 8. *GRI contract No. 5083-211-0813.*

Petrophysical Services, Inc., 1985, Gas Research Institute Tight Gas Sand Core Analysis, S.F.O.T Unit No. No. 1, Revision Level: 4. *GRI contract No. 5083-211-0813.*

Petrophysical Services, Inc., 1986, Gas Research Institute Tight Gas Sand Core Analysis, Prairie Producing Company Mast No. A-1, Final Report, Routine and Special Analysis.

Petrophysical Services, Inc., 1986, Special Analysis Report: Werner-Sawmill No. 5, Marshall Exploration Co. 22F.

Texas Bureau of Economic Geology, 1988, Thin-section point count data from the special-core-analysis vertical plugs from the Clayton Williams No. 1 Sam Hughes well, S.E. Pinehill Field, Panola County, Texas.

Texas Bureau of Economic Geology, 1988, Thin-section point count data from the special-core-analysis vertical plugs from the Werner-Sawmill No. 5 well, Texas.

Texas Bureau of Economic Geology, 1988, Thin-section point count data from the special-core-analysis vertical plugs from the S.A. Holditch Associates, Staged Field Experiment No. 2 well, Nacogdoches County, Texas.

Appendix A

The following table lists data from 88 tight gas sandstones and shales from GRI's cooperative wells in the Travis Peak Formation, East Texas. For more detailed information, the reader is referred to the data sources listed in the References. Columns listed are the following:

1 = **Well**, depth (feet)
2 = Grain density (g/cm^3)
3 = Clay percent by volume (%) (thin-section point count)
4 = Quartz percent by volume (%) (thin-section point count)
5 = Porosity (%) (Helium measurement at 15 - 28 MPa confining pressure)
6 = Permeability (md) (Klinkenberg corrected helium measurement at 15 - 28 MPa confining pressure). Permeability measurements tabulated in decimal notation are accurate to approximately two significant digits. Permeability readings of 0.00001 are close to the limits of measurement resolution and should be viewed accordingly.
7 = P-wave velocity (km/s) (fully water-saturated, 15 - 28 MPa confining pressure)
8 = S-wave velocity (km/s) (fully water-saturated, 15 - 28 MPa confining pressure)

1	2	3	4	5	6	7	8
Well, Depth (feet)	Density (g/cm^3)	Clay (%)	Qtz (%)	Porosity (%)	Perm. (md)	V_p (km/s)	V_s (km/s)
B.F. 8189.5	2.64	7	24	6.86	0.02000	5.131	3.288
Phillips 8190.7	2.64	8	20	5.21	0.00200	5.000	3.182
8195.0	2.67	26	2	6.24	0.00010	4.561	2.988
8213.5	2.65	5	18	10.00	6.40000	4.794	3.106
8216.4	2.65	6	15	11.35	19.20000	4.685	2.967
8243.4	2.64	11	21	9.00	5.90000	4.752	3.045
8246.2	2.64	2	18	14.00	25.00000	4.497	2.839
8368.9	2.65	6	7	4.00	0.00040	4.994	2.897
8382.0	2.64	10	26	7.70	0.00500	4.634	2.930
8385.4	2.64	5	26	4.78	0.00200	5.022	3.212
A.T. 8626.0	2.65	12	5	9.48	0.00500	4.512	2.798
Mast 8643.3	2.66	6	11	6.22	0.00500	4.991	3.119
8646.3	2.66	3	14	7.15	0.01000	4.907	3.110
8666.0	2.68	3	11	6.70	0.00700	4.948	3.053
8667.8	2.67	2	22	4.86	0.00010	5.273	3.226
8675.0	2.72	56	0	2.88		4.598	2.696
9150.8	2.73	1	8	4.41		5.355	3.318

1	2	3	4	5	6	7	8
Well, Depth (feet)	Density (g/cm^3)	Clay (%)	Qtz (%)	Porosity (%)	Perm. (md)	V_p (km/s)	V_s (km/s)
9170.9	2.73	43	0	1.97		4.947	2.892
9180.8	2.65	2	26	4.81	0.00300	5.194	3.235
9204.0	2.66	6	18	4.42	0.00010	5.207	3.375
9229.2	2.65	2	7	4.26	0.00060	5.199	3.257
9932.7	2.65	1	24	2.50	0.00001	5.366	3.526
9943.3	2.66	5	25	3.30	0.00074	5.259	3.337
9952.0	2.65	2	23	3.96	0.00500	5.218	3.334
9975.0	2.65	2	21	2.77	0.00050	5.320	3.457
9980.5	2.70	12	1	0.87		4.977	3.063
9990.1	2.67	1	22	2.88	0.00001	5.539	3.600
S.F.O.T 9665.5	2.66	10	0	10.65	0.01400	4.581	2.615
9666.3	2.70	9	0	5.10		4.477	2.508
9733.3	2.71	15	1	4.27	2.30000	4.126	2.472
9746.2	2.68	19	3	4.39		4.867	2.892
9747.2	2.66	2	0	4.31		4.918	2.922
9750.4	2.65	6	23	3.75	0.42000	5.280	3.307
9753.0	2.67	4	17	4.64	0.79000	5.098	3.232
9754.2	2.68	6	13	6.60	0.69000	4.785	2.976
Werner 6598.1	2.55	22	2	9.40	0.00660	4.500	2.697
Sawmill 6601.0	2.53	14	7	9.30	0.27000	4.752	2.861
6630.0	2.55	5	16	7.70	0.02000	4.782	2.845
6853.9	2.62	31	1	7.50	0.00050	4.758	2.785
6892.0	2.54	1	13	7.10	0.21000	4.897	2.952
6897.2	2.51	3	13	8.80	3.50000	4.846	2.924
6909.5	2.70	57	0	4.10	0.00900	4.428	2.458
7074.8	2.65	57	0	4.00	0.00030	4.815	2.770
7077.0	2.48	12	5	11.30	0.13000	4.349	2.864
7083.0	2.60	27	0	7.00	0.00040	4.449	2.573
7090.1	2.68	5	0	4.60	0.01000	4.464	2.585
7101.9	2.44	8	4	13.50	0.16000	4.058	2.409
7113.0	2.59	18	0	8.00		4.394	2.609
Sam 7047.5	2.66	26	10	7.10	0.00290	4.609	2.888
Hughes 7053.7	2.71	38	1	2.87	0.00020	4.518	2.603
7069.6	2.66	5	27	3.67	0.00020	5.143	3.273
7089.6	2.68	18	14	4.64	0.00002	4.509	2.712
7095.5	2.65	7	24	7.96	0.00400	4.709	3.030
7099.5	2.64	12	18	9.14	0.11000	5.043	3.185
7103.5	2.71	32	2	2.74	0.00002	4.731	2.767
7107.8	2.70	37	4	1.42	0.00001		
Howell 5 5991.5	2.65	16	8	19.95		4.049	2.345
6080.5	2.65	24	10	9.25		4.391	2.642
6029.0	2.72	38	2	6.79		4.303	2.524

1	2	3	4	5	6	7	8
Well, Depth (feet)	Density (g/cm^3)	Clay (%)	Qtz (%)	Porosity (%)	Perm. (md)	V_p (km/s)	V_s (km/s)
6116.5	2.65	21	11	13.12		4.343	2.645
6164.0	2.72	37	3	11.39		4.094	2.318
6186.1	2.65	11	24	7.12		4.573	2.812
6205.9	2.65	10	22	13.70		4.500	2.776
6275.2	2.72	63	1	5.11		4.100	2.194
6297.2	2.65	7	16	13.38		4.503	2.767
7409.7	2.68	42	1	4.87		4.376	2.497
7419.5	2.64	3	19	10.48		4.552	2.933
7428.7	2.70	31	2	5.21		4.506	2.658
7458.5	2.65	11	21	9.74		4.800	3.139
7500.3	2.64	4	23	7.93		4.882	3.036
7560.4	2.65	5	23	8.83		4.997	3.309
S.F.E. 2 9503.0	2.65	2	27	4.34		5.240	3.397
9535.5	2.65	5	20	4.24	0.00179	5.270	3.391
9542.4	2.81	11	0	3.48	0.00290		
9560.4	2.64	1	29	6.61	0.00025	5.212	3.400
9807.5	2.66	14	16	4.97	0.38600	5.234	3.391
9816.3	2.64	3	25	4.00		5.334	3.524
9825.0	2.70	1	21	2.67	0.00019	5.855	3.591
9837.8	2.72	2	6	6.09	0.03100	5.309	3.285
9882.0	2.64	0		6.56		5.209	3.448
9898.3	2.69	42	3	1.24			
9913.2	2.67	2	27	4.91		5.322	3.445
9940.2	2.70	10	7	3.03		5.252	3.264

Appendix B

The method used for calculating quartz overgrowth cementation is outlined briefly (Figure 2.16). Computations were made in APL program language with program listings on the following pages. The first step is to compute initial values of porosity and permeability of the sand/detrital-clay sequence. Initial quartz cement volume is equal to zero. The program $\nabla initial$ generates the initial model. Second, the volumetric flow rate of water is computed for all clay fractions in the sand/detrital-clay sequence. Third, maximum flux is identified and a time increment is set. Fourth, the volume fraction of quartz cement is computed for all clay fractions. Fifth, porosity and permeability are computed, time increment elapsed is recorded, and the procedure is repeated going back to step 2. Procedures 2-5 are computed using the programs ∇run, $\nabla write$, and $\nabla cementation$. P- and S-velocity do not affect the cementation process. They are computed at the end using the computed quartz cement volume fraction and programs, $\nabla cement$, ∇bam, $\nabla fluid$, and $\nabla frame$.

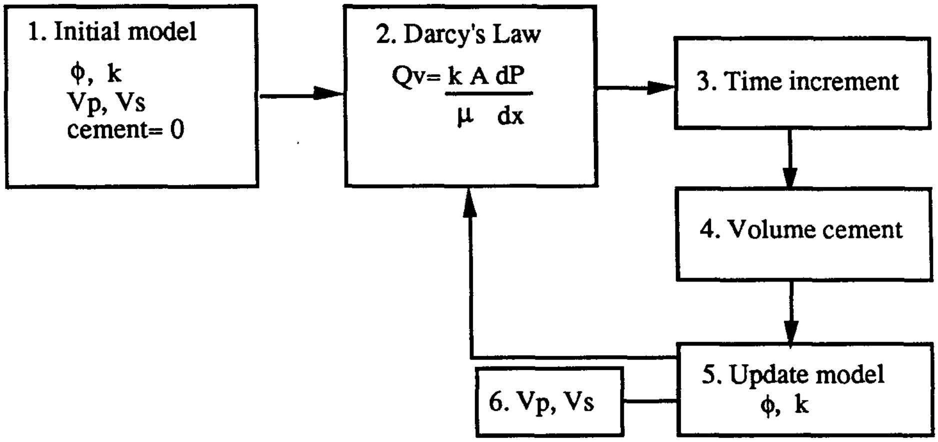

Figure 2.16: Steps used in quartz cementation model.

```
    ∇initial
⍝ SAND AND SHALE POROSITIES AND PERMEABILITIES

⍝ INITIAL MODEL INPUT PARAMETERS
clay←0,(60⍴(⍳60))÷60   ⍝ clay content vector
phis←.36               ⍝ sand porosity
pm←.02  ⋄ pmi←.10      ⍝ micro-porosity of matrix clay
phiaut←.40              ⍝ micro-porosity of authigenic clay
a←.09                   ⍝ initial concentration of feldspar
dw←1.00                ⍝  density water (g/cm3)
dq←2.654               ⍝  density quartz (g/cm3)
dc←2.75                ⍝  density clay mineral (g/cm3)

tc←8    ⋄ ts←1.5        ⍝ shale, sand tortuosity (m2/g)
rq←5×10*¯5              ⍝ sand grain radius, (m2)
ss←3×(1-phis)÷rq        ⍝ sand surface area (1/m) (divide by dens for m2/g)
sc←2.3×10*9             ⍝ shale surface area (1/m) (divide by dens for m2/g)
ko←2.5                  ⍝ constant in Kozeny-Carman eqn.

dp ←.437×10*6           ⍝ pressure differential(Pa), 1 bar=10*5 Pa
vis←2×10*¯4             ⍝ fluid viscosity (Pa.s)
leno←.01                ⍝ length of face of cube (m), we use 1 cm
effic←2.8×(10*¯5)       ⍝ efficiency of quartz precip. (cm3 qtz/ cm3 water)
feffic←.3×effic         ⍝ efficiency of dissolving fsp. (cm3 fsp/ cm3 water)
percent←.03             ⍝ set the maximum increment of porosity reduction


⍝ COMPUTE POROSITY, PERMEABILITY USING INPUT CLAY VECTOR

ivect←(⍴clay)⍴ ⍳ (⍴clay)    ⍝ iota vector
nsand←+/(clay≤phis)         ⍝ no. of values where clay ≤ Φ sand
c1←(nsand)↑ivect            ⍝ index of values where clay ≤ Φ sand
c2←(nsand)↓ivect            ⍝ index of values where clay ≤ Φ sand

⍝ INITIAL VALUES OF QUARTZ CEMENT, FSP, AUTHIGENIC CLAY, SECONDARY POROSITY
qtz←(⍴clay)⍴0 ⋄ fsp←(⍴clay)⍴0  ⋄ aut←(⍴clay)⍴0  ⋄ por2←(⍴clay)⍴0
a←.09          ⍝ initial concentration of feldspar
qtz[c1]←(1-a) ⋄ qtz[c2]←(1-a)×(1-(clay[c2]))
fsp[c1]←(a)   ⋄ fsp[c2]←(a)×(1-(clay[c2]))
fspzero←fsp

⍝ BULK DENSITY
den←((1-phis)×dq) + (clay×(1-phic)×dc) + ((phis - (clay×(1-phic)))×dw)
den[c2]←((1-clay[c2])×dq) +(clay[c2]×(1-phic[c2])×dc)+ (clay[c2]×phic[c2]×dw)

⍝ POROSITY
phic←(⍴clay)⍴0                          ⍝ micro-porosity of detrital clay
slope←(pm-pmi)÷(1-phis)
phic[c1]←pmio
phic[c2]←nsand↓ pmi+(slope×(clay-phis))
por←(⍴clay)⍴0                           ⍝ porosity
por [c1] ← phis-(1-phic[c1])×clay[c1]
por [c2] ← phic[c2]×clay[c2]
por1←(⍴clay)⍴0                          ⍝ free porosity (where qtz deposits)
por1[c1]←phis-clay[c1]
por1[c2]← clay[c2]-clay[c2]
por1[c2]← clay[c2]-clay[c2]

```

```
[58]  ⍝ PERMEABILITY
[59]  tor←(⍴clay)⍴0  ⋄ surf←(⍴clay)⍴0                   ⍝ intial tortuosity
[60]  tor[c1]← ts × (1+ clay[c1]×(tc-1)÷phis)
[61]  tor[c2]← tc × (1+ (clay[c2]-1) × ( (ts-1)÷(phis-1) ) )
[62]  surf[c1]←ss+clay[c1]×sc                            ⍝ surface area
[63]  surf[c2]←(ss×((1-clay[c2]))÷(1-phis))+sc×clay[c2]
[64]  perm1←((10*15)×(por*3))÷( ko× (tor*2)× (surf*2))    ⍝ permeability
[65]  perm←perm1
[66]  permnd←perm1×10*6
[67]
[68]  ⍝ INITIALIZE WRITTEN OUTPUT OF TIME, CEMENT, CLAY, PERM, FLUX
[69]  totime←0  ⋄ toyear←0   ⋄ tocement←0   ⋄ toaut←0   ⋄ toflux←(⍴clay) ⍴ 0
[70]  porzero←por ⋄   permzero←perm
[71]  datatime←0
[72]  dataflux←(⍴clay) ⍴ 0
[73]  datapor←⍉(2,(⍴clay))⍴(clay),(por)
[74]  datapor1←⍉(1,(⍴clay))⍴(por1)
[75]  dataperm←⍉(1,(⍴clay))⍴(perm×10*6)
[76]  datacem←⍉(1,(⍴clay))⍴(clay-clay)
[77]  dataaut←⍉(1,(⍴clay))⍴(clay-clay)
[78]  dataclay←⍉(1,(⍴clay))⍴(clay)
```

```
     ∇run
[1]   ⍝ DRIVER TO RUN PROGRAM
[2]   percent←.03
[3]   cementation .23
[4]   write
[5]   percent←.015
[6]   cementation .15
[7]   write
[8]   percent←.015
[9]   cementation .08
[10]  write
```

```
     ∇write
[1]   ⍝ WRITES DATA OUTPUT FROM ∇cementation PROGRAM
[2]   datatime←datatime,toyear
[3]   datapor←datapor,(por)
[4]   datacem←datacem,tocement
[5]   ⍝ final matrix of data to transfer to a plotting program:
[6]     x←datapor,dataperm,datacem,dataaut,datapor1
[7]   ⍝ x←datapor,dataperm,datacem,dataaut,dataclay
[8]   ⍝ x←datapor,dataperm,datacem
```

```
     ∇cementation  maxpor;porstart
[1]
[2]   ⍝ USES DARCY'S LAW TO COMPUTE VOLUME OF FLUID THAT FLOWS THROUGH THE
[3]   ⍝ PORE SPACE. QUARTZ PRECIPITATES (FELDSPAR MAY BE SET TO DISSOLVE).
[4]   ⍝ AT EACH SUCESSIVE STEP COMPUTE NEW POROSITY AND  PERMEABILITY.
[5]
[6]   ⍝ INITIALIZE LOOP
[7]   ⍝ will loop until maximum porosity in the sand/detrital clay sequence
[8]   ⍝ is less than or equal to the specified value of 'maxpor' in the program
[9]   ⍝ ∇run. At this point, model results are written in the program ∇write. ⍝
[10]  ⍝
```

```
porstart←por
'no,  imax,  oldpor,  ∆por'
n←0                                          ⍝ keep track of no. of steps
L1: →(maxpor ≥(max (por1+clay×phic)) ) /L2
n←n+1
oldpor1←por1   ⋄   oldperm1←perm1
oldpor←por     ⋄   oldperm←perm               ⍝ perm is in units of (md)


⍝ FLUX WATER
flux←(leno×leno×oldperm1×(10*¯15)×dp)÷(vis)  ⍝ units of (m3/s)


⍝ COMPUTE TIME STEPS: FROM MAX POROSITY THAT IS ALLOWED TO DECREASE
⍝ DURING THIS TIME INCREMENT
dtmax←| (percent×(leno*3))÷(flux[imax]×(effic-(feffic×phiaut)))


⍝ QUARTZ CEMENT
cement←(flux×dtmax×effic)÷(leno*3)    ⍝ increment of qtz deposited
tocement←tocement+cement              ⍝ total vol fraction of qtz
toflux←toflux+(flux×dtmax)÷(leno*3)   ⍝ total vol fraction of water

⍝ FELDSPAR
dfsp←(flux×dtmax×feffic)÷(leno*3)     ⍝ increment of fsp dissolved
fsp←  fsp  -  dfsp                    ⍝ total vol fraction of qtz
izero←(fsp≤0)/(⍳⍴fsp)
fsp[izero]←0×clay[izero]
dfsp[izero]←0×clay[izero]
aut←aut +dfsp                         ⍝ total vol fraction of aut clay
por2←por2 +(dfsp × phiaut)            ⍝ total vol fract of secondary por
aut[izero]←(fspzero[izero])
por2[izero]←(phiaut×fspzero[izero])


⍝ UPDATE POROSITY, PERMEABILTIY
por1←oldpor1+(-cement)                   ⍝ primary porosity
por1[(por1≤0)/⍳⍴clay]←.0000001
por←por1+por2+(clay×phic)                           ⍝ total porosity
ss←3×(1-por1)÷rq
surf[c1]←ss[c1]+clay[c1]×sc
surf[c2]←(ss[c2]×((1-clay[c2]))÷(1-phis))+sc×clay[c2]
perm←((10*15)×((por)*3))÷( ko× (tor*2)× (surf*2))   ⍝ permeability
perm1←((10*15)×((por )*3))÷( ko× (tor*2)× (surf*2))
toyear←totime÷3.15×10*7 ⋄totime←totime+dtmax       ⍝ time (yr, sec)

n,imax,oldpor1[imax]+clay[imax]×phic[imax],oldpor1[imax]-por1[imax]
→L1

L2:
'elapsed time (mil. yrs)'⋄ toyear
∇
```

```
     ∇cement
[1]   ⍝ COMPUTES EFFECT OF QUARTZ OVERGROWTH CEMENTATION ON ELASTIC MODULI AND
[2]   ⍝ VELOCITIES
[3]
[4]   ⍝ COEFFICIENTS FOR THE CHANGE IN BULK AND SHEAR MODULI WITH QUARTZ CEMENT
[5]   kslope←73.5   (GPa/qtz cement fraction)
[6]   gslope←87.5   (GPa/qtz cement fraction)
[7]
[8]   ⍝ FIRST STEP OF CEMENT
[9]   ksat1←ksat            ⍝ bulk modulus (GPa)
[10]  gsat1←gsat            ⍝ shear modulus (GPa)
[11]  b← datacem[;2]        ⍝ quartz cement fraction
[12]  kdry←kdryo+b×kslope   ⍝ new frame modulus is original + slope× cement
[13]  gdry←gdryo+b×gslope
[14]  phi←phis-b            ⍝ new lower porosity that is cemented
[15]  ⍝ BAM FOR FLUID SATURATED FRAME
[16]  a←⍉(5,(⍴clay))⍴ kdry,kq,ka,kfl,phi
[17]  ks←bam a
[18]  a←⍉(5,(⍴clay))⍴ gdry, gq, ga, gfl, phi
[19]  gs←bam a
[20]  ksat1[c1]←ks[c1]
[21]  gsat1[c1]←gs[c1]
[22]  den1←den                                ⍝ density (g/cm3)
[23]  den1[c1]←den[c1]+(b[c1]×(dq-dw))
[24]  vp1←((ksat1+(1.333×gsat1))÷den1)⋆.5     ⍝ P-wave velocity (km/s)
[25]  vs1←(gsat1÷den1)⋆.5                     ⍝ S-wave velocity (km/s)
[26]
[27]  ⍝ SECOND STEP OF CEMENT
[28]  ksat2←ksat                              ⍝ notation is similar to first step
[29]  gsat2←gsat
[30]  b← datacem[;3]
[31]  kdry←kdryo+b×kslope
[32]  gdry←gdryo+b×gslope
[33]  phi←phis-b
[34]  ⍝ Bam for fluid satd sandstone frame
[35]  a←⍉(5,(⍴clay))⍴ kdry,kq,ka,kfl,phi
[36]  ks←bam a
[37]  a←⍉(5,(⍴clay))⍴ gdry, gq, ga, gfl, phi
[38]  gs←bam a
[39]  ksat2[c1]←ks[c1]
[40]  gsat2[c1]←gs[c1]
[41]  den2←den
[42]  den2[c1]←den[c1]+(b[c1]×(dq-dw))
[43]  vp2←((ksat2+(1.333×gsat2))÷den2)⋆.5
[44]  vs2←(gsat2÷den2)⋆.5
[45]
[46]  ⍝ THIRD STEP OF CEMENT
[47]  ksat3←ksat
[48]  gsat3←gsat
[49]  b← datacem[;4]
[50]  kdry←kdryo+b×kslope
[51]  gdry←gdryo+b×gslope
[52]  phi←phis-b
[53]  ⍝ Bam for fluid satd sandstone frame
[54]  a←⍉(5,(⍴clay))⍴ kdry,kq,ka,kfl,phi
[55]  ks←bam a
[56]  a←⍉(5,(⍴clay))⍴ gdry, gq, ga, gfl, phi
[57]  gs←bam a
```

```
[58]  ksat3[c1]←ks[c1]
[59]  gsat3[c1]←gs[c1]
[60]  den3←den
[61]  den3[c1]←den[c1]+(b[c1]×(dq-dw))
[62]  vp3←((ksat3+(1.333×gsat3))÷den3)*.5
[63]  vs3←(gsat3÷den3)*.5
[64]
[65]  ⍝ OUTPUT BULK AND SHEAR MODULI
[66]  ⍝a0←(por),ksat,gsat
[67]  ⍝a1←(por-datacem[;2]),ksat1,gsat1
[68]  ⍝a2←(por-datacem[;3]),ksat2,gsat2
[69]  ⍝a3←(por-datacem[;4]),ksat3,gsat3
[70]  ⍝x←⍉((4+3×4) ,(⍴clay))⍴ clay,a0,a1,a2,a3,vpor,kfl,gfl
[71]
[72]  ⍝ OUTPUT P- AND S- WAVE VELOCITIES
[73]  a0←(por),vp,vs,den
[74]  a1←(por-datacem[;2]) ,vp1,vs1,den1
[75]  a2←(por-datacem[;3]) ,vp2,vs2,den2
[76]  a3←(por-datacem[;4])  ,vp3,vs3,den3
[77]  ⍝ a4←(por-datacem[;5])  ,vp4,vs4,den4
[78]  x←⍉((1+4×4) ,(⍴clay))⍴ clay,a0,a1,a2,a3
```

```
    ∇ m1← bam a
[1]   ⍝ Bound Averaging Method to compute fluid saturated moduli knowing
[2]   ⍝ elastic moduli of  fluid, and gas saturants, and the dry rock.
[3]
[4]   ⍝ Input matrix a
[5]   ⍝  m1   fluid satd. rock
[6]   mo←,a[;1]     ⍝  dry frame modulus
[7]   mq←,a[;2]     ⍝  mineral modulus
[8]   ma←,a[;3]     ⍝  gas (dry)  modulus
[9]   mfl←,a[;4]    ⍝  fluid1  modulus
[10]  phis←a[;5]    ⍝  volume fraction of fluid1 (dry) porosity
[11]
[12]  ⍝ Bound Average Method
[13]  ⍝ subscript=o dry rock
[14]  p←1                       ⍝ upper bound for dry rock
[15]  mou←( ((1-phis)×(mq*p)) +  ((phis)×(ma*p)) ) * (1÷p)
[16]  p←¯1                      ⍝ lower bound for dry rock
[17]  mol←( ((1-phis)×(mq*p)) +  ((phis)×(ma*p)) ) * (1÷p)
[18]
[19]  ⍝ subscript=1 fluid filled
[20]  p←1                       ⍝ upper bound for satd. rock
[21]  m1u←( ((1-phis)×(mq*p)) +  ((phis)×(mfl*p)) ) * (1÷p)
[22]  p←¯1                      ⍝ lower bound for satd. rock
[23]  m1l←( ((1-phis)×(mq*p)) +  ((phis)×(mfl*p)) ) * (1÷p)
[24]
[25]  ⍝ result m1, moduli of the fluid saturated rock
[26]  m1←m1l+ (mo- mol)×((m1u-m1l)÷(mou-mol))
    ∇
```

```
     ∇fluid
[1]   ⍝ clay and water suspension using power average of data from Yin
[2]
[3]   ko←24 ⋄ go←10  ⍝ bulk and shear modulus of clay mineral (GPa)
[4]   kw←2  ⋄ gw←0   ⍝ bulk and shear modulus of water (GPa)
[5]   p←.8           ⍝ power used in averaging
[6]
[7]   ⍝ power average for bulk and shear modulus of clay-water mixture
[8]   vpor←(phis-clay×(1-phic))÷phis
[9]   kfl←( ((1-vpor)×(ko*p)) +  ((vpor)×(kw*p)) ) * (1÷p)
[10]  gfl←( ((1-vpor)×(go*p)) +  ((vpor)×(gw*p)) ) * (1÷p)
[11]  vpor[c2]←phic[c2]
[12]  kfl[c2]←( ((1-vpor[c2])×(ko*p)) +((vpor[c2])×(kw*p)) ) * (1÷p)
[13]  gfl[c2]←( ((1-vpor[c2])×(go*p)) +((vpor[c2])×(gw*p)) ) * (1÷p)
```

```
     ∇frame
[1]   ⍝ COMPUTES FLUID SATURATED MODULI FOR INITIAL SAND/DETRITAL CLAY MODEL
[2]
[3]   ⍝ Initial values of dry uncemented bulk and shear modulus
[4]   mkdryo←((ρclay),1)ρ 1.8   ⍝ dry frame bulk modulus (Ottowa sand)(GPa)
[5]   kdryo←,mkdryo
[6]   mgdryo←((ρclay),1)ρ 1.7   ⍝ dry frame shear modulus (Ottowa sand)(GPa)
[7]   gdryo←,mgdryo
[8]
[9]   mkq←((ρclay),1)ρ 38       ⍝ mineral bulk modulus (quartz) (GPa)
[10]  kq←,mkq
[11]  mgq←((ρclay),1)ρ 44       ⍝ mineral shear modulus (quartz) (GPa)
[12]  gq←,mgq
[13]
[14]  mka←((ρclay),1)ρ .001     ⍝ bulk modulus of air (GPa)
[15]  ka←,mka
[16]  mga←((ρclay),1)ρ 1×10*¯9  ⍝ shear modulus of air (GPa)
[17]  ga←,mga
[18]
[19]  mkfl←((ρclay),1)ρ kfl     ⍝ bulk modulus of fluid (from ∇fluid)(GPa)
[20]  kfl←,mkfl
[21]  mgfl←((ρclay),1)ρ gfl     ⍝ shear modulus of fluid (from ∇fluid)(GPa)
[22]  gfl←,mgfl
[23]
[24]  ⍝ COMPUTE FLUID SATURATED BULK AND SHEAR MODULI
[25]  mphis←((ρclay),1)ρ phis   ⍝ sand porosity
[26]  phis←,mphis
[27]
[28]  ⍝ For sandstone and shaley sandstones use Bound Averaging Method
[29]  ⍝ Uses the function ∇bam
[30]  a←mkdryo,mkq,mka,mkfl,mphis
[31]  ksat←bam a
[32]  a←mgdryo,mgq,mga,mgfl,mphis
[33]  gsat←bam a
[34]
[35]  ⍝ For shales use power average of qtz and clay
[36]  p←¯1               ⍝ power for average
[37]  ksat[c2]←( ((1-clay[c2])×((kq[c2])*p))+((clay[c2])×(kfl[c2]*p)))*(1÷p)
[38]  gsat[c2]←( ((1-clay[c2])×((gq[c2])*p))+((clay[c2])×(gfl[c2]*p)))*(1÷p)
[39]  pssat←((ksat+1.333×gsat)÷gsat )*2
[40]
[41]  ⍝ P and S wave velocities (km/s)
[42]  vp←((ksat+(1.333×gsat))÷den)*.5
[43]  vs←(gsat÷den)*.5
```

Chapter 3

Static and Dynamic Moduli

Abstract

Using laboratory measurements, we investigate the relationship between static and dynamic moduli in tight gas sandstones and shales. Static and dynamic measurements were made simultaneously on room-dry samples as a function of confining pressure from 5-125 MPa. We find in the data set, composed of 473 data points, that static moduli are generally lower than dynamic. The discrepancy can be as great as a factor of 5. We observe that the relationship between static and dynamic moduli is greatly scattered. This scatter may be attributed to two parameters: (1) shaliness and (2) confining pressure. In shales, we find that the ratio of dynamic to static moduli is rather insensitive to confining pressure. The ratio ranges between 1.1 and 1.6. In contrast, sandstones exhibit strong dependence of the ratio of dynamic to static moduli on confining pressure. This behavior may be attributed to the differing sensitivity of static and dynamic moduli to cracks.

For saturated rocks, we show that the discrepancy is a combination of both strain amplitude and frequency. A model is proposed (Mavko and Jizba, 1991) to estimate the effect of frequency on velocity by quantifying the effects of pore fluid flow that occur at the scale of undrained pores. High-frequency unrelaxed bulk and shear moduli are computed in terms of measured fluid and mineral moduli. The results,

when combined with the Biot formulation explain the measured total P and S wave dispersion for a variety of saturated rocks.

3.1 Introduction

The determination of in-situ rock mechanical properties such as static moduli and shear strength is essential in a variety of reservoir production and engineering tasks that include hydraulic fracturing, estimation of reserves, prediction of well bore stability and platform subsidence. Information on rock mechanical properties may be obtained in several ways. In situ and laboratory tests can be performed to measure rock mechanical properties directly. However, due to expense, and difficulty of core recovery and reconstruction of in situ conditions in the case of laboratory measurements, these tests are not performed extensively. An alternative is to obtain the elastic moduli using methods based on wave propagation. Velocity measurements are advantageous in that they are recorded on a fairly routine basis and provide extensive measurement coverage at in situ conditions. Methods based on propagation of P- and S-waves are consequently powerful tools provided we understand how to relate the dynamic moduli from wave propagation to the static moduli measured mechanically.

The static bulk moduli of rocks from stress-strain measurements often differ considerably from the dynamic moduli obtained from ultrasonic P and S-wave velocity measurements. The difference between static and dynamic moduli in many rocks may be attributed to departure from linear elastic deformation. In laboratory investigations, Simmons and Brace (1965), King (1969), and Cheng and Johnston (1981) found that at low confining pressure, the static moduli are generally less than the dynamic deformation. Walsh and Brace (1966) concluded that the discrepancy is attributed to the presence of highly compliant cracks which affect the static deformation differently than the dynamic. When the concentration of cracks is low, the static modulus in dry rock approaches the dynamic value. Shales may behave differently. In investigating a shale that lacked measurable microcrack porosity, Cheng and Johnston (1981) found the static and dynamic ratio to be nearly constant at pressures up to 200 MPa.

There are two main causes for the origin of this discrepancy: frequency and strain amplitude. Dynamic methods from seismic wave propagation cover a wide range of frequencies from exploration (< 100 Hz), to logging ($\approx 10^4$ Hz), and laboratory ($10^5 - 10^6$ Hz) measurements. These are all characterized by small strain amplitude (10^{-7} or less). Static measurements in which the rock is stressed at a much slower rate, are characterized by low frequency and large strain amplitude (10^{-4} or more). Strain-amplitude dependent mechanisms are generally attributed to frictional losses that are important in the domain of static measurements (Gordon and Davis, 1968; Mavko, 1979; Winkler, 1979). Frequency-dependent mechanisms are ascribed mostly to inertial and viscous losses associated with wave propagation in saturated rocks (Biot, 1956; Mavko and Jizba, 1990). Viscoelasticity of the rock frame itself may also be important in shales (Johnston, 1987). A combination of both mechanisms is likely to account for the discrepancy in moduli obtained from static vs. dynamic methods.

In this chapter we focus on laboratory observations and mechanisms that may be used to explain the discrepancy between static and dynamic moduli in tight gas sandstones and shales. First, we present laboratory results of static and dynamic bulk moduli on 43 tight gas sandstones and shales. Second, the effect of frequency is modeled and comparisons with laboratory data are made.

3.2 Observations on laboratory data

In this section we present laboratory results on static and dynamic bulk moduli on 43 tight gas sandstones and shales with porosity ranging from .2 to 14 percent and clay content ranging from 0 to 66 percent. Data for individual rocks are listed in Chapter 6.

3.2.1 Experimental method

The static and dynamic tests were performed by New England Research Incorporated. Ultrasonic compressional V_p and shear V_s velocities were measured using the pulse transmission technique (Birch, 1960) with central frequencies of 1MHz for the piezoelectric P and S wave signals. Measurements were performed on room-dry cores of 2.5 cm in diameter and 3.4 to 5.0 cm in length, with propagation direction parallel to the core axis. The samples were pressurized hydrostatically, recording P and S wave travel times during a hydrostatic stress cycle. Shortening of the sample during testing was measured by recording axial strain of the sample. Bulk density, ρ, was computed by measuring weight and core dimensions. Dynamic bulk moduli were computed from velocity and density data using the relationship:

$$K_{dyn} = \rho({V_p}^2 - (4/3){V_s}^2) \tag{3.1}$$

Strains were measured using strain gauges epoxied to a copper jacketed sample. Core surfaces were first polished smooth using 400 grit sandpaper. In coarse-grained samples, a thin layer of epoxy was applied to the rock surface to prevent the strain gauge from embedding into the pore space at high confining stress. Samples were next placed into a 0.13 mm thick copper jacket. The copper jacket was seated against the sample by pressurizing the sealed core and jacket assembly under 14 MPa argon gas. The copper jacket was then sanded and cleaned with acetone. Two strain gauges, Micro-Measurements CEA-06-250UW-120, were epoxied to the jacket surface. One gauge was positioned on the cylindrical surface with its grid aligned parallel to the sample axis with the other gauge oriented normal to the core axis. P and S velocity transducers were used to seal sample ends. Figure 3.1 shows configuration of the sample, transducers, and strain gauges.

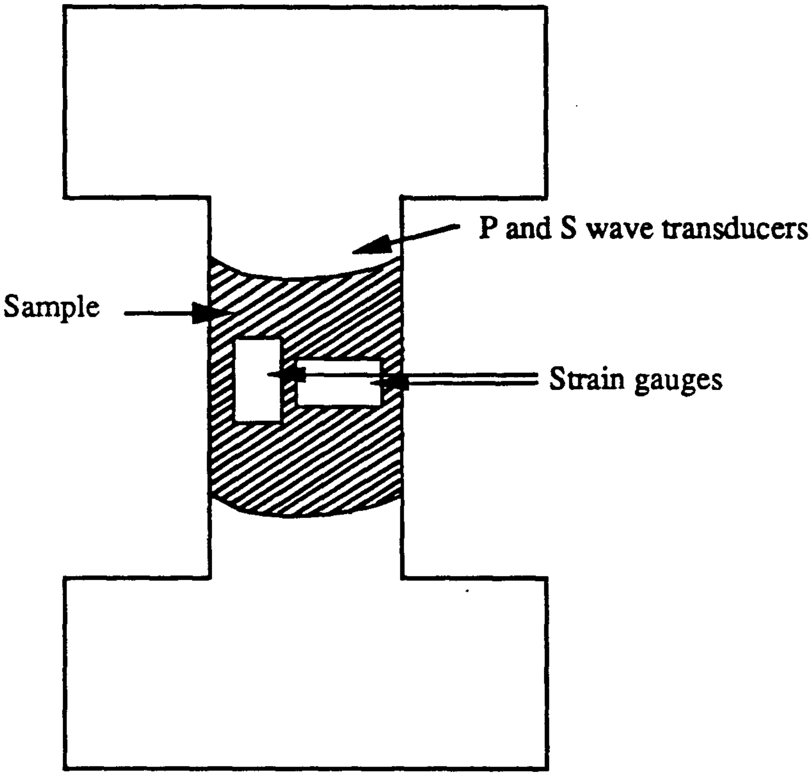

Figure 3.1: Configuration of transducers, strain gauges, and sample.

The fully jacketed assembly was placed in a pressure vessel where a pre-stress pressure cycle of 20 MPa was applied to seat the sample in the vessel and to check strain-gauge response. Hydrostatic confining pressure was next increased manually at a constant rate of approximately 0.5 MPa per second with pauses at 5, 10, 20, 40, 75, and 125 MPa holding pressure constant to record P and S wave velocities. The sample was then unloaded, recording P and S wave velocities with the same procedure. Static bulk modulus is given by the slope of the stress strain curve

$$K_{stat} = \frac{dP}{d\epsilon_{vol}} \tag{3.2}$$

To obtain static bulk moduli, slopes were computed using line segment least squares fits to the pressure versus volumetric strain data over a pressure range. This typically includes 20-50 data points.

We estimate a 2 percent error in computing static bulk modulus from the slope of the stress-strain data. We note that static measurements are subject to the greatest error at low stress where (1) the rock is most compliant and (2) strains from the rock and jacket assembly may be recorded. To minimize the second effect we applied a pre-stress to the rock and jacket assembly. We suggest that one does not focus attention on the measurements at low confining pressure. A reasonable minimum confining pressure to examine the data quantitatively is the in situ overburden pressure which ranges between 20-40 MPa for these rocks.

Measurement error associated with the dynamic bulk modulus from velocity and density measurements is approximately 5 percent. We note that a major assumption in our analysis is isotropy of the rocks. Most of the rocks tested exhibit a certain degree of anisotropy in the stress-strain data that ranges from 5 to 20 percent. The results should be viewed with this point in mind.

3.2.2 Experimental results

Figure 3.2 shows static and dynamic moduli data collected from the 43 tight gas sandstones. We observe that the relationship between static and dynamic moduli is largely scattered. In investigating this data set, we find that the relation between static and dynamic moduli is dictated (1) by lithology and (2) by confining pressure.

We find that there is a distinct difference in behavior between sandstones and shales. Figure 3.3 shows volumetric stress-strain and static (Ks) and dynamic (Kd) moduli data for a clean sandstone containing 3 percent porosity and 2 percent clay. The sandstone exhibits non-linear volumetric strain with pressure (upper left figure) that may be attributed to the closure of cracks (Walsh 1965). Static and dynamic bulk moduli (upper right figure) are in relatively close agreement over the full range of confining pressure. The ratio of dynamic to static modulus (lower figure) is close

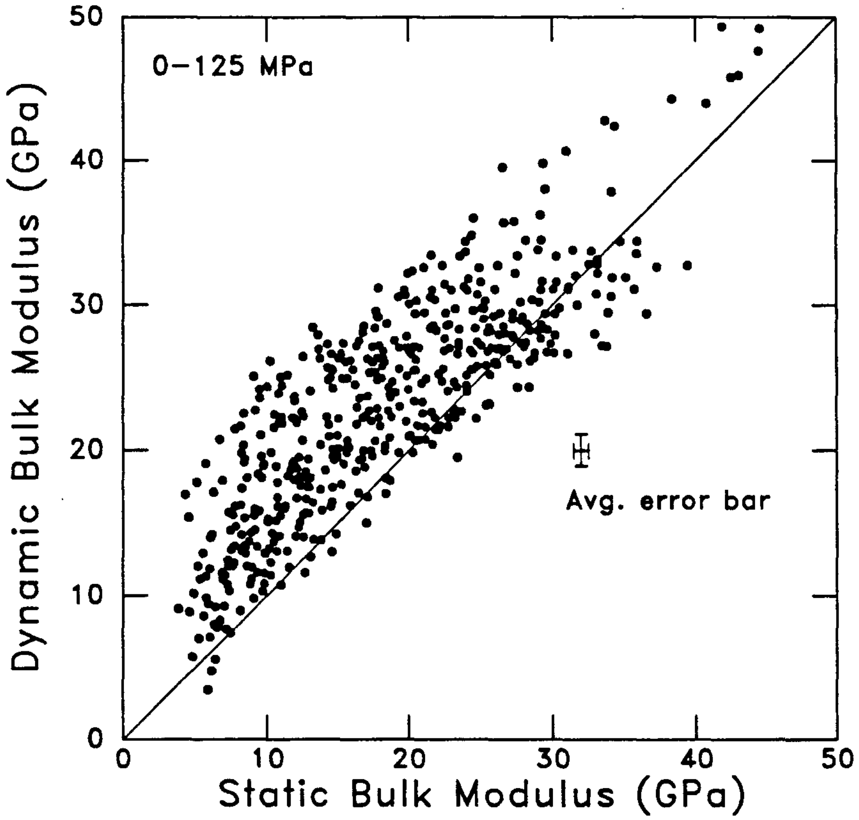

Figure 3.2: Dynamic bulk moduli exceed static moduli in most sandstones and shales. Data are from 43 tight gas sandstones measured in room-dry condition at various confining pressures from 5 to 125 MPa.

to unity except at stresses less than 40 MPa. This departure occurs at the same pressures where we observe slight hysteresis in the static stress-strain diagram, and may indicate that a correlation exists between the static stress-strain hysteresis and the ratio of dynamic to static moduli.

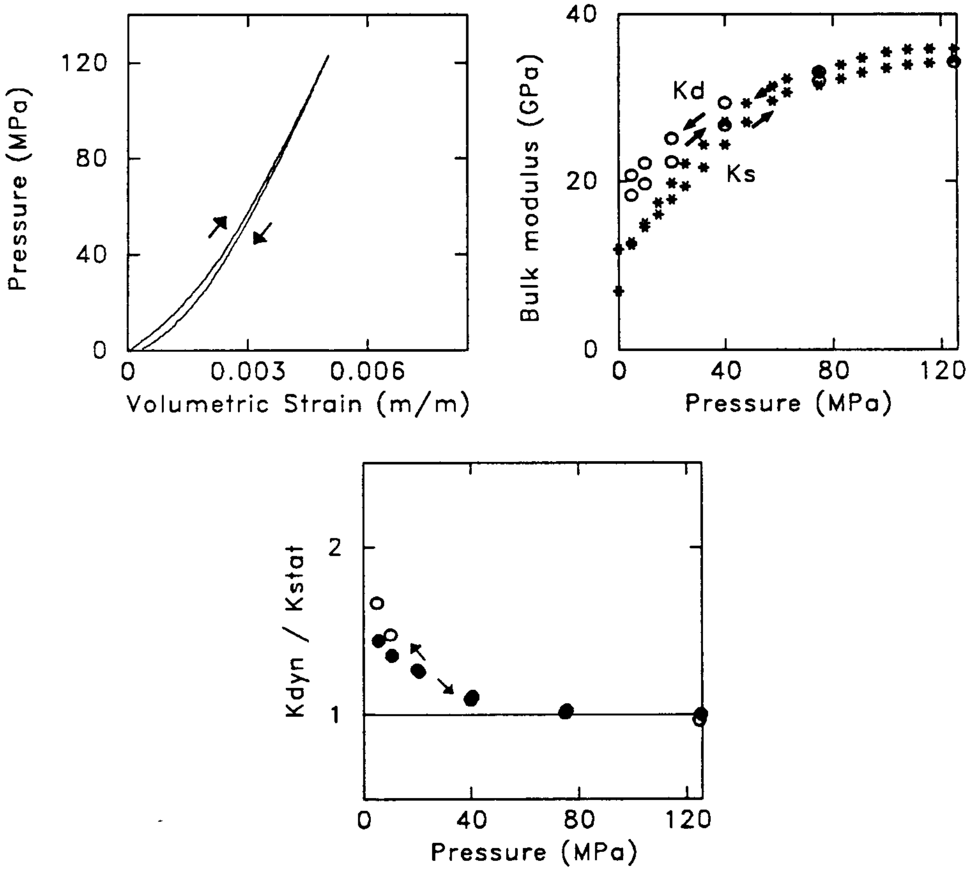

Figure 3.3: Dynamic vs. static moduli in a clean sandstone containing 3 % porosity and 2 % clay. This rock is from the A.T. Mast well at 9975 feet.

Figure 3.4 shows volumetric stress-strain and static and dynamic moduli data for a shaley sandstone containing 8 percent porosity and 10 percent clay. The shaley sandstone exhibits a non-linear static stress-strain behavior, and therefore a pressure dependence of the static and dynamic bulk moduli. In the stress-strain diagram we also notice hysteresis and permanent compaction. As with the clean sandstone in Figure 3.3, there appears to be a close association between the ratio of dynamic to static moduli and static hysteresis. With increasing confining pressure the hysteresis decreases and the ratio Kd/Ks decreases from a maximum at 2.4 at 5MPa to unity at pressures greater than 100 MPa where no more hysteresis in the stress-strain data occurs.

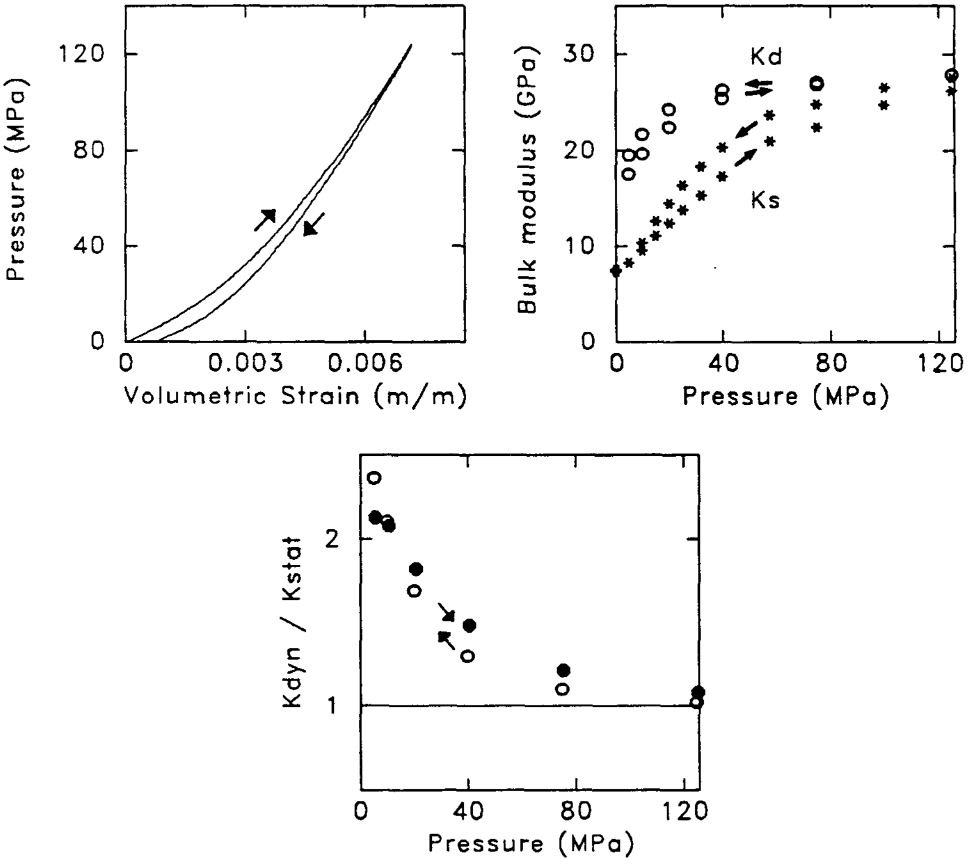

Figure 3.4: Dynamic vs. static moduli in a shaley sandstone containing 8 % porosity and 10 % clay. This rock is from the Sam Hughes well at 7096 feet depth.

In Figure 3.5 we see volumetric stress-strain and static and dynamic moduli data in a shale, containing 2 percent porosity and 39 percent clay. We notice that the

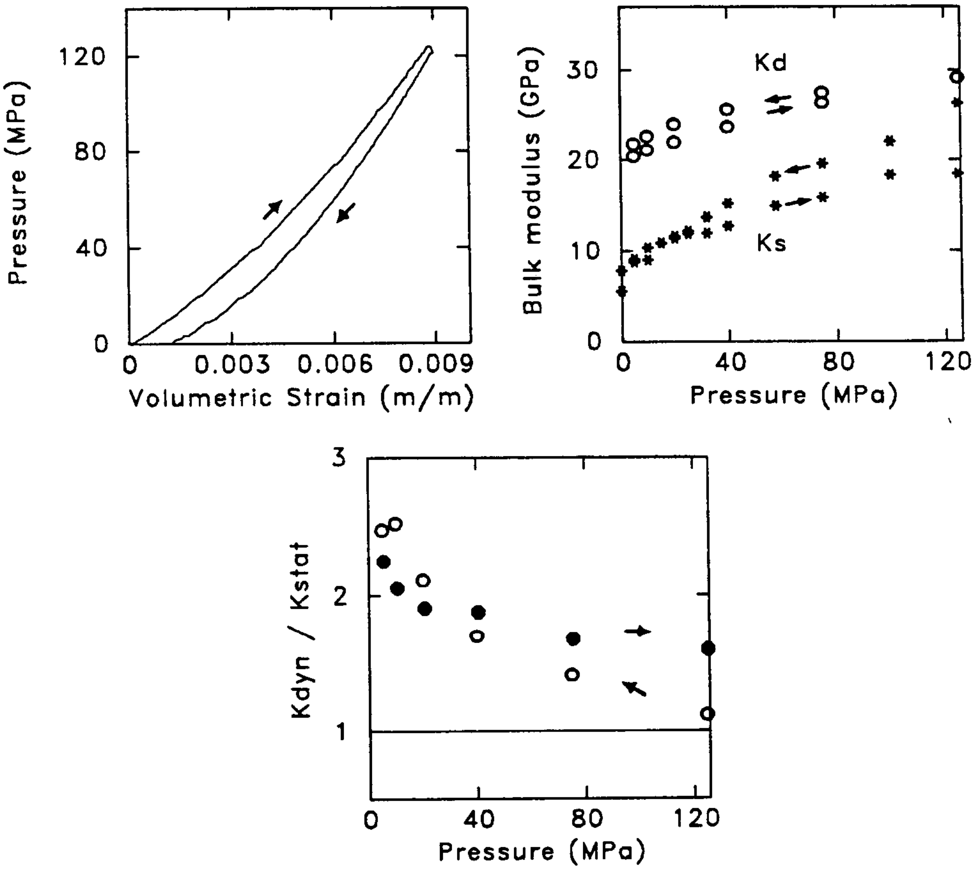

Figure 3.5: Dynamic vs. static moduli in a shale containing 2 % porosity and 39 % clay. This rock is from the Sam Hughes well at 7057 feet depth.

shale, unlike the sandstones, exhibits very little non-linearity in the static stress-strain data. The static moduli are only weakly pressure dependent during loading, increasing from 9 to 18 GPa. The static bulk modulus jumps from 18 to 26 GPa in going from loading to unloading at 125 MPa confining pressure. This is seen by the discontinuity in slope of the stress vs. strain data when unloading begins. We attribute this behavior to frictional effects that may delay the grains from immediately sliding against each other in the opposite sense upon unloading (Walsh 1965). The dynamic bulk moduli are on the order of 50 percent larger than the static and unlike the other samples, the difference between static and dynamic persists to high pressure. As with the other samples, there is an apparent association between hysteresis and a large ratio of dynamic to static modulus.

Figure 3.6 shows the moduli ratios from seven sandstones (clay volume fraction less than 17 percent), which exhibit a strong pressure dependence similar to the sandstone shown in Figure 3.3. Values of the dynamic to static ratio at low confining pressure range from 1.0 to 1.7 and asymptotically reach values between 0.8 and 1.0 at high confining pressure.

For shaley sandstones and shales (clay volume fraction greater than 17 percent) (Figure 3.7) there is a distinction between loading and unloading. During loading the ratio of dynamic to static bulk modulus is systematically independent of pressure and may range from 1.1 to 1.6 depending on the sample. During unloading the ratio becomes systematically larger at low pressure. We find that for samples which contain a high amount of ankerite, a clay-sized pore-filling carbonate, the overall behavior is very similar to shale.

3.2.3 Summary

We have found that the relation between static and dynamic moduli in tight gas sandstones is dictated by (1) lithology and (2) confining pressure. As a summary, we

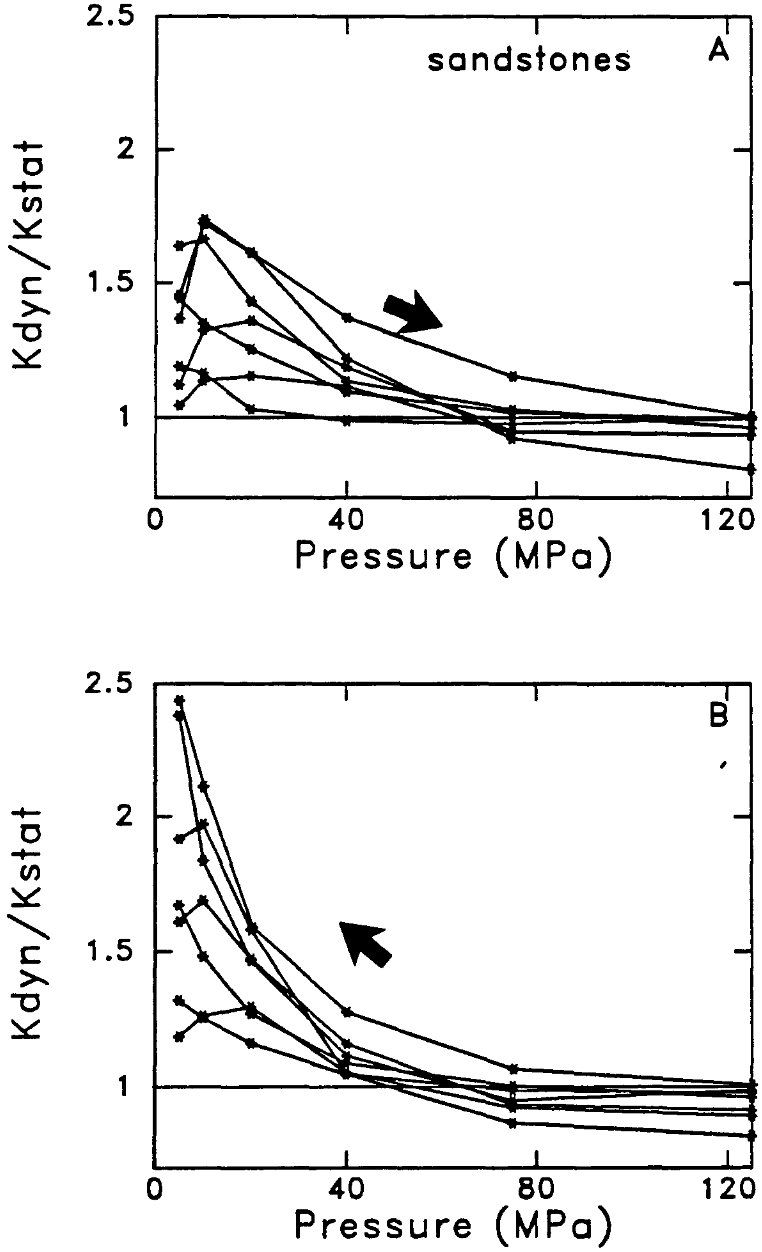

Figure 3.6: Ratio of dynamic to static bulk modulus vs. confining pressure in sandstones. Sandstones exhibit strong dependence on pressure and the ratio may range between 1.0 to 1.7 at low confining pressure and 0.8 to 1.0 at high stress.

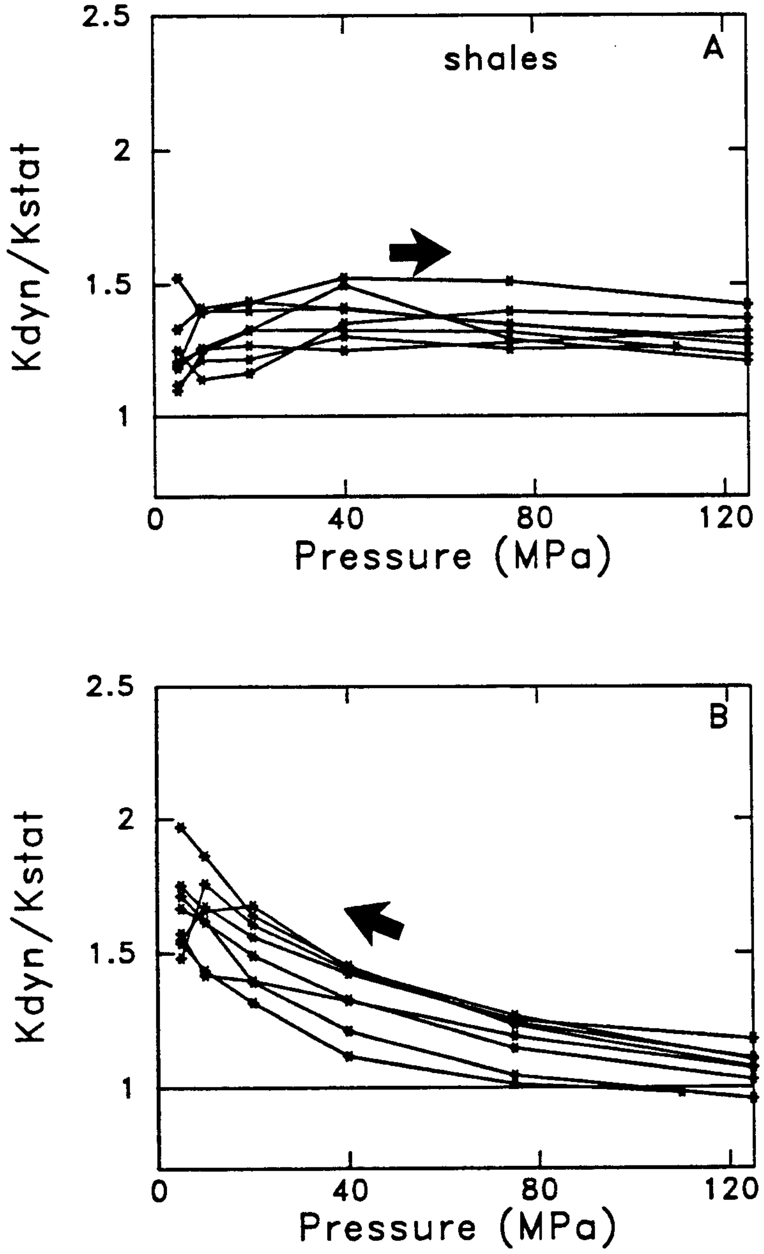

Figure 3.7: Ratio of dynamic to static bulk modulus vs. confining pressure in shales. The ratio of dynamic to static in shales is quasi pressure independent ranging in samples shown here from 1.1 to 1.6.

show in Figure 3.8 the relationship between static and dynamic moduli and its dependence on lithology. At high confining pressure (75 to 125 MPa) the dynamic moduli in the sandstones range from 17 to 35 GPa and are directly proportional to the static moduli with a slope of unity. In shales the dynamic moduli range from 20 to 38 GPa and are 25 percent larger on average than the static values which range from 15 to 35 GPa.

We have found that confining pressure has little influence on the the ratio of dynamic to static moduli in shales (Figure 3.7). We attribute this behavior to inelastic deformation in the shales. In contrast, we find that in sandstones, a large part of the scatter in the dynamic to static ratio can be attributed to confining pressure. Figure 3.9 shows dynamic bulk modulus plotted as a function of static bulk modulus in 19 sandstones. Coefficients of linear least-squares fits of static bulk modulus as a function of dynamic bulk modulus for these 19 sandstones are shown in Table 3.1 for the lines drawn in Figure 3.9.

For both sandstones and shales we suspect that the difference between dynamic and static moduli is related more to the amplitude of the measurement than to the frequency. Very low amplitude P and S waves are not expected to cause frictional sliding and therefore only sense open pore space. Static measurements cause sliding and therefore the rock appears to be more compliant.

Table 3.1

Pressure	$K_{stat} = a + bK_{dyn}$		R^2
(MPa)	a (GPa)	b	
5	0.98	.490	.71
20	3.16	.567	.77
40	1.85	.822	.81
125	-1.85	1.13	.89

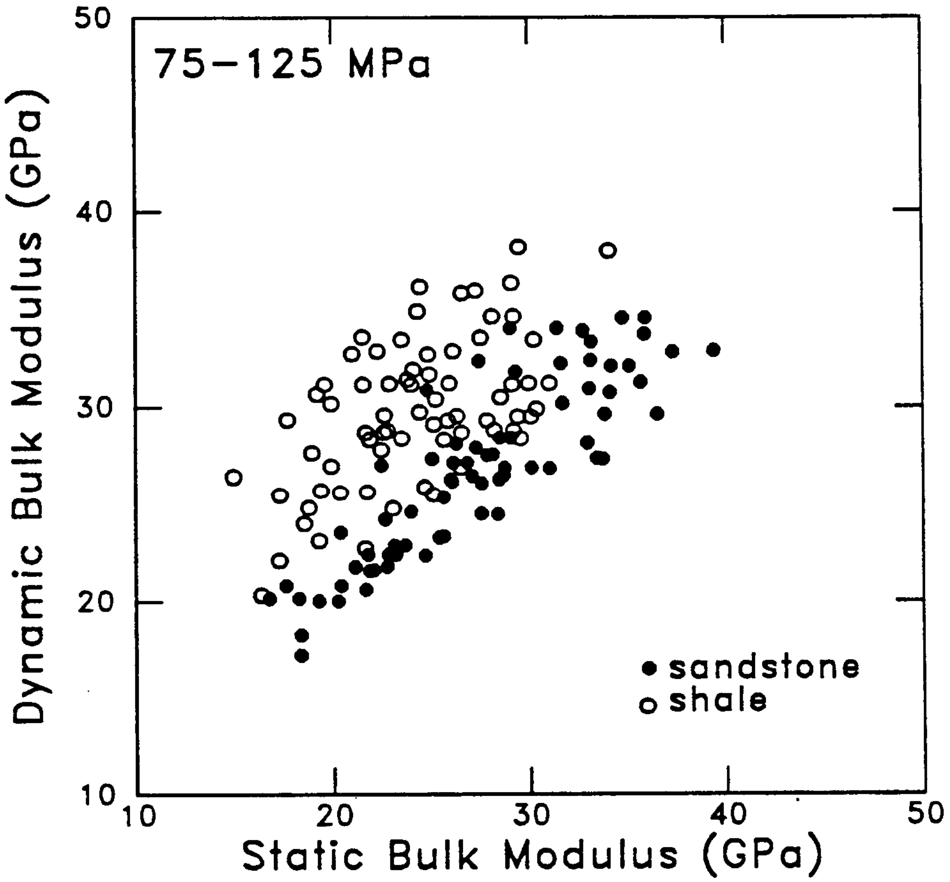

Figure 3.8: Influence of lithology on static versus dynamic moduli in tight gas sandstones. Data shown are from loading and unloading cycles at 75-125 MPa. At these stresses, sandstones exhibit static and dynamic values which are within approximately 5 percent agreement. In contrast the dynamic moduli of shales are higher than the static ones by approximately 25 percent.

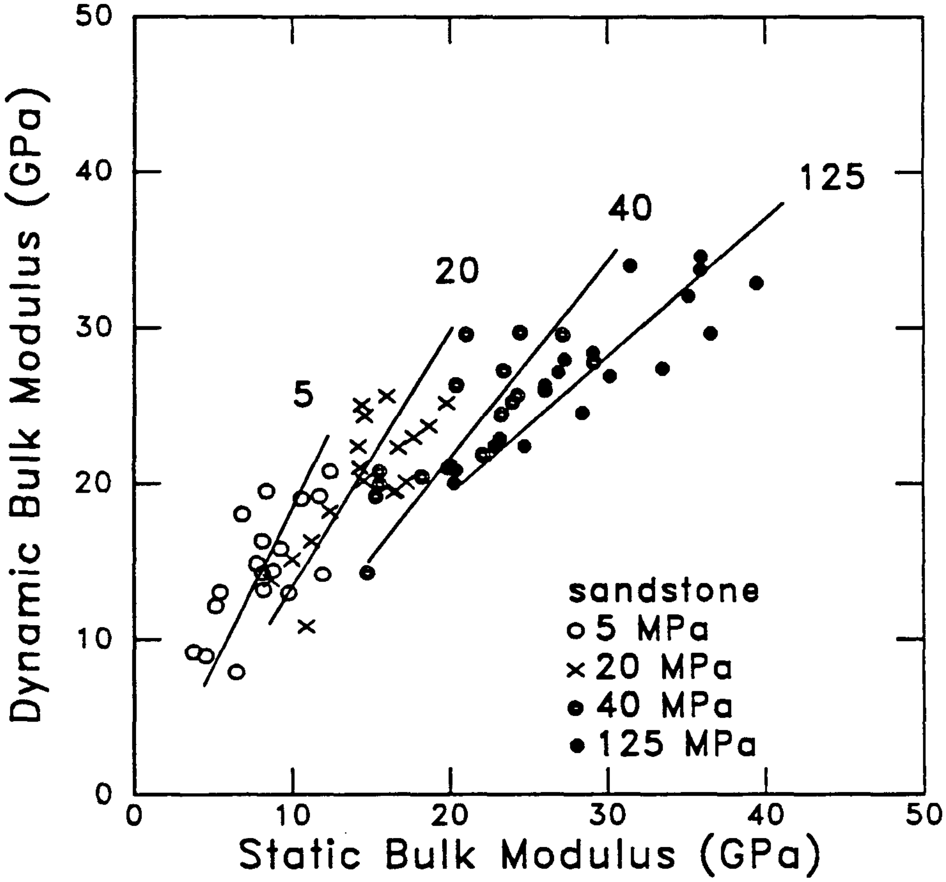

Figure 3.9: Influence of confining pressure on static vs dynamic moduli in sandstones. Pressure dependence of the moduli in shales is attributed to the differing sensitivity of static and dynamic moduli to the presence of cracks. Data shown are from the unloading cycle.

3.3 Effect of frequency

In this section we investigate the effect of frequency on velocities in rocks. This effect is superposed on the strain-amplitude effects in going from dry to saturated sandstones. In dry rocks, it is generally considered that velocity dispersion is negligible (Winkler, 1986). Hence in dry rock, the discrepancy between static and dynamic moduli may be due primarily to strain amplitude. In saturated rock, differential movement of the fluid and rock phase creates energy loss that is frequency dependent. Hence the ratio of dynamic to static moduli in saturated rocks depends on both strain amplitude and frequency.

3.3.1 Theoretical background

In this section we propose a model to estimate the effect of frequency on velocity measurements on fully-saturated rocks.

Dispersion in fluid-saturated rocks appears to be dominated by two mechanisms: large-scale average motion of the fluid phase relative to the solid phase, and local fluid flow due to grain-scale motion. In the case of large-scale motion, the passing wave creates differential motion of the fluid phase with respect to the solid as analyzed by Biot (1962a,b). In the case of local flow, high-frequency waves compress the rock unequally and induce local pore-pressure gradients. Stiff pores have relatively low induced pore pressures. Compliant pores transfer more of the load to the fluid, causing higher induced pore pressures. The unequilibrated pore pressures at high-frequency cause the rock to be stiffer in bulk and shear than at low frequencies when the pore pressure can equilibrate. This mechanism has been modeled in terms of idealized ellipsoidal pore shapes by O'Connell and Budiansky (1974, 1977). Mavko and Jizba (1991) have analyzed it in a more general way independent of pore shape.

The effects of unrelaxed local pore pressures are incorporated by replacing in Biot's earlier (1956a,b) formulation the normally elastic dry mineral frame with a viscoelastic frame. The formulation considers the saturated compliant fraction of the pore space to be a part of the viscoelastic frame. This assumes that at high frequencies the thin compliant pore space is relatively isolated with respect to the Biot flow that occurs in the stiffer, more equant fraction of the pore space. Consequently the saturated compliant fraction is considered part of the 'dry' frame relative to the Biot model. At sufficiently high confining pressure most of the compliant porosity is assumed to be compressed closed, so this effect should disappear. This is consistent with the observation that non-Biot dispersion tends to decrease at high confining pressure (Winkler, 1986). The unrelaxed frame bulk modulus can be approximated as (Mavko and Jizba, 1991):

$$\frac{1}{K_{uf}(\sigma)} \approx (\frac{1}{K_{rf}})_{high\sigma} + (\frac{1}{K_f} - \frac{1}{K_0})\phi_{soft}(\sigma) \tag{3.3}$$

where K_{uf} is the unrelaxed frame bulk modulus, and K_0 and K_f are the bulk moduli of the rock forming mineral and the fluid. $(K_{rf})_{high\sigma}$ is the relaxed frame modulus at high pressure. $\phi_{soft}(\sigma)$ is the compliant porosity, estimated from porosity vs. pressure data as the difference between the total porosity and the extrapolation of the high pressure porosity vs. pressure trend (Figure 3.10).

Similarly the unrelaxed frame shear modulus can be approximated as:

$$\frac{1}{\mu_{uf}} - \frac{1}{\mu_{rf}} \approx \frac{4}{15}(\frac{1}{K_{uf}} - \frac{1}{K_{rf}}) \tag{3.4}$$

where μ_{uf} and μ_{rf} are the unrelaxed and relaxed frame shear moduli. Note that the relaxed frame moduli are what we conventionally call the dry moduli, $\mu_{rf} = \mu_{dry}$ and $K_{rf} = K_{dry}$, since in this case the thin porosity is assumed to be drained. Then equations 3.3 and 3.4 can be written as (Mavko and Jizba, 1991):

$$\frac{1}{K_{uf}(\sigma)} \approx (\frac{1}{K_{dry}})_{high\sigma} + (\frac{1}{K_f} - \frac{1}{K_0})\phi_{soft}(\sigma) \tag{3.5}$$

$$\frac{1}{\mu_{uf}} \approx \frac{1}{\mu_{dry}} + \frac{4}{15}(\frac{1}{K_{uf}} - \frac{1}{K_{dry}}) \tag{3.6}$$

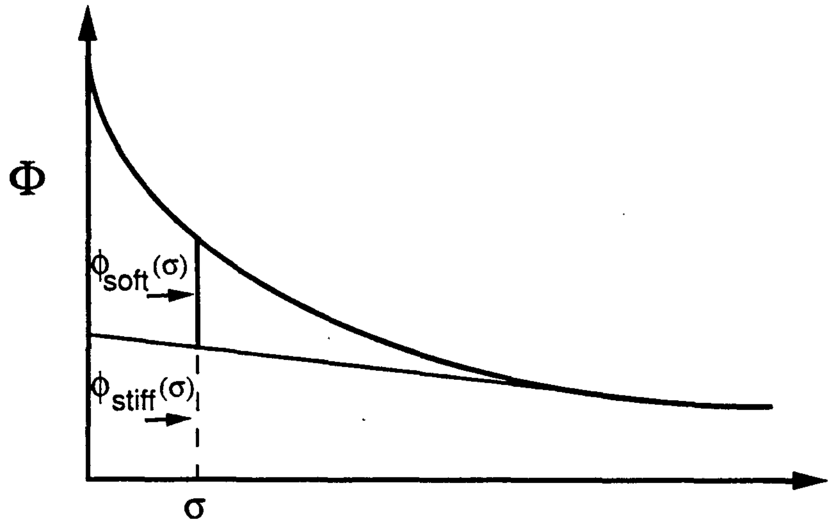

Figure 3.10: Schematic plot of dry rock porosity vs. confining pressure.

Note that $(\frac{1}{K_{dry}})_{high\sigma}$ in equation 3.5, is not always measured. In the following section we propose a method to estimate $(K_{dry})_{high\sigma}$. We also test the model for bulk and shear dispersion, and we finally compare model results with experimental data.

3.3.2 High pressure moduli

Our goal here is to estimate values of $(K_{dry})_{high\sigma}$ in equation 3.5 for sandstones of varying clay content and porosity. We discuss the observation that in spite of the scatter shown in Figure 3.11, the *high pressure* moduli of sandstones appears to be systematically related to porosity and clay content (Wyllie et al., 1958; Han et al, 1986). Since for sandstones most of the porosity appears to be stiff, one can often estimate the high pressure dry and saturated velocities from dry measurements of velocity and porosity at any lower pressure. Our analysis here includes a variety of rock types and is not restricted to tight gas sandstones.

Figure 3.11 shows dry moduli, K_{max} and μ_{max}, vs. porosity for 35 sandstones. The values are also listed in Table 3.2, along with their clay content, maximum confining pressure, P_{max}, and the sources of the data. Most of the samples appear as multiple

Table 3.2

High-pressure dry bulk and shear moduli for a variety of rocks

Figure Key	ϕ (%)	Clay (%)	P_{max} (MPa)	K_{max} (GPa)	μ_{max} (GPa)	Rock Name	Data Source
1	5.8	0	50	28.3	32.2	Beaver	1
2	18.7	6	50	15.9	14.9	Berea 100	1
3	21.7	6	50	14.8	13.0	Berea 350	1
4	21.2	3	50	13.5	13.1	Berea 400	1
5	24.5	6	50	12.9	9.4	Boise	1
6	10.3	6	50	22.6	22.5	Coconino	1
7	22.3	4	50	12.6	12.6	Connotton	1
8	10.0	5	50	21.3	20.5	Delaware Brown	1
9	5.9	7	50	27.5	24.9	Delaware Grey	1
0	15.0	3	50	20.4	20.4	Delaware Tan	1
A	14.4	0	50	21.1	22.4	Fontainebleau A	1
B	18.7	0	50	16.9	18.1	Fontainebleau B	1
C	25.4	16	50	9.6	9.7	Indiana Dark	1
D	23.4	10	50	12.3	11.5	Indiana Light	1
E	23.2	3	50	13.2	12.6	Massillon Burgundy	1
F	17.5	6	50	17.8	16.1	Massillon Dark	1
G	20.1	4	50	14.8	13.2	Massillon Light	1
H	9.0	8	50	24.0	24.4	Nugget H	1
I	8.9	8	50	20.3	22.8	Nugget V	1
J	15.0	28	50	15.4	9.8	Redstone	1
K	16.9	0	50	19.8	18.8	St. Peter	1
L	12.7	14	50	16.9	16.0	Torrey	1
M	18.5	5	50	17.1	15.2	Union	1
N	9.8	5	48	24.8	26.5	Tight Gas 8213.5	3
O	8.0	11	48	22.1	25.4	Tight Gas 8243.4	3
P	13.5	2	125	21.7	22.0	Tight Gas 8246.2	3
Q	5.8	6	125	26.9	27.5	Tight Gas 9754.2	3
R	13.9	27	50	13.3	11.0	Gulf 12409	1
S	24.1	12	50	11.2	8.8	Gulf 12416	1
T	12.6	37	50	10.7	10.4	Gulf 12418	1
U	9.8	21	50	16.3	14.9	Gulf 15845	1
V	14.6	6	50	20.6	17.2	Gulf 15879	1
W	8.8	23	50	17.1	16.5	Gulf 158xx	1
X	36.2	0	34	2.2	1.7	Ottawa sand	2
Y	35.4	0	34	1.8	1.7	Glass beads	2

(1) Han et al. (1986)
(2) Domenico (1977)
(3) Jizba, personal communication

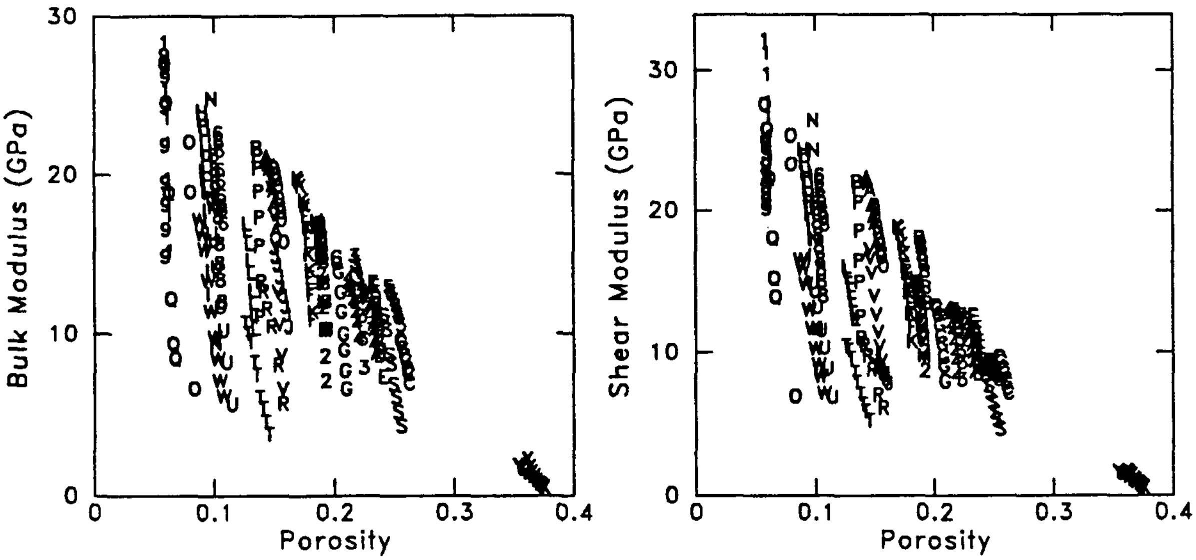

Figure 3.11: Bulk and shear dry rock modulus versus confining pressure for a variety of sandstones. Apparent lack of correlation is attributed to clay content and pore compressibility. Symbols used are listed in Table 3.2.

plotted points, reflecting the range of values obtained as a function of confining pressure. In general there is a large increase of modulus with pressure and a very small decrease of porosity with pressure. These effects are both interpreted as resulting from the closing of high-compliance, low-porosity microcracks with confining pressure. Typical modulus vs. pressure curves for individual samples are shown in Figure 3.12.

Figure 3.13 shows the dry bulk and shear moduli at the highest confining pressure measured for each of the samples (usually at 40-50 MPa), plotted vs. porosity. These are obviously more tightly clustered than those of Figure 3.11. The corresponding high-pressure dry P and S-wave velocities, from which the moduli were derived, are shown in Figure 3.14. To quantify the effects of clay on the remaining scatter, we computed regression analyses on porosity ϕ and clay volume fraction C, similar to those of Tosaya and Nur (1982) and Han et al. (1986).

In both forms the effect of clay by volume is about 1/2.4 the effect of porosity on reducing the bulk modulus and about 1/2.2 the effect of porosity on reducing the

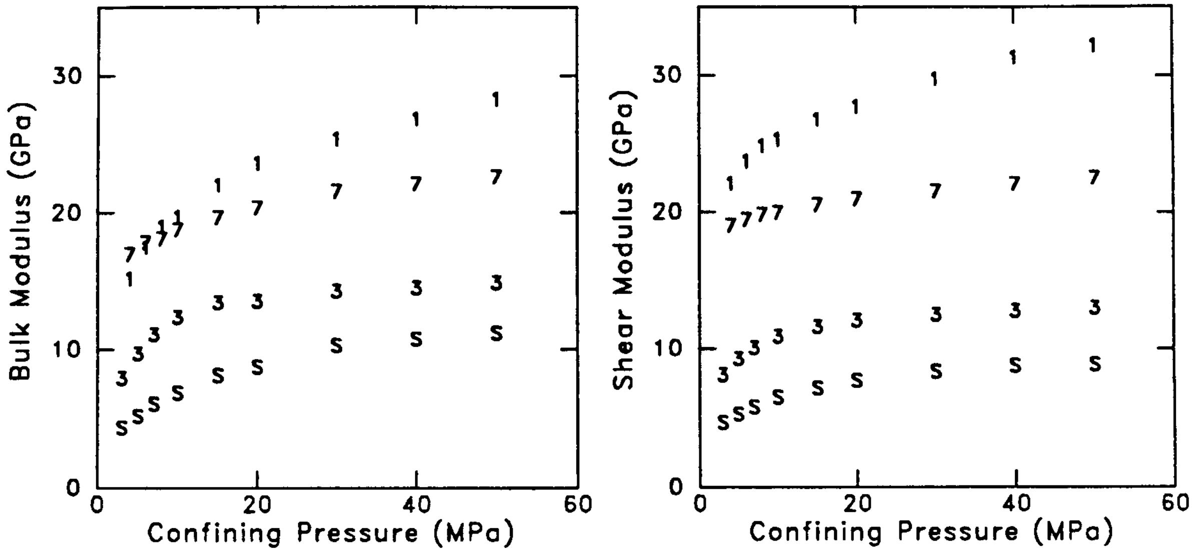

Figure 3.12: Typical moduli versus confining pressure curves for sandstones. Dependence of bulk and shear modulus on pressure is attributed to closure of highly compliant low porosity pores. Symbols correspond to key in Table 3.2.

shear modulus. Using this relation, we converted the clay content of the samples to equivalent porosity $\phi_{equiv} = \phi + \frac{C}{2.4}$ for K and $\phi_{equiv} = \phi + \frac{C}{2.2}$ for μ, and replotted them as moduli in Figure 3.15 and as velocities in Figure 3.16. The tight clustering confirms the previous observations (Tosaya and Nur, 1982; Han et al., 1986) that the effect of clay is fairly independent of composition and location within the rock matrix.

Table 3.3. Regression analyses of the effects of porosity and clay content.
K (GPa) $= 31.8 - 73.5\phi - 30.2C$ μ (GPa) $= 34.1 - 87.5\phi - 38.5C$

It is important to note that the confining pressures at which the 'high pressure' data in Figure 3.13 - 3.15 were measured (40-50 MPa) are not necessarily high enough for the modulus vs. pressure or velocity vs. pressure behavior to level off to an approximate limiting value. This is evident in the nonlinear slope and curvature at high pressure in Figure 3.12. We *define* heuristically approximate asymptotic stiffness vs.

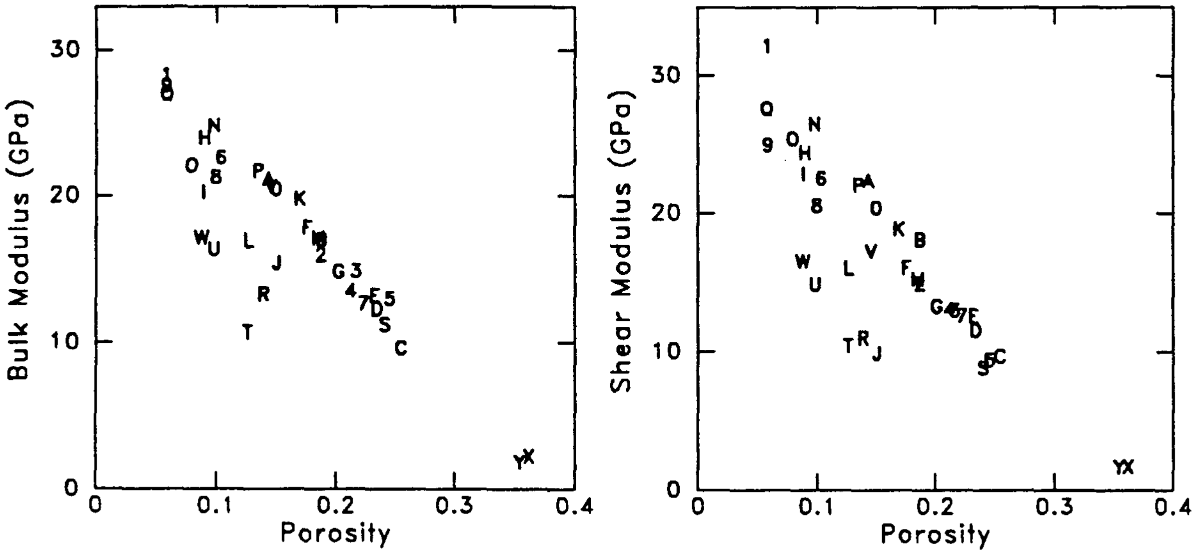

Figure 3.13: Dry bulk and shear modulus versus porosity at high confining pressure (most data at 40-50 MPa). Symbols used are listed in key of Table 3.2.

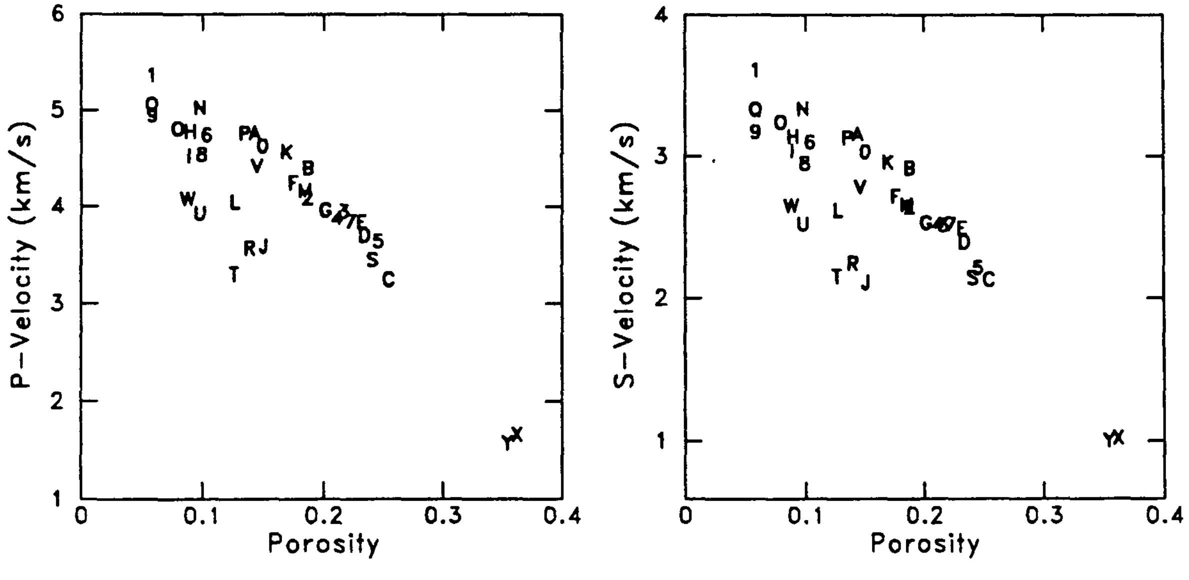

Figure 3.14: Dry P and S-wave velocity versus porosity at high confining pressure (most data at 40-50 MPa). Symbols used are listed in key of Table 3.2.

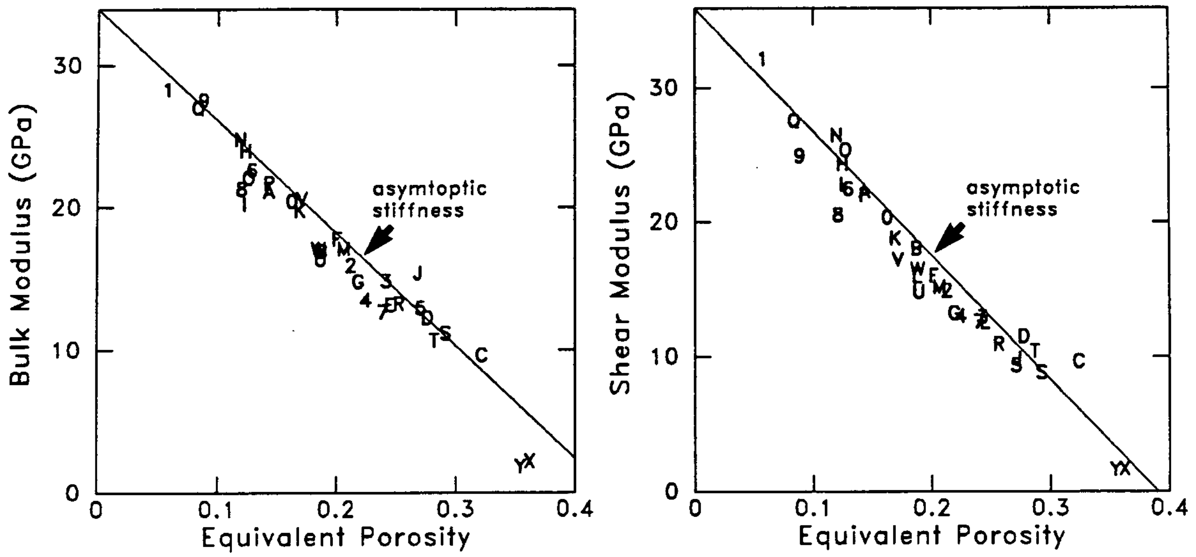

Figure 3.15: High pressure bulk and shear moduli versus equivalent porosity. We define an approximate asymptotic stiffness as the solid line (equations 3.7 and 3.8) .

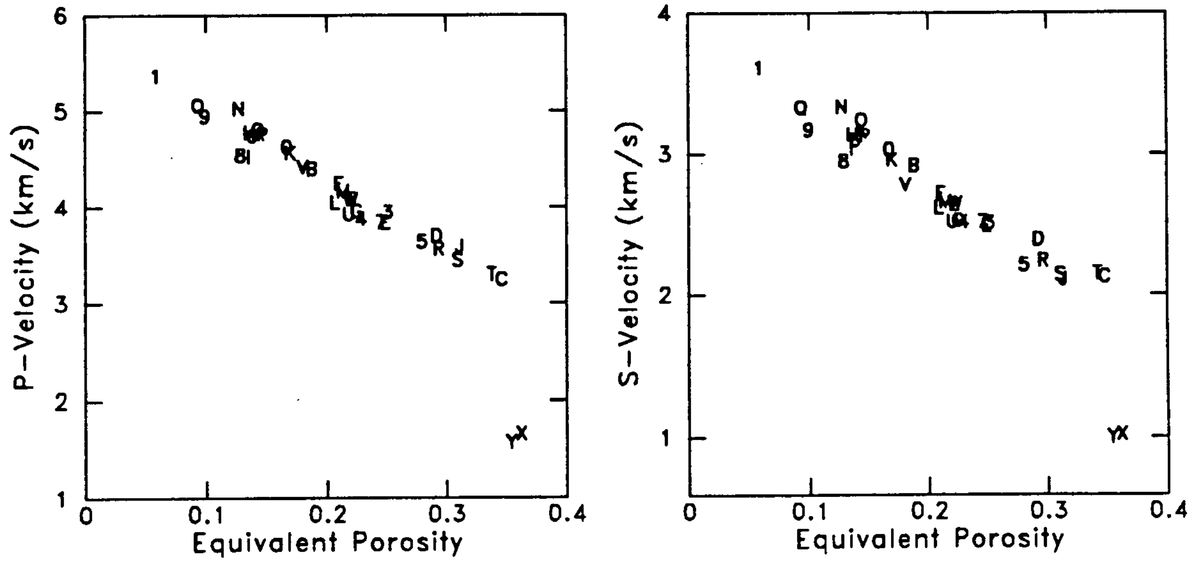

Figure 3.16: High pressure P and S-wave velocities versus equivalent porosity. Sandstone data and confining pressures are listed in Table 3.2.

porosity relations by fitting, by eye, a straight line along the upper edge of the data in Figure 3.15, giving

$$K(GPa) \approx 34 - 79\phi_{equiv} \tag{3.7}$$

$$\mu(GPa) \approx 36 - 92\phi_{equiv} \tag{3.8}$$

where ϕ_{equiv} is the equivalent porosity including the reduced effect of the clay.

Note that these are not the same as the regressions that best fit the data, but are estimates of the high-pressure 'bounds' on moduli which can be used to estimate $(\frac{1}{K_{dry}})_{high\sigma}$ in equation 3.5 when data are not available.

3.3.3 Comparison with experimental data

In this section we use our model to predict high-frequency saturated velocities in four rocks which span a range of porosity from .8 to 16 percent. We compare our predictions with the observed high-frequency laboratory data, with high-frequency predictions of Biot (1956a,b) and with low-frequency predictions of Gassmann (1951). Input parameters used in the Biot and Gassmann models are the dry bulk and shear moduli, K_{dry} and μ_{dry}, respectively (computed from the dry P and S- wave velocity data), the porosity, grain density, and mineral bulk modulus, K_0. The sample properties listed in Table 3.4 are all laboratory measured values, except for the mineral bulk modulus of Fontainebleau and the tight gas sandstone. For these two rocks we use a value of 38 GPa for quartz (Carmicheal, 1981). Variation of the mineral bulk modulus within a reasonable range of ± 5 % has a negligible impact on the computed P and S- wave velocities for these two rocks. In addition, a tortuosity factor set equal to 2.0 is used in the Biot model predictions for all of the rocks. We find that variation of tortuosity within a typical range of 1 to 3 has a negligible impact on calculated velocities.

In our calculation of high-frequency saturated unrelaxed velocities (UV) we first compute the unrelaxed frame bulk and shear moduli, K_{uf} and μ_{uf}, from equations 3.6

3.6 and 3.7. The unrelaxed frame bulk and shear moduli are then used in Biot's theory to estimate the high-frequency saturated unrelaxed velocities. The model predictions are computed at each stress where dry velocities were measured. The additional input parameter used in our model is the soft porosity calculated using porosity vs. pressure data. Note that in the absence of porosity vs. pressure data, regression equation 3.7 may be used as a first order estimate for the unrelaxed frame bulk modulus $(\frac{1}{K_{uf}(\sigma)} \approx (\frac{1}{K_{dry}})_{high\sigma}$ in equation 3.5).

Westerly Granite

Figure 3.17 shows compressional and shear ultrasonic velocity data for Westerly granite (Coyner, 1984) and a comparison between Biot, Gassmann, and our prediction for saturated velocity. The pressure dependent porosity data are also shown in Figure 3.17. At high stress the Biot prediction is in good agreement with the saturated compressional velocity data. At low stress the saturated compressional velocity data exceed the Biot predictions by as much as 5 percent. In this case, the difference between the Biot and Gassmann predictions is not resolvable due to the low porosity, $\phi \approx .8$ %, of Westerly granite. Our model is identical to Biot's model at the highest stress (100 MPa) where porosity is dominated by stiff pores of comparable compressibility. At low stress, a distribution of pore compressibilities due to the presence of both soft and stiff porosity leads to unrelaxed pore pressure gradients within the pore space and hence our unrelaxed velocity predictions are higher than the Biot predictions. Our model is within 1 % agreement with the compressional velocity over the full range of stress from .3 to 100 MPa. For shear velocity, our model predicts higher velocities than Biot and Gassmann predictions at low stress, and is within 3

% agreement of shear velocity over the full range of stress.

Tight Gas Sandstone

Figure 3.18 shows ultrasonic compressional and shear velocity data and a comparison between Biot, Gassmann, and our prediction for saturated velocity in a tight gas sandstone from the Travis Peak Formation. The pressure dependent porosity data are shown in Figure 3.18. Similar behavior to Westerly granite is observed for both compressional and shear velocity data against the various model predictions. For compressional and shear velocity, saturated data are within 2 % of our model predictions.

Navajo Sandstone

Figure 3.19 shows ultrasonic compressional and shear velocity data for Navajo sandstone (Coyner, 1984) with Biot, Gassmann, and our model predictions. The porosity data are also shown in Figure 3.19. Because of higher porosity in Navajo sandstone, $\phi \approx 11.8$ %, the difference between Biot and Gassmann predictions can be resolved. Again, Biot is within 1 % agreement of compressional velocity at high stress. At low stress, Biot and Gassmann underestimate the data by as much as 5 %. In contrast, our prediction is in mostly good agreement except for stresses lower than 20 MPa where it overestimates the saturated data by 3 %. (An overestimation is acceptable since our model attempts to estimate the high frequency limit or upper bound to the unrelaxed velocities.) Similarly, our model predictions for shear velocity are in much better agreement with the saturated data than the Biot and Gassmann predictions.

Fontainebleau Sandstone

Figure 3.20 shows ultrasonic compressional and shear velocity data for Fontainebleau sandstone (Han, 1986) with Biot, Gassmann, and our model predictions for saturated velocity. The porosity versus stress data are shown in Figure 3.20. Overall agreement of our model is good, within 2 %, for both compressional and shear velocity. We note however, in the case of Fontainebleau, that our predictions underestimate the data at the highest pressure (50 MPa). We believe that this lack of agreement at high pressure may be attributed to the fact that measurements were not taken to sufficiently high pressures so that the high pressure dry bulk modulus (taken from the data at 50 MPa) may be lower than the asymptotic value, $(K_{dry})_{high\sigma}$ in equation 3.5, due to the presence of remaining soft porosity.

Table 3.4

Sample Properties

Rock Sample	Porosity (%)	Grain Density (g/cm^3)	Mineral Bulk Modulus (GPa)
Westerly granite	.8	2.64	56
Tight gas sandstone	8.0	2.63	38
Navajo sandstone	11.8	2.63	36
Fontainebleau sandstone	16.0	2.65	38

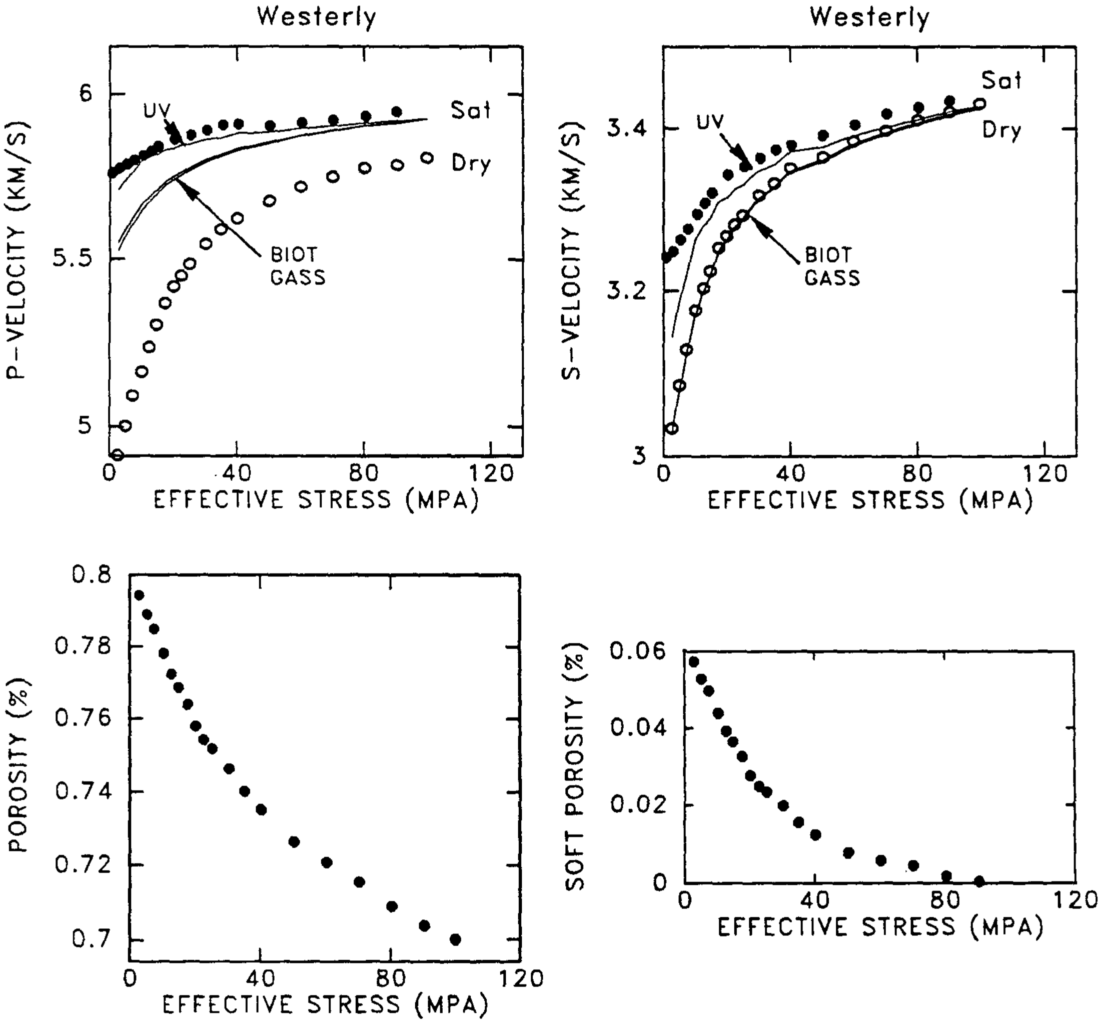

Figure 3.17: Dry and fully water-saturated P and S velocities as a function of effective stress in Westerly granite (Coyner, 1984). Good agreement between the data and our high-frequency prediction suggests that pore fluids at lab frequency (.8-.9 MHz) are unrelaxed. Porosity vs. effective stress, and soft porosity calculated from total porosity vs. stress data, used in model predictions for unrelaxed P and S velocities.

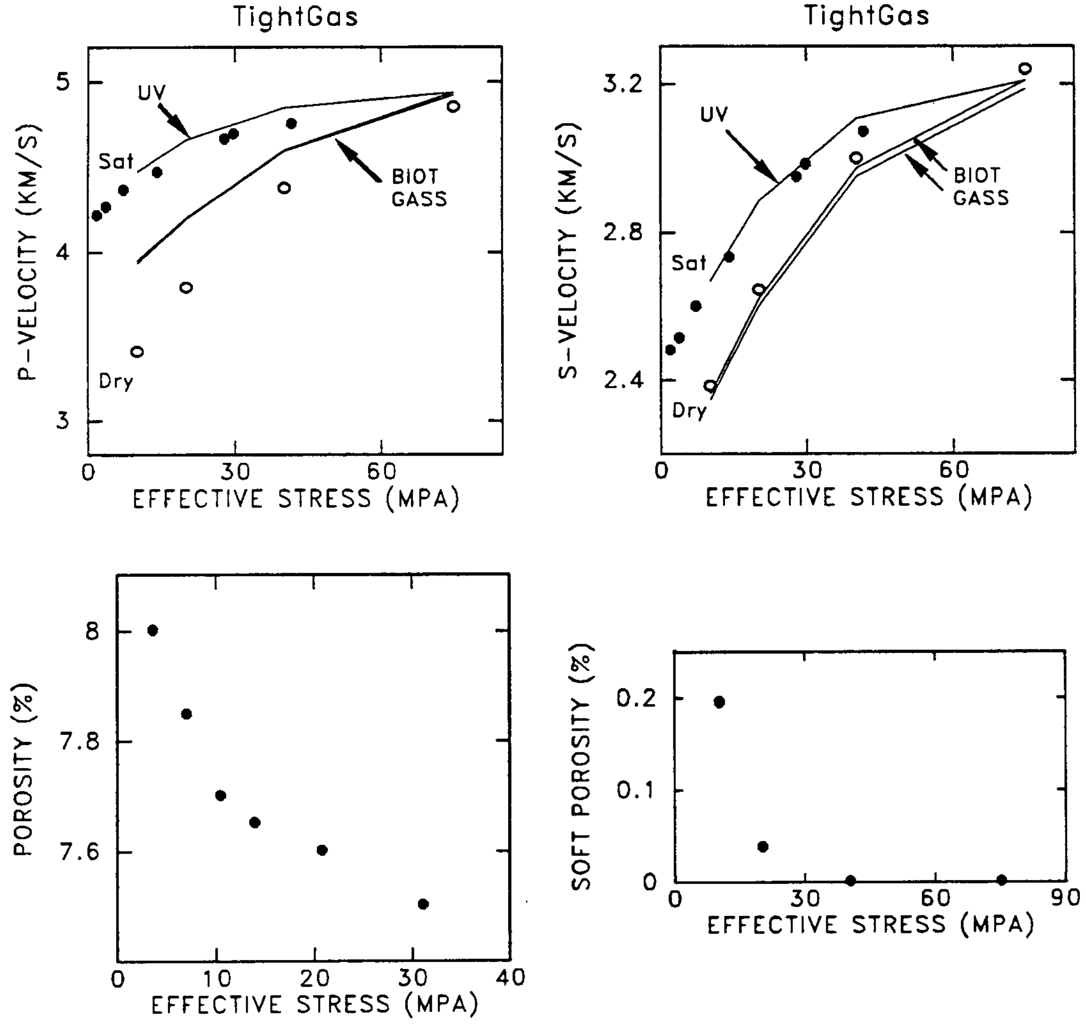

Figure 3.18: Dry and brine saturated P and S velocities as a function of effective stress in a tight gas sandstone. Good agreement between the data and our high-frequency prediction suggests that pore fluids at lab frequency (1 MHz) are unrelaxed. Porosity vs. effective stress and soft porosity calculated from total porosity vs. stress data is used in model predictions for unrelaxed P and S velocities.

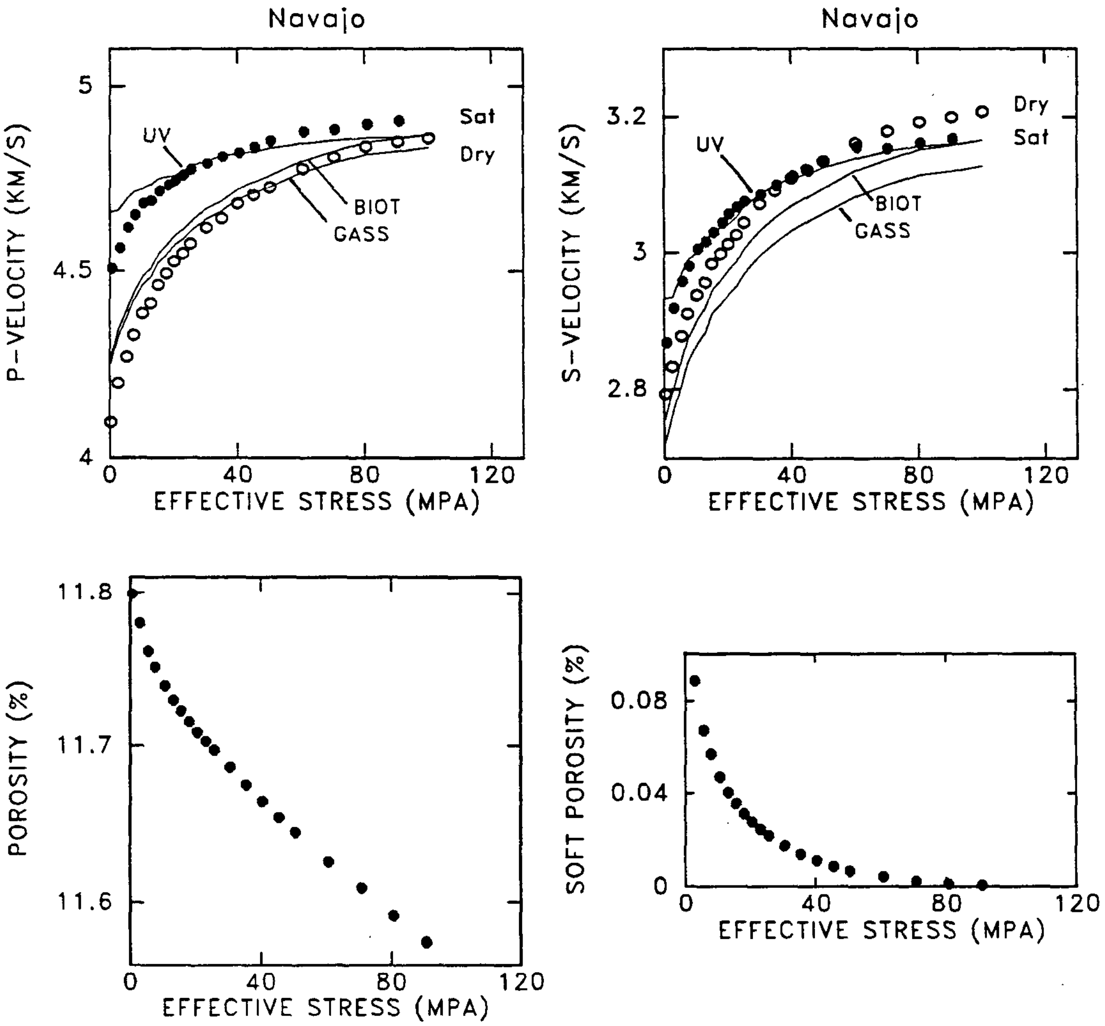

Figure 3.19: Dry and water-saturated P and S velocities as a function of effective stress in Navajo sandstone (Coyner, 1984). Good agreement between the data and our high-frequency prediction suggests that pore fluids at lab frequency (.8-.9 MHz) are unrelaxed. Porosity vs. effective stress, and soft porosity calculated from total porosity vs. stress data, used in model predictions for unrelaxed P and S velocities.

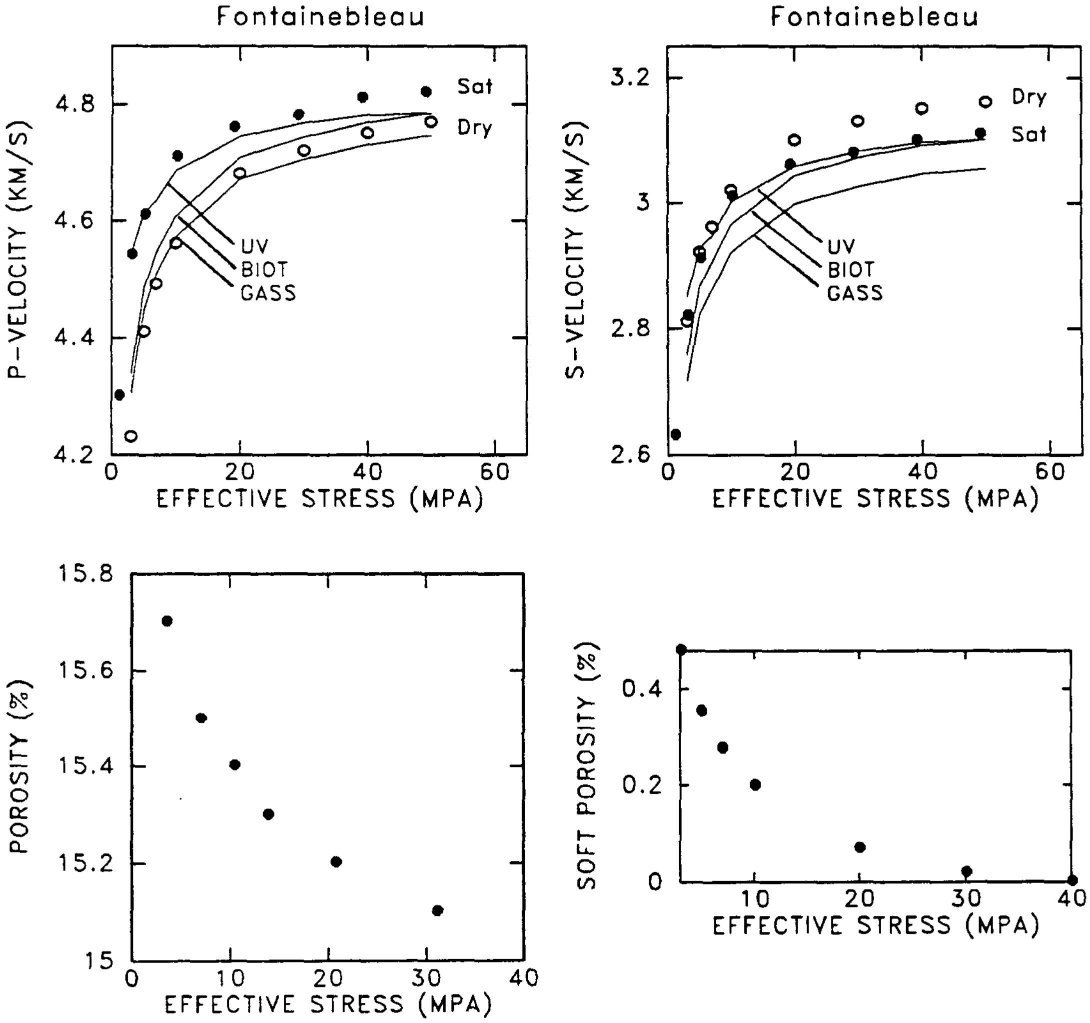

Figure 3.20: Dry and water-saturated P and S velocities as a function of effective stress in Fontainebleau (Han, 1986). Good agreement between the data and our high-frequency prediction suggests that pore fluids at lab frequency (.8-.9 MHz) are unrelaxed. Porosity vs. effective stress, and soft porosity calculated from total porosity vs. stress data, used in model predictions for unrelaxed P and S velocities.

3.3.4 Relation between P and S wave dispersion

Equation 3.6 predicts that the shear and bulk dispersion of the dry frame are proportional. To estimate the total dispersion in a saturated rock resulting from the local mechanism we substitute the unrelaxed and relaxed frame moduli into the low frequency Biot-Gassmann equations. A simplified relation between the saturated shear dispersion and bulk dispersion (Mavko and Jizba, 1991) can be written that is analogous to equation 3.6:

$$(\frac{1}{\mu_{us}} - \frac{1}{\mu_{dry}}) \approx \frac{4}{15}\left[(\frac{1}{K_{us}} - \frac{1}{K_{dry}})_{\sigma} - (\frac{1}{K_{us}} - \frac{1}{K_{dry}})_{high\sigma}\right] \tag{3.9}$$

where μ_{us} and K_{us} are the unrelaxed saturated shear and bulk moduli. The right hand side of equation 3.9 is the difference between saturated and dry compressibilities at any confining pressure, σ, less their difference at very high confining pressure, when it is assumed that only the stiff fraction of the pore space remains. Therefore the right hand side can be interpreted as the influence of only the compliant fraction of the pore space on the difference between dry and saturated compressibilities. Similarly the difference between dry and saturated compliances is assumed to result only from the compliant fraction of the pore space.

To test the relation 3.9, dry and saturated moduli were computed from velocities measured on a variety of rocks (Table 3.5) using the usual relations

$$\mu = \rho V_s^2 \qquad K = \rho(V_p^2 - (4/3)V_s^2) \tag{3.10}$$

where ρ is the total density. These are plotted as $(\frac{1}{\mu_{sat}} - \frac{1}{\mu_{dry}})$ vs. $[(\frac{1}{K_{sat}} - \frac{1}{K_{dry}})_{\sigma} - (\frac{1}{K_{sat}} - \frac{1}{K_{dry}})_{high\sigma}]$ in Figure 3.22. Our model (equation 3.9) predicts that when local flow dominates the dispersion the data should fall along the solid line with slope = $\frac{4}{15}$. When there is no dispersion, the low-frequency Biot-Gassmann theory predicts that $\mu_{sat} = \mu_{dry}$, so that the data should fall near the horizontal axis. The high-frequency Biot predictions cannot be stated so simply. The high-frequency Biot velocities are

Table 3.5

ρ (g/ cm^3)	ϕ (%)	Clay (%)	Rock Name	Data Source
2.47	6.4	0	Beaver ss.	Han (1986)
1.92	25.9	6	Boise ss.	Han (1986)
2.48	6.0	7	Delaware light ss.	Han (1986)
2.22	16.0	3	Delaware tan ss.	Han (1986)
2.12	20.0	0	Fontainebleau ss.	Han (1986)
2.17	18.4	6	Massillon dark ss.	Han (1986)
2.15	19.4	5	Union ss.	Han (1986)
2.39	9.5	8	Weber ss.	Coyner (1984)
2.02	23.1	5	Kayenta ss.	Coyner (1984)
2.32	11.8	3	Navajo ss.	Coyner (1984)
2.64	0.7	0	Barre granite	Coyner (1984)
2.64	0.8	0	Westerly granite	Coyner (1984)
2.44	8.0	10	Tight gas ss.	Jizba (1990), pers. comm.

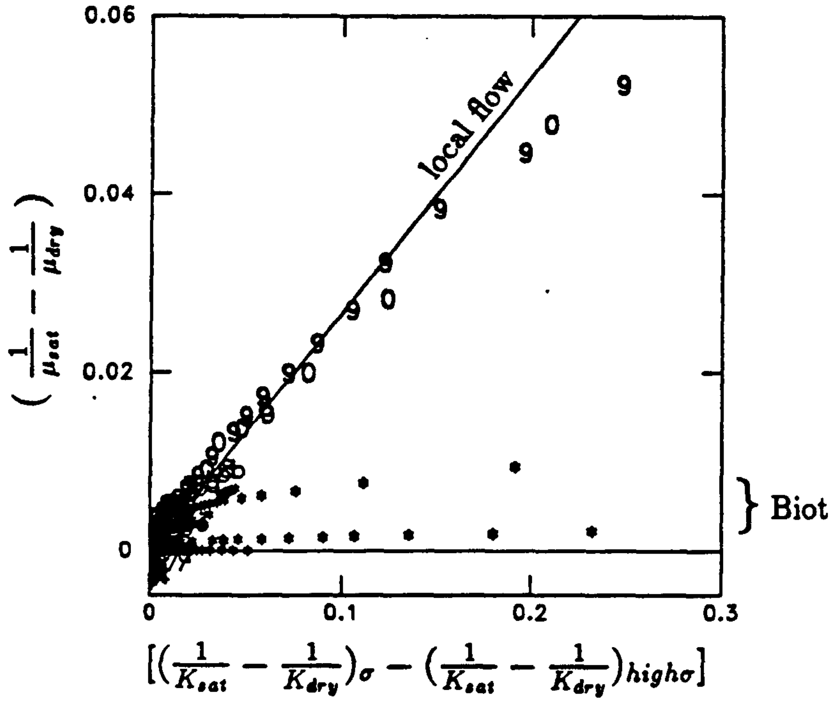

Figure 3.22: Shear versus bulk modulus dispersion. Data are plotted as digits, compared with our model prediction (solid line) and Biot's (*).

complicated expressions including both elastic and inertial effects, making the meaning of effective moduli unclear. Nevertheless, for purposes of comparison we predicted numerically the Biot high-frequency saturated velocities from the dry velocity data and converted both to effective moduli using equations 3.10. These Biot predictions all plot slightly above the horizontal axis in Figure 3.22.

In summary, by plotting the ratio of shear to bulk dispersion (Figure 3.22) we can identify when pore-pressure gradients are unrelaxed locally. From laboratory data we find that well-consolidated rocks at ultrasonic frequencies under low confining pressure exhibit local flow dispersion.

3.4 Conclusion

We have found that the relation between static and dynamic moduli in tight gas sandstones is dictated by (1) lithology and (2) confining pressure. In shales the confining pressure has little influence on the ratio of dynamic to static moduli. A large difference in the moduli persists to high pressure, and it appears to correlate with a large hysteresis that persists to high pressure. In sandstones the difference between dynamic and static moduli and the hysteresis can both be large at low pressures; however both tend to disappear at high pressures. In all cases the hysteresis indicates an inelastic, dissipative mechanism. In sandstones it may be frictional sliding on cracks, which is suppressed at high pressures when the cracks are tightly compressed. In shales it may be frictional or plastic sliding or compaction of mineral grains; plastic deformation of clay minerals might explain the lower sensitivity to pressure.

For saturated rocks, a model has been proposed to predict the high-frequency velocity dispersion. The difference between static and dynamic moduli in saturated rocks is hence a combination of both strain amplitude and frequency. This point is illustrated in the following figure that summarizes the additional effect that frequency has on static and dynamic measurements. We compute the fully-saturated ratio of dynamic to static bulk modulus using Gassmann's equation and our high-frequency predictions. In Figure 3.23 we see that in a typical tight gas sandstone that frequency can account for 50 percent of the dynamic vs. static discrepancy at in situ stresses, 20-40 MPa.

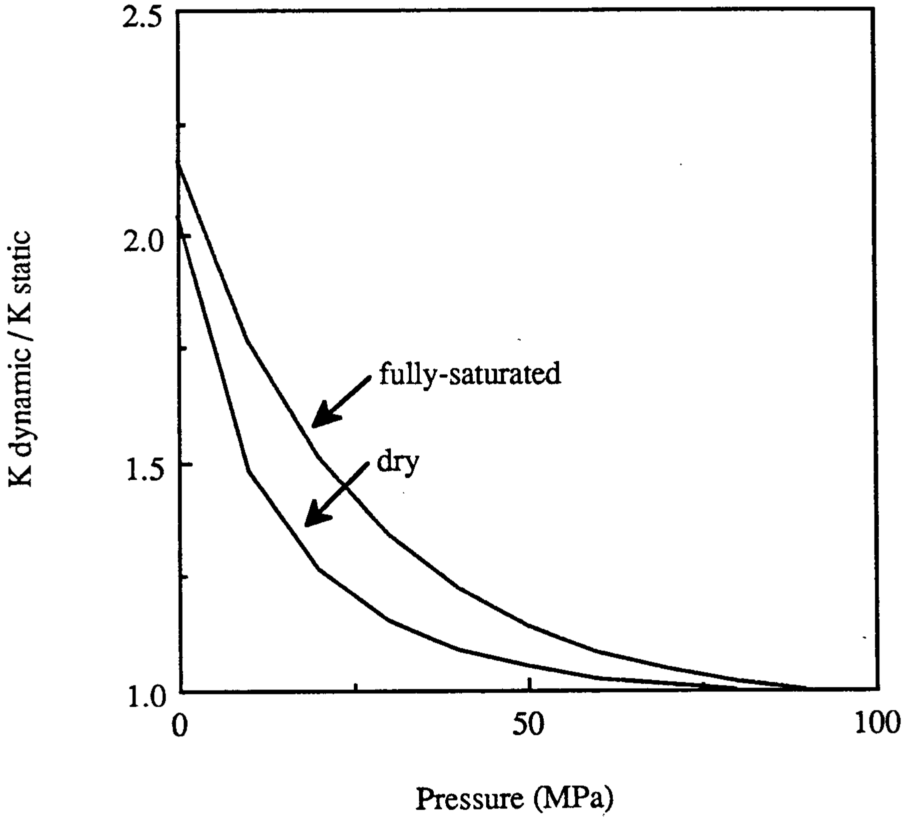

Figure 3.23: Predicted influence of saturation and confining pressure on the discrepancy between dynamic and static moduli in a tight gas sandstone. Dry curve is from laboratory data. Fully-saturated curve is computed using Gassmann and our high-frequency model.

Acknowledgements

Financial support was provided by the Stanford Rock Physics Project and the Gas Research Institute through a contract with CER corporation (Contract no. 9977-0275). Petrography data were provided by the Bureau of Economic Geology in Austin. New England Research performed static and dynamic measurements.

References

Birch, F., 1960, The velocity of compressional waves in rocks to 10 kilobars, 1: J. Geophys. Res., **65**, 1083-1102.

Biot, M. A., 1956a, Theory of propagation of elastic waves in a fluid saturated porous solid. I. Low-frequency range: J. Acoust. Soc. Amer., **28**, 168-178.

Biot, M. A., 1956b, Theory of propagation of elastic waves in a fluid-saturated porous solid. II. Higher-frequency range, 1956b: J. Acoust. Soc. Amer., **28**, 179-191.

Biot, M. A., 1962a, Generalized theory of acoustic propagation in porous dissipative media: J. Acoust. Soc. Amer., **34**, 1254-1264.

Biot, M. A., 1962b, Mechanics of deformation and acoustic propagation in porous media: J. Appl. Physics, **33**, 1482-1498.

Carmichael, R. S., 1981, Handbook of physical properties of rocks, C.R.C. press.

Cheng, C.H., and Johnston, D.H., 1981, Dynamic and static moduli, Geophys. Res. Let., **8**, 39-42.

Coyner, K. B., 1984, Effects of stress, pore pressure, and pore fluids on bulk strain, velocity, and permeability in rocks: Ph.D. thesis, Massachusetts Institute of Technology.

Domenico, S.N., 1977, Elastic properties of unconsolidated sand reservoirs, Geophysics, **41**, 882-894.

Gassmann F., 1951, Uber die elastizitat poroser medien: Vier. der Natur Gesellschaft, **96**, 1-23.

Gordon, R. B., and Davis, L. A., 1968, Velocity and attenuation of seismic waves in imperfectly elastic rock: J. Geophys. Res., **73**, 3917-3935.

Han, D-h., 1986, Effects of porosity and clay content on acoustic properties of sandstones and unconsolidated sediments: Ph.D. thesis, Stanford University.

Han, D-h., Nur, A., and Morgan, D., 1986, Effects of porosity and clay content on wave velocities in sandstones, Geophysics, **51**, 2093-2107.

Johnston, D. H., 1987, Physical properties of shale at temperature and pressure: J. Geoph. Res., **52**, 1391-1401.

King, M. S., 1969, Static and dynamic elastic moduli of rocks under pressure, in:

Rocks Mechanics - Theory and Practice, W. H. Somerton, ed., Proc. 11th Symp. Rock Mech., University of Calif., June 16-19.

Lin, W., and Heuze, F.E., 1986, In-situ dynamic moduli of Mesaverde rocks, compared to static and dynamic laboratory moduli, 27th U.S. Symposium on Rock Mechanics: Key to Energy Production.

Mavko, G., 1979, Frictional attenuation: An inherent amplitude dependence: J. Geophys. Res., **84**, 4769-4775.

Mavko, G., and Jizba, D., 1991, Estimating grain-scale fluid effects on velocity dispersion in rocks, submitted to Geophysics.

O'Connell, R., and Budiansky B., 1974, Seismic velocities in dry and saturated cracked solids: J. Geophys. Res., **79**, 5412-5426.

O'Connell, R., and Budiansky B., 1977, Viscoelastic properties of fluid-saturated cracked solids: J. Geophys. Res., **82**, 5719-5736.

Simmons, G., and Brace, W. F., 1965, Comparison of static and dynamic measurements of compressibility of rocks: J. Geophys. Res., **70**, 5649-5656.

Tosaya, C. and Nur, A., 1982, Effects of diagenesis and clays on compressional velocities in rocks, Geophysical Research Letters, **9**, 5-8.

Walsh, J., 1965, The effect of cracks on the compressibility of rock: J. Geophys. Res., **70**, 381-389.

Walsh, J., and Brace, W., 1966, Elasticity of rock: a review of some recent theoretical studies: Rock Mechanics and Engineering Geology, **4**, 283-297.

Walsh, J., 1980, Static deformation of rock: Journal of the Engineering Mechanics Division, Proceedings of the American Society of Civil Engineers, **106**, 1005-1019.

Winkler, K., 1979, Friction and seismic attenuation in rocks: Nature, **277**, 528-531.

Winkler, K., 1986, Estimates of velocity dispersion between seismic and ultrasonic frequencies: Geophysics, **51**, 183-189.

Wyllie, M.R.J., Gregory, A.R., and Gardner, G.H.F., 1958, An experimental investigation of factors affecting elastic wave velocities in porous media, Geophysics, **23**, 459-493.

Chapter 4

Uniaxial compressive strength

Abstract

Laboratory tests of uniaxial confined compression were performed on tight gas sandstones and shales measured in room-dry condition. Using test results we investigate the relationship between rock strength and formation properties. In addition to compressive strength, measurements of static and dynamic moduli were made during some of the tests. Based on the strength data and petrographic descriptions we find in this data set two regimes: (1) For clay volume fractions less than 17 percent (domain of sandstones), strength is strongly dependent on confining pressure and porosity. A relation of the form $\tau = \tau_0(\phi_c - \phi)^m \sigma^n$ describes the dependence of brittle strength τ on confining pressure σ and porosity ϕ in the sandstones investigated. (2) For clay volume fractions greater than 17 percent (domain of shaley sandstones and shales), strength is sensitive to confining pressure and weakly sensitive to clay content. Strength in shaley sandstones and shales depends on confining pressure and clay content C, following a relation of the form $\tau = \tau_0(1 - aC) + \mu\sigma$. A correlation is also observed between velocity and strength which depends on confining pressure and clay content.

4.1 Introduction

Knowledge of rock strength is important in the engineering of hydraulic fractures and for estimation of conditions for well-bore stability. There are several methods to obtain estimates of in situ rock strength. In situ tests can be performed to measure directly the rock strength, but they are expensive, and limited in measurement coverage. Velocity measurements, being cheap, and providing good measurement coverage, are a potentially useful means to obtain estimates of rock strength in situ.

In order to use velocity measurements as an indicator of rock strength, we need to understand how rock strength might be related to velocities. Numerous laboratory and theoretical investigations have demonstrated how velocities in sedimentary rocks are affected by porosity (Wyllie et al., 1957); clay content (Tosaya and Nur, 1982; Kowallis, 1984; Han et al., 1986); overburden stress and pore fluid (Nur and Simmons, 1969; King, 1983). Our understanding of how these parameters control rock strength is poor. Correlations are used to relate strength to velocities (Coates and Denoo, 1981; Wuerker, 1962; Stein, 1985), but there has been less work done on investigating the dependence of strength on formation properties. Consequently, the scatter observed in strength-velocity and strength-moduli correlations is poorly understood. Laboratory investigations have documented the influence of confining stress on rock strength extensively (Griggs, 1936; Robertson, 1955; Handin and Hager, 1957; Murrell, 1965). Brace and Riley (1972), Dunn et al. (1973), and Scott (1989) identify the importance of porosity on decreasing the brittle failure strength in sandstones. Wang and Mao (1979) investigate strength behavior of clays.

In this chapter we present strength and velocity data from laboratory uniaxial confined compression tests on tight gas sandstones and shales. We propose a simple model that helps us to understand the dependence of rock strength on porosity, clay content, and confining pressure. We also examine the correlation between rock strength and velocity.

4.2 Experimental method

Sixteen rocks were tested in confined uniaxial compression in room-dry condition. The rocks are tight gas sandstones and shales from seven of the Gas Research Institute's (GRI) cooperative wells and are from the Travis Peak formation in East Texas. Porosity ranges from 1 to 15 percent, and clay content from thin-section point count ranges from 2 to 63 percent. Rock samples are identified by well, depth, porosity, grain density, and clay content in Table 4.1. Confined uniaxial compression tests were performed by Science Applications International Corporation. Test results on individual rocks are listed in Chapter 6.

Table 4.1

Well	Depth (feet)	Porosity* (%)	Grain Density* (g/cm ^{3})	Clay volume (%)	Comment
A.T. Mast	9980	1.2	2.70	12	
B.F. Phillips	8368	5.0	2.65	6	
A.T. Mast	9975	4.8	2.65	3	
W. Sawmill	6897	9.3	2.51	3	
W. Sawmill	7077	12.6	2.48	11.5	
B.F. Phillips	8246	15.4	2.64	2	
Howell 5	5991	14.1	2.65	15.5	
S.F.O.T	9763	4.8	2.69	20	
W. Sawmill	6853	5.4	2.62	31	
Sam Hughes	7053	5.2	2.71	38	
S.F.E. 2	9898	3.3	2.69	41.5	
S.F.O.T	10151	4.9	2.68	52	
A.T. Mast	8675	5.8	2.72	56	
Howell 5	6275	5.0	2.72	63	
S.F.O.T.	9666	9.0	2.70	9.2	50 % ankerite
W. Sawmill	7074	7.1	2.65	8.5	48 % dolomite

* Average of measurements on four cores.

Confined uniaxial compression tests were performed on four core specimens at each sample depth. One core was tested at ambient pressure. The three other cores were tested at 15, 50, and 100 MPa confining pressure respectively (1 MPa = 145 psi). During the 15 and 50 MPa confining pressure tests, velocities were measured as a function of confining pressure so that comparisons between dynamic moduli, static moduli, and strength can be made.

Cores were 2.5 cm diameter, end-faced, and surface ground to have a length to diameter ratio of 2. Parallelism of samples was verified following ISRM standards (Brown, 1981). Tests were performed in a servo-controlled loading frame. The static moduli were obtained using a standard triaxial pressure cell. Axial and confining stresses were hydraulically applied and controlled with an electro-hydraulic servo-system. Measurement of axial strain was recorded with two LVDT's (Linear Variable Differential Transducers) attached to the endcaps, and radial strain was monitored using two clip gauges (half circle strain gauge mounted aluminum bands) mounted at the center of the specimen at 90 degrees opposing. Axial stress was measured using an internal load cell. A schematic of the sample assembly is shown in Figure 4.1.

Data acquisition was computer controlled using an IBM-AT style computer and 16-Bit Scientific Solutions A/D Board. Measuring accuracy of the sensor signals was ±0.001 volts or better. Prior to testing, each sensor was individually calibrated using an NBS traceable calibration device. Sensor accuracy was better than ±0.5 % FS. In addition, operation of the complete test apparatus was verified using an aluminum specimen with known elastic properties.

The room-dry specimen was placed between two endcaps. Isolation of the test specimen from the confining fluid was achieved by using a 'heat-shrink' Teflon jacketing. This jacketing was then secured to the endcaps with a wire tie. Strain sensors were then attached and the electrical signals zeroed. Pore lines were left open allowing for a drained test. The specimen was then sealed within the pressure vessel and the vessel filled with hydraulic oil. Hydrostatic pressure was applied at the rate of 3.4 MPa/min. After achieving hydrostatic conditions, an axial strain rate of 7×10^{-6} strain/second was applied. Data was recorded at 8 second intervals during both the hydrostatic and axial loading cycles. Axial strain measurements up to 5 % total strain

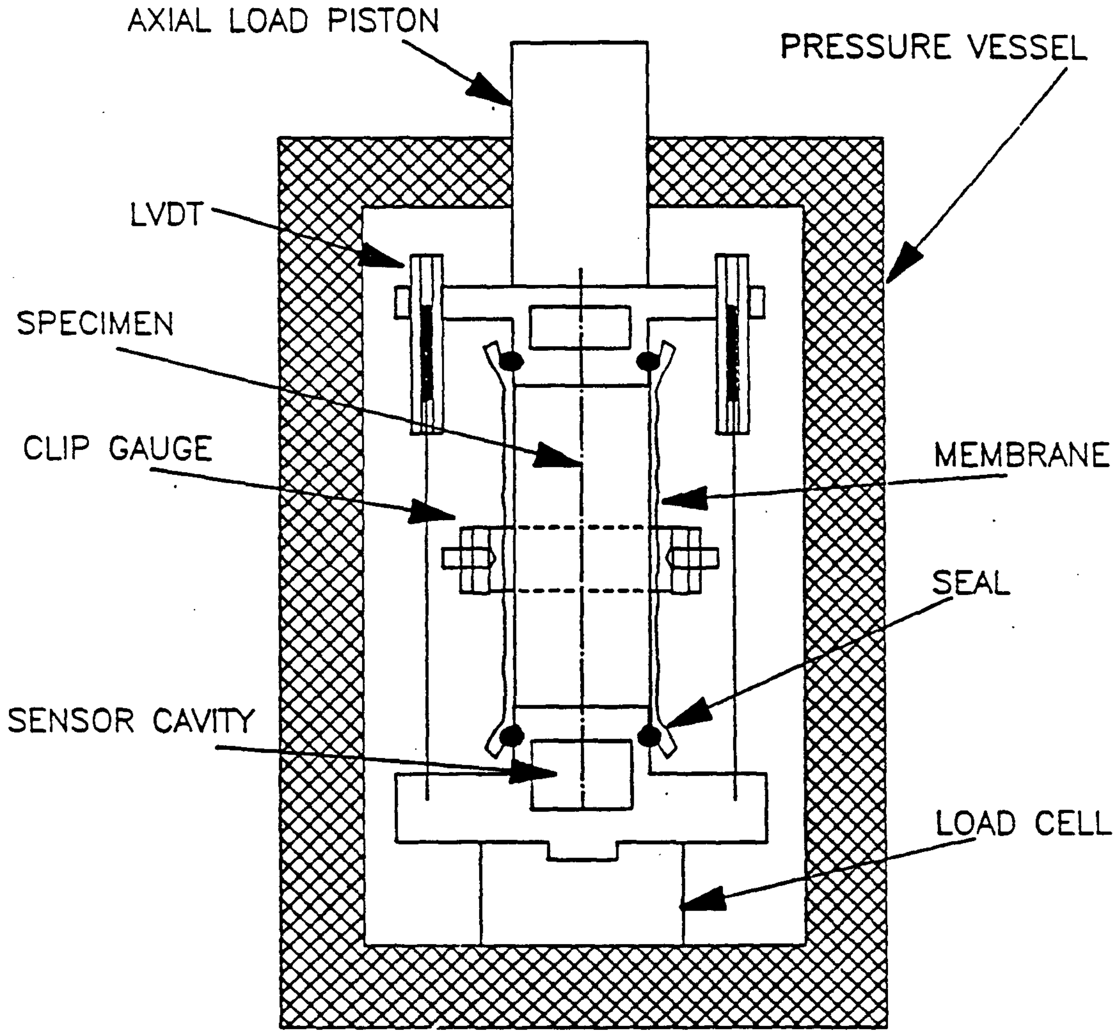

Figure 4.1: Schematic of rock specimen in triaxial pressure vessel assembly.

were taken when specimen behavior permitted. All tests were conducted at ambient temperatures.

Ultrasonic compressional and shear wave velocity determinations were made in conjunction with the 15 and 50 MPa confining pressure triaxial tests. The wave velocities were determined using a system composed of triaxial endplugs fitted with piezoelectric crystals, a pulse generator, and an oscilloscope. Central frequency of the piezoelectric crystals is 1.0 MHz for both P- and S- waves. The P- and S- wave sensors were analyzed prior to and after the test program to determine the appropriate offset time of the system. This was accomplished by placing the endplugs face-to-face and measuring the travel time of both the P- and S-waves in the absence of a specimen. These times were subtracted from all subsequent measurements. The accuracy of these wave velocities were within 2 percent of the expected values for aluminum (Kolsky, 1963). Figure 4.2 shows the velocity measurement setup.

Wave velocities determined from each specimen tested under the 15 MPa and 50 MPa confining pressure conditions are included in Science Applications International Corporation, report No. P-9955-0275-0.

Regrettably, reliable wave-form information from nine tests was not obtained (missing values in Table 6.1 in Chapter 6). Despite testing and calibration of the ultrasonic crystal sets prior to each triaxial test series using 15 MPa and 50 MPa as confining pressure, reliable wave information was not obtained. The tests in question were performed during two testing intervals in which the crystals had been damaged in previous testing. Waveform recordings appeared correct, but upon final evaluation, they showed no useful information.

4.2.1 Data reduction

In the confined compression tests, the rock specimen was loaded to failure. When a sample exhibited brittle failure, compressive strength was calculated at the point of maximum difference between axial stress and confining pressure. When a sample

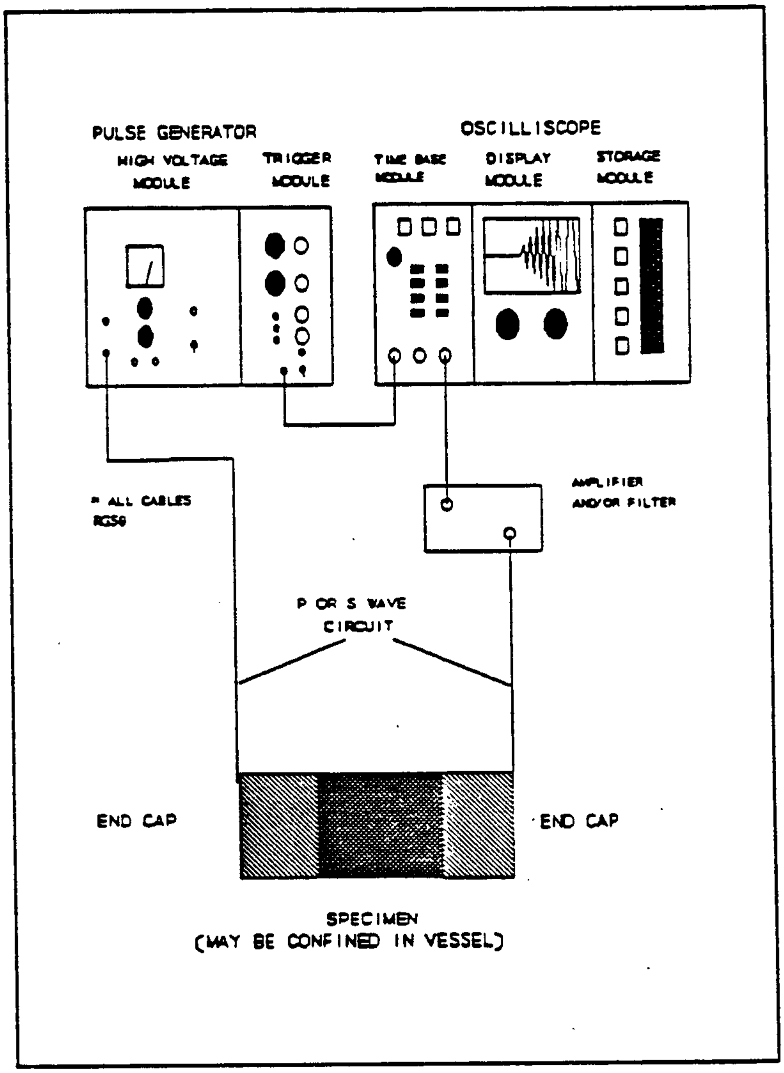

Ultrasonic Measurements System

Figure 4.2: Schematic of velocity measurement apparatus.

exhibited ductile deformation and work hardening, the value of differential stress at an axial shortening of 30 % beyond the linear elastic deformation was chosen arbitrarily as the peak compressive strength (value selected is indicated with a dot on the stress strain curves). In these samples, the stress-strain behavior during the ductile deformation and work hardening is influenced by stiffness of the testing machine, and accuracy is lost in the region near failure. The convention followed for strain plots is that positive values correspond to compression and negative values correspond to expansion.

Static moduli are computed from the slope of the stress-strain curve computed at 50 % of the peak compressive strength using the isotropic relations

$$E_{stat} = \frac{d\sigma_{ax}}{d\epsilon_{ax}} \tag{4.1}$$

$$\nu_{stat} = -\frac{d\epsilon_r}{d\epsilon_{ax}} \tag{4.2}$$

where E_{stat} is the Young's modulus, ν_{stat} is the Poisson's ratio, σ_{ax} is the axial stress difference or 'differential stress', ϵ_{ax} is the axial strain, and ϵ_r is the radial strain.

P and S wave velocities are taken from the 15 and 50 MPa confining pressure tests in which velocities were measured. Dynamic bulk and shear moduli are computed from the P and S wave velocities and bulk density using the relations

$$K_{dyn} = \rho(V_p{}^2 - (4/3)V_s{}^2) \tag{4.3}$$

$$\mu_{dyn} = \rho V_s{}^2 \tag{4.4}$$

where V_p, V_s, and ρ are the P wave velocity, S-wave velocity, and bulk density respectively.

The stresses at failure for each of the four compressive strength samples are plotted as Mohr circles, and a Mohr envelope is obtained for each rock using either a linear or curved envelope. Linear failure envelopes, when appropriate, were determined using a least-squares fitting of a Mohr envelope (Lisle and Strom, 1982). Curved failure envelopes were determined by a least-squares fit of points taking the tangent line to two Mohr circles at a time on a logarithmic plot of shear vs. normal stress. In constructing the failure envelopes we note that four core measurements must be combined. Hence, accuracy of the envelope is affected by variability in porosity, clay content, bedding anisotropy, and sample length, etc. We are unable to identify the influence of clay content and bedding variability on the failure envelopes as these were not determined on individual cores. However, core porosity and sample length were measured and are listed in the tabulated data in Chapter 6.

4.2.2 Results

In examining the data, we find that there are distinct differences in strength behavior between sandstones, shaley sandstones, and shales. Compressive strengths from all the rocks tested are shown in Figure 4.3. In this section we discuss test results for several rocks.

Figure 4.4 shows data for a clean sandstone containing 1 percent porosity and 12 percent clay. From the stress-strain diagram, we note that compressive strength of the sandstone increases with increasing confining pressure from 340 MPa in the unconfined test to 775 MPa at 50 MPa confining pressure. We also note that the sandstone exhibits linear elastic deformation and almost no ductile deformation prior to rupture. Rupture occurs in a brittle manner with a sudden decrease in slope, followed by a down break in the stress-strain curve. On the lower figure the stresses at failure are plotted on a Mohr diagram. We note that the Mohr envelope is curved. This is commonly observed in sandstones (Handin and Hager, 1957; Murrell, 1965; Scott, 1989). We find that in all of the sandstones tested the actual shape of the failure envelopes is best described using an equation of the form $\tau = a\sigma^n$ suggested by Murrell (1965). Murrell suggests the curvature in the envelopes may be understood

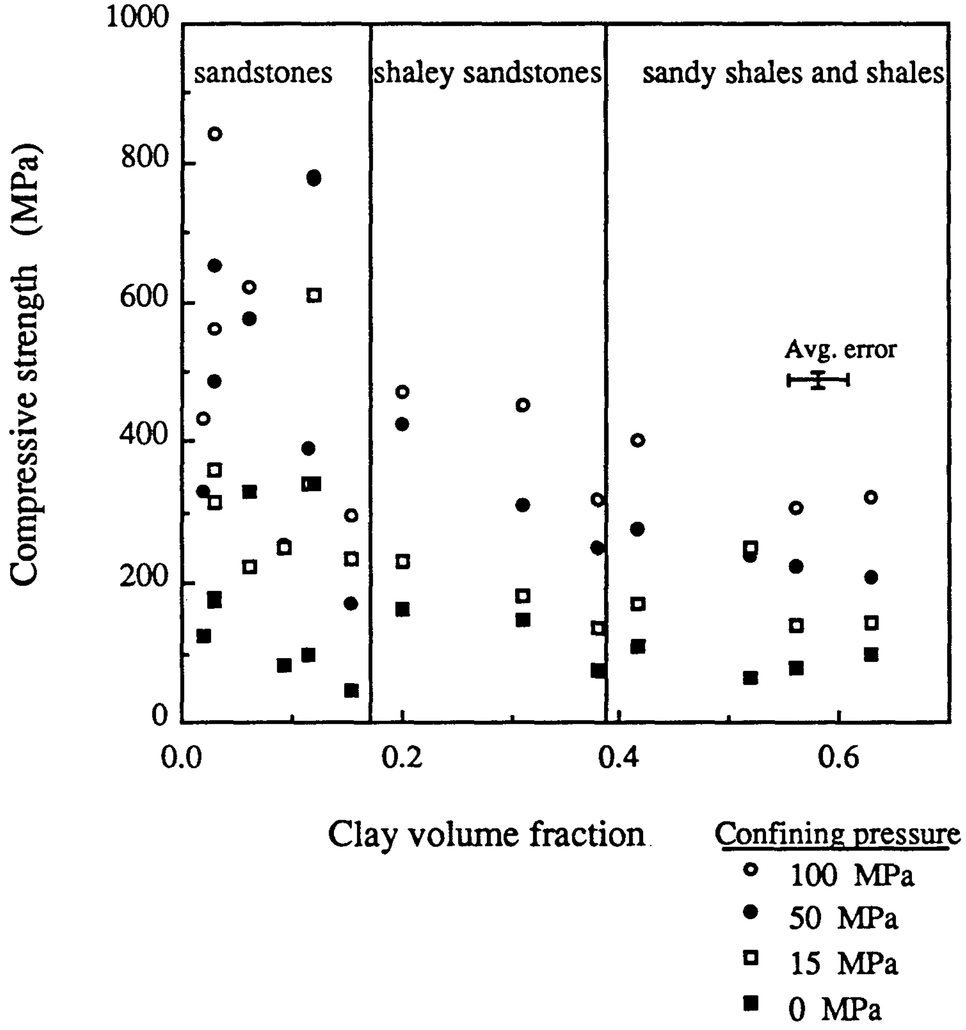

Figure 4.3: Compressive strength vs. clay volume fraction in the tight gas rocks tested. We identify 3 domains based on petrography: sandstones $(0 < C < .17)$ shaley sandstones $(.17 \leq C \leq .38)$ and sandy shales and shales $(C > .38)$, where C is clay the volume fraction. Error bars are shown in figure. One measurement of clay content was made on the whole core. Strength tests were made on four different cores.

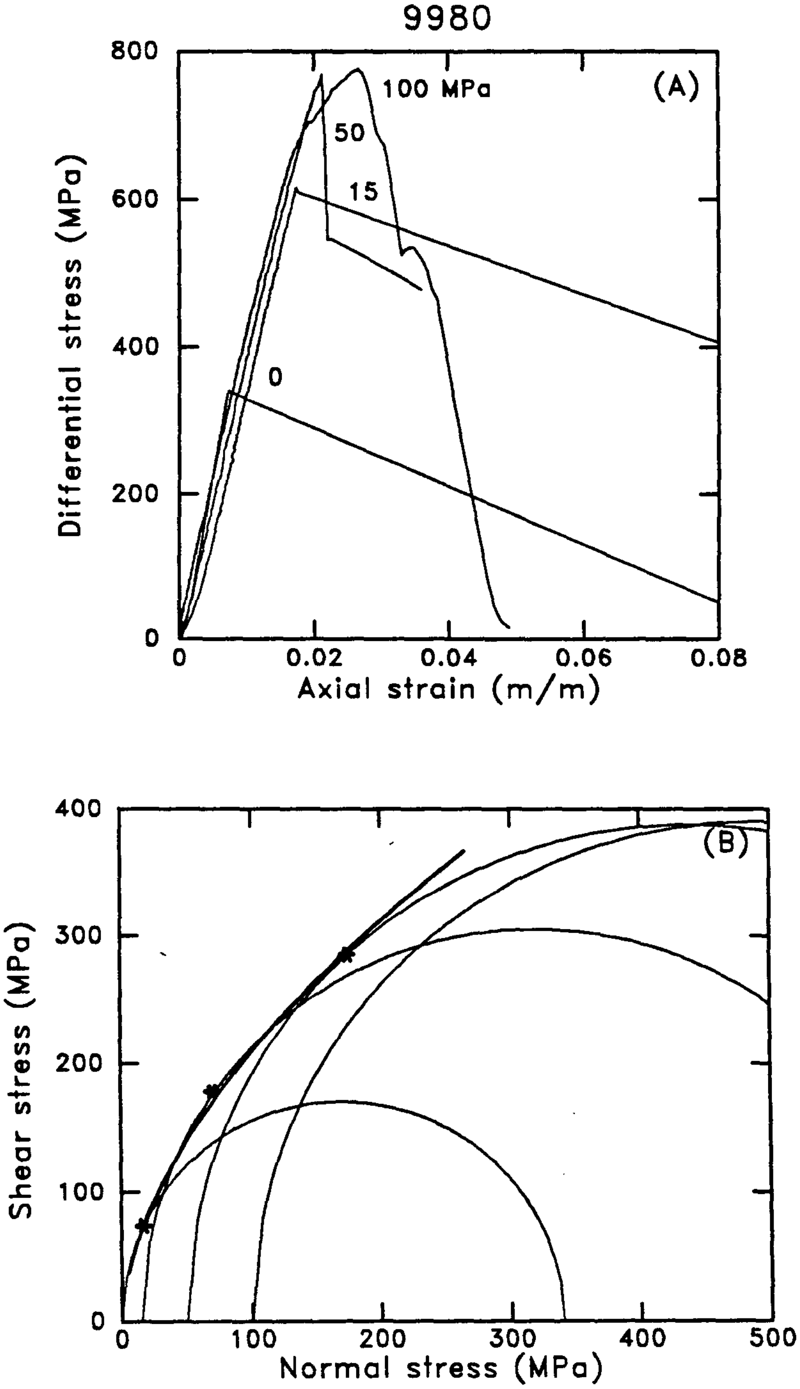

Figure 4.4: (A) Compressive strength and axial stress-strain curves (B) Mohr circles and failure envelope in a low porosity sandstone, A.T. Mast 9980 (1 % porosity and 12 % clay). This sandstone exhibits brittle failure and curvature of the failure envelope. Confining pressures are indicated in figure. (The 100 MPa confining pressure test was not considered in computing the failure envelope. A larger capacity load cell was needed and the core sample was consequently stressed twice.)

in terms of frictional resistance: Contact occurs between asperities. Deformation occurs by shearing of the asperities. Strength is proportional to the contact area. If the rock deforms elastically, contact area is proportional to stress to some power (2/3 in the case of Hertz theory for grains in contact).

Figure 4.5 shows data for a sandstone containing 9 percent porosity and 3 percent clay. From the stress-strain diagram, we note that compressive strength of the sandstone increases with increasing confining pressure from 176 to 560 MPa at 0 and 100 MPa confining pressure respectively. We also note that the sandstone exhibits linear elastic deformation and almost no ductile deformation prior to rupture. Rupture occurs in a brittle manner. On the lower figure compressive strengths are plotted on a Mohr diagram. Curvature of the failure envelope in Figure 4.5 is quasi-parabolic in shape and is in broad qualitative agreement with parabolic envelopes using Griffith hypothesis for brittle failure.

In Figure 4.6 we show data for a shaley sandstone containing 5 percent porosity and 31 percent clay. From the stress-strain diagram, we observe the dependence of compressive strength on confining pressure. We also note that the shaley sandstone exhibits nearly linear elastic deformation followed by some ductile deformation (15 to 30 % additional strain in the 15, 50, and 100 MPa tests) prior to rupture. On the lower figure, the compressive strengths are plotted on a Mohr diagram. Here we note that a linear envelope provides best fit to the data.

In Figure 4.7 we show data for a shale containing 5 percent porosity and 63 percent clay. From the stress-strain diagram we notice that in the 50 and 100 MPa confining pressure tests, the shale exhibits ductile deformation and work hardening that contribute approximately 75 % additional axial strain prior to rupture. On the lower figure, we see that a linear envelope describes the shale data. In all of the shaley sandstones and shales tested, linear Coulomb envelopes of the form, $\tau = S_0 + \mu\sigma$, describe the data. The compressive strength, ductile deformation, and work

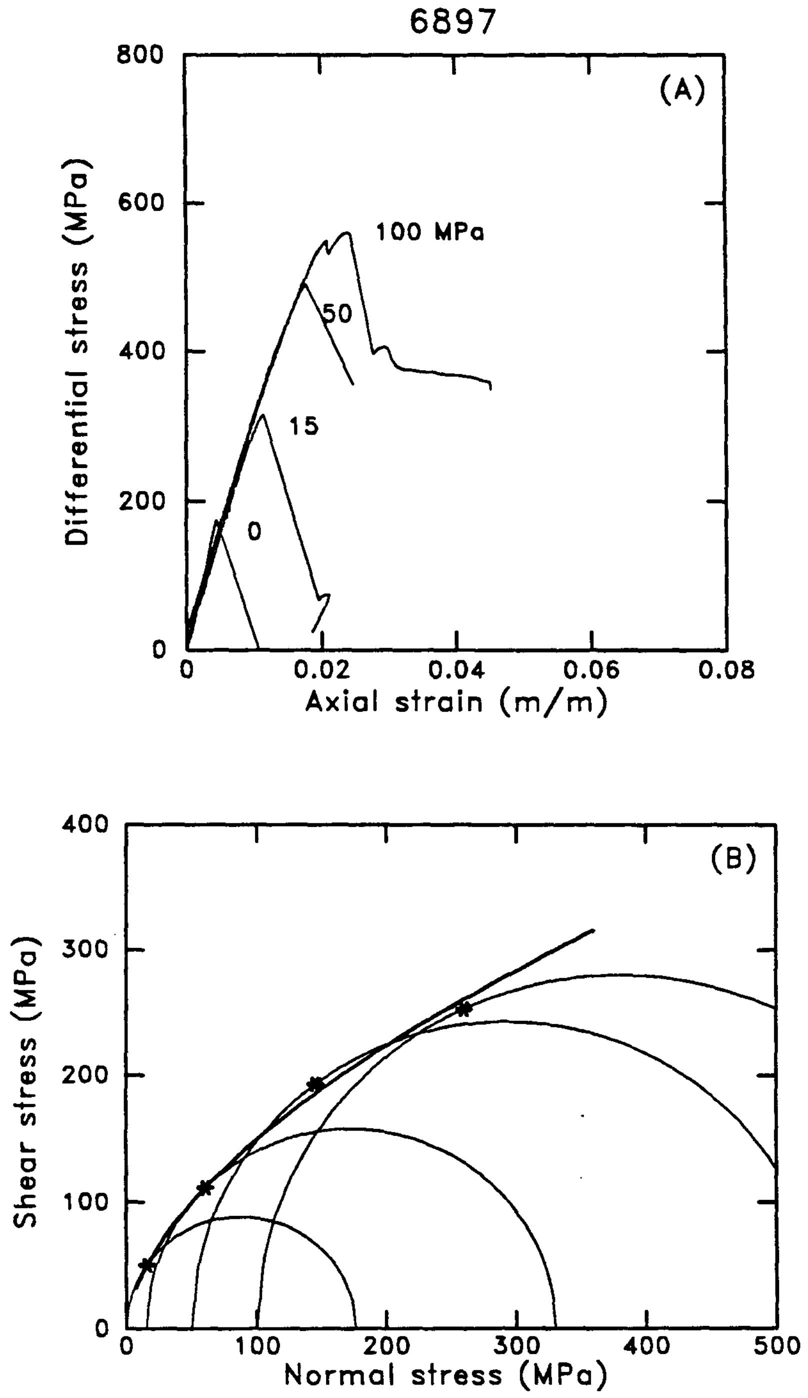

Figure 4.5: (A) Compressive strength and axial stress-strain curves. (B) Mohr circles and failure envelope in a clean sandstone, Werner Sawmill 6897 (9 % porosity and 3 % clay). This sandstone exhibits brittle failure and curvature of the failure envelope. Confining pressures are indicated in figure.

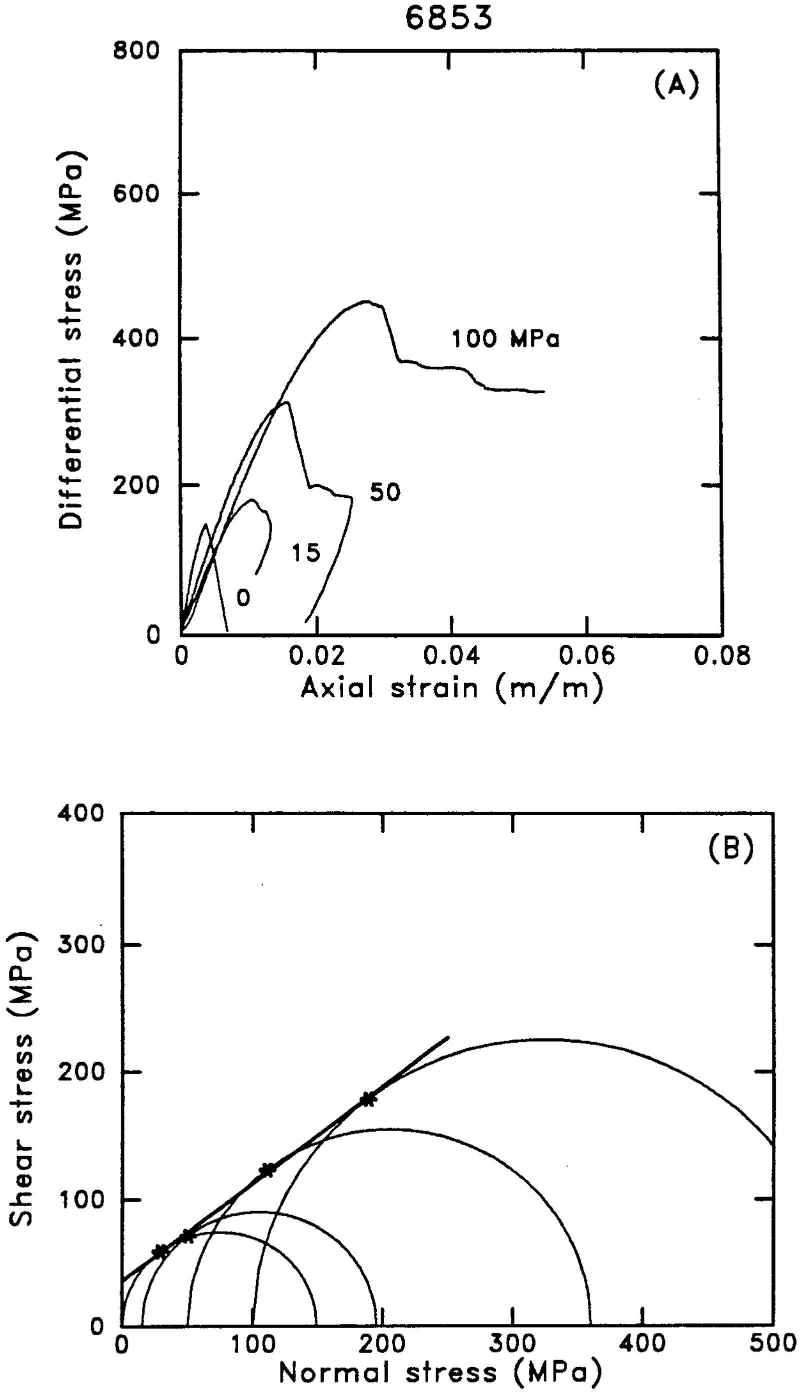

Figure 4.6: (A) Compressive strength and axial stress-strain curves. (B) Mohr circles and failure envelope in a shaley sandstone, Werner Sawmill 6853 (5 % porosity and 31 % clay). Confining pressures are indicated in figure.

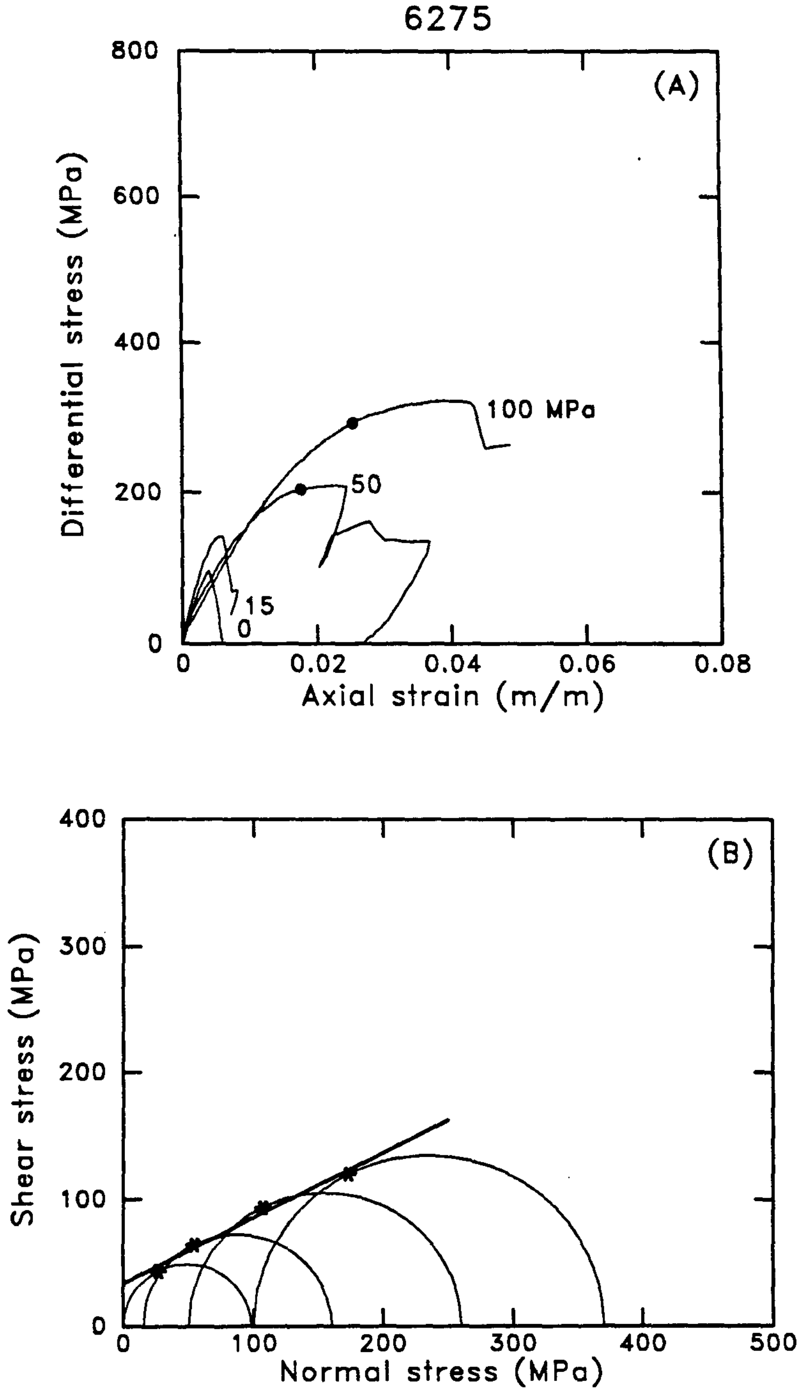

Figure 4.7: (A) Compressive strength and axial stress-strain curves. (B) Mohr circles and failure envelope in a shale, Howell 5 (5 % porosity and 63 % clay). This shale exhibits ductile deformation and work hardening. In the 100 and 50 MPa confining pressure tests the shale exhibits ductile deformation and work hardening leading to additional axial deformation prior to failure. Compressive strengths are chosen are indicated in the top diagram.

hardening characteristics observed on these Travis Peak shales are qualitatively similar to results on dry Muddy shale (Handin and Hager, 1957) and Mesa Verde shales (Lin, 1985).

4.3 Model for shear strength

We now examine the behavior of different rocks combined. In this section we investigate simple relations that may be used to describe the functional dependence of strength on rock properties.

4.3.1 Area of contact idea

To gain some idea of how failure stresses may be related functionally to porosity, we consider the concept of measured vs. actual stress. From the definition of stress as force per unit area we have

$$F = \sigma A \tag{4.5}$$

where A is the total cross-sectional area of the sample to which the force is applied, and σ is defined as the 'measured' stress. In porous rocks, we need to consider the actual area of solid-solid contact to which the force is applied. Intuitively we might approximate this as the sample cross-sectional area times the fraction of solid grains, $(1 - \phi)A$. This is the solid area that would be observed on an average cut through the sample. Hence, the force may also be written

$$F = \sigma_A(1 - \phi)A \tag{4.6}$$

where σ_A is defined as the 'actual' stress across the solid surfaces on such a cut. Equating 4.5 and 4.6 we obtain

$$\sigma = \sigma_A(1 - \phi) \tag{4.7}$$

$$\tau = \tau_A(1-\phi) \tag{4.8}$$

where we consider that a similar relation holds for shear stress.

A slight modification of these relations comes from considering more carefully the area-of-contact through which stresses may be transmitted effectively. Consider, for example, a suspension of solid spheres in water with equal volumes of the two phases, corresponding to a porosity of 50 %. A cut through the suspension would show 50 % solid giving the solid area defined above as $(1-.5)A$. However, virtually no spheres would be in contact so that the area of solid contact for transmitting stresses would be zero. In general, stresses can not be transmitted effectively at porosities greater than some critical value, ϕ_c, (say 38 percent for a sphere pack). Following the concept of percolation theory (Stauffer, 1985) which can be used to describe rigidity of granular media, we consider that equations 4.7 and 4.8 may be in fact

$$\sigma = \sigma_A(\phi_c-\phi) \tag{4.9}$$

$$\tau = \tau_A(\phi_c-\phi) \tag{4.10}$$

where ϕ_c is the critical value of porosity above which stresses can not be transmitted effectively. Equations 4.7 and 4.8 reflect the idea that strength is lost at some finite porosity substantially less than 1.

4.3.2 Sandstones

From experiments on a variety of sandstones, Dunn et al. (1973) proposed that brittle compressive strength in sandstones exhibits a power dependence on porosity. This functional dependence is explained qualitatively by Dunn et al. in terms of the increased number of grains that must be fractured, and hence the increasing differential stress that must be overcome as porosity decreases, to propagate a through-going fracture. We find that compressive strengths of the sandstones tested agree qualitatively with results obtained by Dunn et al. (1973). We wish to examine further how the effect of porosity may be cast in terms of a failure criterion.

We investigate how the the area-of-contact idea discussed in the previous section might affect a curved failure envelope of the form

$$\tau_A = a{\sigma_A}^n \tag{4.11}$$

where τ_A, σ_A, are the actual stresses, and a and n are constants. We start by assuming that equation 4.11 describes the behavior of pure solid-solid contacts where the stresses are σ_A and τ_A. Using relations 4.9 and 4.10, these 'actual' stresses can be written in terms of the 'measured' stresses, and equation 4.11 becomes

$$\tau = \tau_0(\phi_c - \phi)^{(1-n)}\sigma^n \tag{4.12}$$

In equation 4.12 one expects the quantity $\tau_0(\phi_c - \phi)^{(1-n)}$ to vary with porosity, but not the exponent n that describes dependence on normal stress.

We now examine how the sandstone strength data compares with equation 4.12. In Figure 4.8, failure envelopes obtained on the sandstones (clay volume fraction less than 17 percent) are superposed. We include data from Scott (1989) in the range of porosity from 20 to 22 percent, that is not represented in the sandstones tested. From values used in constructing the curved failure envelopes (Table 4.2), we find that the exponent n is quasi-constant, (.6 on average), and the coefficient a varies from 4.4 to 14 MPa. This value of $n \approx .6$ is found to describe the dependence of strength on confining pressure in a variety of sandstones (Murrell, 1965; Handin et al., 1957).

Figure 4.9 shows shear stress at failure vs. porosity, plotting values from the envelopes shown in Figure 4.8 at various normal stresses. We note that shear stress at failure decreases linearly with increasing porosity. Least-squares fits to these data at various normal stresses are shown in Table 4.3. Notably, the data tend to all

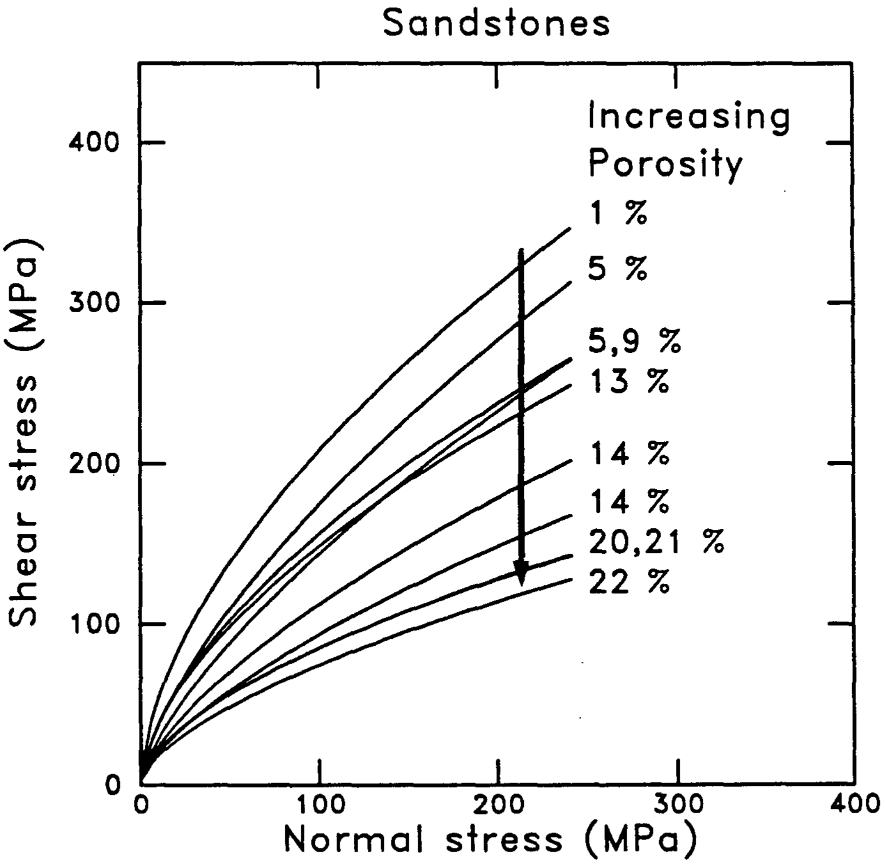

Figure 4.8: Sandstones (listed in Table 4.2) exhibit a power law dependence of shear failure stress on normal stress. At a given pressure increasing porosity causes the shear strength to decrease.

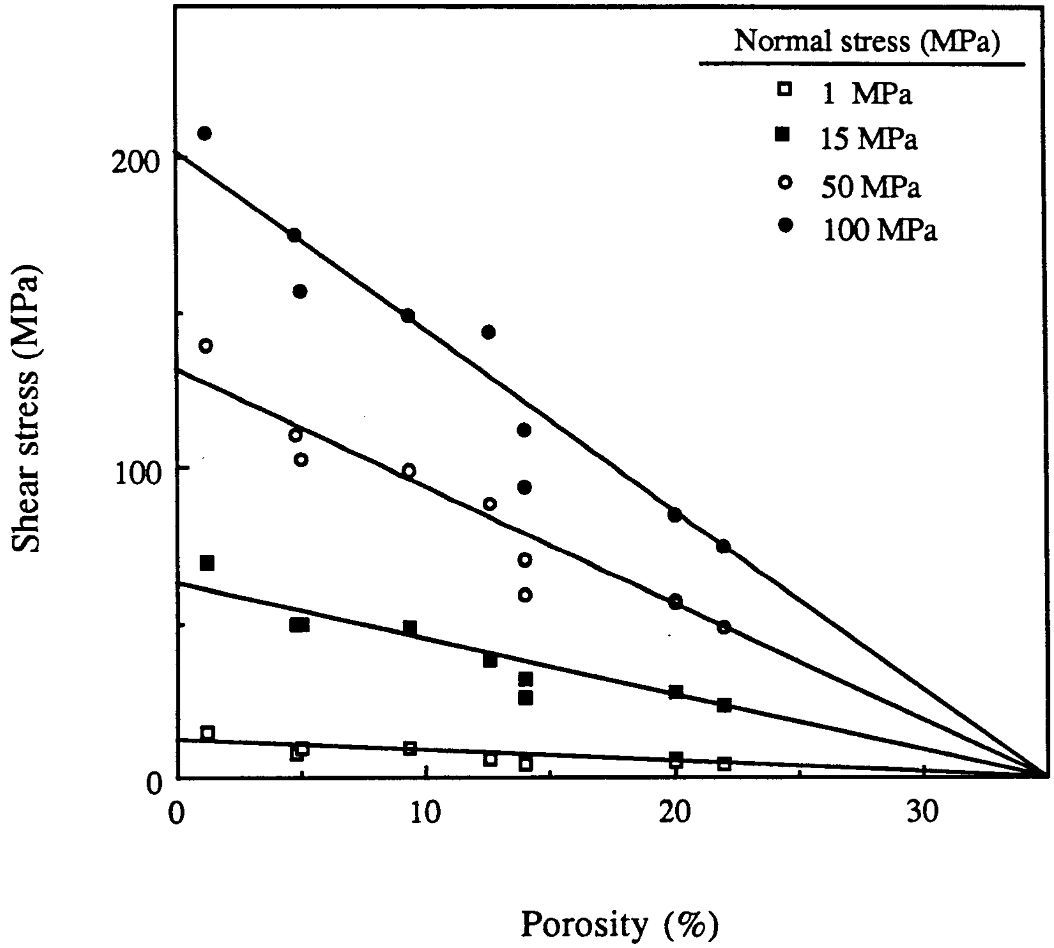

Figure 4.9: Shear stress at failure increases linearly with decreasing porosity in sandstones. The common intercept of least-squares fits to the data at various normal stresses suggests the inability of sandstones to sustain shear stress above a critical porosity of approximately 35 percent.

have a common zero-strength intercept at approximately 35 percent porosity (Table 4.3). This suggests that the shear strength in sandstones may depend on a critical porosity, ϕ_c, as suggested by the area-of-contact idea. However $n = .6$ implies that strength should depend on porosity to the power $1 - n = .4$ instead of the strictly linear dependence of strength on porosity that we observe (Figure 4.9).

Table 4.2

Failure envelopes on sandstones

Sample	Porosity (%)	n	a
9980	1.2	.58	14
8368	5.0	.60	9.7
9975	4.8	.66	8.2
6897	9.3	.59	10
7077	12.6	.69	5.9
8246	14.1	.67	5.3
5991	14.1	.66	4.4
Berea*	19.9	.58	5.8
DV 1*	20.9	.59	5.6
DV 2*	22.2	.61	4.5

* Data from Scott (1989).

Table 4.3

Normal stress (MPa)	Least-squares equation (MPa)	τ=0 intercept	R^2
100	$\tau = 203.0 - 579\phi$	.35	.96
50	$\tau = 132.4 - 380\phi$	.35	.95
15	$\tau = 63.2 - 183\phi$	.35	.91
1	$\tau = 12.1 - 35.6\phi$	.34	.73

From the above observations, we consider that the functional dependence of brittle strength on porosity and confining pressure may be described better using an equation of the form

$$\tau = \tau_0(\phi_c - \phi)^m \sigma^n \tag{4.13}$$

A regression of equation 4.14 is performed using as input variables, the porosity of each core, and one value of normal and shear stress from each core tested that lies on the Mohr circle which is tangent to the failure envelope (columns 3, 6, and 7 Table 6.1 in Chapter 6 for the sandstones listed in Table 4.2). Two data points are not considered in our regression analyses: the 50 and 100 MPa confining pressure tests on sample 5991 which exhibit ductile deformation. The coefficients τ_0, m, and n are determined using the least-squares estimate. To determine ϕ_c, we consider a range of values and select the one that produces the best overall fit to the data.

Table 4.4

Sandstones: $\tau = \tau_0(\phi_c - \phi)^m \sigma^n$
$\tau_0 = 37$ MPa $\phi_c = .36$ $m = 1.05$ $n = .6$ Coefficient of determination, $R^2 = .988$

Table 4.4 shows regression results. Predicted and measured shear strengths are in excellent agreement (Figure 4.10). To illustrate the influence of porosity on shear strength in sandstones, Figure 4.11(A) shows Mohr circles in the region of tangency to failure envelopes. Apparent scatter in the data is attributed primarily to porosity. When we attempt to remove the effect of porosity by dividing shear stress on the y-axis by $(.36 - \phi)^{1.05}$, we see that Mohr circles in the region of tangency to failure envelope collapse to the resulting curve of the form $\tau = \tau_0 \sigma^n$ (Figure 4.11(B)).

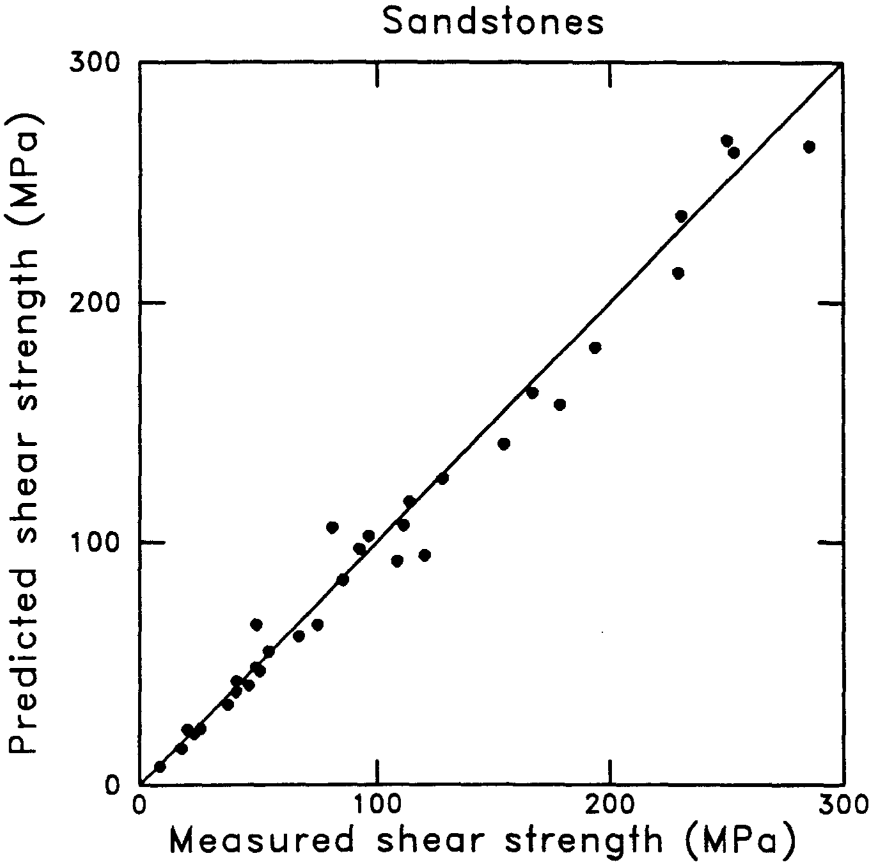

Figure 4.10: Excellent agreement between predicted vs. measured shear strength in a variety of sandstones (Table 4.2) is obtained using $\tau_{pred} = 37(.36 - \phi)^{1.05}\sigma^{.6}$ where ϕ is porosity and σ is normal stress.

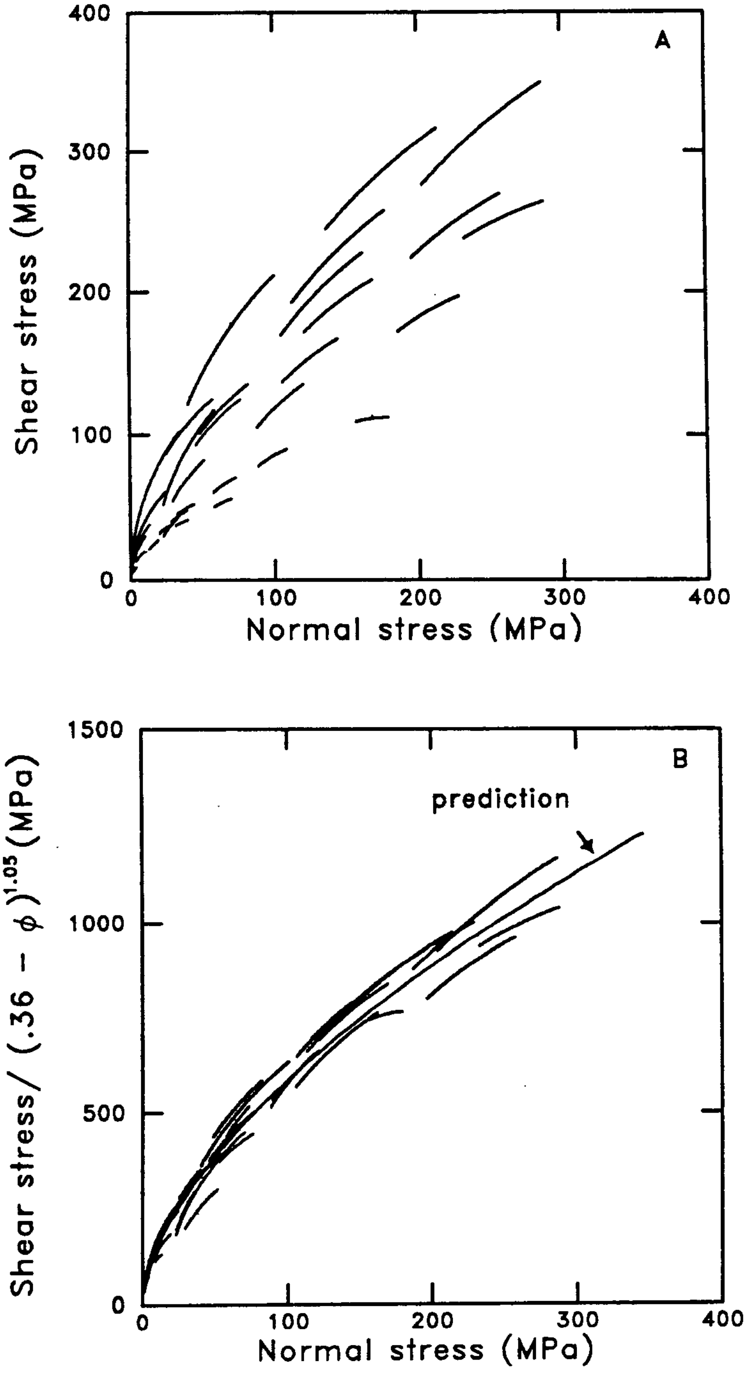

Figure 4.11: (A) Strength of sandstones shown as portions of Mohr circles. Apparent scatter in the data is attributed to porosity. (B) When strength data is corrected for the effect of porosity, failure envelopes collapse to an equation of the form, $\tau = \tau_0 \sigma^n$.

4.3.3 Shaley sandstones and shales

We wish to examine how the area-of-contact idea may lead us to understand some of the strength behavior observed in shaley sandstones and shales. We consider a linear Coulomb envelope:

$$\tau_A = S_0 + \mu\sigma_A \tag{4.14}$$

where τ_A, σ_A, S_0, and μ are the actual shear stress, the actual normal stress, the unconfined shear strength, and the coefficient of friction respectively. To apply the area-of-contact idea, we consider the definition of stress:

$$F = \sigma A \tag{4.15}$$

where A is the total cross-sectional area of the sample to which the force is applied, and σ is the measured stress. Next, we consider how force may be defined in terms of actual stresses for the case of a sandy shale. In the domain of sandy shales and shales, we consider a simple description of the rock to consist of two components: quartz grains having volume fraction equal to $(1 - C)$, and clay matrix having volume fraction equal to C. Porosity is not treated as an additional component, because we assume that only micro-porosity associated with clay occurs in sandy shales and shales. The total cross-sectional area of the quartz and clay components is approximated to be proportional to their volume fraction, $(1 - C)A$ and CA, respectively. We write an equation for the force applied in terms of the actual stress

$$F = \sigma_A((1 - C)x + C(1 - x))A \tag{4.16}$$

where x is the fraction of the load carried by quartz. Equation 4.16 can be generalized to

$$F = \sigma_A(1 - aC)A \tag{4.17}$$

where a is a constant. Combining equation 4.15 and 4.17, we obtain the following expressions for the relation between measured and actual stresses.

$$\sigma = \sigma_A(1 - aC) \tag{4.18}$$

$$\tau = \tau_A(1 - aC) \tag{4.19}$$

where we consider that a similar relation holds for shear stress. Substituting equations 4.18 and 4.19 into the linear failure envelope equation, 4.14 we obtain an equation of the form:

$$\tau = \tau_0(1 - aC) + \mu\sigma \tag{4.20}$$

Hence we expect to see the intercept, or unconfined compressive strength vary with clay content.

We now examine the data, to get an idea of how strength of shales and shaley sandstones compares with equation 4.20. Figure 4.12 shows the linear failure envelopes on all of the shaley sandstones and shales (clay volume fraction greater than 17 %). Values of S_0 and μ from the failure envelopes are listed in Table 4.5. The area-of-contact idea would suggest that only the intercept, S_0, or unconfined compressive strength, should depend on clay content. We note however, that both the slope, μ and the intercept S_0 tend to show an overall decrease with increasing clay, though values are fairly scattered (Table 4.5).

In terms of the lithologies identified in Figure 4.3, we note that in the domain of shales (clay volume fraction greater than 38 %), shear strength is nearly independent of clay content. This would be expected in the case where quartz grains are suspended in a matrix of clay. In the domain of shaley sandstones (clay volume fraction between 17 and 38 %), the shear strength decreases slightly with increasing clay content

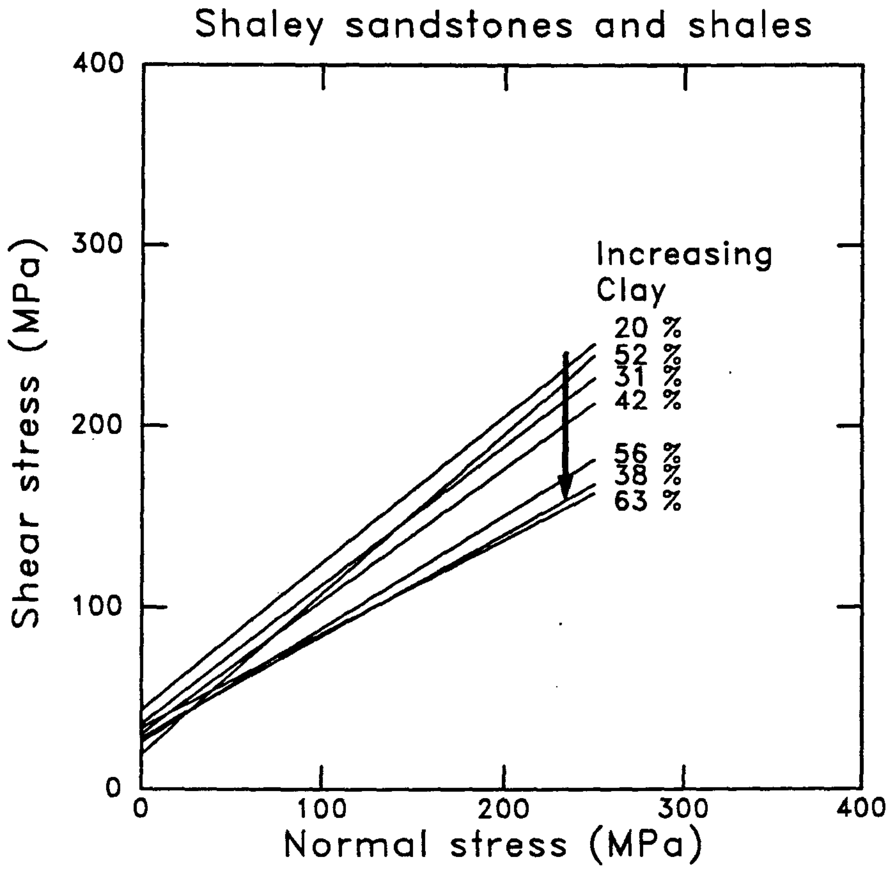

Figure 4.12: Shaley sandstones and shales listed in Table 4.5 exhibit linear failure envelopes. Increasing clay content causes shear strength to decrease slightly.

Table 4.5

Failure envelopes on shaley sandstones and shales

Sample	Clay (%)	S_0 (MPa)	μ
9763	20	44	.81
6853	31	36	.77
7053	38	29	.56
9898	42	31	.73
10151	52	20	.88
8675	56	26	.62
6275	63	33	.52

suggesting that quartz grains carry more of the load than the shale. For this analysis, we consider that we can group shaley sandstones and shales together (Figure 4.13). We do this, because in both shaley sandstones and shales the overall dependence on clay content is weak and shear strength depends primarily on confining pressure.

In Figure 4.13 we plot shear stress at failure from the failure envelopes shown in Figure 4.12 as a function of clay volume fraction. We note that in shaley sandstones and shales, shear strength exhibits an overall decrease with increasing clay content. Table 4.6 lists least-squares fits to strength vs. clay content at various confining pressures. Confining pressure is an important variable that controls the strength of shales. From the shale data (Figure 4.13), we see that a decrease in confining pressure causes shear strength to decrease by a corresponding factor of .7.

Table 4.6

Normal stress (MPa)	Least-squares equation	R^2
100	$\tau = 133.1 - 74.6C$	.53
50	$\tau = 89.16 - 53.7C$	.64
15	$\tau = 58.37 - 38.8C$	.56
0	$\tau = 45.17 - 32.4C$	.41

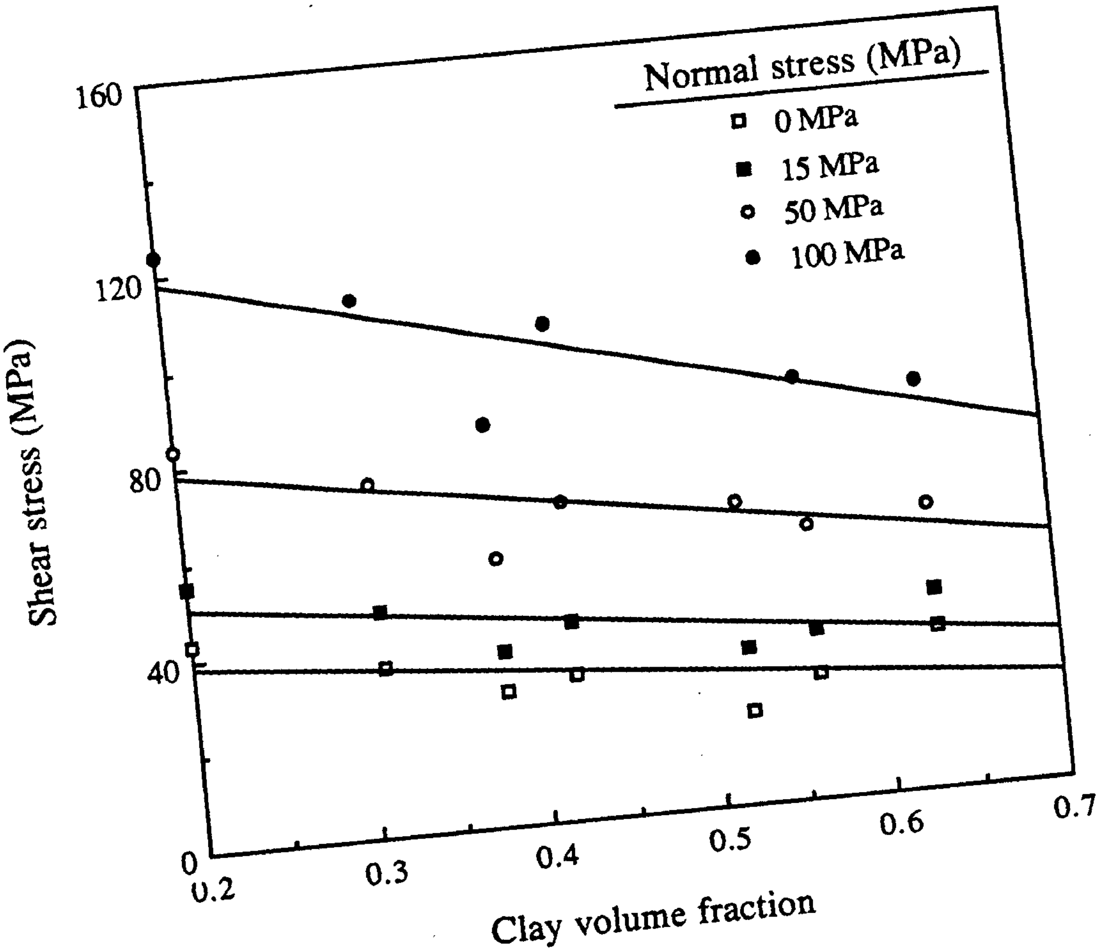

Figure 4.13: Shear stress at failure decreases slightly with increasing clay content in the room-dry shaley sandstones and shales tested. Confining pressure accounts for most variability of shear strength in shaley sandstones and shales, and has consequences for strength in overpressured shales.

From the above observations we investigate functional dependence of shales on clay content and confining pressure of the form

$$\tau = \tau_0(1 - aC) + \mu\sigma \tag{4.21}$$

where τ_0, a, and μ are constants. A regression of equation 4.21 is made using as input variables, the clay content, and the normal and shear stress from each core tested that corresponds to the point on the Mohr circle which is tangent to the failure envelope (columns 2, 6, and 7 in Table 6.1 of Chapter 6 for the rocks listed in Table 4.5). The coefficients a, τ_0, and μ are determined using a least-squares estimate.

Results of the regression are shown in Table 4.7. Predicted shear strengths are in good agreement with measured shear strengths (Figure 4.14). Figure 4.15(A) shows the corresponding Mohr circles in the region of tangency to failure envelopes. We see that shear strength in shaley sandstones and shales is affected primarily by confining pressure. Scatter about this trend is attributed to the presence of clay. When the effect of clay is accounted for by scaling the normal and shear stresses by, $1 - 1.15C$, Mohr circles collapse reasonably well to an envelope of the form $\tau = S_0 + \mu\sigma$ (Figure 4.15(B)).

Table 4.7

Shaley sandstones and shales : $\tau = \tau_0(1 - a) + \mu\sigma$
$\tau_0 = 63$ (MPa) $a = 1.15$ $\mu = .70$ Coefficient of determination, $R^2 = .946$

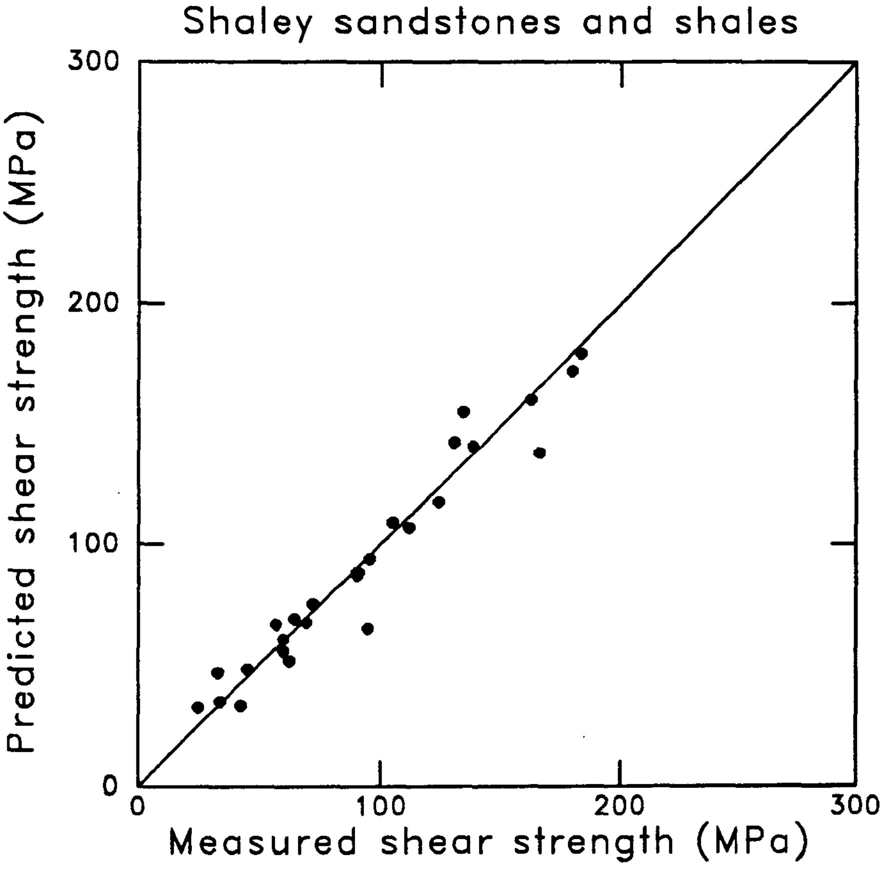

Figure 4.14: Good agreement between predicted vs. measured shear strength in room-dry tight gas shaley sandstones and shales (Table 4.5) is obtained using $\tau_{pred} = 63(1 - 1.15C) + .7\sigma$ (MPa) where C is clay volume fraction and σ is normal stress.

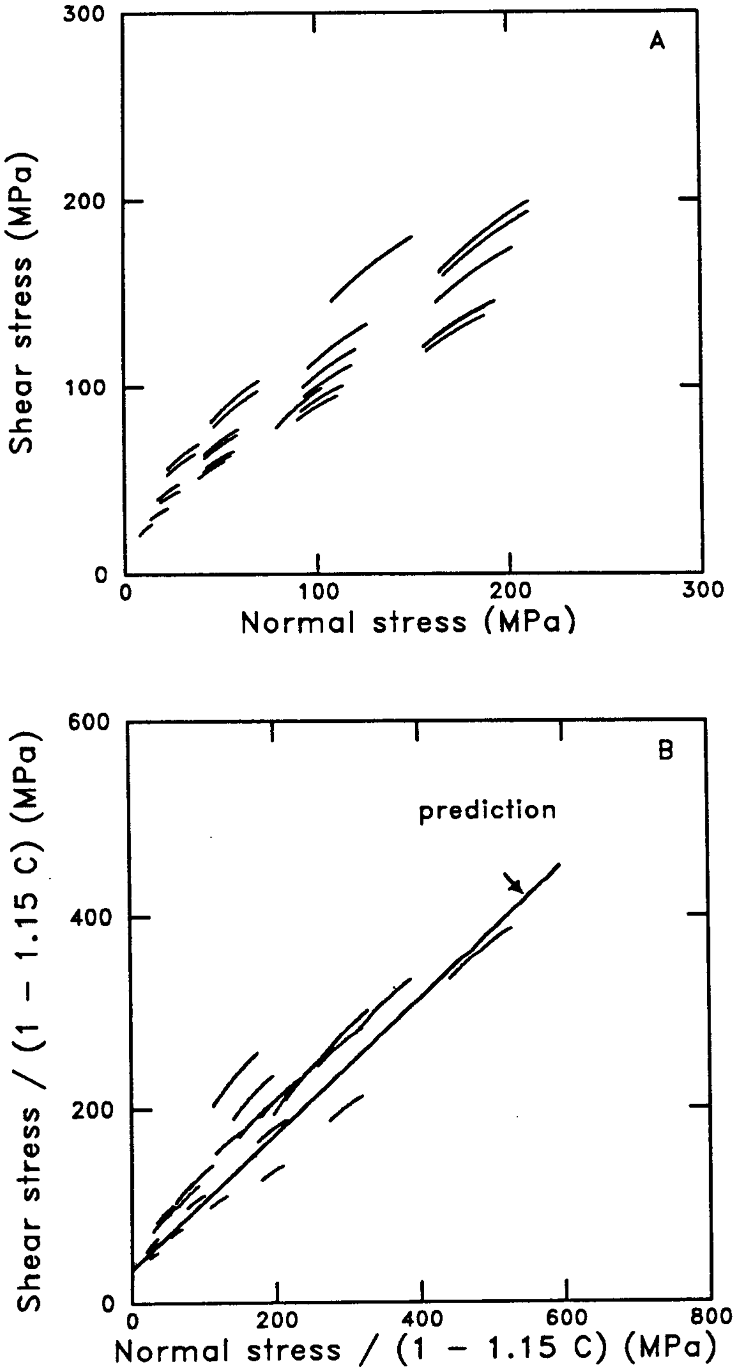

Figure 4.15: (A) Strength of shaley sandstones and shales shown as portions of Mohr circles. Apparent scatter in the data is attributed primarily to clay content. (B) When strength data is corrected for the volume of clay, C, failure envelopes collapse to an equation of the form, $\tau = S_0 + \mu\sigma$.

4.4 Relation between velocity and strength

In this section we examine how shear strength compares with velocity data. Note that the original data set consisted of 32 velocity measurements. The lack of successful velocity measurements on 10 tests, and presence of high concentrations of carbonate on samples from 4 more tests reduces the size of our data set to 18 total rocks. As we feel the link between between velocity and strength is an important one, we present the results for the benefit they may provide qualitatively.

In Figure 4.16 we show strength vs. P and S wave velocity. We see an overall increase of strength with increasing velocity but the data are scattered considerably. We note that scatter in the data is attributed to (1) confining pressure and (2) lithology.

Figure 4.17 shows the influence of lithology on the relation between velocity and strength. From the data in Figure 4.17, we see that at low confining pressure (upper diagrams), one value of velocity may correspond to two different strengths depending on whether the measurement is made on a sandstone or shale. Hence, we suggest that an additional measurement that indicates shaliness is needed in order to make an accurate estimation of strength at low confining pressure or at shallow depth. At high confining pressure (lower diagrams), scatter in the data is reduced and we observe a somewhat more direct correlation of shear strength and velocity with a slope of approximately 70 MPa/(km/s) for shear velocity.

Figure 4.18 shows how confining pressure may account for scatter in the relation between velocity and strength. In Figure 4.18 we notice that within the sandstone shale lithologies, scatter is due to confining pressure. Two distinct trends are seen at 15 MPa and 50 MPa confining pressure data.

In summary, we identified that confining pressure and clay content are important variables to consider when describing strength using velocity measurements. In terms of practical applications, our data set indicates how the knowledge of confining

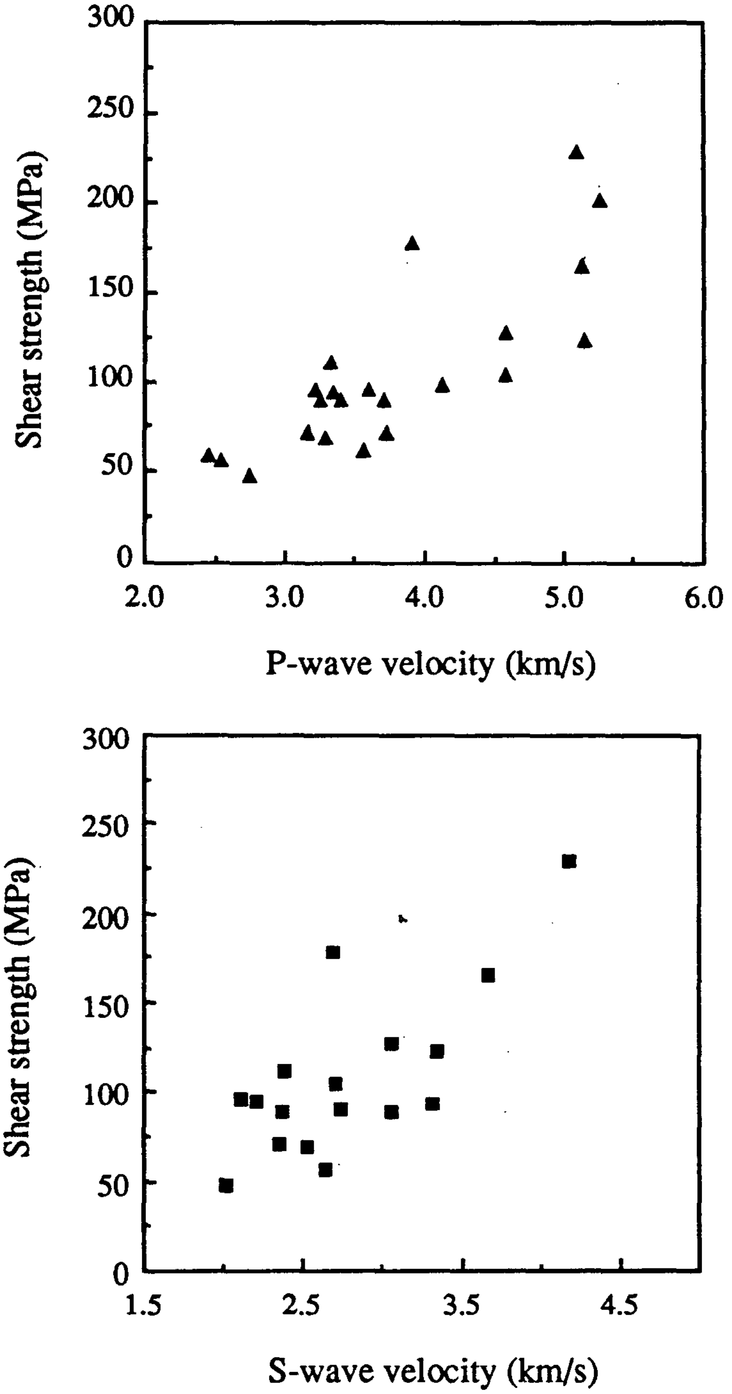

Figure 4.16: Relation between shear strength and P and S wave velocity in room-dry tight gas sandstones. Scatter in these data is attributed to confining pressure and clay content.

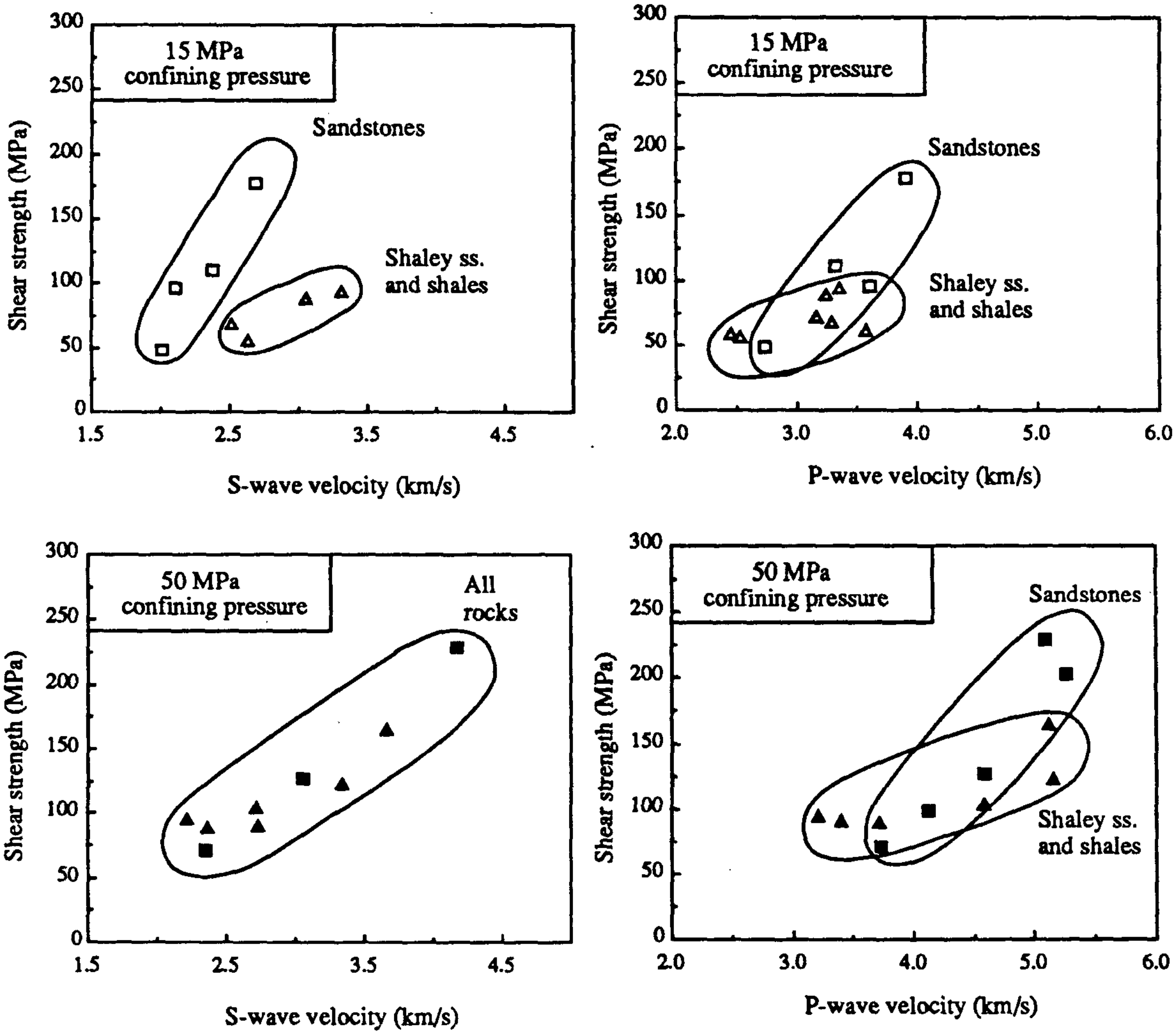

Figure 4.17: Influence of lithology on the relation between strength and shear velocity. At low confining pressure, the an estimate of lithology must be obtained in order to determine shear strength (top). At high confining pressure, a more unique relation between shear velocity and shear strength is observed (bottom left).

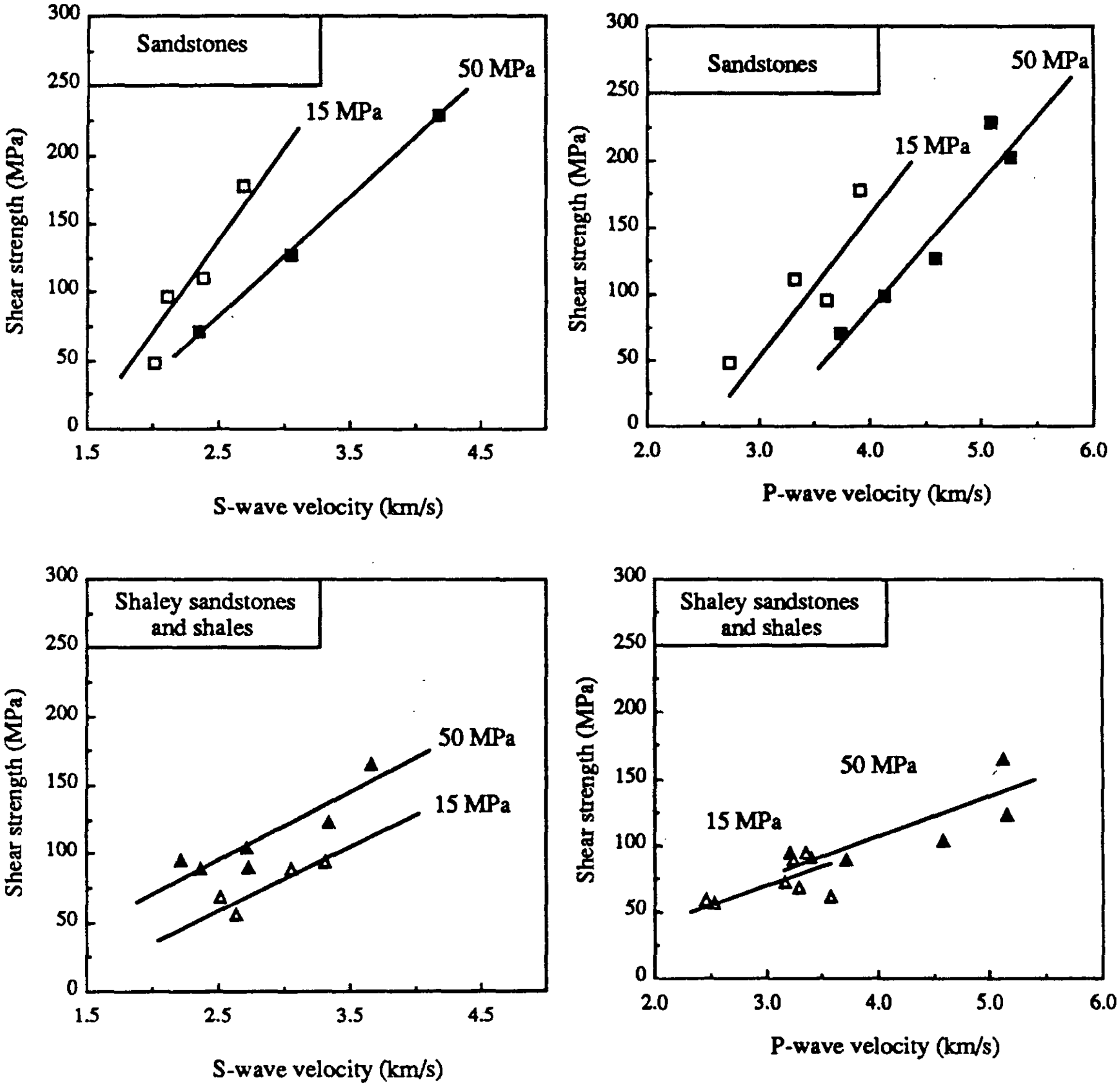

Figure 4.18: Influence of confining pressure on the relation between strength and velocity. Two distinct trends are seen at 15 MPa and 50 MPa confining pressure.

pressure and clay content may lead to improved estimates of rock strength using the acoustic logging response.

4.5 Conclusion

Using laboratory measurements of uniaxial compressive strength and velocities in tight gas sandstones we investigated the functional dependence of strength on rock properties. We find that the area-of-contact idea helps to determine the functionality for the dependence of strength on rock properties in sandstones and shales. In sandstones strength depends on confining pressure and porosity following a relation of the form $\tau = \tau_0(\phi_c - \phi)^m \sigma^n$. Strength in shales is sensitive primarily to confining pressure $\tau = \tau_0(1 - aC) + \mu\sigma$.

Results are aimed towards the estimation of strength based on using P and S velocity measurements and information on formation lithology. Possible applications include hydraulic fracture design, prediction of sanding production, and determination of well-bore stability.

Acknowledgements

Financial support for this work was provided by the Gas Research Institute through a contract (GRI contract no. 5089-211-1842) managed by CER corporation, and by the Stanford Rock Physics Project. Science Applications International Corporation performed confined uniaxial compressive strength measurements. Cores and petrographic data were provided by the Bureau of Economic Geology in Austin, Texas. Supplemental petrographic data was provided by Core Laboratories.

References

Brown, E. T., 1981, Rock Characterization Testing and Monitoring, ISRM Suggested Methods: Pergamon Press.

Brace, W. F., and Riley, D., K., 1972, Static and uniaxial deformation of 15 rocks to 30 kb, Int. J. Rock Mech. Mining Sci., **9**, 271-288.

Coates, G. R., and Denoo, S. A., 1981, Mechanical properties program using borehole analysis and Mohr's circle: Presented at the Soc. Prof. Well-log Anal. Mtg., paper DD.

Dunn D. E., La Fountain, L. J., and Jackson, R. E., 1973, Porosity dependence and mechanism of brittle fracture in sandstones, J. Geophys. Res., **78**, 2403-2417.

Han, D., Nur, A., and Morgan, D., 1986, Effect of porosity and clay content on wave velocity in sandstones: Geophysics, **51**, 2093-2107.

Handin, J., and Hager, R. V. Jr., 1957, Experimental deformation of sedimentary rocks under confining pressure: tests at room temperature on dry samples: Am. Assoc. Petroleum Geologists Bull.,**41** , 1-50.

Griggs, D. T., 1936, Deformation of rocks under high confining pressure; Jour. Geology, **44** , 541-577.

King, M.S., 1983, Static and dynamic elastic properties of rocks from the Canadian Shield, Int. J. Rock Mech. Min. Sci. & Geomech. Abstr., **20**, 237-241.

Kolsky, H., 1963, Stress Waves in Solids: Dover Publications, New York, 201 pp.

Kowallis, B. Jones, L. E. A., and Wang H. F., 1984, Velocity-porosity-clay content; systematics of poorly consolidated sandstones: J. Geophys. Res., **89**, 10355-10364.

Lin, W., 1985, Strength and static elastic moduli of Mesaverde rocks, Lawrence Livermore National Laboratory, UCID-20370, March, 1985.

Lisle, R. J., and Strom, C. S., 1982, Least-squares fitting of the linear Mohr envelope, Q. J. Env. Geol. London, **15**, 55-56.

Murrell, S. A. F., 1965, The effect of triaxial stress systems on the strength of rocks at atmospheric temperatures, Geophys. J. R. Astr. Soc., **10**, 231-281.

Nur, A., and Simmons, G., 1969, The effect of saturation on velocity in low porosity rocks, Earth Science and Planetary Let., **7**, 183-193.

Robertson, E. C., 1955, Experimental study of the strength of rocks, Bull. Geol. Soc. Amer., **66**, 1275-1314.

Scott, T. E., 1989, The effects of porosity on the mechanics of faulting in sandstones, Ph.D. Thesis, The University of Texas at Dallas.

Stauffer, D., 1985, Introduction to Percolation Theory: Taylor and Francis, London, 124 pp.

Stein, N., 1985, Strength of cementation is estimated from well logs: Oil and Gas Journal, 15 July, 132-133.

Tosaya, C., and Nur, A., 1982, Effect of the diagenesis of clays on compressional velocity in rocks: Geophys. Res. Let., **9**, 5-8.

Wang, C., and Mao, N., 1979, Shearing of saturated clays in rock joints at high confining pressures: Geophys. Res. Let., **6**, 825-828.

Wuerker, R. G., 1962, Annotated table of strength and elastic properties of rocks: Petroleum Transactions Reprint Series No. 6, Drilling.

Wyllie, M. R., Gregory, A. R., and Gardner, G. H. F., 1957, An experimental investigation of factors affecting elastic wave velocities in porous media: Geophysics, **23**, 459-493.

Chapter 5

Fluid overpressuring in association with kerogen maturation

Abstract

In this chapter, modes of primary hydrocarbon migration are reviewed. Attention is focused on hydrocarbon migration as a separate phase involving fluid pressurization as a driving mechanism. The association of fluid overpressures in hydrocarbon source rocks is reviewed through field, laboratory, and theoretical considerations. Calculations have been made that estimate the increase in pore pressure and pore volume resulting from maturation of kerogen in an isolated pore. The increase in pore pressure relative to pore volume is determined by the degree to which kerogen is confined by the surrounding rock matrix. In an extremely compliant tabular pore, the maturation of kerogen will generate a large pore-volume increase relative to pore pressure. In a noncompliant pore of spherical or tubular shape, maturation of kerogen will generate a large increase in pore pressure relative to pore volume. In a geological context the extremely compliant pore is analogous to a highly fractured source rock. The noncompliant pore may be analogous to unfractured shale or tight sandstone. In terms of fluid flow, maturation of kerogen in an isolated pore is equivalent to undrained conditions.

5.1 Introduction

The occurence of overpressures in hydrocarbon source rocks has been identified in numerous oil fields (Lucas and Drexler, 1975; Schaar, 1976; Meissner, 1978). The the maturation of kerogen has been postulated to be a possible source of overpressuring (Palciauskas and Dominico, 1980; McAuliffe, 1980; Du Rochet, 1981). The kerogen maturation process has been studied extensively from a chemical point of view (Ungerer et al., 1981; Momper, 1980). However, little emphasis has been placed on evaluation of its mechanical consequences. In situ, kerogen is confined by the surrounding rock which may inhibit volume expansion of hydrocarbon products from occuring during kerogen maturation to form hydrocarbon products. Excess pore pressures may therefore develop.

Our goal is to try to estimate the consequences that kerogen maturation has on pore pressure build up. We consider an isolated source rock. To evaluate the pore pressure build up we use two pieces of information. First, estimates are made of the unconfined volume expansion of initially immature kerogen that transforms into hydrocarbons and residual kerogen. Second, we consider compressibility of the surrounding rock for different pore geometries. Using these, we compute the pore-pressure and pore-volume increase for maturation of three types of kerogen for various pore geometries. Our results suggest that pore pressure build up is inevitable in all except for possibly fractured source rock pore geometries.

5.2 Possible modes of primary hydrocarbon migration

Of the many possible modes accounting for primary migration of hydrocarbons from a source rock, migration in solution, by diffusion, or as a separate phase appears to be most important. Tissot and Welte (1984) have reviewed possible modes accounting for primary hydrocarbon migration upon which the following summary is based.

Migration in solution involves the transport of soluble hydrocarbon products by moving pore water. Tissot and Welte (1984) have suggested that large quantities of water may be available for transport of hydrocarbons in shallow, up to 1000 to 1500 m depth, unconsolidated source rocks that have not yet reached the main phase of hydrocarbon generation. Migration in solution may also take place at greater depths and higher temperatures. Several problems with consideration of migration in solution have been noted. Price (1976) experimentally observed low solubility of hydrocarbons in water under subsurface conditions. Durand (1980) noted that in many hydrocarbon pools whereby solution is believed to be the active mode of transportation, the observed distributions of hydrocarbon products show opposite concentrations than would be expected. Another problem with hydrocarbon migration in solution is the likelihood of insufficient pore water for hydrocarbon transportation at greater depths. Clay dehydration reactions such as alteration of montmorillonite to illite have been postulated to be a source of pore fluids at depths roughly between 1200 and 5000 m (Powers, 1967; Burst, 1969). Tissot and Welte (1984) have concluded that although migration in solution accounts for the transportation of hydrocarbons from some source rocks, it is probably not a dominant mode of primary hydrocarbon migration.

Migration by diffusion involves the transport of hydrocarbon products along chemical pressure gradients, usually related to temperature or pressure gradients, towards regions of lower chemical potential. Unlike migration in solution, diffusive migration does not require the presence of pore water as a transporting phase. Leythauser et al. (1982) have shown that transport by diffusion favors lower molecular-weight hydrocarbons. They suggest that diffusive migration of gasses from a source rock may be significant in the formation of gas accumulations. Tissot and Welte (1984) suggest that while diffusive transport of hydrocarbons is probably important for the formation of gas accumulations at depth and during late stages of hydrocarbon evolution, it is not a very important mode of primary migration in most source rocks during the main stage of oil generation.

Migration of hydrocarbons as a separate phase occurs via flow of pressurized hydrocarbons towards regions of lower potential. Migration of hydrocarbons as a separate phase is presumably favored by absence of pore water which aids in the formation of a continuous oil phase of greatly reduced capillary pressures. The effectiveness of hydrocarbon migration as a separate phase is expected to be strongly influenced by the concentration and distribution of kerogen in the source rock (Durand, 1980). McAuliffe (1980) and Snarsky (1962) attempted to describe the pathways along which hydrocarbon migration as a separate phase may take place. Snarsky (1962) suggested that pressurization of hydrocarbons by a factor of 1.4 to 2.4 above hydrostatic should create microfractures in the source rock serving as transport avenues for the migration of hydrocarbons. McAuliffe (1980) suggested that transportation of hydrocarbons could occur along a continuous oil-wet network in the source rock. Despite lack of knowledge on details of the process, migration of hydrocarbons as a separate phase is generally acknowledged to be the most effective and dominant mode of primary hydrocarbon migration. The focus of this paper is on consideration of primary hydrocarbon migration as a separate phase.

5.3 Association of excess fluid pressure in hydrocarbon source rocks

5.3.1 Field data

Field studies documenting the existence of overpressures in hydrocarbon source rocks are numerous. Three examples are cited here.

Fluid pressure data from producing areas in Europe (Hunt, 1979) are shown in Figure 5.1. The normal lithostatic pressure gradient, top line, is approximately 230 bars/km (1 psi/ft). The hydrostatic pressure gradient, bottom line, is approximately 100 bars/km (0.4 psi/ft). All fluid pressure data shown in Figure 5.1 exceed

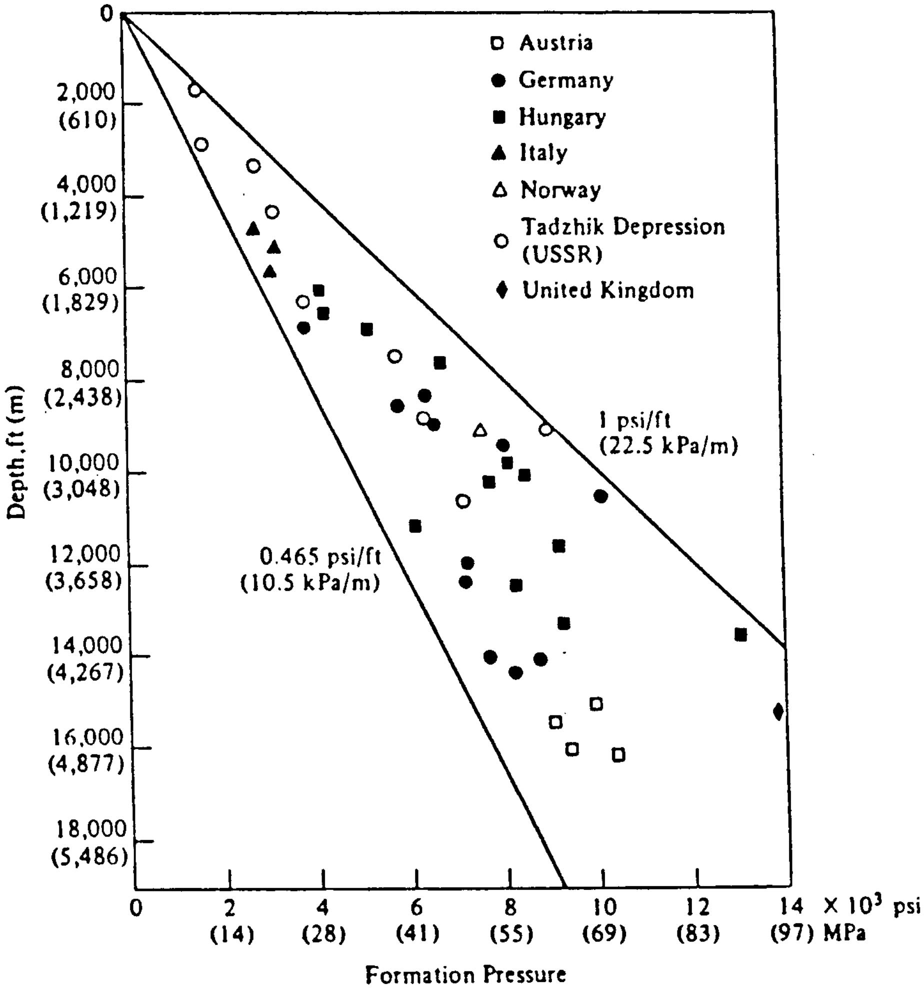

Figure 5.1: Abnormal formation pressures in European basins (Fertl, 1972; Kalomazov and Vakhitov, 1975) (figure from Hunt, 1979).

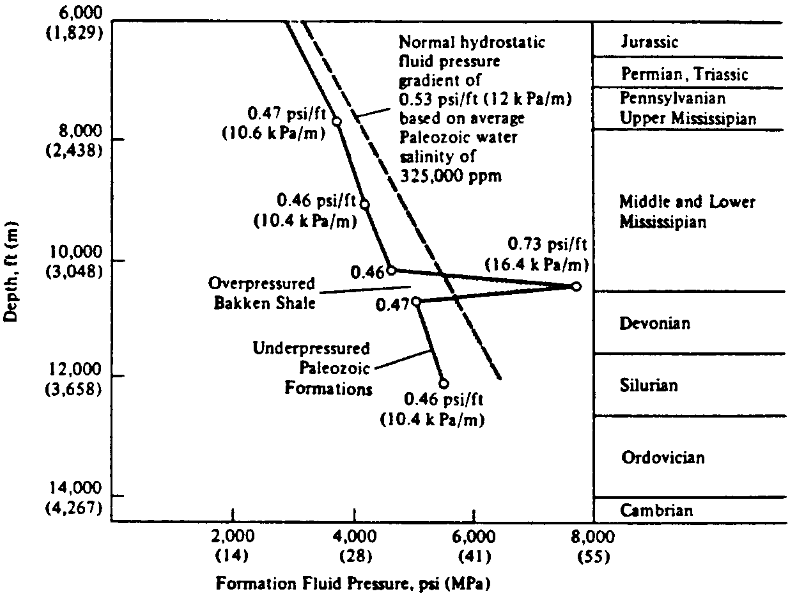

Williston Basin, North Dakota

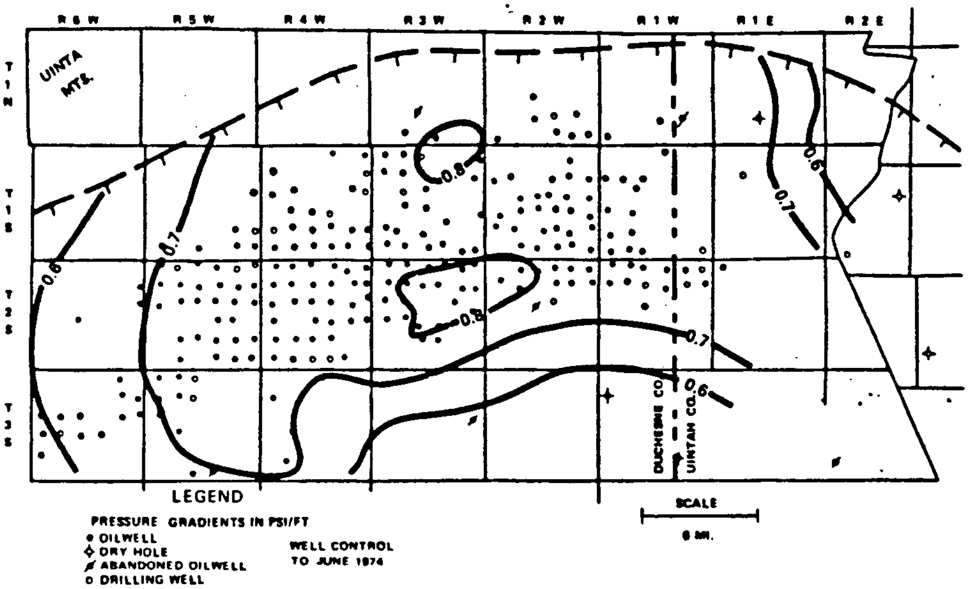

Uinta Basin, Utah

Figure 5.2: Overpressure gradients measured in Williston Basin, North Dakota, .73 psi/ft (Meissner, 1979) (figure from Hunt, 1979) and Uinta Basin, Utah, .83 psi/ft (Lucas and Drexler, 1975).

hydrostatic. Values in the Tadzhik depression, USSR, have been recorded at as much as 2.3 times hydrostatic pressure (Kalomazov and Vakhitov, 1975).

Commonly cited formations in the United States include the Bakken Shale in the Williston Basin, North Dakota (Meissner, 1978), and the Altamont Formation in the Uinta Basin, Utah (Lucas and Drexler, 1975). As seen in Figure 5.2, pressure gradients in the Bakken Shale and the Altamont Formation have been recorded to be as high as 158 to 180 bar/km (0.7-0.8 psi/ft). These basins are highly fractured source-rock reservoirs having low permeability and hydrocarbons as the dominant movable fluid.

Overpressured wells in the Baram Delta offshore Sarawak, Malaysia, have been characterized by Schaar (1976). Two types of fluid overpressures were distinguished using sonic porosity log data. The first type of fluid overpressure was found in rocks of high sonic porosity suggesting undercompaction of sediments. The second type of overpressure was found in rocks having normal sonic porosity suggesting normal compaction of sediments. Of the 17 wells noted as having high sonic porosity, no hydrocarbons were found. Of the 10 wells noted as having normal sonic porosity, 6 contained hydrocarbons. These data may suggest that a correlation exists between hydrocarbon occurrence and the type of overpressuring in a source rock.

5.3.2 Experimental observations

Until recently, much research on kerogen maturation focused on chemical identification of products from kerogen pyrolysis experiments. Lack of many pyrolysis experiments under confinement made it difficult to study the role of pressure in kerogen maturation. Generation of excess pressure in a hydrocarbon source rock was observed by Tissot and Pelet (1971) who while holding a shale under 440 bars confining pressure recorded an increase up to 540 bars pore pressure from gas generation until microfracturing occurred. Recently, Monthioux et al. (1985) carried out confined pyrolysis experiments on type III kerogen. During pyrolysis experiments, the effect of confining pressure was found to be negligible with no visible change in hydrocarbon products upon increasing confining pressure from 0.5 to 4 kbars. However, attainment of a geologically small pore pressure, about 10 bars, was found to be necessary for generation of hydrocarbon products that are qualitatively similar to those observed in natural systems. Monthioux et al. (1985) observed that in confined pyrolysis, oxygen tended to depart as CO_2 as observed in natural systems in contrast to unconfined pyrolysis where departure of most oxygen occurs as H_2O.

5.4 Possible pressure-generating mechanisms in a source rock

Literature on pressure-generating mechanisms in sedimentary basins is extensive. For reviews see Fertl (1976), Gretener (1978), Magara (1978), and Tissot and Welte (1984). In considering overpressures in hydrocarbon source rocks, the following pressure-generation mechanisms may be relevant.

(1) Loading. Pressure generation may be due to rapid sedimentation, compaction, and the formation of low-permeability seals inhibiting fluid flow. When rapid sedimentation and compaction are the active loading mechanisms, the sediments are characterized as having high porosity from the presence of excess fluids. This loading mechanism is termed nonequilibrium compaction and is acknowledged as being a predominant pressure-generating mechanism in many compacting sedimentary sequences. Models of pressure generation in sedimentary columns incorporating loading mechanisms include Bredehoeft and Hanshaw (1968), Smith (1971), and Keith and Rimstidt (1985).

(2) Fluid specific-volume increase. Pressure generation may be due to a decrease in fluid density causing fluid pressurization. Some mechanisms include:

a. Thermal expansion of water with increasing depth has been suggested by Barker (1972) based on density data of water under geologic pressure and temperature gradients. This effect may be important only in cases of rapid burial with confined pore volume. Calculations by Shi and Wang (1985) show that excess pore water can be easily accommodated with normal pore compliances and hydraulic conductivities.

b. Volume expansion from kerogen maturation may be due to decrease in average density of kerogen residue and hydrocarbon products. Momper (1980) and Ungerer et al. (1981) have made estimates of net volume expansion for the maturation of various types of kerogen.

c. Decrease in density from clay dehydration reactions, based on the idea that chemically bound water in clay interlayers has higher density than free water in the pore space. Using a density of 1.4 g/ for chemically bound water (Martin, 1962), Powers (1967) proposed that fluid-pressure generation may occur from the dehydration of montmorillonite to form illite at depths of roughly 1200 to 5000 m. Data from Anderson and Low (1958) indicate that bound water may have a density of less than 1 g/cc. Lack of exact determination of the density of bound water on clay surfaces make conclusions regarding this mechanism questionable.

(3) Internal fluid source. Pressurization caused by fluid or gas generation from chemical reactions in the rock matrix. Dehydration reactions have been found to generate significant fluid pressures experimentally. In a triaxial compression test of polycrystalline gypsum, Heard and Rubey (1966) measured a ten-fold decrease in strength from 2.7 to 0.25 kbars when temperature was increased from 100 to 150 ^{o}C. This increase in pressure was attributed to dehydration of gypsum as an internal fluid source causing a subsequent rise in fluid pressure to approach overburden. Bredehoeft and Hanshaw (1968) quantified the observations of Heard and Rubey (1966) by determining the values for reaction rate and hydraulic diffusivity that are needed to approach lithostatic fluid pressures. In hydrocarbon source rocks pressurization may result from clay and evaporite dehydration reactions and kerogen maturation. DuRouchet (1981) suggested that during kerogen maturation, stress of the rock matrix may be imparted to the generated hydrocarbons and result in plastic flow of organic matter from the pore space.

Pressure-generating mechanisms are likely to be specific to the geologic processes in a source rock. In many attempts to model overpressures, a forward approach has been taken by incorporating presumably relevant pressure-generation and pressure-dissipation mechanisms. Models applicable to hydrocarbon source rocks include Palciauskas and Dominico (1980) and Durand et al. (1983). Palciauskas and Dominico (1980) presented a nonisothermal sedimentation model incorporating water expansion and gravitational loading as pressure-generating mechanisms and microfracture dilation and porous fluid flow as pressure-dissipation mechanisms. Durand et al. (1983) developed a two-dimensional sedimentation model with compaction as the most important pressure-generating mechanism and kerogen maturation as a secondary source of excess fluid pressure. Durand et al. (1983) successfully applied their model to prediction of excess pressure and oil accumulations in the Viking Graben in the North Sea and the Mahakam delta, Indonesia.

5.5 Material balance

A detailed mathematical model describing kerogen degradation has been developed by Tissot and Welte (1984). A schematic of the reaction shown in Figure 5.3 describes kerogen maturation as taking place in two stages. The first main stage of kerogen maturation corresponds to the maximum phase of oil generation and is generally observed at vitrinite reflectance values of about $R_o = 0.9$ %. The second main stage of kerogen maturation corresponds to gas formation from oil-cracking reactions and generally occurs at vitrinite reflectance values of approximately $R_o = 1.3$ %. In this paper I am concerned with the pressure and volume changes that take place upon the maturation of initially immature kerogen at $R_o = 0.5$ % to the first stage of maximum oil generation at approximately $R_o = 0.9$ %.

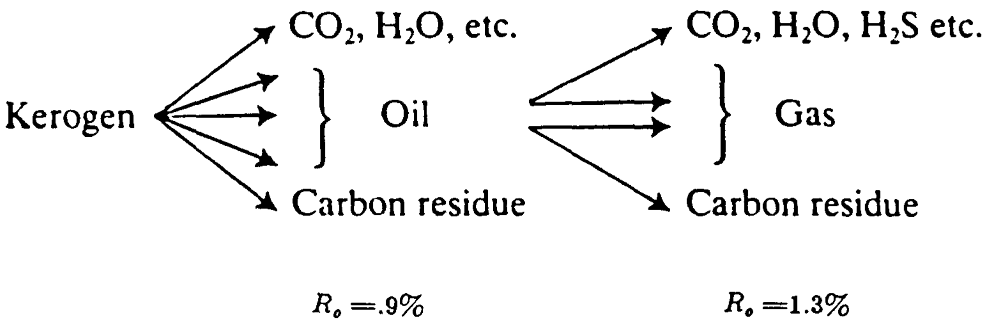

Figure 5.3: General scheme of kerogen degradation and hydrocarbon generation (Tissot and Welte, 1984).

Three types of kerogen, types I, II, and III (Figure 5.4), have been considered. Maximum and minimum estimates of hydrocarbon yield for each type of kerogen have been made from Orr (1983) (Table 5.3 and Figure 5.5). Density and bulk modulus values from literature references are shown in Tables 5.1 and 5.2. Liquid and gaseous products have been grouped together and assigned a single value of density and bulk modulus. Bulk modulus used in the calculations for mature kerogen is estimated by addition in series of bulk modulus of the residual kerogen and the hydrocarbon liquid and gaseous products.

A schematic of diagram of material balance for each type of kerogen is shown in Figure 5.5. The notation used in Figure 5.5 is based on Ungerer et al. (1981) who have made detailed calculations of volume expansion of kerogen types II and III at several levels of maturation.

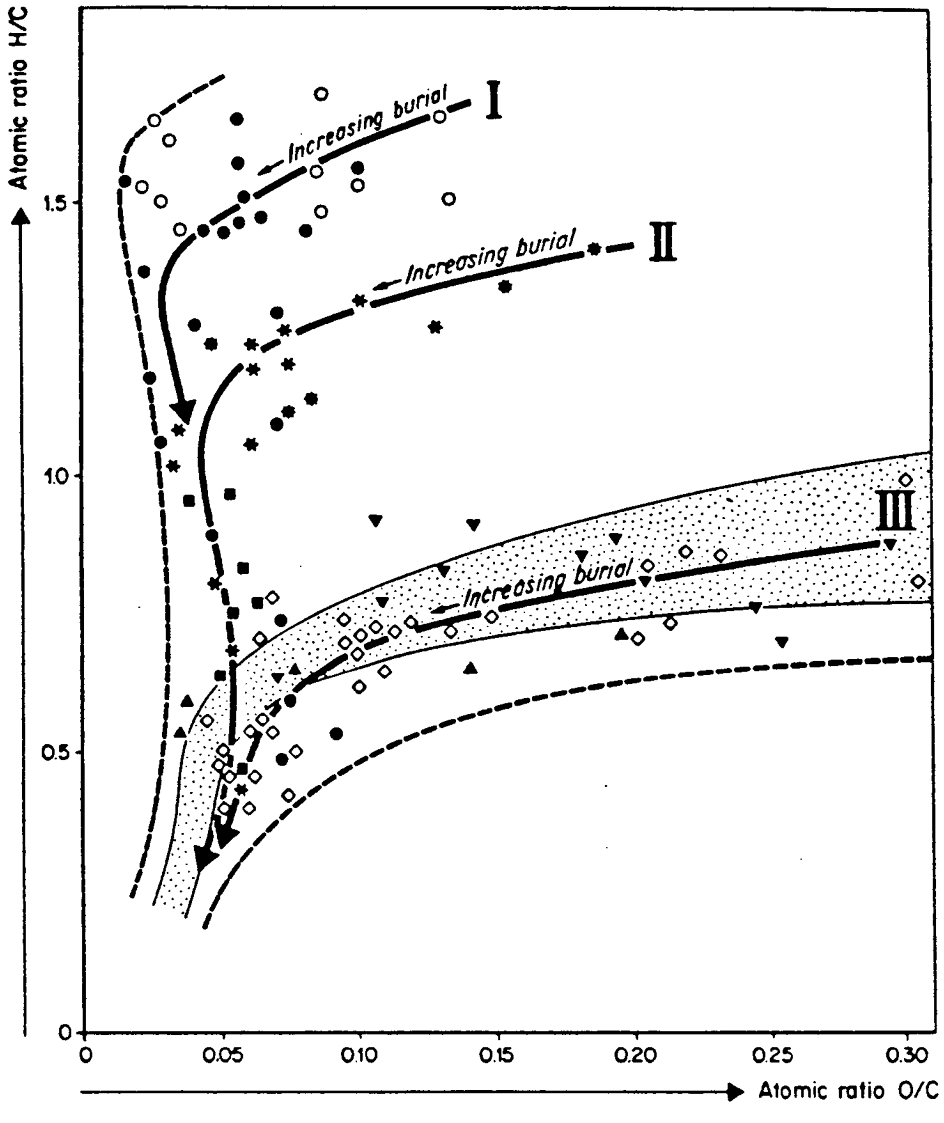

Figure 5.4: Evolution paths for the principle types of kerogen, I, II, and III (Tissot and Welte, 1984).

Table 5.1

Density of kerogen and hydrocarbon products

	ρ (g/cc)
Hydrocarbon products [1]	.8-1
Kerogen [2] type I, immature	1.12
mature	1.16
type II, immature	1.15
mature	1.15
type III, immature	1.37
mature	1.30

[1] Data from Ungerer et al. (1981) and Wang (1985). [2] Data from Van Krevelen (1961) and Momper (1978).

Table 5.2

Bulk moduli of kerogen and hydrocarbon products

	K (kbar)
Hydrocarbon products [1]	8-18
Kerogen [2] type I, immature	15-25
type II, immature	22-54
type III, immature	38-51

[1] Based on data from Wang (1985). [2] Data from coals Van Krevelen (1961).

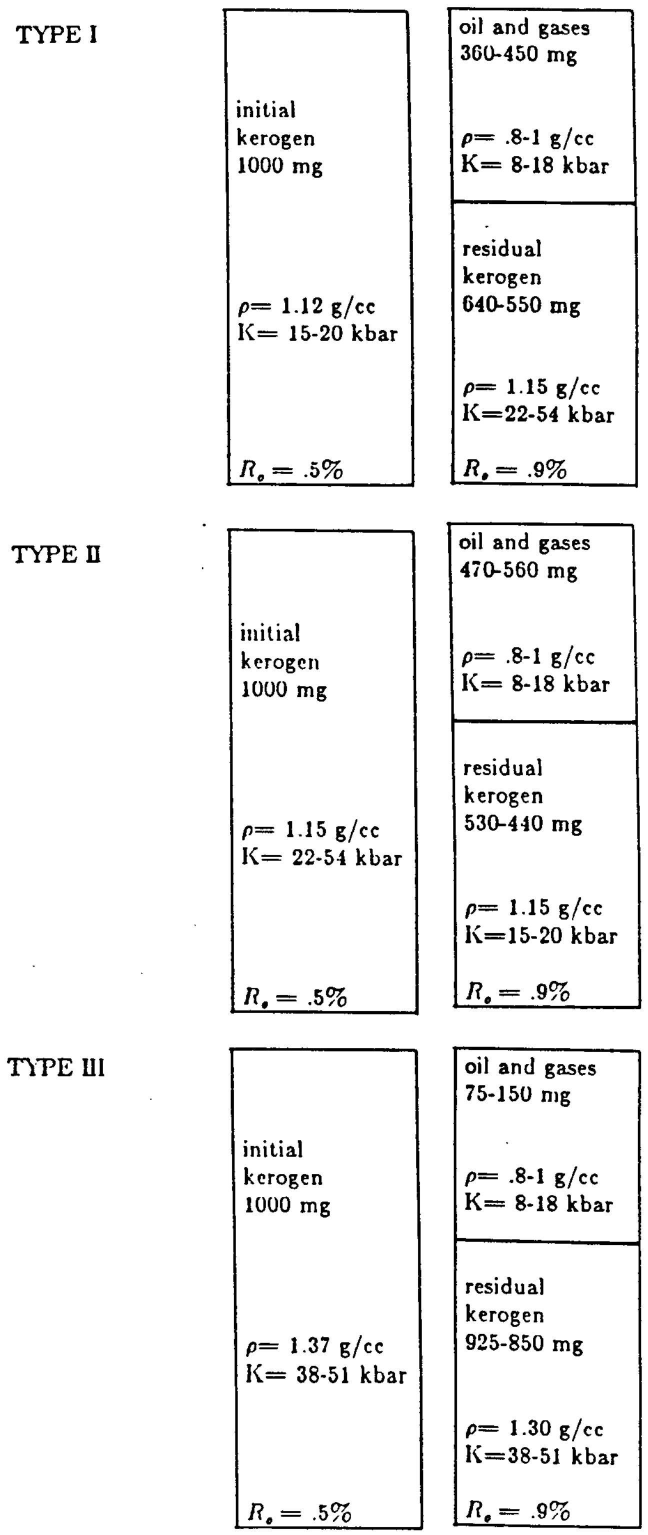

Figure 5.5: Mass balance, density, and compressibility for type I, II, and III kerogen and evolution products (diagrams based on Ungerer et al., 1981).

Table 5.3

Genetic potential estimates for kerogen type I, II, and III [1]

Kerogen	$(\frac{gHC}{gKer})$ [2]
type I	.47 - .56
type II	.36 - .45
type III	.08 - .15

[1] Values from pyrolysis data (Orr, 1983) assuming 75 % organic carbon in immature kerogen. [2] Genetic potential expressed as weight fraction producible hydrocarbons per unit weight kerogen.

5.6 Undrained conditions

Calculations have been made assuming undrained conditions exist in the source rock. This assumption is reasonable for source rocks of low permeability or having low-permeability horizons. By comparing kerogen maturation rate versus hydraulic diffusivity, the permeability needed for attainment of undrained conditions in a source rock may be estimated. Calculations have not been made here. Bredehoeft and Hanshaw (1969) have carried out such estimates for gypsum and montmorillonite dehydration reactions.

Of interest here is determination of pore-volume and pore-pressure increase upon kerogen maturation with the mass of kerogen and hydrocarbon products held constant. In order to compute these quantities, we use equations for pore and fluid compressibility.

Volumetric strain of the pore space is given by

$$\frac{\Delta V_{pore}}{V_{pore}} = C_{PP}\Delta P \tag{5.1}$$

where $\frac{\Delta V_{pore}}{V_{pore}}$, C_{PP}, and ΔP, are the pore volume strain, pore compressibility, and change in excess pore pressure respectively. Equation 5.1 can be expressed in terms of pressure and volume difference (Figure 5.6) as

$$\frac{V - V_K}{V_K} = C_{PP}P \qquad (5.2)$$

where V_K, is the initial volume of immature kerogen that is at zero excess pore pressure, V is the pore volume of mature kerogen and hydrocarbon products, and P is the excess pore pressure (pore pressure minus hydrostatic pressure) of mature kerogen and hydrocarbon products.

A second volumetric strain is defined by the fluid compressibility

$$\frac{\Delta V_{fluid}}{V_{fluid}} = -C_{HC}\Delta P \qquad (5.3)$$

where $\frac{\Delta V_{fluid}}{V_{fluid}}$, C_{HC}, and ΔP, are the volumetric strain of the fluid, fluid compressibility, and change in excess pore pressure respectively. From the diagram in Figure 5.6, equation 5.3 can be expressed in terms of pressure and volume difference as

$$\frac{V - V_{HC}}{V_{HC}} = -\ C_{HC}P \qquad (5.4)$$

where V_{HC} is the initial volume of mature hydrocarbon products and residual kerogen at zero excess pore-pressure, V is the pore volume of the mature hydrocarbon products and residual kerogen, and P is the excess pore pressure.

Final volume and excess pore pressure change caused by kerogen maturation is solved for using equations (5.2) and (5.4)

$$P = \frac{V_{HC} - V_K}{C_{PP}\,V_K + C_{HC}\,V_{HC}} \qquad (5.5)$$

$$V = \frac{C_{PP} + C_{HC}}{\left(\frac{C_{PP}}{V_{HC}} + \frac{C_{HC}}{V_K}\right)} \qquad (5.6)$$

where V_{HC}, V_K, C_{PP}, and C_{HC} are as defined above.

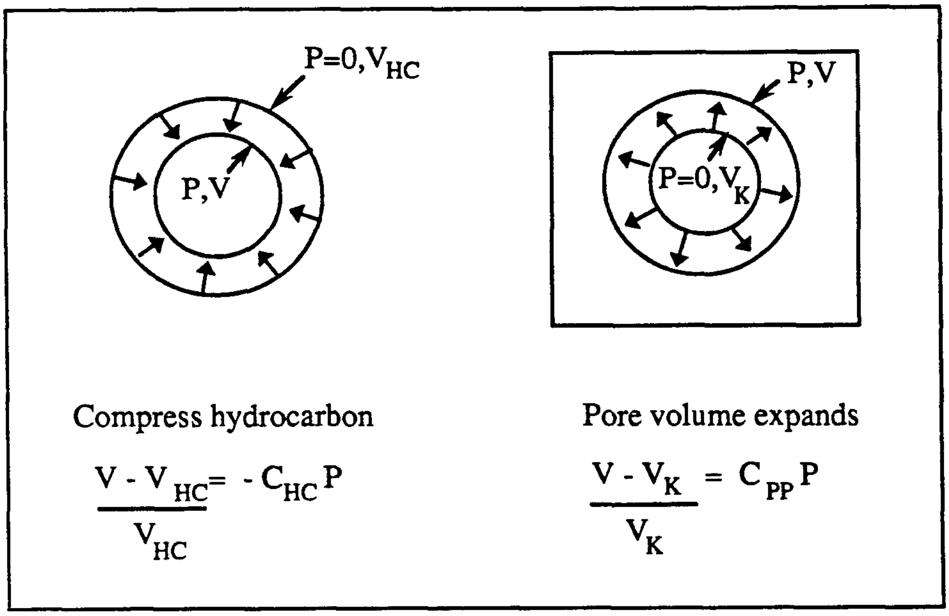

Figure 5.6: Volumetric strains associated with change in pore pressure in an undrained pore. Arrows indicate applied stress.

5.7 Extreme cases of pressure and volume increase

As a result of kerogen maturation in an undrained system two extremes in pore pressure and volume increase may result. One extreme is noncompliance of the pore space resulting in no volume increase and pore pressure increase determined by hydrostatic compression of the mature kerogen products to the original volume of immature kerogen. The other extreme case is infinite compliance of the pore space resulting in total accommodation of mature kerogen product volume and no generation of excess pressure.

Pore pressure and pore volume increase corresponding to the two extremes in pore compliance are shown in Table 5.4 using minimum estimates of hydrocarbon yield (Table 5.3), density (Table 5.1), and bulk modulus (Table 5.2) in the calculations. Volume expansion values calculated by other authors are indicated in superscript and have implicitly assumed infinite compliance of the pore space. Values of pore pressure in the case of a totally non compliant pore space are extremely high. It is rock matrix. In a laboratory experiment by Tissot and Pelet (1971) 0.1 kbar excess pressure was recorded in a shale held under confining pressure until microfracturing caused pressure release.

Table 5.4

Pore pressure and volume increase for extreme cases of pore compliance

		P (kbar)	V (%)
type I,	no pore compliance	.43	0
	infinite pore compliance	0	4.5 [1]
type II,	no pore compliance	.63	0
	infinite pore compliance	0	5.7 [2]
type III,	no pore compliance	2.0	0
	infinite pore compliance	0	9.6 [3]

Calculations of volume expansion from the literature are indicated by superscript: [1] volume expansion type I kerogen (Momper, 1980), [2] volume expansion type II kerogen in closed system (Ungerer et al., 1981), and [3] volume expansion type III kerogen in closed system (Ungerer et al., 1981).

5.8 Pressure and volume increase given pore geometry

In an undrained source rock, the magnitude of pressure increase is expected to depend dramatically on the degree of confinement of kerogen by the pore space. Figure 5.7 shows the effect of pore geometry on pore compressibility of an isolated spheroidal pore (Zimmerman, 1985). In Table 5.5 estimates of pore compressibility for various pore shapes in a hydrocarbon source rock are made. Knowing the pore compressibility, equations (5.5) and (5.6) may be used to calculate values of pore pressure and pore volume increase. These values shown in Table 5.6 fall between the two extremes of pore compliance previously discussed.

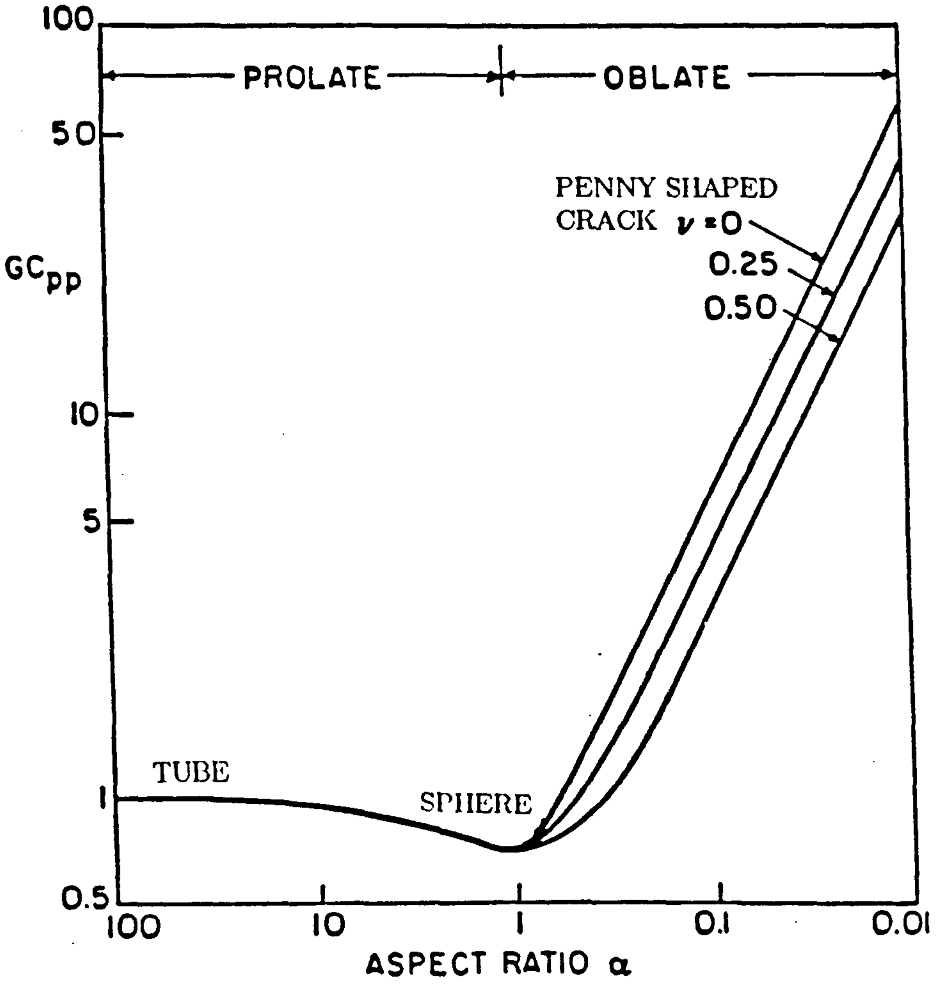

Figure 5.7: Product of compressibility of a spheroidal pore and shear modulus of the rock (Zimmerman, 1985). Note this is a log-log plot.

Table 5.5

Pore bulk modulus for various pore shapes (Zimmerman, 1985)

	$K_{PP} = \frac{1}{C_{PP}}$
no pore compliance	*infinite*
tube	52
sphere	39
penny-shaped crack	
$\sigma = .25$ $\alpha = .1$	5.7
$\alpha = .05$	2.7
$\alpha = .01$	.5
infinite pore compliance	0

For formulas see Zimmerman (1985). Estimates made here have assumed reasonable elastic constants for a hydrocarbon source rock. For calculation of tube and sphere pore compressibility, shear modulus of the rock-forming mineral was chosen to be 390 kbar. For calculation of pore compressibility of the penny-shaped crack bulk modulus of the rock-forming mineral was chosen to be 400 kbar. Poisson's ratio is denoted by σ and the aspect ratio α is defined as the ratio of the minor axis to the major axis of the pore.

5.9 Conclusion and implications for primary hydrocarbon migration

Values in Table 5.6 show that in an undrained system, maturation of kerogen results in a combination of pore pressure and pore volume increase which is determined by compressibility of the pore space with pore pressure. If the rate of kerogen maturation sufficiently exceeds the ability of fluids to flow from the pore space, the undrained source rock may be considered as an initial condition with subsequent decrease of excess pressure over time by various pressure dissipation mechanisms.

Implications for primary hydrocarbon migration are most easily made in terms of two extreme cases of pore compliance. In a very compliant pore space, which may be geologically analogous to a fractured source rock, maturation of kerogen is expected to cause dilation of the pore space with subsequent fluid flow upon the attainment of some critical value of fluid content or pore pressure. This scenario of pressurized hydrocarbon migration by repeated episodes of flow through a network of fractures

Table 5.6

Pore pressure and volume increase as a function of pore compliance

	type I P (kbar)	type I V(%)	type II P (kbar)	type II V(%)	type III P (kbar)	type III V(%)
no pore compliance	.43	0	.63	0	2.0	0
tube	.35	0.7	.51	1.0	1.3	2.6
sphere	.33	0.9	.48	1.2	1.2	3.2
penny-shaped crack						
$\sigma = .25$ $\alpha = .1$	.16	2.8	.21	3.7	.42	7.4
$\alpha = .05$	.09	3.5	.12	4.6	.23	7.9
$\alpha = .01$	.02	4.3	.03	5.0	.05	9.4
infinite compliance	0	4.5	0	5.7	0	9.6

been suggested by many authors (McAuliffe, 1980; Momper, 1980; Tissot and Welte, 1984).

In the other extreme case of totally noncompliant pore space, it is presumable that high pore pressures will be easily achieved and microfracturing of the source rock may occur. The implications for primary migration appear to be similar to the case of compliant pore space with pressurized flow of hydrocarbons through the pore space towards microfractures with subsequent pressure release by fluid flow upon attainment of critical pore pressure or fluid content in the microfractures.

The Williston basin, North Dakota, and Uinta basin, Utah, are believed to be possible regimes where such mechanisms of primary migration may be operating in hydrocarbon source rocks. Increased study through modeling and field observations would be valuable.

References

Anderson, D. M. and Low, P. F. (1958) Density of water absorbed by lithium-, sodium-, and potassium-bentonite. Soil Sci. Soc. Am. Proc. 22: 97-103.

Barker, C. (1972) Aquathermal pressuring - role of temperature in development of abnormal pressure zones. Bull. Am. Assoc. Pet. Geol. 56: 2068-2071.

Beseme, P. (1972) Bitumes figures et deplaces en association dans cinq series a kerogene d'Anatolie (Turquie); description et origine de ces kerabitumes. Inst. Francais Petrole. Rev., 27: 885-912.

Bredehoeft, J. D. and Hanshaw, B. B. (1968) On the maintenance of anomalous fluid pressures, I, thick sedimentary sequences. Geol. Soc. Amer. Bull. 79: 1097-1106.

Bredehoeft, J. D. and Hanshaw, B. B. (1968) On the maintenance of anomalous fluid pressures, II, source layer at depth. Geol. Soc. Amer. Bull. 79: 1107-1122.

Burst, J. F. (1969) Diagenesis of Gulf Coast clayey sediments and its possible relation to petroleum migration. Bull. Am. Assoc. Pet. Geol., 53: 73-93.

Durand, B., Ungerer, Ph., Chiarelli, A., and J. L. Oudin (1983) Modelisation de la migration de l'huile. Application a deux examples de bassins sedimentaires. In: 11th World Petroleum Congress, Proc., 3: 3-15.

Durand, B. (1980) Present trends in organic geochemistry in research on migration of hydrocarbons. In: Advances in Organic Geochemistry 1981, Bjoroy, M. et al. (eds.), Chichester: Wiley, publ. 1983, 117-128.

Du Rouchet, J. (1981) Stress fields, a key to oil migration: Bull. Am. Assoc. Pet. Geol., 65: 74-85.

Fertl, W. H. (1976) Abnormal formation pressures: implications to exploration, drilling, and production of oil and gas reservoirs, Elsevier, Amsterdam, 382pp.

Gretener, P. E. (1978) Pore pressure: fundamentals, general ramifications, and implications for structural geology. Am. Assoc. Pet. Geol. continuing education course note series, no. 4, 87 pp.

Heard, H. C. and Rubey W. W. (1966) Tectonic implications of gypsum dehydration. Geol. Soc. Amer. Bull., 77: 741-760.

Hunt, J. M. (1979) Petroleum Geochemistry and Geology, W. H. Freeman, San Francisco, 617pp.

Kalomazov, R. U. and M. A. Vakhitov (1975) Appearance and nature of anomalously high formation pressures in the Kuyab Mega syncline of the Tadzhik depression. Nefti Gazovaya Geolog. Geofiz., 10: 3-6.

Keith, L. A. and J. D. Rimstidt (1985) A numerical compaction model overpressuring in shales. Mathematical Geology, 17(2): 115-135.

Leythaeuser, D., Schaefer, R. G., and A. Yukler (1982) Role of diffusion in primary migration of hydrocarbons. Bull. Am. Assoc. Pet. Geol., 66: 408-429.

Lucas, P. T., and J. M. Drexler (1975) Altamont-Bluebell- A major, naturally fractured stratigraphic trap, Uinta Basin, Utah. Am. Assoc. Pet. Geol. Memoir, 24: 121-135.

Magara, K. (1978) Compaction and Fluid Migration, Elsevier, Amsterdam, 319 pp.

Martin, R. T. (1962) Adsorbed water on a clay: a review. Clays Clay Miner., 9 (Proc. 9th Natl. Conf. Clays and Clay Minerals, 1960), Pergamon, New York, 28-270.

McAuliffe, (1980) Oil and gas migration: chemical and physical constraints. In: Am. Assoc. Pet. Geol. Studies in Geology No. 10, Problems of Petroleum Migration, Roberts, III, W. H., Cordell, J. R. (eds.), 87-107.

Meissner, F. F. (1978) Petroleum geology of the Bakken Formation, Williston Basin, North Dakota and Montana. Proceedings of 1978 Williston Basin Symposium, Montana Geological Society, Billings, 207-227.

Momper, J. A. (1980) Oil expulsion: a consequence of oil generation. Am. Assoc. Pet. Geol. studies in geology.

Monthioux, M., P. Landais, and J. C. Monin (1985) Comparison between natural and artificial maturation series of humic coals from the Mahakam delta, Indonesia. Organic Geochemistry, 8(4): 275-292.

Orr, W. L. (1981) Comments on pyrolitic hydrocarbon yields in source rock evaluation. Advances in Organic Geochemistry 1981, Bjoroy, M. et al. (eds.), Chichester: Wiley, publ. 1983, 775-786.

Palciauskas, V. V., and P. A. Dominico (1980) Microfracture development in compacting sediments: Relation to hydrocarbon-maturation kinetics. Bull. Am. Assoc. Petrol. Geol. 64: 927-937.

Powers, M. C. (1967) Fluid release mechanisms in compacting marine mudrocks and their implications in oil exploration. Bull. Am. Assoc. Petrol. Geol. 51: 1240-1254.

Price, L. C. (1976) Aqueous solubility of petroleum as applied to its origin and primary migration. Bull. Am. Assoc. Pet. Geol., 60: 213-244.

Schaar G. (1976) The occurrence of hydrocarbons in overpressured reservoirs of the Baram Delta (offshore Sarawak, Malaysia) Proceedings of the Indonesian Petroleum Assoc., 5th annual convention, June 1976, 163-169.

Shi, Y. and C. Y. Wang (1985) Pore pressure generation in sedimentary basins: overloading versus aquathermal. Dept. of Geol. and Geophys. University of California Berkeley.

Smith, J. E. (1971) The dynamics of shale compaction and the evolution of pore fluid pressures. Jour. Math Geol. 3: 329-263.

Snarsky, A. N. (1962) Die primare Migration des Erdols. Freiberger Forschungsh. C 123: 63-73.

Tissot, B. P., and R. Pelet (1971) Nouvelles donees sur les mecanismes de denese et de migration du petrole, simulation mathematique et application a la prospection. In: 8th World Petroleum Congress, Proc., 2: 35-46.

Tissot, B. P., and D. H. Welte (1984) Petroleum Formation and Occurrence, Springer-Verlag, Berlin, 699pp.

Ungerer, E., E. Behar, D. Discamps, (1981) Tentative calculation of the overall volume expansion of organic matter during hydrocarbon genesis from geochemistry data: implications for primary migration. In: Advances in Organic Geochemistry 1981, Bjoroy, M. (ed.), Chichester: Wiley, publ. 1983, 129-135.

Van Krevelen, D. W. (1961) Coal, Elsevier, Oxford, 514pp.

Wang, Z. (1985) Ultrasonic wave velocities in hydrocarbons, Stanford Rock Physics Project.

Zimmerman, R. W. (1985) The effect of pore structure on the pore and bulk compressibilities of consolidated sandstones. Ph.D. thesis, University of California, Berkeley.

Chapter 6: Test data

This chapter contains the full data set of confined uniaxial compressive strength tests and static and dynamic bulk modulus measurements performed on tight gas rocks.

6.1 Uniaxial compressive strength

Table 6.1 lists confined uniaxial compression test data from 16 tight gas sandstones and shales from GRI's cooperative wells in the Travis Peak Formation, East Texas. Measurements were performed by Science Applications International Corporation (Report No. P-9955-0275-0). Stress-strain curves and Mohr failure envelopes on the individual rocks are shown on the following pages, with rocks listed in the same order as in Table 6.1. Details of the experimental procedure and test results are discussed in Chapter 4. Columns listed in Table 6.1 are the following:

1 = Sample depth (feet)

2 = Clay by volume (%) (thin-section point count) * One measurement of clay volume fraction was made on the whole core at this depth. Clay volume fraction is listed next to each core for easier reference.

3 = Porosity (%)

4 = P_c, Confining pressure (MPa)

5 = P_d, Differential stress at failure (MPa)

6 = P_n, Normal stress (from Mohr circle) (MPa)

7 = P_s, Shear stress (from Mohr circle) (MPa)

8 = P-wave velocity (km/s) (at maximum hydrostatic confining pressure)

9 = S-wave velocity (km/s) (at maximum hydrostatic confining pressure)

10 = Young's modulus (GPa) (at 50 % of peak compressive strength)

11 = Poisson's ratio (at 50 % of peak compressive strength)

Table 6.1

1	2 *	3	4	5	6	7	8	9	10	11
Dep.	Clay	Por	P_c	P_d	P_n	P_s	V_p	V_s	E	ν
9980	12	1.05	0.	340.	17.	74.				
9980	12	0.77	15.	610.	70.	178.	3.91	2.69	39.00	0.190
9980	12	1.71	50.	775.	175.	285.			40.80	0.180
9980	12	1.24	100.	780.						
8368	6	2.96	0.	330.	41.	80.				
8368	6	6.69	15.	225.	40.	108.	3.05	2.30	22.50	0.180
8368	6	4.37	50.	575.	166.	230.	5.26		34.00	0.230
8368	6	6.17	100.	620.	227.	250.				
9975	3	4.50	0.	177.	10.	40.				
9975	3	5.32	15.	360.	40.	92.			31.00	0.090
9975	3	5.05	50.	650.	145.	229.	5.09	4.18	37.00	0.110
9975	3	4.36	100.	840.	245.	317.				
6897	3	9.39	0.	176.	16.	50.				
6897	3	9.49	15.	315.	61.	111.	3.33	2.38	31.00	0.090
6897	3	9.39	50.	485.	145.	193.			31.00	0.220
6897	3	8.88	100.	560.	260.	253.				
7077	11.5	12.60	0.	99.	5.	23.				
7077	11.5	11.19	15.				3.60	2.15	23.80	0.180
7077	11.5	13.23	50.	340.	65.	120.	3.65	2.17	23.80	0.180
7077	11.5	13.23	100.	390.	125.	154.				
8246	2	14.01	0.	125.	23.	48.				
8246	2	13.86	15.	125.	38.	48.	2.74	2.02	15.00	0.260
8246	2	13.95	50.	330.	110.	128.	4.58	3.06	26.00	0.260
8246	2	14.77	100.	430.	179.	166.				
5991	15.5	18.60	0.	47.	11.	20.				
5991	15.5	11.24	15.	235.	64.	96.	3.60	2.11	25.60	0.280
5991	15.5	15.63	50.	170.	88.	71.	3.73	2.35	13.80	0.300
5991	15.5	10.81	100.	260.	185.	133.				

1	2	3	4	5	6	7	8	9	10	11
Dep.	Clay	Por	P_c	P_d	P_n	P_s	V_p	V_s	E	ν
9763	20	5.09	0.	164.	30.	64.				
9763	20	3.93	15.	230.	58.	89.	4.73	3.06	25.00	0.175
9763	20	5.19	50.	425.	129.	165.	5.12	3.66	24.40	0.146
9763	20	4.84	100.	470.	187.	183.				
6853	31	5.57	0.	149.	29.	59.				
6853	31	6.25	15.	180.	50.	71.			23.30	0.170
6853	31	4.81	50.	310.	111.	123.	5.15	3.34	24.40	0.170
6853	31	4.93	100.	450.	188.	179.				
7053	38	5.24	0.	78.	17.	32.				
7053	38	5.12	15.	135.	45.	56.	4.60	2.64	15.80	0.140
7053	38	5.05	50.	230.	106.	104.	4.59	2.71	18.90	0.169
7053	38	5.45	100.	260.	172.	133.				
9898	41.5	3.38	0.	110.	23.	44.				
9898	41.5	3.15	15.	170.	50.	69.	3.49	2.52	25.00	0.210
9898	41.5	3.34	50.	275.	106.	111.			25.00	0.210
9898	41.5	3.21	100.	400.	182.	162.				
10151	52	3.89	0.	64.	11.	24.				
10151	52	5.11	15.	250.	57.	94.	4.15	3.31	23.80	0.260
10151	52	3.27	50.	240.	91.	90.	3.40	2.73	23.80	0.260
8675	56	5.77	0.	78.	18.	33.				
8675	56	5.94	15.	140.	48.	59.			14.00	0.200
8675	56	5.84	50.	223.	103.	95.	3.21	2.21	16.90	0.180
8675	56	5.68	100.	305.	172.	130.				
6275	63	4.60	0.	98.	23.	42.				
6275	63	4.58	15.	145.	50.	62.			32.00	0.170
6275	63	5.34	50.	202.	100.	90.	3.71	2.37	16.60	0.220
6275	63	5.36	100.	270.	177.	137.				
7074	8.5	7.04	0.	150.	31.	61.				
7074	8.5	7.15	15.	245.	66.	99.			23.80	0.310
7074	8.5	7.15	50.	300.	112.	122.	3.82	2.17	23.80	0.310
9666	9.2	9.39	0.	85.	15.	33.				
9666	9.2	9.17	15.	250.	60.	96.			26.30	0.290
9666	9.2	8.78	50.	255.	96.	98.	4.12	3.06	26.30	0.290

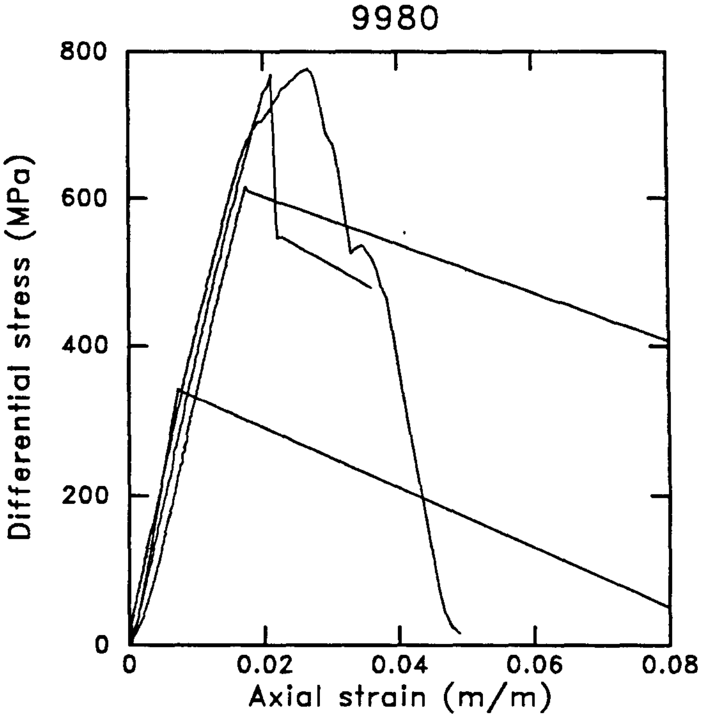

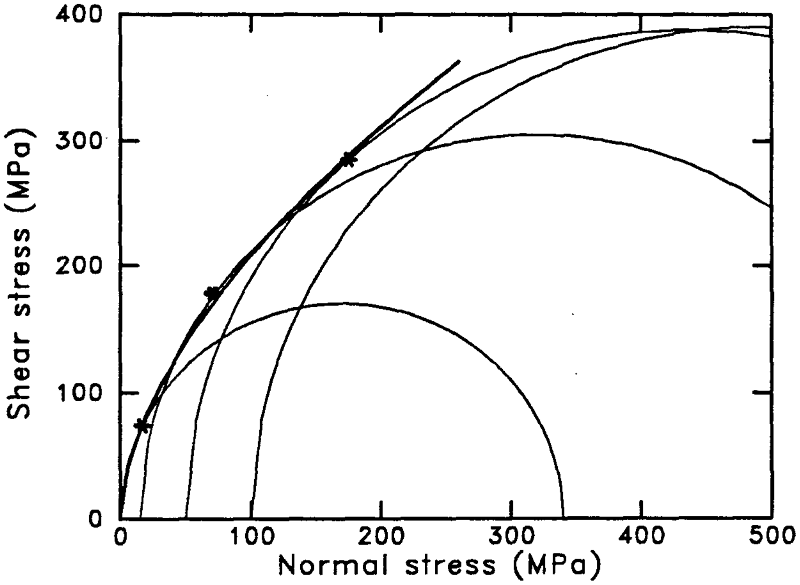

A.T. Mast 9980.0

P_c (MPa)	P_d (MPa)	Porosity (%)	Length (cm)	Comments
0.	340.	1.05	5.07	
15.	610.	0.77	4.99	
50.	775.	1.71	5.01	
100.	780.	1.24	5.09	Test loaded twice for larger load cell

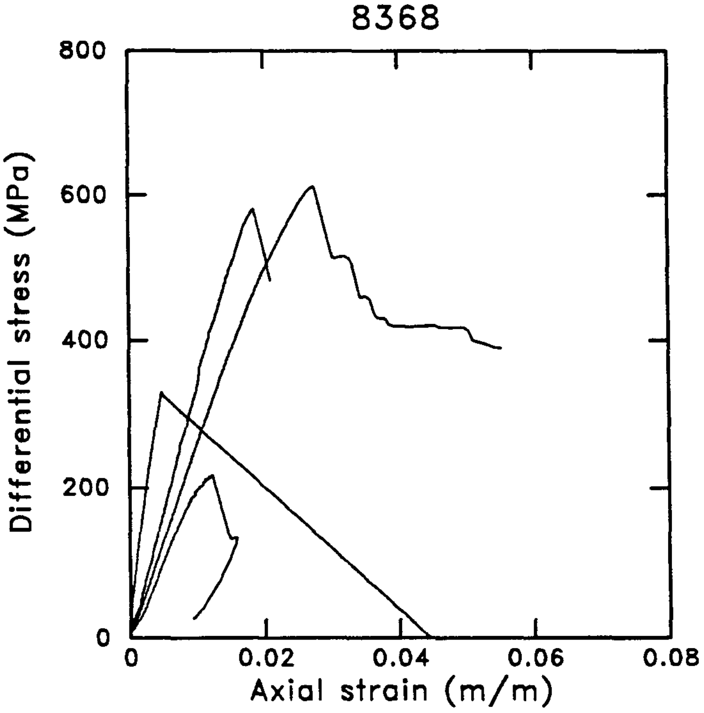

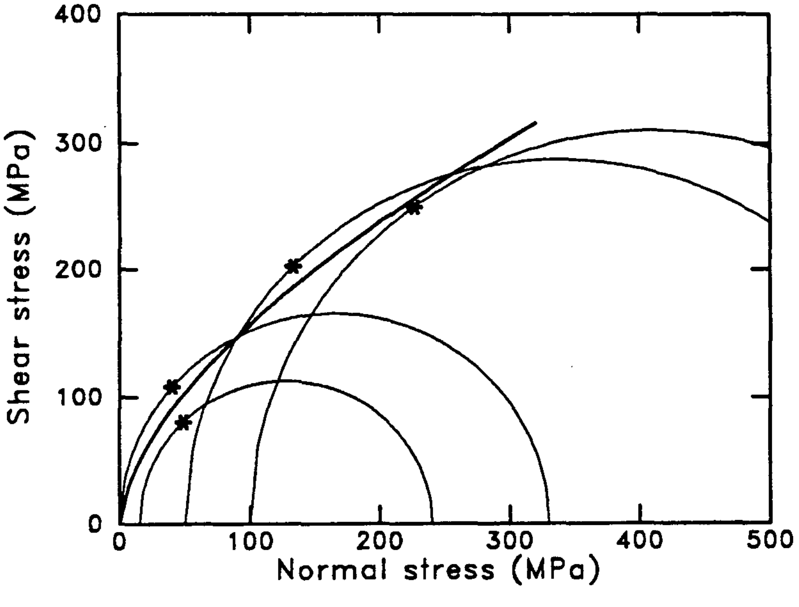

B.F. Phillips 8368.0

P_c (MPa)	P_d (MPa)	Porosity (%)	Length (cm)	Comments
0.	330.	2.96	5.01	
15.	225.	6.69	5.01	
50.	575.	4.37	5.01	
100.	620.	6.17	3.61	short

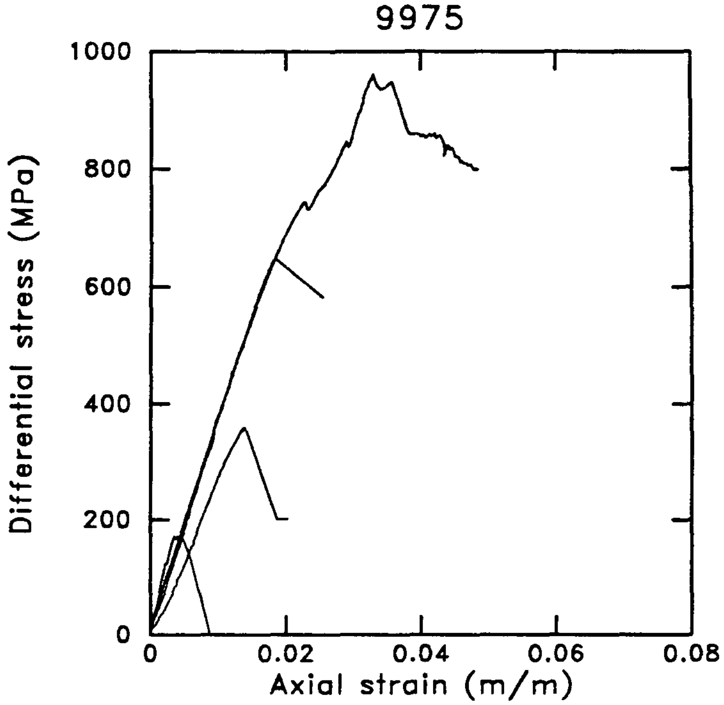

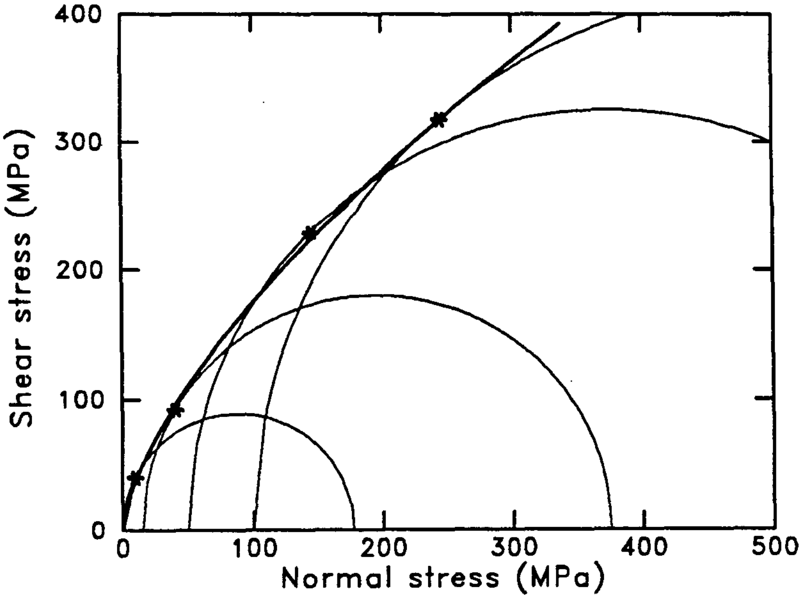

A.T. Mast 9975.0

P_c (MPa)	P_d (MPa)	Porosity (%)	Length (cm)	Comments
0.	177.	4.50	5.03	
15.	360.	5.32	4.58	
50.	650.	5.05	4.90	
100.	840.	4.36	4.91	nat. vertical fracture

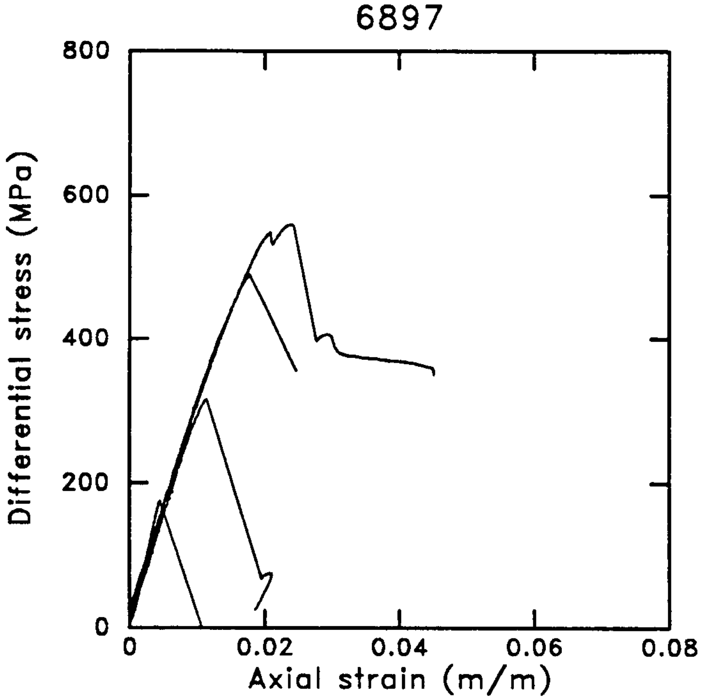

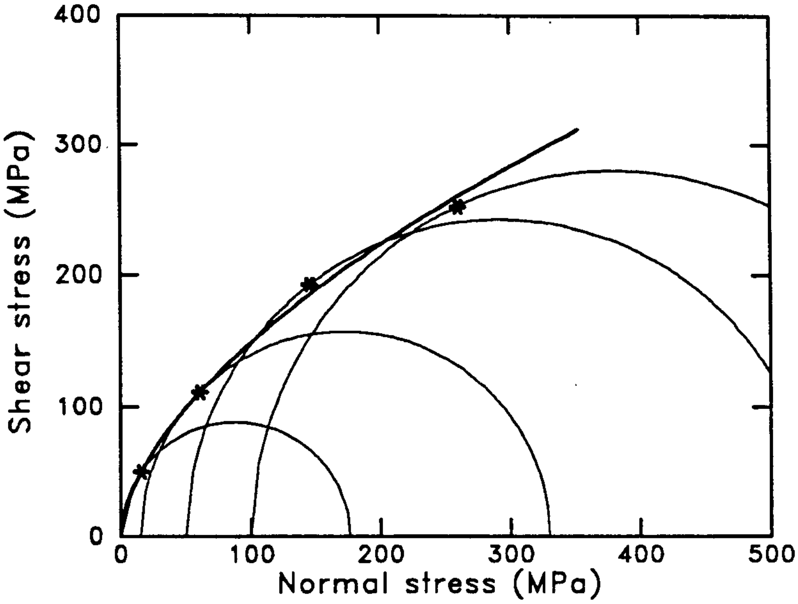

W. Sawmill 6897.0

P_c (MPa)	P_d (MPa)	Porosity (%)	Length (cm)	Comments
0.	176.	9.39	4.91	
15.	315.	9.49	5.01	
50.	485.	9.39	4.90	
100.	560.	8.88	5.04	nat. vert. fracture

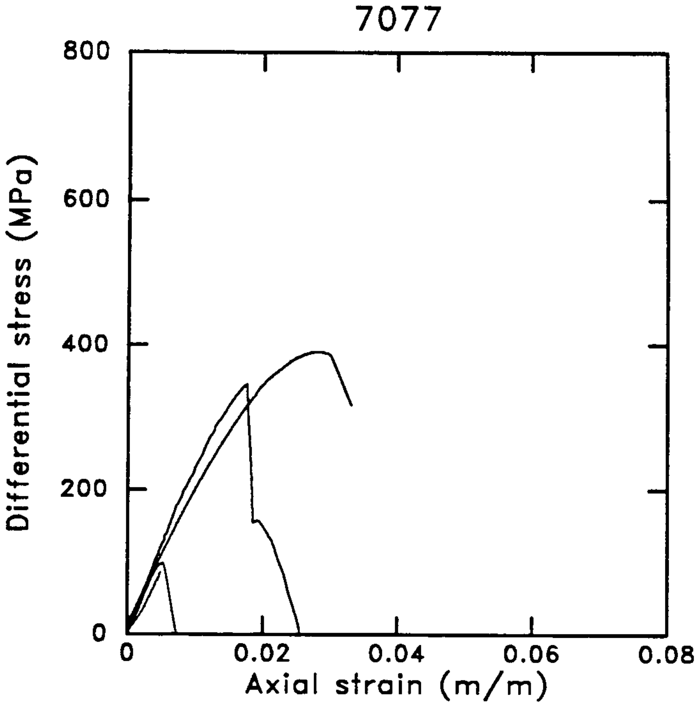

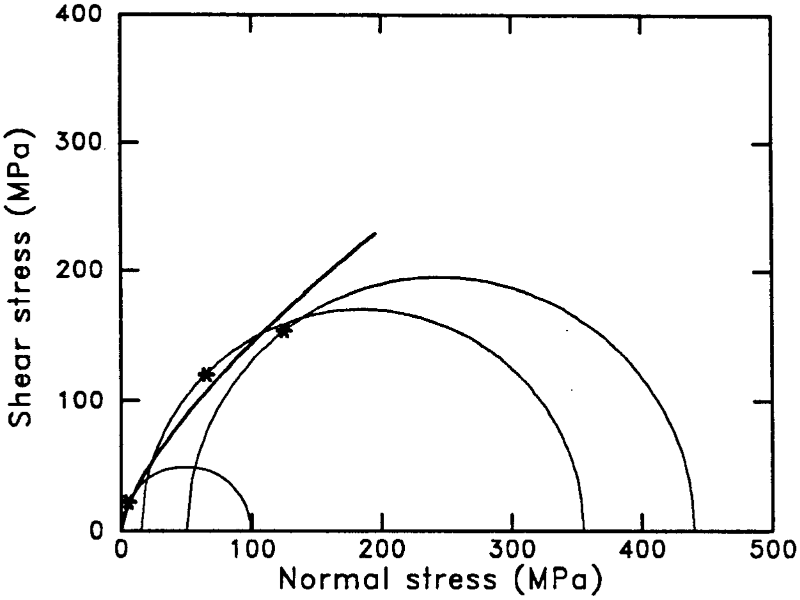

W. Sawmill 7077.0

P_c (MPa)	P_d (MPa)	Porosity (%)	Length (cm)	Comments
0.	99.	12.60	4.92	
15.		11.19	4.85	power failure
50.	340.	13.23	4.94	
100.	390.	13.23	3.88	

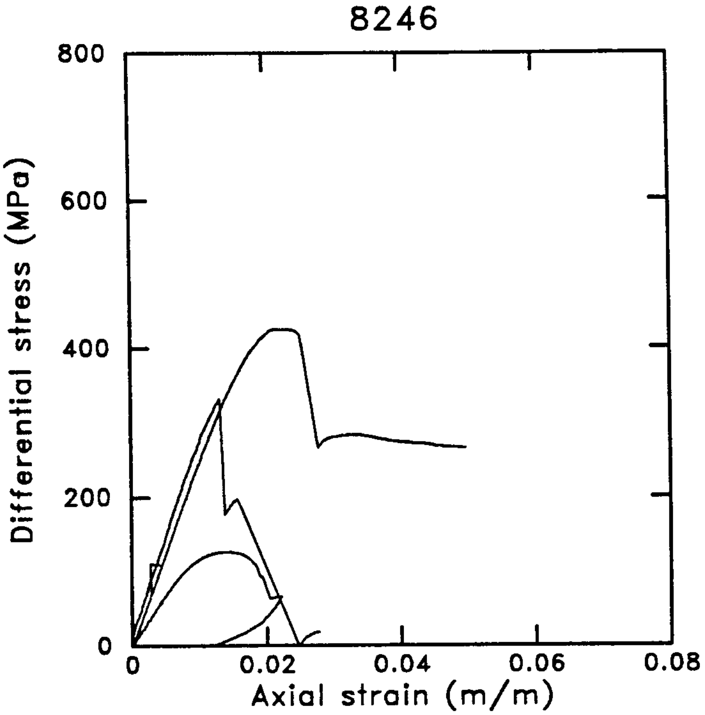

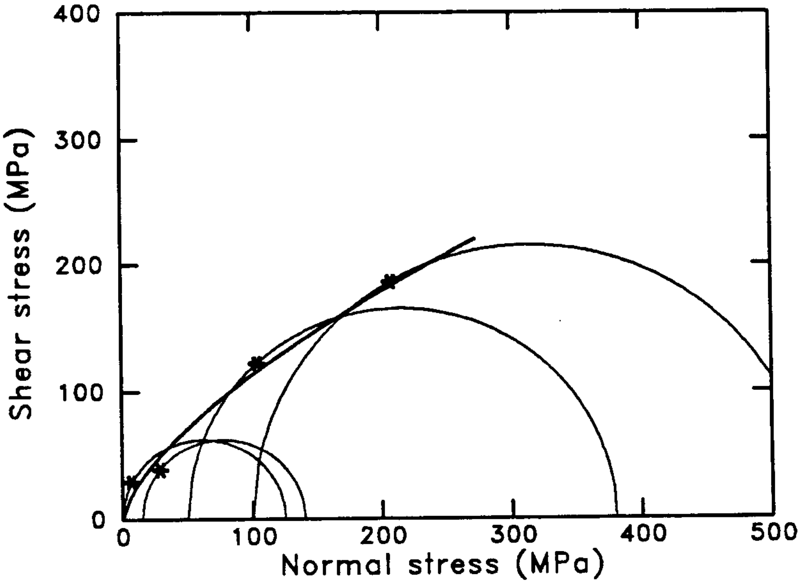

B.F. Phillips 8246.0

P_c (MPa)	P_d (MPa)	Porosity (%)	Length (cm)	Comments
0.	125.	14.01	4.91	
15.	125.	13.86	4.69	
50.	330.	13.95	4.83	minor core barrel
100.	430.	14.77	4.84	two natural fractures

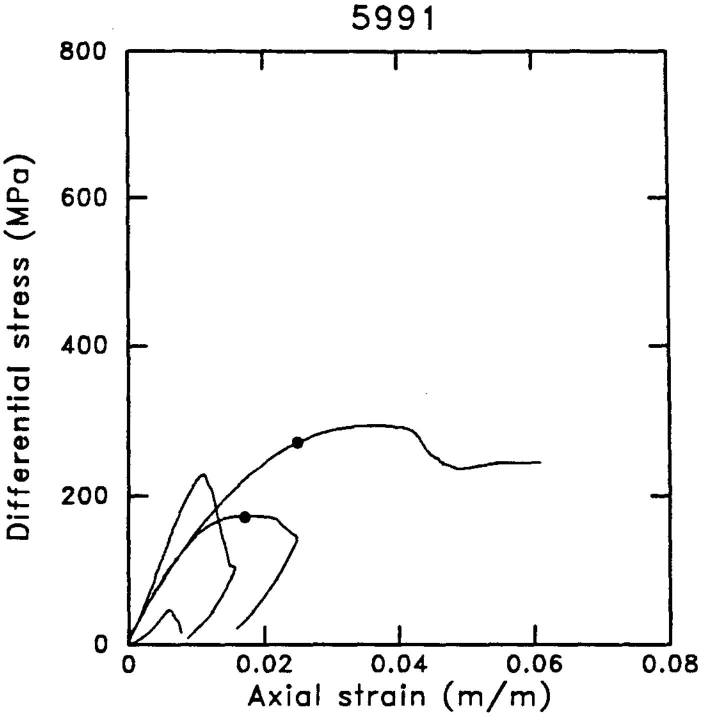

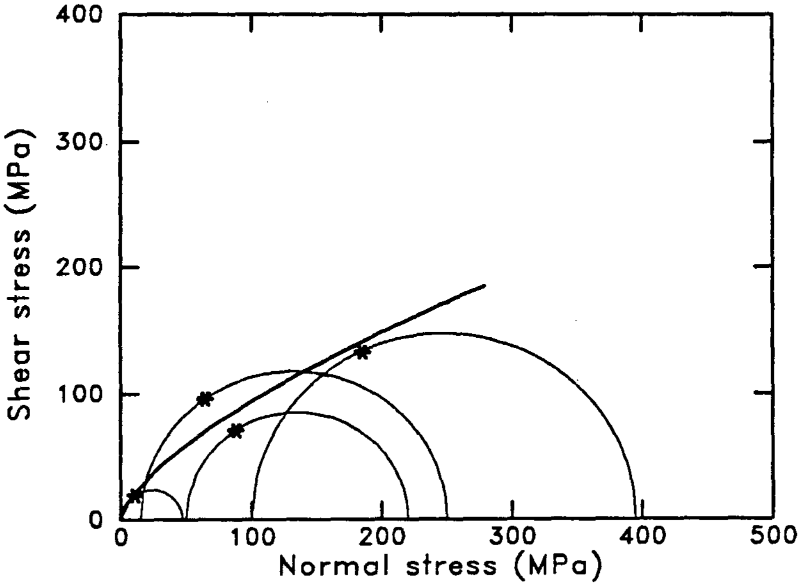

Howell 5 5991.0

P_c (MPa)	P_d (MPa)	Porosity (%)	Length (cm)	Comments
0.	47.	18.60	4.90	
15.	235.	11.24	4.63	
50.	170.	15.63	4.84	
100.	260.	10.81	4.91	

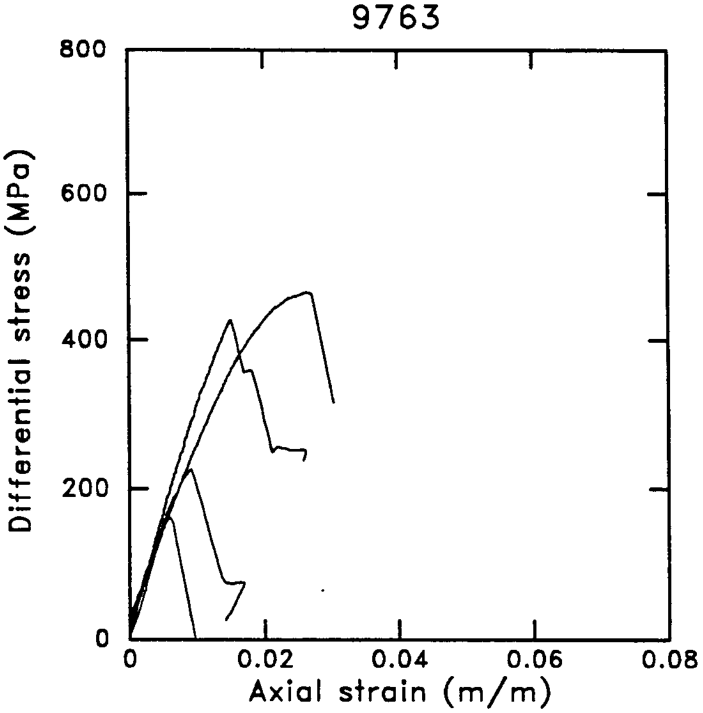

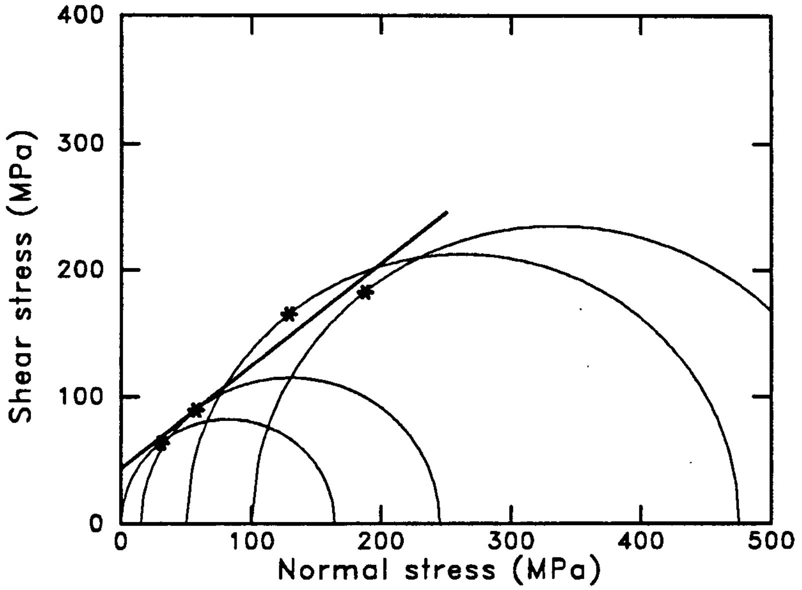

S.F.O.T 9763.0

P_c (MPa)	P_d (MPa)	Porosity (%)	Length (cm)	Comments
0.	164.	5.09	4.78	
15.	230.	3.93	4.99	
50.	425.	5.19	5.00	
100.	470.	4.84	4.77	two core barrel cuts

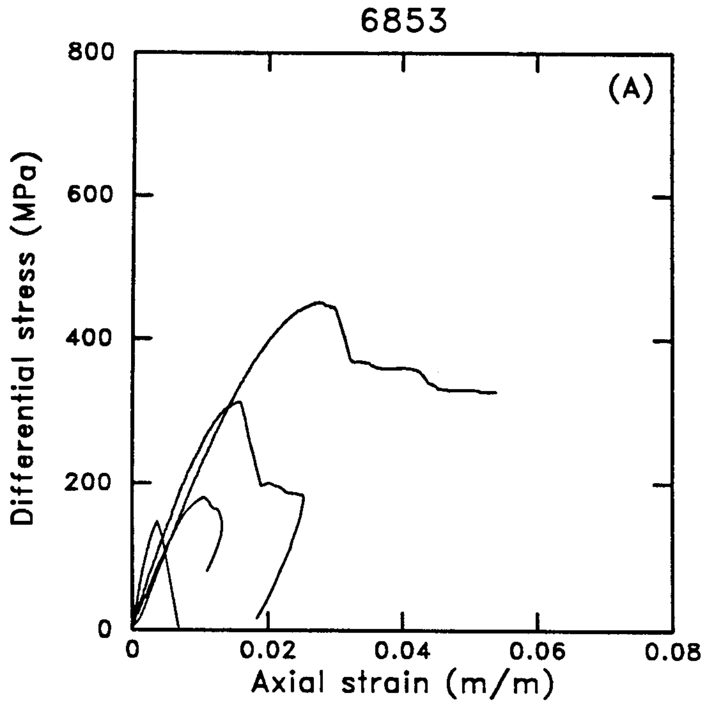

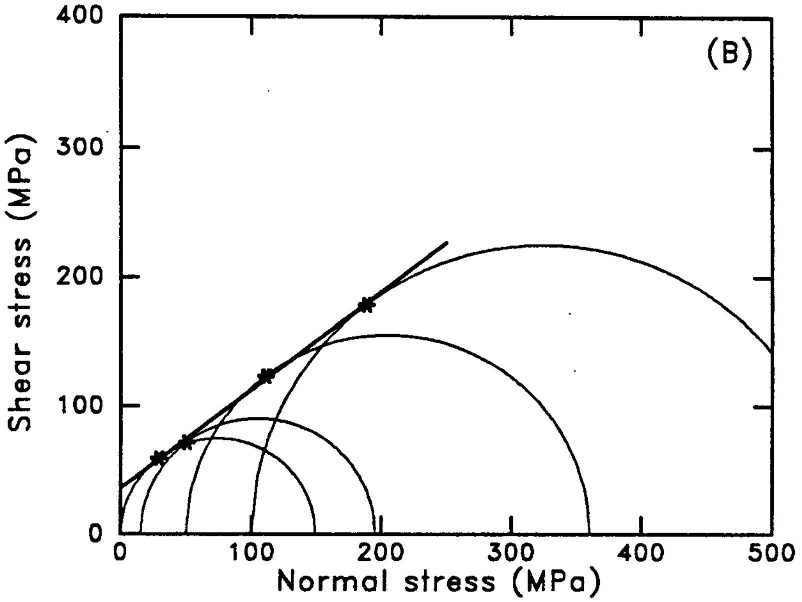

W. Sawmill 6853.0

P_c (MPa)	P_d (MPa)	Porosity (%)	Length (cm)	Comments
0.	149.	5.57	4.90	
15.	180.	6.25	4.78	
50.	310.	4.81	5.03	
100.	450.	4.93	3.42	short sample

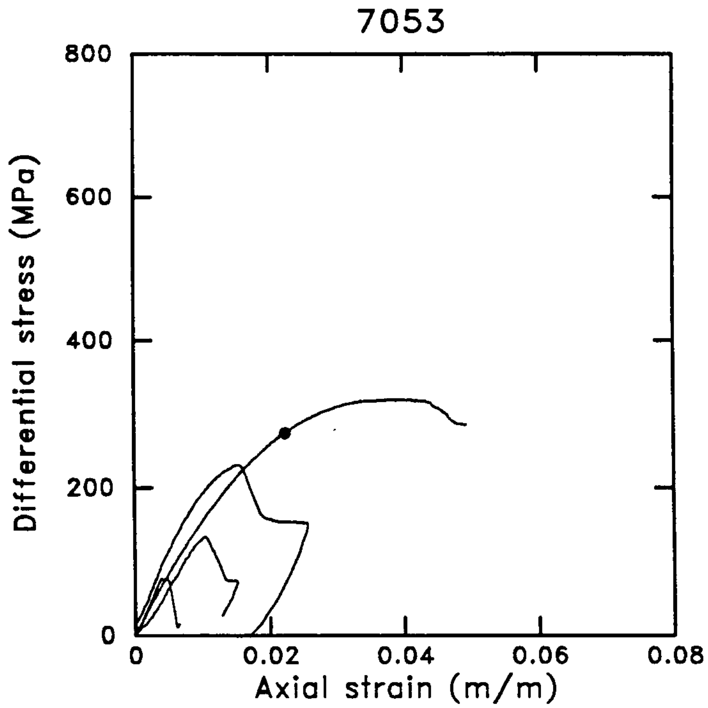

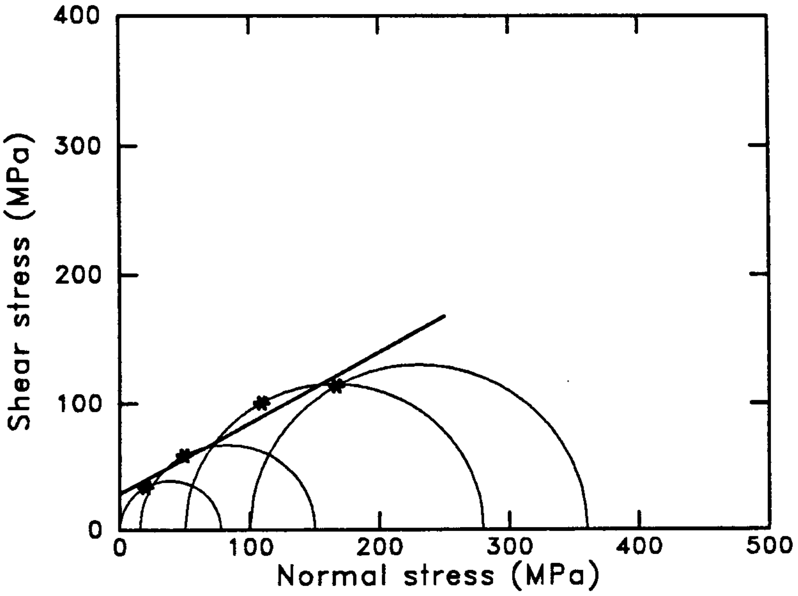

Sam Hughes 7053.0

P_c (MPa)	P_d (MPa)	Porosity (%)	Length (cm)	Comments
0.	78.	5.24	5.08	
15.	135.	5.12	4.82	
50.	230.	5.05	4.90	
100.	260.	5.45	2.69	v. short sample

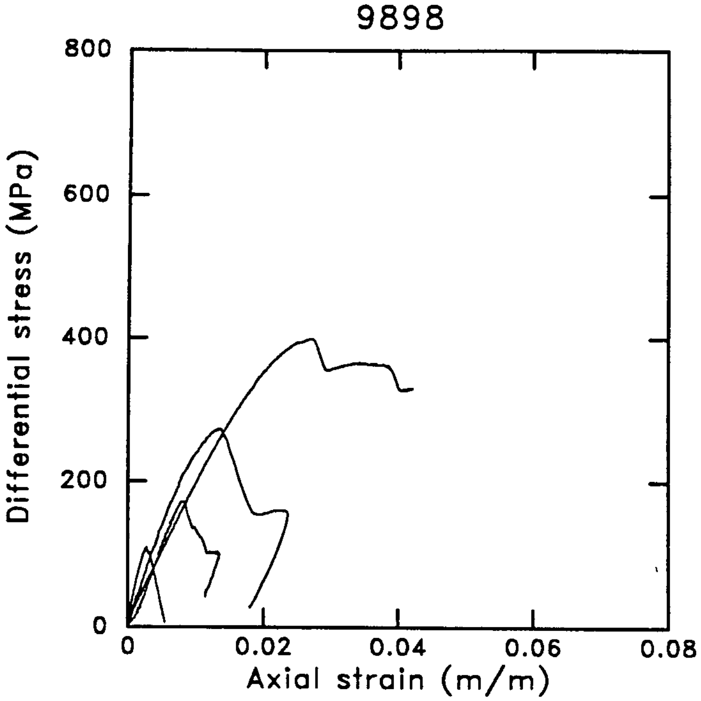

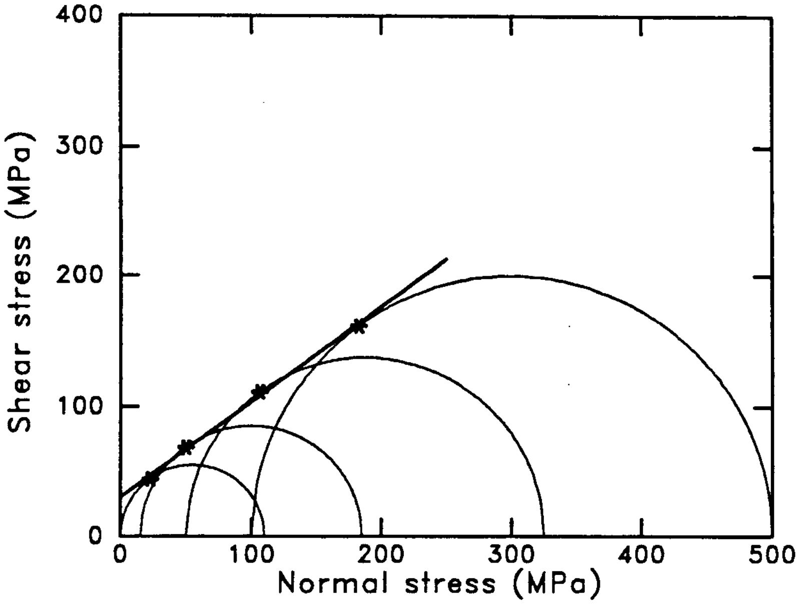

S.F.E. 2 9898.0

P_c (MPa)	P_d (MPa)	Porosity (%)	Length (cm)	Comments
0.	110.	3.38	3.73	short
15.	170.	3.15	4.76	
50.	275.	3.34	4.76	very short
100.	400.	3.21	2.69	

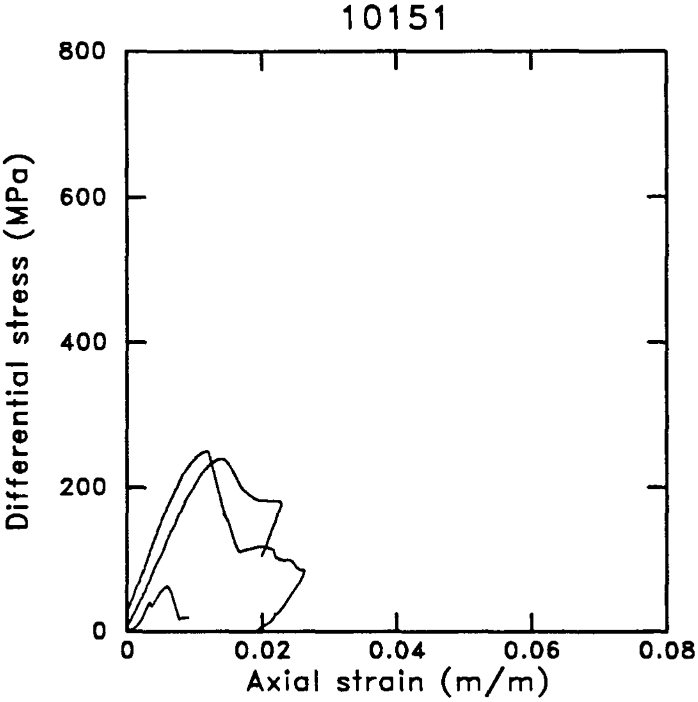

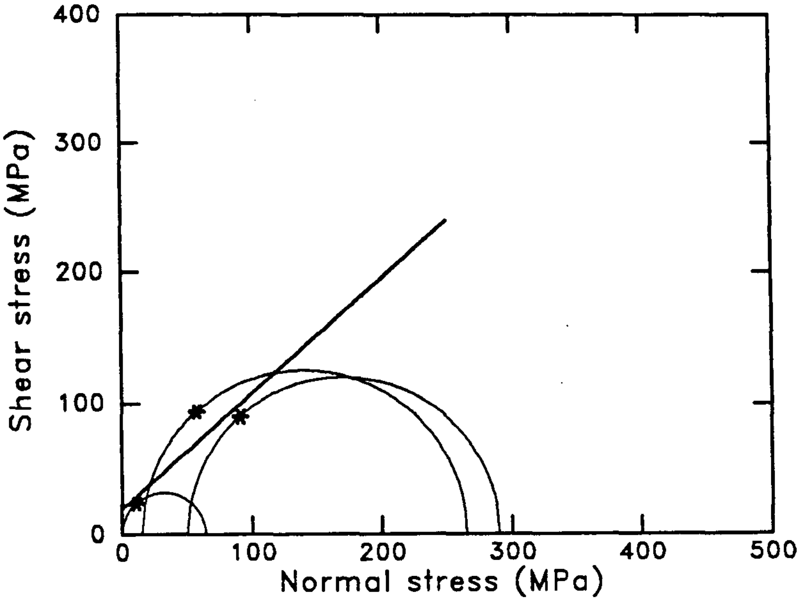

S.F.O.T 10151.0

P_c (MPa)	P_d (MPa)	Porosity (%)	Length (cm)	Comments
0.	64.	3.89	3.78	short
15.	250.	5.11	4.90	
50.	240.	3.27	4.22	low angle hairline fract

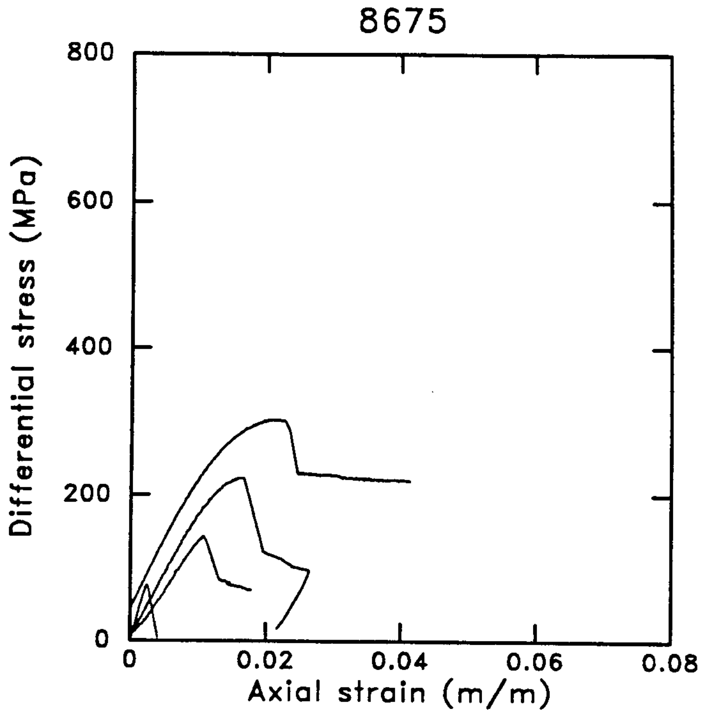

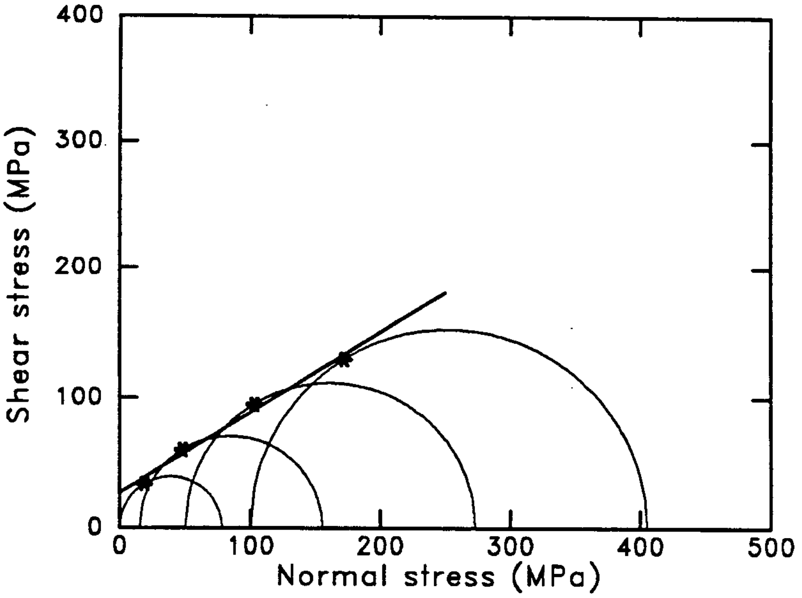

A.T. Mast 8675.0

P_c (MPa)	P_d (MPa)	Porosity (%)	Length (cm)	Comments
0.	78.	5.77	5.06	
15.	140.	5.94	3.77	sample re-cut and ground
50.	223.	5.84	4.92	
100.	305.	5.68	4.95	vert. fract. prior to test

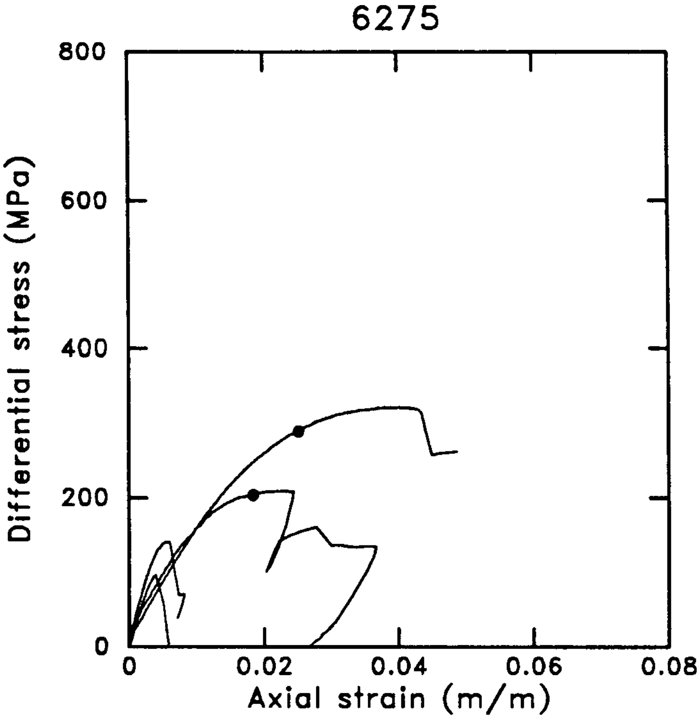

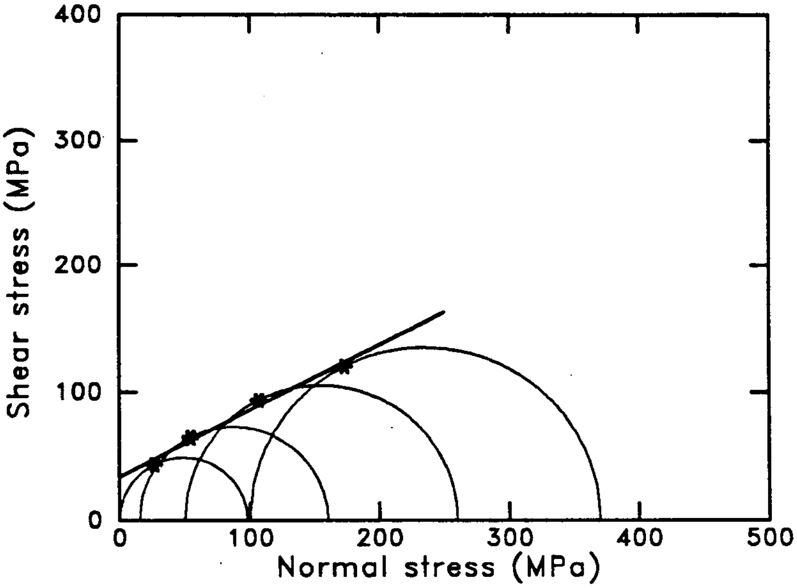

Howell 5 6275.0

P_c (MPa)	P_d (MPa)	Porosity (%)	Length (cm)	Comments
0.	98.	9.39	4.81	
15.	145.	9.17	4.64	
50.	202.	8.78	5.04	
100.	270.	0.00	3.26	out of round .043 cm

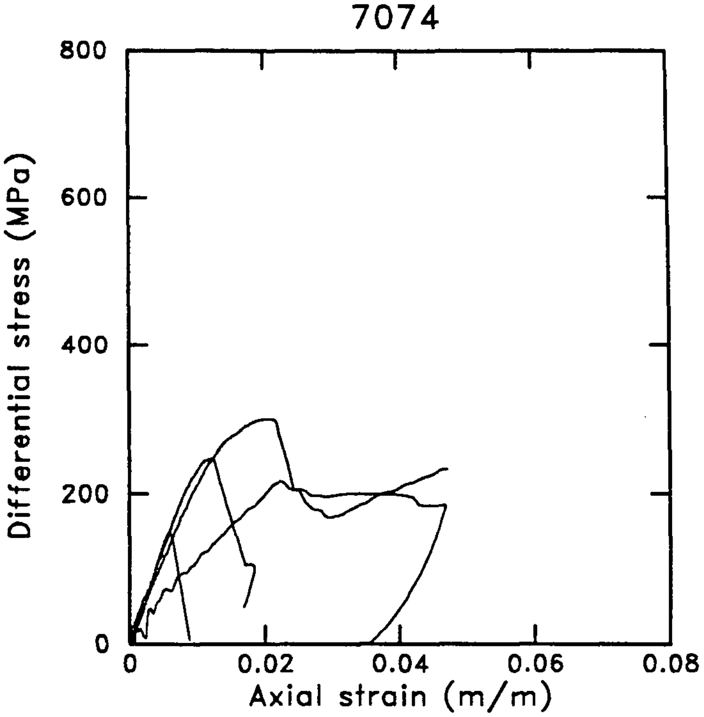

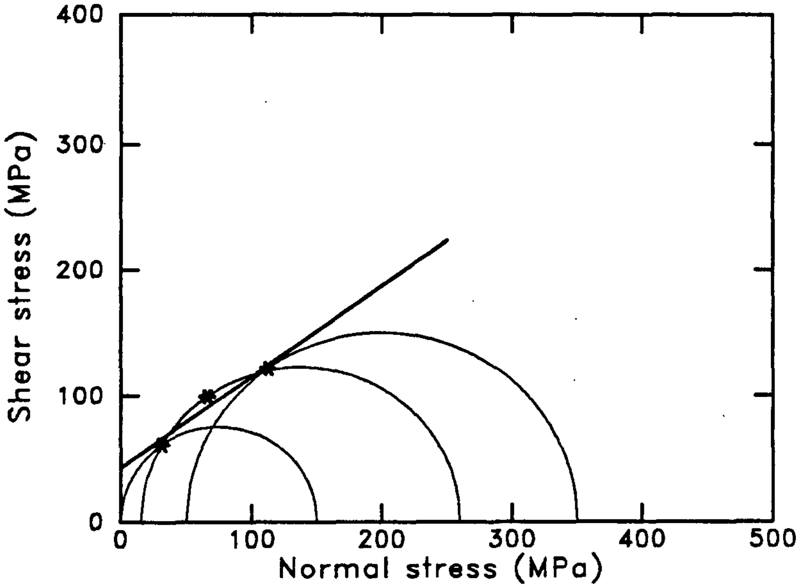

W. Sawmill 7074.0

P_c (MPa)	P_d (MPa)	Porosity (%)	Length (cm)	Comments
0.	150.	7.04	4.95	core barrel cut out
15.	245.	7.15	4.85	
50.	300.	7.15	5.04	
100.		7.15	4.89	horiz. fracture

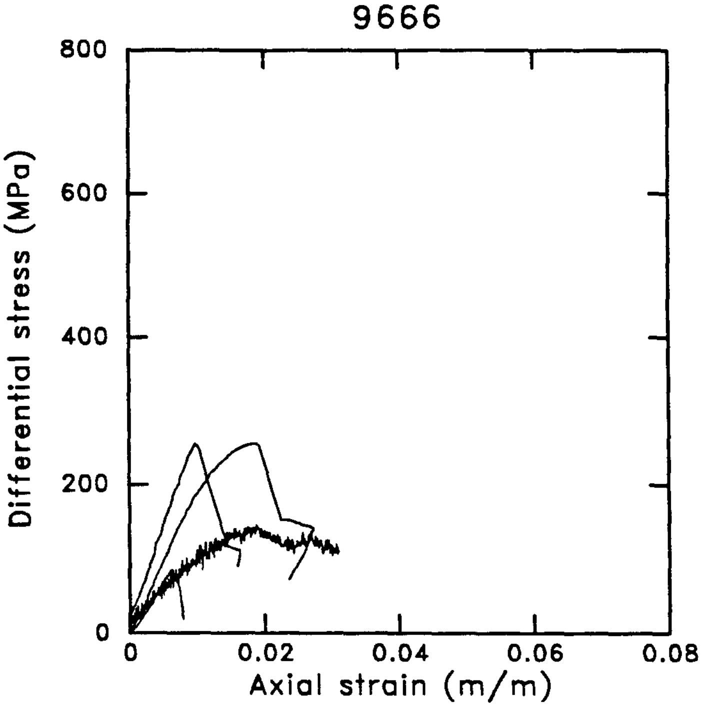

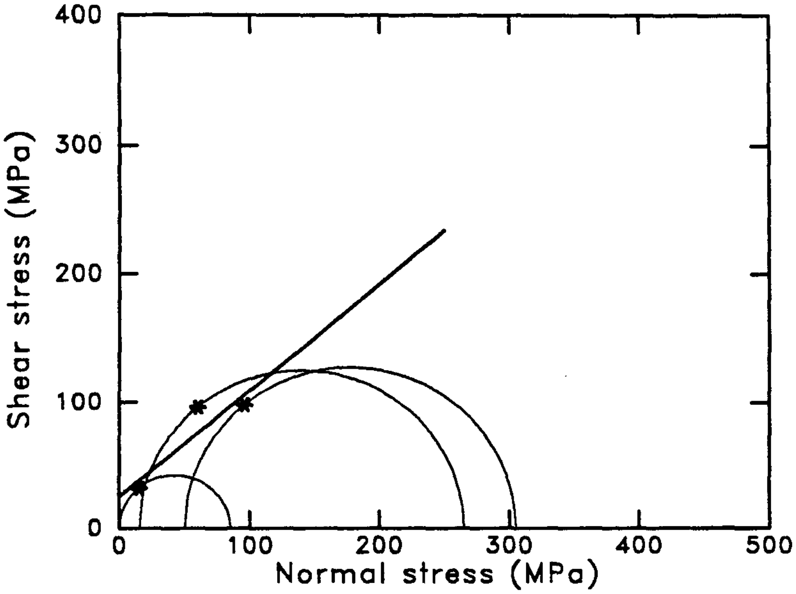

S.F.O.T. 9666.0

P_c (MPa)	P_d (MPa)	Porosity (%)	Length (cm)	Comments
0.	85.	9.39	5.03	
15.	250.	9.17	5.00	
50.	255.	8.78	5.00	
100.		6.74	5.04	nat. vert. fracture

6.2 Static and dynamic moduli

In this section we present the test data on static and dynamic bulk modulus performed by New England Research Incorporated. The samples consist of 43 tight gas sandstones and shales from GRI's cooperative wells in the Travis Peak Formation in East Texas. Table 6.2 lists core depth, porosity, grain density, and petrographic data. Porosity is a helium measurement at 15-28 MPa confining pressure. Framework (authigenic) clay, matrix (detrital) clay, dolomite, and ankerite are expressed as volume percentages from thin-section point count. Total clay is the sum of framework and matrix clay. Data on individual rock samples on the pages that follow are listed in the same order as shown in Table 6.2.

For information on geology of these rocks, see Dutton and Finley (1986) referenced in Chapter 2. Detailed information on porosity, grain density, and petrographic data measurements may be found in data sources listed in the references in Chapter 2. Experimental details of static and dynamic measurements are described in Chapter 3.

Symbols used:

P_c = Confining pressure (MPa)

ϵ_{vol} = Volumetric strain (mstr = 10^3 m/m in table)

K_{stat} = Static bulk modulus (GPa)

K_{dyn} = Dynamic bulk modulus (GPa)

V_p = P-wave velocity (km/s)

V_s = S-wave velocity (km/s)

V_p / V_s = Ratio of P to S-wave velocity

G_{dyn} = Dynamic shear modulus (GPa)

σ_{dyn} = Dynamic Poisson's ratio

Table 6.2

Well	Depth (feet)	Porosity (%)	Grain Density (g/cm^3)	Framework Clay (%)	Matrix Clay (%)	Dolomite (%)	Ankerite (%)
S.F.O.T.	10135.0	3.38	2.64	0.8	0.0	0.8	0.0
S.F.O.T.	10139.0	2.75	2.66	0.0	65.5	0.0	0.0
S.F.O.T.	10151.0	0.70	2.68	0.0	52.0	0.0	1.0
Howell 5	5991.0	12.40	2.58	5.5	10.5	0.5	1.0
W. Sawmill	6053.0	4.26	2.60	0.0	31.0	3.0	6.0
Howell 5	6189.0	13.82	2.64	1.0	2.0	0.0	0.0
Howell 5	6275.0	1.45	2.62	0.0	63.0	0.0	0.5
W. Sawmill	6598.0	8.91	2.61	10.5	11.5	0.0	0.5
Sam Hughes	6838.0	1.17	2.67	0.8	22.8	10.0	9.6
Sam Hughes	6841.0	4.45	2.64	8.8	11.2	0.4	0.8
W. Sawmill	6897.0	9.25	2.63	2.0	1.0	5.0	2.5
Sam Hughes	7053.0	1.57	2.63	0.0	38.0	0.0	0.0
Sam Hughes	7057.0	1.63	2.62	0.0	38.8	1.6	0.0
W. Sawmill	7074.0	3.73	2.65	0.0	9.0	48.5	13.0
W. Sawmill	7077.0	9.99	2.56	1.0	10.5	2.0	1.5
Sam Hughes	7096.0	8.04	2.63	7.6	2.4	0.0	0.0
B.F. Phillips	8189.0	6.75	2.64	4.0	3.0	0.0	0.0
B.F. Phillips	8195.0	7.02	2.67	6.0	20.0	0.0	0.0
B.F. Phillips	8227.0	5.56	2.70	0.4	54.8	6.4	3.6
B.F. Phillips	8246.0	14.31	2.64	2.0	0.0	0.0	0.0
B.F. Phillips	8368.0	3.84	2.65	0.0	6.0	0.0	0.0
B.F. Phillips	8382.0	7.91	2.64	7.0	3.0	0.0	0.0
B.F. Phillips	8385.0	5.36	2.64	2.0	3.0	0.0	1.0
A.T. Mast	8628.0	10.42	2.63	6.4	1.2	0.4	0.0
A.T. Mast	8634.0	0.76	2.64	0.0	0.0	36.4	9.6
A.T. Mast	8642.0	3.56	2.65	0.4	0.0	.4	1.2
A.T. Mast	8666.0	4.47	2.68	0.0	3.0	0.0	19.0
A.T. Mast	8672.0	2.0	2.66	2.0	0.0	.4	1.2
A.T. Mast	8674.0	0.98	2.70	12.4	3.2	18.4	2.8
A.T. Mast	8675.0	1.97	2.66	0.0	56.0	0.0	2.0
A.T. Mast	9170.0	1.11	2.68	0.0	43.0	0.0	30.0
S.F.O.T	9665.0	5.30	2.69	0.0	0.0	50.0	50.0
S.F.O.T	9666.0	5.21	2.69	0.0	0.0	0.0	50.0
S.F.O.T	9733.0	3.01	2.66	6.0	9.0	0.0	14.0
S.F.O.T	9736.0	2.58	2.67	0.4	0.4	10.8	6.0
S.F.O.T	9747.0	4.04	2.67	11.0	8.0	1.0	69.0
S.F.O.T	9750.0	3.75	2.65	0.0	0.0	0.8	2.0
A.T. Mast	9753.0	4.51	2.66	0.8	0.0	15.2	3.2
S.F.O.T	9754.0	6.94	2.68	6.0	0.0	0.0	11.0
S.F.O.T	9756.0	6.14	2.65	10.0	0.0	0.0	2.0
S.F.O.T	9763.0	3.45	2.66	1.0	19.0	0.0	13.0
S.F.E. 2	9898.0	1.63	2.70	0.0	41.5	0.0	0.0
A.T. Mast	9975.0	2.95	2.67	2.0	0.0	0.0	0.0

Depth (feet) = 10135.0
Length (cm) = 3.78
Grain density (g/cm^3) = 2.64
Porosity (%) = 3.4

Petrographic data:
framework clay= 0.8
matrix clay = 0.0
ankerite = 0.0
dolomite = 0.8

Strain, Static Bulk Moduli, and Dry Velocities

P_c (MPa)	ϵ_{vol} (mstr)	K_{stat} (GPa)	K_{dyn} (GPa)	V_p (km/s)	V_s (km/s)	V_p/V_s	G_{dyn} (GPa)	σ_{dyn}
5.	0.35	12.65	16.81	4.260	2.961	1.44	22.80	0.033
10.	0.78	12.63	18.68	4.420	3.044	1.45	24.11	0.049
20.	1.54	14.25	21.89	4.719	3.224	1.46	27.06	0.062
40.	2.69	20.57	27.24	5.173	3.497	1.48	31.85	0.079
75.	4.08	29.13	31.79	5.497	3.678	1.49	35.27	0.095
125.	5.63	32.56	33.88	5.604	3.717	1.51	36.07	0.107
125.	5.61	36.01	33.84	5.611	3.722	1.51	36.03	0.107
75.	4.20	32.92	32.31	5.537	3.697	1.50	35.50	0.098
40.	3.06	24.29	29.75	5.356	3.595	1.49	33.54	0.090
20.	2.07	15.86	25.66	5.028	3.397	1.48	29.94	0.080
10.	1.35	11.88	22.00	4.713	3.209	1.47	26.70	0.068
5.	0.89	11.54	19.19	4.478	3.081	1.45	24.60	0.051

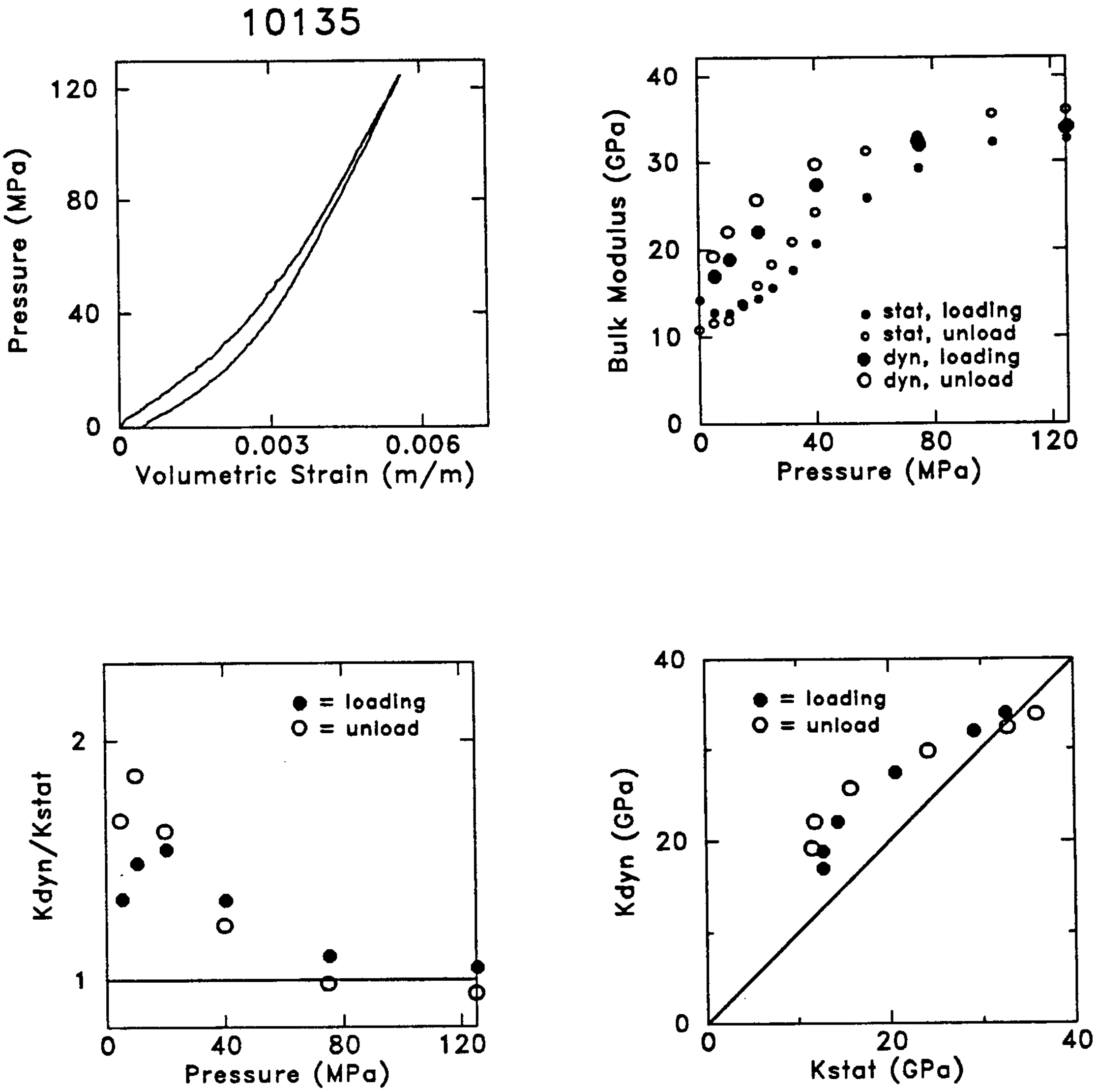
10135
Pressure (MPa)
120
80
40
0
0
0.003
0.006
Volumetric Strain (m/m)
Bulk Modulus (GPa)
40
30
20
10
0
0
40
80
120
Pressure (MPa)
● stat, loading
○ stat, unload
● dyn, loading
○ dyn, unload
Kdyn/Kstat
2
1
0
40
80
120
Pressure (MPa)
● = loading
○ = unload
Kdyn (GPa)
40
20
0
0
20
40
Kstat (GPa)
● = loading
○ = unload

Depth (feet) = 10139.0
Length (cm) = 3.80
Grain density (g/cm^3) = 2.66
Porosity (%) = 2.8

Petrographic data:
framework clay= 0.0
matrix clay = 65.5
ankerite = 0.0
dolomite = 0.0

Strain, Static Bulk Moduli, and Dry Velocities

P_c (MPa)	ϵ_{vol} (mstr)	K_{stat} (GPa)	K_{dyn} (GPa)	V_p (km/s)	V_s (km/s)	V_p/V_s	G_{dyn} (GPa)	σ_{dyn}
5.	0.53	10.12	19.97	4.189	2.728	1.54	19.50	0.132
10.	0.97	12.35	22.81	4.383	2.807	1.56	20.65	0.152
20.	1.64	17.11	25.46	4.552	2.873	1.58	21.65	0.169
40.	2.57	24.22	27.06	4.675	2.942	1.59	22.72	0.172
75.	3.89	28.18	28.88	4.812	3.020	1.59	23.95	0.175
125.	5.58	29.39	29.54	4.905	3.101	1.58	25.29	0.167
125.	5.55	30.16	29.50	4.912	3.106	1.58	25.26	0.167
75.	3.89	27.79	29.31	4.862	3.053	1.59	24.38	0.174
40.	2.61	25.30	28.20	4.776	3.003	1.59	23.56	0.173
20.	1.77	19.93	26.96	4.682	2.949	1.59	22.71	0.171
10.	1.20	14.00	25.81	4.591	2.897	1.58	21.91	0.169
5.	0.80	9.72	24.48	4.483	2.834	1.58	20.96	0.167

10139

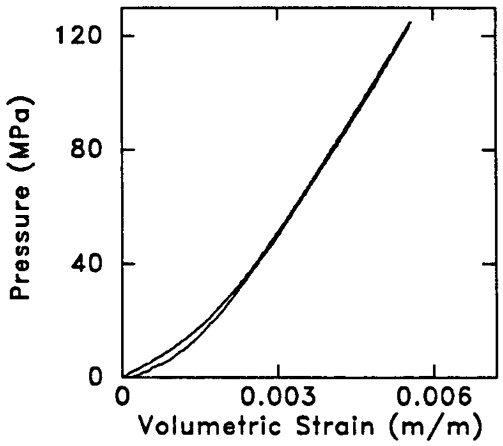
Pressure (MPa)
120
80
40
0
0
0.003
0.006
Volumetric Strain (m/m)

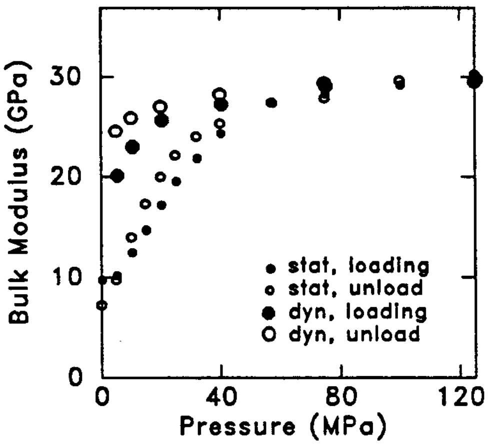
Bulk Modulus (GPa)
30
20
10
0
0
40
80
120
Pressure (MPa)
• stat, loading
∘ stat, unload
● dyn, loading
○ dyn, unload

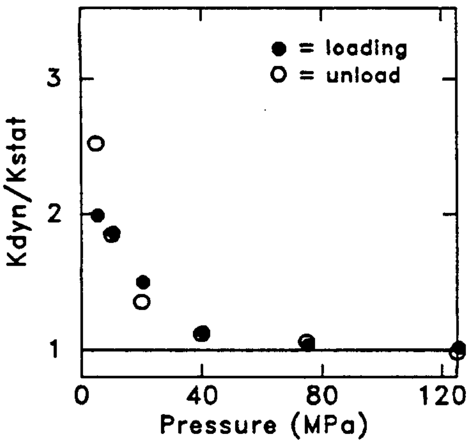
Kdyn/Kstat
3
2
1
0
40
80
120
Pressure (MPa)
● = loading
○ = unload

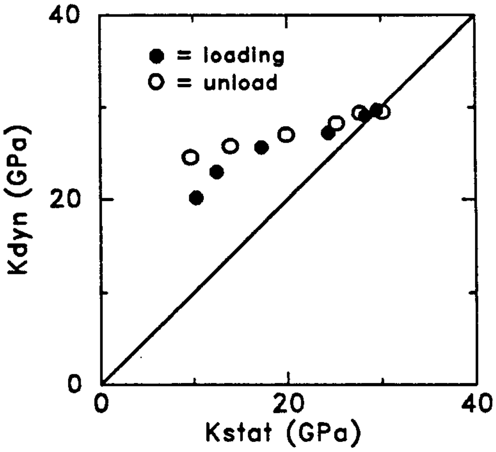
Kdyn (GPa)
40
20
0
0
20
40
Kstat (GPa)
● = loading
○ = unload

Depth (feet) = 10151.0
Length (cm) = 4.79
Grain density (g/cm^3) = 2.68
Porosity (%) = 0.8

Petrographic data:
framework clay= 0.0
matrix clay = 52.0
ankerite = 1.0
dolomite = 0.0

Strain, Static Bulk Moduli, and Dry Velocities

P_c (MPa)	ϵ_{vol} (mstr)	K_{stat} (GPa)	K_{dyn} (GPa)	V_p (km/s)	V_s (km/s)	V_p/V_s	G_{dyn} (GPa)	σ_{dyn}
5.	0.51	16.03	24.59	4.393	2.767	1.59	20.69	0.171
10.	0.81	18.01	25.02	4.421	2.779	1.59	20.89	0.173
20.	1.33	18.05	25.83	4.470	2.798	1.60	21.19	0.178
40.	2.46	17.79	27.27	4.547	2.823	1.61	21.61	0.187
75.	4.36	19.96	30.13	4.697	2.871	1.64	22.43	0.202
125.	6.50	23.62	33.40	4.865	2.928	1.66	23.41	0.216
125.	6.55	30.15	33.40	4.865	2.928	1.66	23.41	0.216
75.	4.86	25.13	31.59	4.781	2.906	1.65	22.99	0.207
40.	3.34	20.18	29.42	4.666	2.864	1.63	22.28	0.198
20.	2.27	16.26	27.51	4.562	2.829	1.61	21.69	0.188
10.	1.60	15.65	26.18	4.491	2.806	1.60	21.33	0.180
5.	1.30	14.43	25.46	4.450	2.792	1.59	21.10	0.175

10151

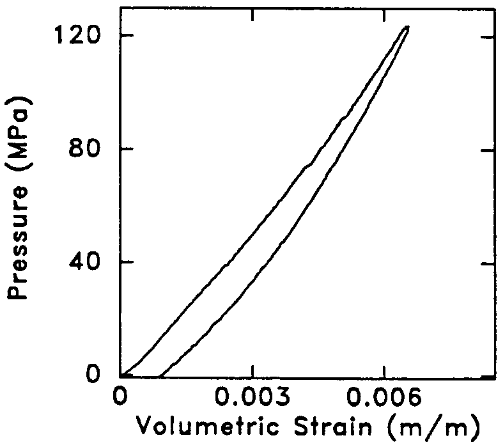
Pressure (MPa)
0
40
80
120
Volumetric Strain (m/m)
0
0.003
0.006

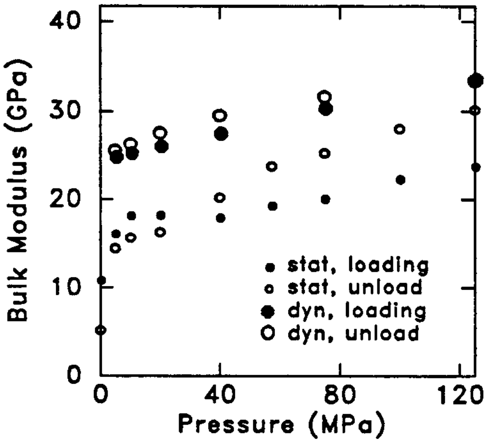
Bulk Modulus (GPa)
0
10
20
30
40
Pressure (MPa)
0
40
80
120
• stat, loading
∘ stat, unload
● dyn, loading
○ dyn, unload

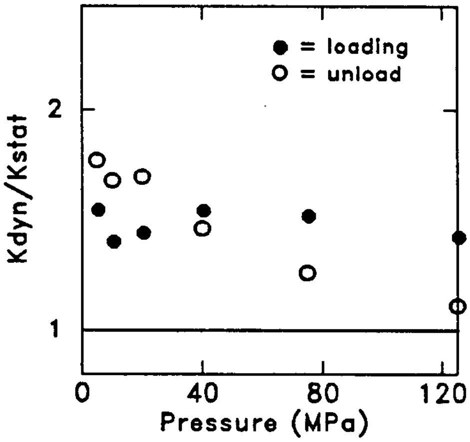
Kdyn/Kstat
1
2
Pressure (MPa)
0
40
80
120
● = loading
○ = unload

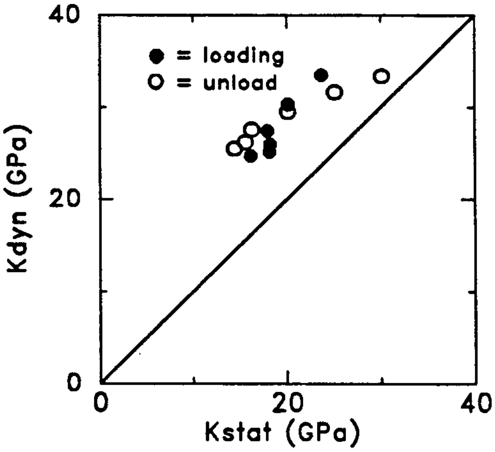
Kdyn (GPa)
0
20
40
Kstat (GPa)
0
20
40
● = loading
○ = unload

Depth (feet) = 5991.0
Length (cm) = 4.30
Grain density (g/cm^3) = 2.58
Porosity (%) = 12.5

Petrographic data:
framework clay= 5.5
matrix clay = 10.5
ankerite = 1.0
dolomite = 0.5

Strain, Static Bulk Moduli, and Dry Velocities

P_c (MPa)	ϵ_{vol} (mstr)	K_{stat} (GPa)	K_{dyn} (GPa)	V_p (km/s)	V_s (km/s)	V_p/V_s	G_{dyn} (GPa)	σ_{dyn}
5.	1.19	4.59	15.44	3.683	2.396	1.54	14.98	0.133
10.	2.36	5.10	17.86	3.896	2.502	1.56	16.37	0.149
20.	3.94	6.65	20.80	4.197	2.695	1.56	19.04	0.149
40.	6.43	9.61	24.22	4.562	2.951	1.55	22.93	0.140
75.	9.43	12.79	26.52	4.831	3.160	1.53	26.42	0.126
125.	13.07	13.36	28.52	4.993	3.264	1.53	28.34	0.127
125.	13.04	17.40	28.54	4.992	3.264	1.53	28.35	0.127
75.	10.14	14.37	26.68	4.868	3.197	1.52	27.08	0.121
40.	7.41	10.96	24.49	4.660	3.053	1.53	24.59	0.124
20.	5.33	7.77	21.50	4.371	2.863	1.53	21.54	0.124
10.	3.94	5.72	19.13	4.118	2.692	1.53	19.00	0.127
5.	2.93	4.33	16.99	3.892	2.548	1.53	16.99	0.125

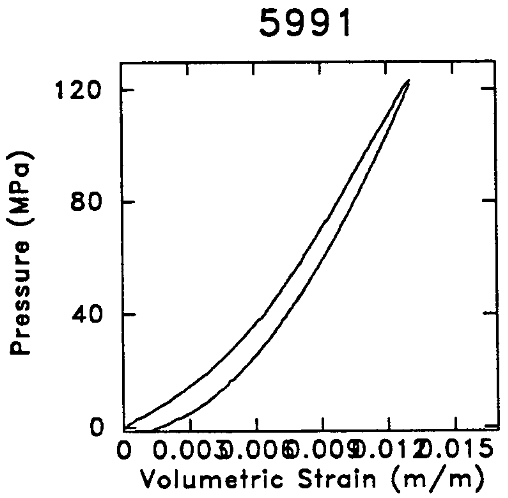
5991
Pressure (MPa)
120
80
40
0
0
0.003
0.006
0.009
0.012
0.015
Volumetric Strain (m/m)

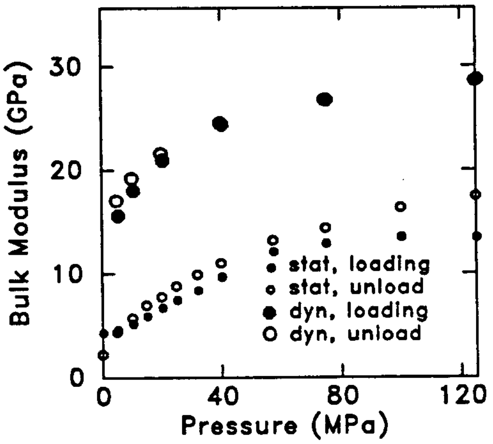
Bulk Modulus (GPa)
30
20
10
0
0
40
80
120
Pressure (MPa)
• stat, loading
∘ stat, unload
● dyn, loading
○ dyn, unload

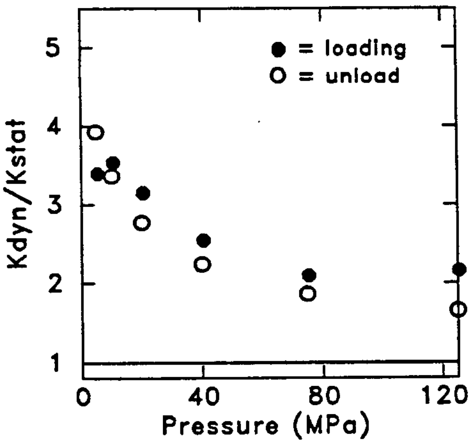
Kdyn/Kstat
5
4
3
2
1
0
40
80
120
Pressure (MPa)
● = loading
○ = unload

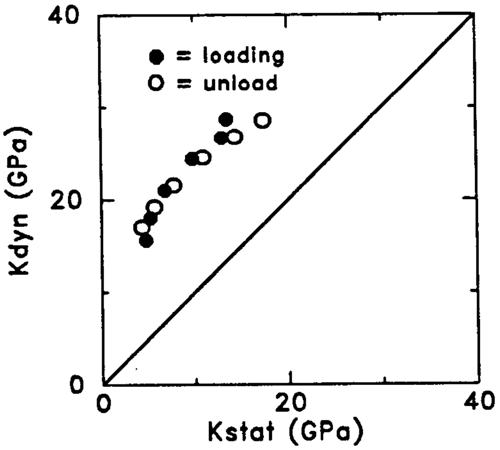
Kdyn (GPa)
40
20
0
0
20
40
Kstat (GPa)
● = loading
○ = unload

Depth (feet) = 6053.0
Length (cm) = 4.57
Grain density (g/cm^3) = 2.60
Porosity (%) = 4.3

Petrographic data:
framework clay= 0.0
matrix clay = 31.0
ankerite = 6.0
dolomite = 3.0

Strain, Static Bulk Moduli, and Dry Velocities

P_c (MPa)	ϵ_{vol} (mstr)	K_{stat} (GPa)	K_{dyn} (GPa)	V_p (km/s)	V_s (km/s)	V_p/V_s	G_{dyn} (GPa)	σ_{dyn}
5.	0.43	12.62	11.65	3.672	2.582	1.42	16.92	0.011
10.	0.78	13.74	13.88	3.857	2.657	1.45	17.92	0.049
20.	1.47	17.02	16.85	4.138	2.806	1.48	20.01	0.075
40.	2.53	20.90	22.65	4.578	3.009	1.52	23.05	0.120
75.	4.00	25.71	28.29	4.911	3.127	1.57	24.97	0.159
125.	5.66	30.02	31.16	5.077	3.193	1.59	26.08	0.173
125.	5.65	31.06	31.18	5.076	3.193	1.59	26.10	0.173
75.	4.19	30.41	29.82	5.002	3.164	1.58	25.57	0.167
40.	2.92	25.75	27.11	4.849	3.108	1.56	24.62	0.151
20.	2.06	20.54	21.74	4.531	2.998	1.51	22.87	0.111
10.	1.53	16.40	17.10	4.199	2.860	1.47	20.79	0.067
5.	1.22	12.90	15.74	4.026	2.741	1.47	19.09	0.068

6053

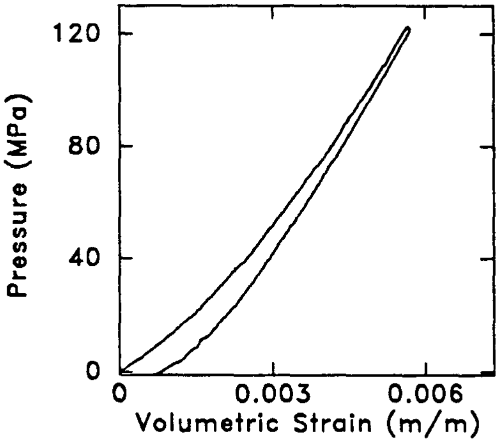
Pressure (MPa)
0
40
80
120
Volumetric Strain (m/m)
0
0.003
0.006

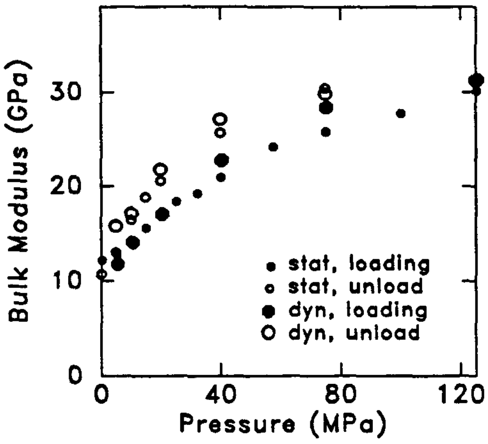
Bulk Modulus (GPa)
0
10
20
30
Pressure (MPa)
0
40
80
120
● stat, loading
○ stat, unload
● dyn, loading
○ dyn, unload

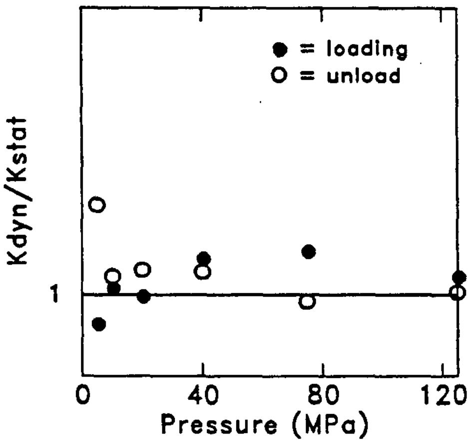
Kdyn/Kstat
1
Pressure (MPa)
0
40
80
120
● = loading
○ = unload

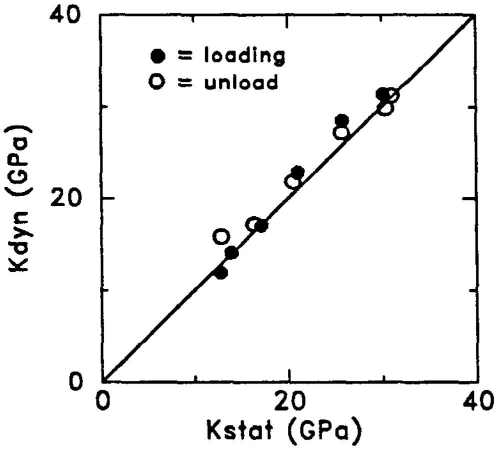
Kdyn (GPa)
0
20
40
Kstat (GPa)
0
20
40
● = loading
○ = unload

Depth (feet) = 6189.0
Length (cm) = 3.58
Grain density (g/cm^3) = 2.64
Porosity (%) = 13.9

Petrographic data:
framework clay= 1.0
matrix clay = 2.0
ankerite = 0.0
dolomite = 0.0

Strain, Static Bulk Moduli, and Dry Velocities

P_c (MPa)	ϵ_{vol} (mstr)	K_{stat} (GPa)	K_{dyn} (GPa)	V_p (km/s)	V_s (km/s)	V_p/V_s	G_{dyn} (GPa)	σ_{dyn}
5.	0.94	5.84	9.57	2.998	1.913	1.57	8.53	0.156
10.	1.71	7.24	12.15	3.335	2.107	1.58	10.36	0.168
20.	2.77	10.85	15.67	3.836	2.450	1.57	14.02	0.156
40.	4.15	17.31	19.80	4.356	2.807	1.55	18.42	0.145
75.	5.92	21.13	21.81	4.570	2.946	1.55	20.31	0.145
125.	7.99	23.79	22.89	4.658	2.992	1.56	20.98	0.149
125.	7.81	22.79	22.79	4.678	3.004	1.56	20.89	0.149
75.	5.83	21.57	20.49	4.613	3.052	1.51	21.53	0.111
40.	4.09	18.27	20.40	4.375	2.780	1.57	17.84	0.161
20.	2.85	12.27	18.19	4.167	2.666	1.56	16.39	0.153
10.	1.90	8.06	15.37	3.783	2.394	1.58	13.21	0.166
5.	1.20	5.24	12.97	3.440	2.157	1.59	10.72	0.176

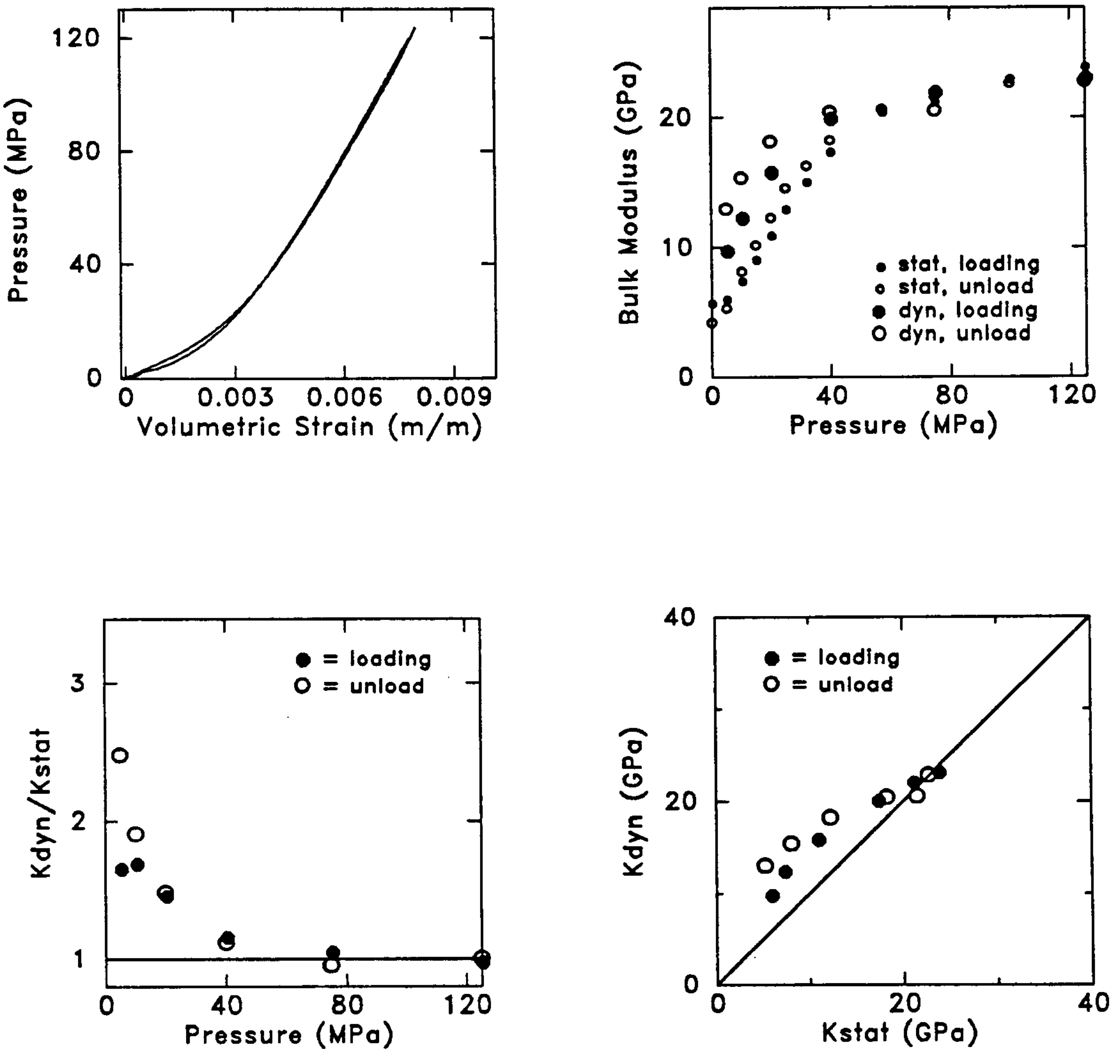

6189

Pressure (MPa)
120
80
40
0
0
0.003
0.006
0.009
Volumetric Strain (m/m)
Bulk Modulus (GPa)
20
10
0
0
40
80
120
Pressure (MPa)
• stat, loading
o stat, unload
● dyn, loading
O dyn, unload
Kdyn/Kstat
3
2
1
0
40
80
120
Pressure (MPa)
● = loading
O = unload
Kdyn (GPa)
40
20
0
0
20
40
Kstat (GPa)
● = loading
O = unload

Depth (feet) = 6275.0
Length (cm) = 3.59
Grain density (g/cm^3) = 2.62
Porosity (%) = 1.5

Petrographic data:
framework clay= 0.0
matrix clay = 63.0
ankerite = 0.5
dolomite = 0.0

Strain, Static Bulk Moduli, and Dry Velocities

P_c (MPa)	ϵ_{vol} (mstr)	K_{stat} (GPa)	K_{dyn} (GPa)	V_p (km/s)	V_s (km/s)	V_p/V_s	G_{dyn} (GPa)	σ_{dyn}
5.	0.53	12.63	15.75	4.036	2.770	1.46	19.95	0.055
10.	0.87	14.52	16.53	4.081	2.780	1.47	20.11	0.067
20.	1.57	15.21	17.69	4.165	2.814	1.48	20.62	0.080
40.	2.94	14.94	20.17	4.322	2.866	1.51	21.44	0.108
75.	5.12	17.02	23.76	4.544	2.947	1.54	22.76	0.137
125.	7.69	19.82	27.12	4.743	3.023	1.57	24.05	0.158
125.	7.72	26.31	27.12	4.743	3.023	1.57	24.05	0.158
75.	5.75	22.01	25.31	4.649	2.996	1.55	23.54	0.145
40.	3.99	17.16	22.80	4.499	2.940	1.53	22.60	0.127
20.	2.70	13.73	20.47	4.351	2.883	1.51	21.69	0.108
10.	1.83	11.57	18.68	4.234	2.841	1.49	21.03	0.091
5.	1.47	10.70	17.83	4.171	2.813	1.48	20.60	0.083

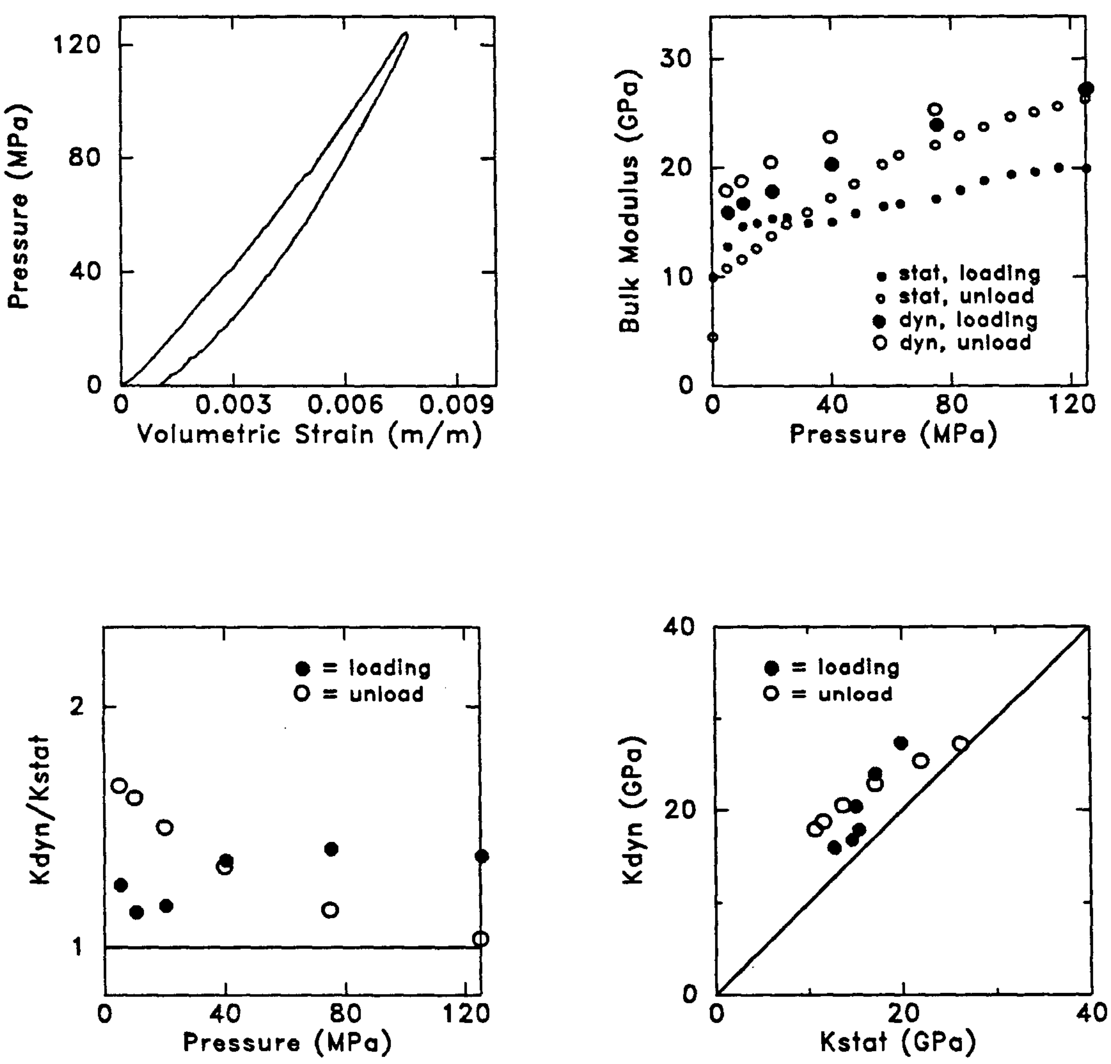

6275

Pressure (MPa)
120
80
40
0
0
0.003
0.006
0.009
Volumetric Strain (m/m)
Bulk Modulus (GPa)
30
20
10
0
0
40
80
120
Pressure (MPa)
• stat, loading
∘ stat, unload
● dyn, loading
○ dyn, unload
Kdyn/Kstat
2
1
0
40
80
120
Pressure (MPa)
● = loading
○ = unload
Kdyn (GPa)
40
20
0
0
20
40
Kstat (GPa)
● = loading
○ = unload

Depth (feet) = 6598.0
Length (cm) = 5.09
Grain density (g/cm^3) = 2.61
Porosity (%) = 8.9

Petrographic data:
framework clay= 10.5
matrix clay = 11.5
ankerite = 0.5
dolomite = 0.0

Strain, Static Bulk Moduli, and Dry Velocities

P_c (MPa)	ϵ_{vol} (mstr)	K_{stat} (GPa)	K_{dyn} (GPa)	V_p (km/s)	V_s (km/s)	V_p/V_s	G_{dyn} (GPa)	σ_{dyn}
5.	0.44	10.60	13.11	3.681	2.464	1.49	14.60	0.094
10.	0.92	10.81	14.13	3.810	2.546	1.50	15.60	0.096
20.	1.72	14.43	16.20	4.067	2.714	1.50	17.75	0.099
40.	2.81	21.08	20.83	4.480	2.930	1.53	20.72	0.126
75.	4.24	25.38	23.19	4.694	3.056	1.54	22.60	0.132
125.	6.09	27.51	24.42	4.782	3.100	1.54	23.33	0.138
125.	5.98	28.33	24.42	4.782	3.100	1.54	23.32	0.138
75.	4.28	25.59	23.26	4.711	3.072	1.53	22.85	0.130
40.	2.88	22.12	21.79	4.581	2.995	1.53	21.66	0.127
20.	1.84	16.42	19.42	4.356	2.862	1.52	19.74	0.120
10.	1.16	11.19	16.06	4.046	2.697	1.50	17.52	0.100
5.	0.59	8.81	14.38	3.857	2.583	1.49	16.05	0.093

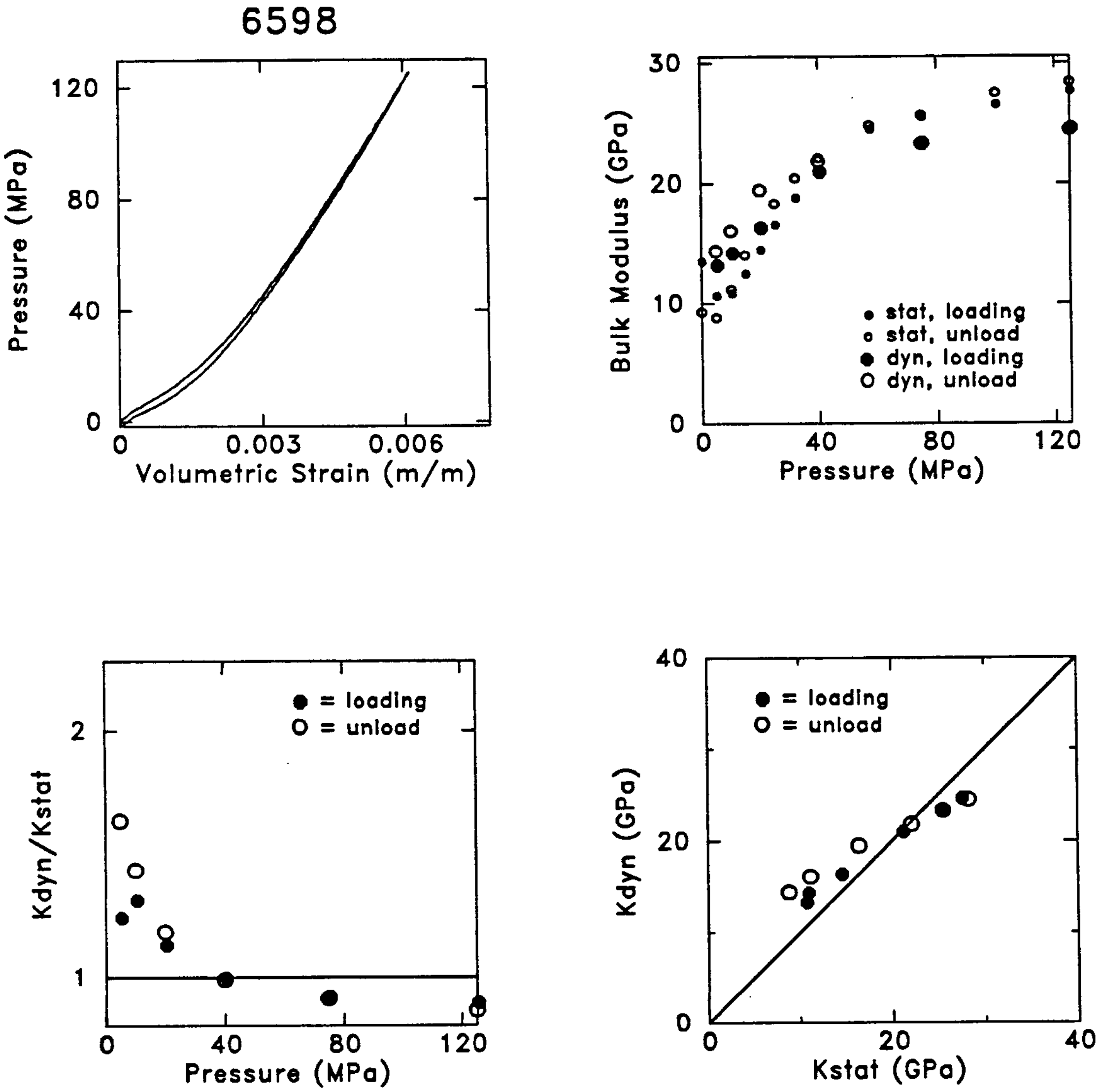

6598

120
80
40
0
Pressure (MPa)
0
0.003
0.006
Volumetric Strain (m/m)
30
20
10
0
Bulk Modulus (GPa)
0
40
80
120
Pressure (MPa)
● stat, loading
○ stat, unload
● dyn, loading
○ dyn, unload
2
1
Kdyn/Kstat
● = loading
○ = unload
0
40
80
120
Pressure (MPa)
40
20
0
Kdyn (GPa)
● = loading
○ = unload
0
20
40
Kstat (GPa)

Depth (feet) = 6838.0
Length (cm) = 3.81
Grain density (g/cm^3) = 2.67
Porosity (%) = 1.2

Petrographic data:
framework clay= 0.8
matrix clay = 22.8
ankerite = 9.6
dolomite = 10.0

Strain, Static Bulk Moduli, and Dry Velocities

P_c (MPa)	ϵ_{vol} (mstr)	K_{stat} (GPa)	K_{dyn} (GPa)	V_p (km/s)	V_s (km/s)	V_p/V_s	G_{dyn} (GPa)	σ_{dyn}
5.	0.33	18.42	22.80	4.767	3.121	1.53	22.82	0.125
10.	0.58	18.42	24.40	4.889	3.181	1.54	23.71	0.133
20.	1.14	18.18	26.11	5.010	3.237	1.55	24.57	0.142
40.	2.31	17.71	29.25	5.190	3.296	1.57	25.53	0.162
75.	4.20	19.68	31.08	5.304	3.348	1.58	26.42	0.169
125.	6.42	21.50	33.51	5.457	3.422	1.59	27.71	0.176
125.	6.48	26.91	33.51	5.457	3.422	1.59	27.71	0.176
75.	4.75	24.03	31.84	5.370	3.392	1.58	27.14	0.168
40.	3.17	19.49	30.74	5.289	3.344	1.58	26.32	0.167
20.	2.05	16.60	28.15	5.144	3.295	1.56	25.49	0.152
10.	1.46	15.02	26.73	5.050	3.253	1.55	24.84	0.145
5.	1.07	14.00	24.91	4.927	3.200	1.54	24.01	0.135

6838

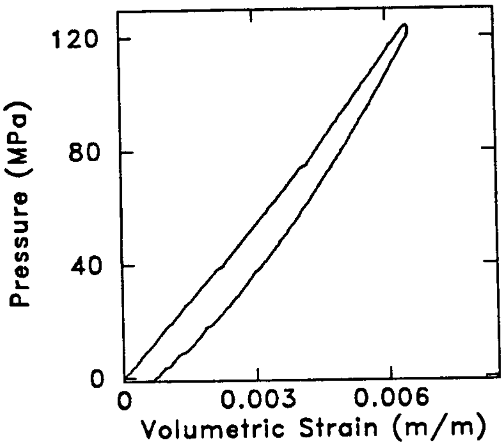
Pressure (MPa)
120
80
40
0
0
0.003
0.006
Volumetric Strain (m/m)

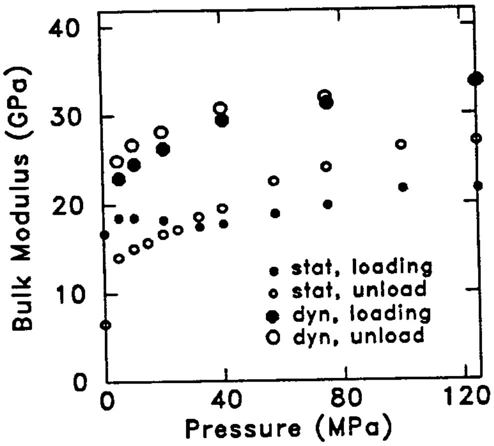
Bulk Modulus (GPa)
40
30
20
10
0
0
40
80
120
Pressure (MPa)
• stat, loading
∘ stat, unload
● dyn, loading
○ dyn, unload

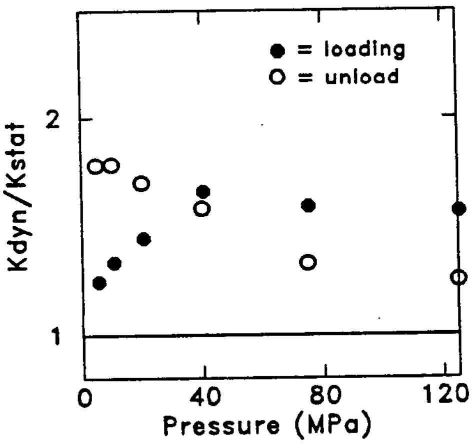
Kdyn/Kstat
2
1
0
40
80
120
Pressure (MPa)
● = loading
○ = unload

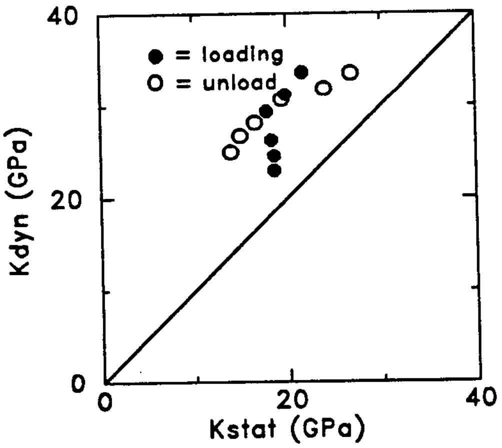
Kdyn (GPa)
40
20
0
0
20
40
Kstat (GPa)
● = loading
○ = unload

Depth (feet) = 6841.0
Length (cm) = 3.47
Grain density (g/cm^3) = 2.64
Porosity (%) = 4.5

Petrographic data:
framework clay= 8.8
matrix clay = 11.2
ankerite = 0.8
dolomite = 0.4

Strain, Static Bulk Moduli, and Dry Velocities

P_c (MPa)	ϵ_{vol} (mstr)	K_{stat} (GPa)	K_{dyn} (GPa)	V_p (km/s)	V_s (km/s)	V_p/V_s	G_{dyn} (GPa)	σ_{dyn}
5.	0.55	10.86	21.89	4.313	2.788	1.55	20.65	0.141
10.	1.00	11.76	22.28	4.378	2.845	1.54	21.51	0.135
20.	1.70	14.60	24.32	4.561	2.958	1.54	23.29	0.137
40.	2.95	18.13	26.90	4.777	3.091	1.55	25.47	0.140
75.	4.64	21.66	28.63	4.912	3.173	1.55	26.92	0.142
125.	6.74	24.16	31.09	5.028	3.205	1.57	27.55	0.158
125.	6.74	29.14	31.09	5.028	3.204	1.57	27.56	0.158
75.	5.00	24.67	29.67	4.968	3.193	1.56	27.28	0.148
40.	3.44	19.60	27.85	4.864	3.149	1.54	26.47	0.139
20.	2.31	15.18	27.35	4.781	3.073	1.56	25.16	0.148
10.	1.60	11.23	25.17	4.623	2.989	1.55	23.78	0.141
5.	1.14	8.87	22.77	4.451	2.905	1.53	22.44	0.129

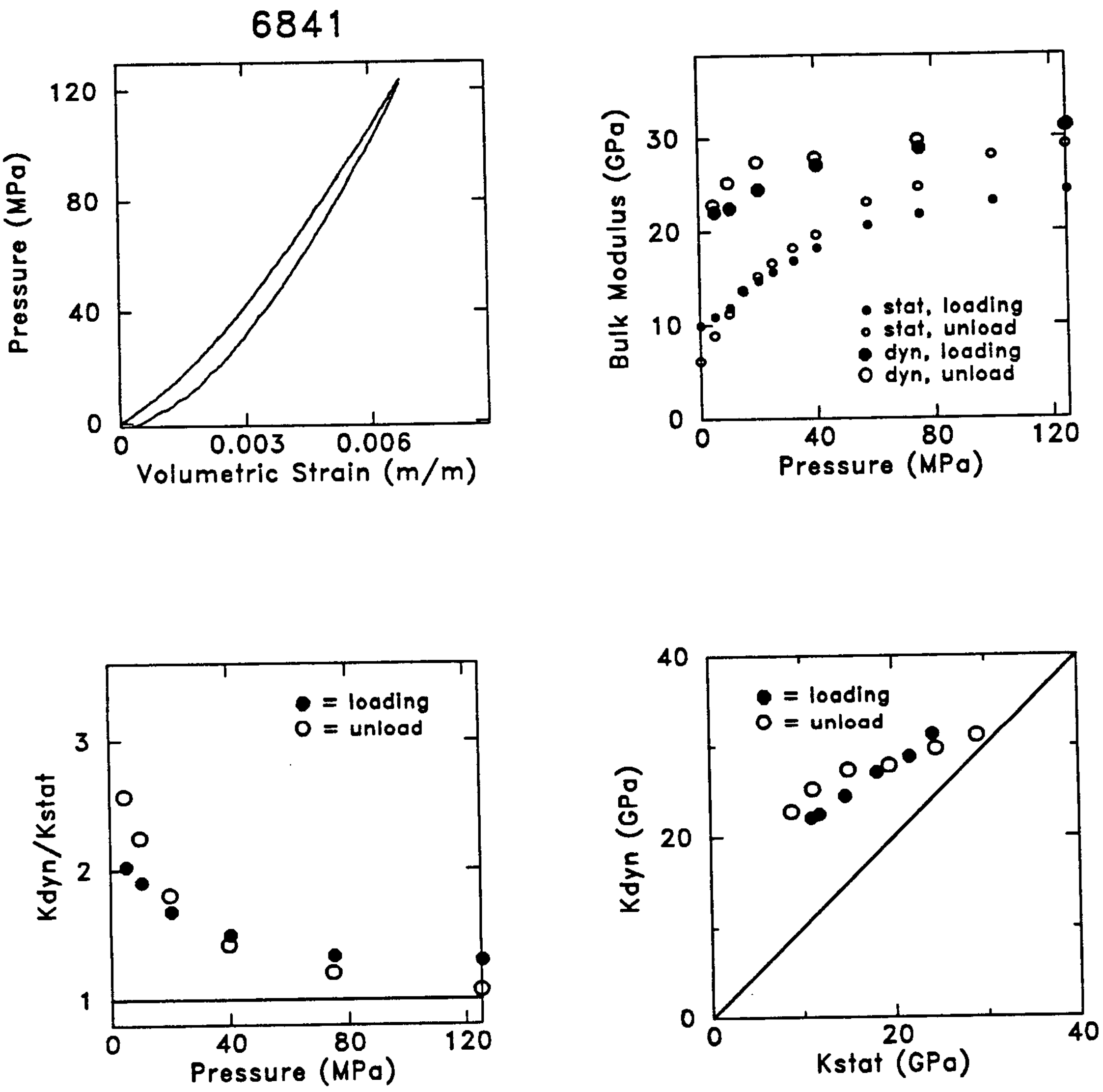
6841
Pressure (MPa)
0
40
80
120
0
0.003
0.006
Volumetric Strain (m/m)
Bulk Modulus (GPa)
0
10
20
30
0
40
80
120
Pressure (MPa)
● stat, loading
○ stat, unload
● dyn, loading
○ dyn, unload
Kdyn/Kstat
1
2
3
0
40
80
120
Pressure (MPa)
● = loading
○ = unload
Kdyn (GPa)
0
20
40
0
20
40
Kstat (GPa)
● = loading
○ = unload

Depth (feet) = 6897.0
Length (cm) = 3.81
Grain density (g/cm^3) = 2.63
Porosity (%) = 9.3

Petrographic data:
framework clay= 2.0
matrix clay = 1.0
ankerite = 2.5
dolomite = 5.0

Strain, Static Bulk Moduli, and Dry Velocities

P_c (MPa)	ϵ_{vol} (mstr)	K_{stat} (GPa)	K_{dyn} (GPa)	V_p (km/s)	V_s (km/s)	V_p/V_s	G_{dyn} (GPa)	σ_{dyn}
5.	0.57	9.69	11.58	3.664	2.542	1.44	15.57	0.036
10.	1.11	11.34	13.14	3.892	2.696	1.44	17.53	0.038
20.	1.80	15.83	16.28	4.279	2.946	1.45	20.95	0.050
40.	2.79	23.08	22.88	4.823	3.218	1.50	25.04	0.099
75.	4.12	27.02	26.39	5.080	3.345	1.52	27.12	0.117
125.	5.89	27.95	28.31	5.192	3.389	1.53	27.92	0.129
125.	5.81	29.00	28.31	5.192	3.389	1.53	27.92	0.129
75.	4.17	27.64	27.43	5.155	3.383	1.52	27.75	0.122
40.	2.85	23.11	24.39	4.961	3.301	1.50	26.36	0.103
20.	1.91	17.02	20.06	4.611	3.117	1.48	23.46	0.079
10.	1.23	12.47	15.64	4.200	2.893	1.45	20.19	0.049
5.	0.78	9.68	12.91	3.900	2.718	1.43	17.81	0.028

6897

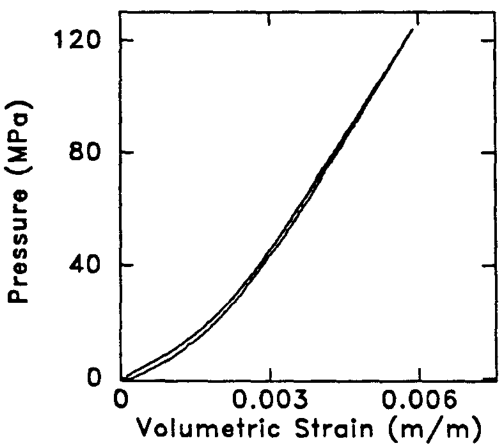
Pressure (MPa)
0
40
80
120
0
0.003
0.006
Volumetric Strain (m/m)

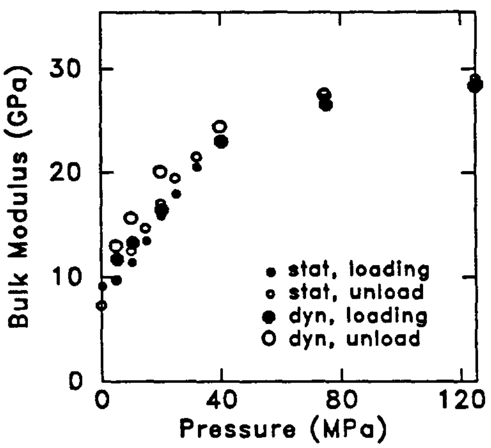
Bulk Modulus (GPa)
0
10
20
30
0
40
80
120
Pressure (MPa)
• stat, loading
∘ stat, unload
● dyn, loading
O dyn, unload

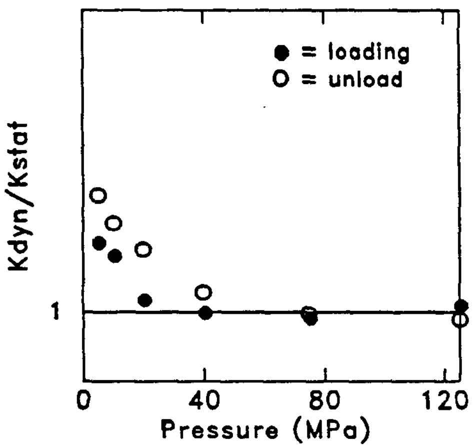
Kdyn/Kstat
1
0
40
80
120
Pressure (MPa)
● = loading
O = unload

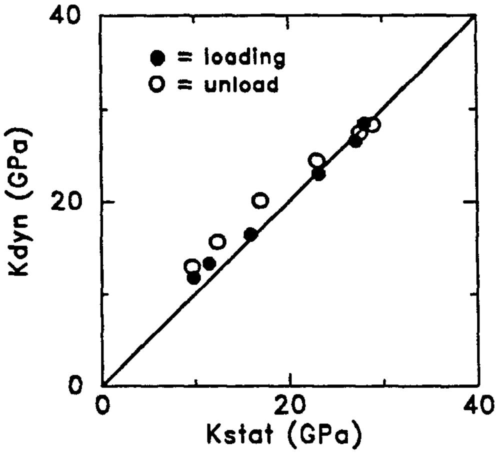
Kdyn (GPa)
0
20
40
0
20
40
Kstat (GPa)
● = loading
O = unload

Depth (feet) = 7053.0
Length (cm) = 4.32
Grain density (g/cm^3) = 2.63
Porosity (%) = 1.6

Petrographic data:
framework clay= 0.0
matrix clay = 38.0
ankerite = 0.0
dolomite = 0.0

Strain, Static Bulk Moduli, and Dry Velocities

P_c (MPa)	ϵ_{vol} (mstr)	K_{stat} (GPa)	K_{dyn} (GPa)	V_p (km/s)	V_s (km/s)	V_p/V_s	G_{dyn} (GPa)	σ_{dyn}
5.	0.31	16.93	22.47	4.251	2.661	1.60	18.45	0.178
10.	0.63	16.32	23.02	4.293	2.682	1.60	18.75	0.180
20.	1.26	16.49	23.63	4.348	2.717	1.60	19.26	0.180
40.	2.40	17.72	24.91	4.466	2.795	1.60	20.41	0.178
75.	4.27	19.95	26.90	4.617	2.880	1.60	21.74	0.182
125.	6.50	22.62	28.66	4.744	2.952	1.61	22.93	0.184
125.	6.30	26.59	28.65	4.745	2.952	1.61	22.92	0.184
75.	4.60	22.49	27.75	4.682	2.916	1.61	22.31	0.183
40.	2.91	18.15	26.38	4.584	2.863	1.60	21.44	0.180
20.	1.73	15.24	25.00	4.478	2.803	1.60	20.51	0.178
10.	0.99	12.97	24.15	4.402	2.754	1.60	19.78	0.178
5.	0.52	11.91	23.45	4.345	2.722	1.60	19.30	0.177

7053

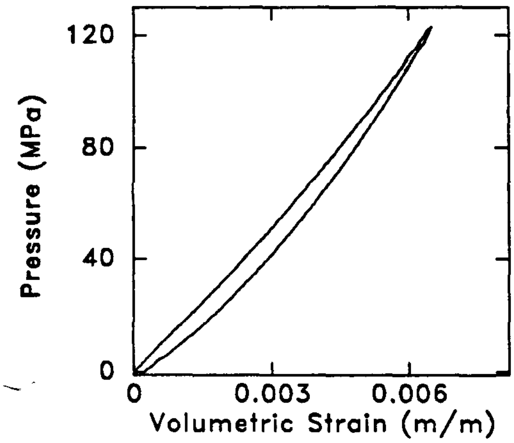
Pressure (MPa)
120
80
40
0
0
0.003
0.006
Volumetric Strain (m/m)

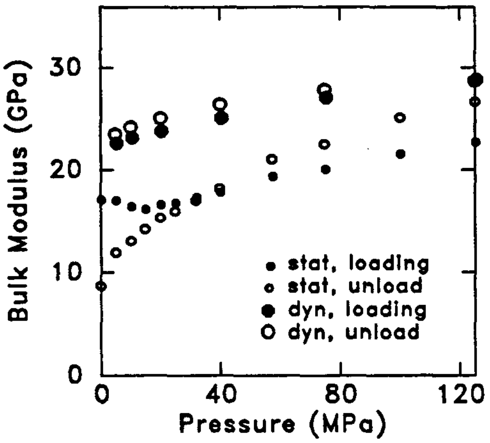
Bulk Modulus (GPa)
30
20
10
0
0
40
80
120
Pressure (MPa)
• stat, loading
○ stat, unload
● dyn, loading
O dyn, unload

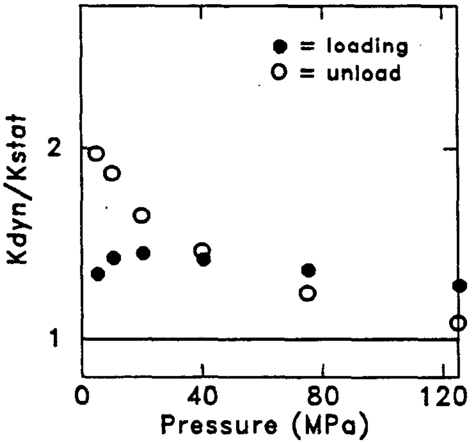
Kdyn/Kstat
2
1
0
40
80
120
Pressure (MPa)
● = loading
O = unload

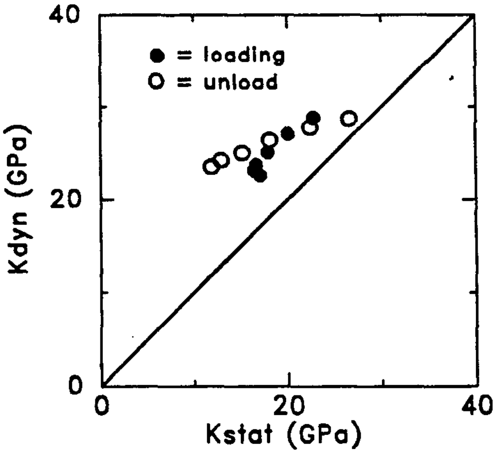
Kdyn (GPa)
40
20
0
0
20
40
Kstat (GPa)
● = loading
O = unload

Depth (feet) = 7057.0
Length (cm) = 3.47
Grain density (g/cm^3) = 2.62
Porosity (%) = 1.7

Petrographic data:
framework clay= 0.0
matrix clay = 38.8
ankerite = 0.0
dolomite = 1.6

Strain, Static Bulk Moduli, and Dry Velocities

P_c (MPa)	ϵ_{vol} (mstr)	K_{stat} (GPa)	K_{dyn} (GPa)	V_p (km/s)	V_s (km/s)	V_p/V_s	G_{dyn} (GPa)	σ_{dyn}
5.	0.69	9.09	20.38	4.281	2.811	1.52	20.65	0.121
10.	1.26	10.33	21.09	4.323	2.824	1.53	20.86	0.128
20.	2.13	11.59	21.97	4.382	2.848	1.54	21.26	0.134
40.	3.81	12.69	23.72	4.491	2.891	1.55	21.97	0.146
75.	6.27	15.87	26.40	4.652	2.954	1.57	23.04	0.162
125.	8.92	18.43	29.30	4.822	3.024	1.59	24.22	0.176
125.	8.90	26.21	29.32	4.821	3.023	1.59	24.23	0.176
75.	6.82	19.59	27.61	4.727	2.987	1.58	23.57	0.168
40.	4.81	15.13	25.66	4.609	2.937	1.57	22.71	0.158
20.	3.32	11.37	23.97	4.506	2.895	1.56	22.01	0.149
10.	2.42	8.96	22.57	4.421	2.865	1.54	21.52	0.138
5.	1.87	8.80	21.73	4.366	2.842	1.54	21.16	0.132

7057

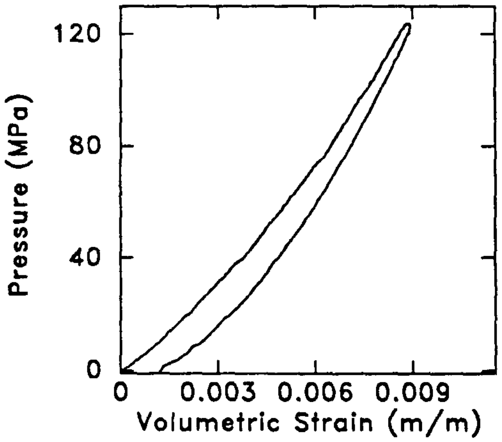
Pressure (MPa)
120
80
40
0
0
0.003
0.006
0.009
Volumetric Strain (m/m)

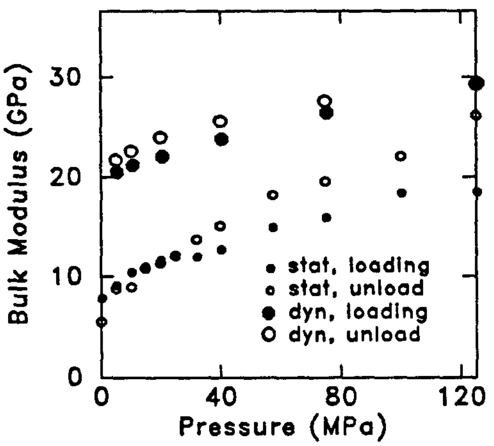
Bulk Modulus (GPa)
30
20
10
0
0
40
80
120
Pressure (MPa)
• stat, loading
∘ stat, unload
● dyn, loading
○ dyn, unload

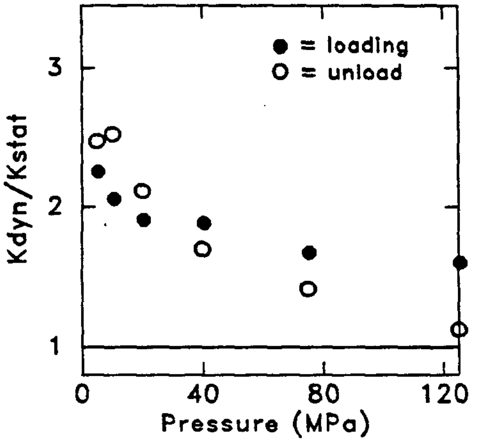
Kdyn/Kstat
3
2
1
0
40
80
120
Pressure (MPa)
● = loading
○ = unload

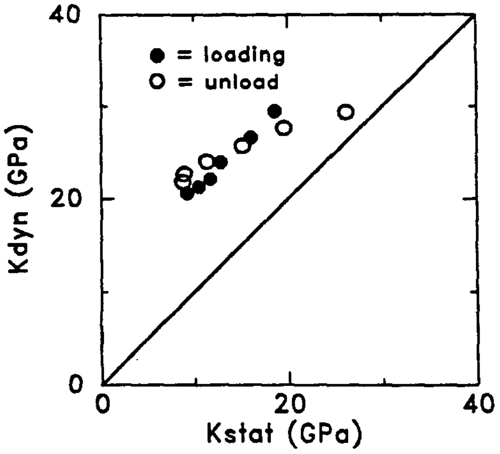
Kdyn (GPa)
40
20
0
0
20
40
Kstat (GPa)
● = loading
○ = unload

Depth (feet) = 7047.0
Length (cm) = 3.74
Grain density (g/cm^3) = 2.65
Porosity (%) = 3.8

Petrographic data:
framework clay= 0.0
matrix clay = 9.0
ankerite = 13.0
dolomite = 48.5

Strain, Static Bulk Moduli, and Dry Velocities

P_c (MPa)	ϵ_{vol} (mstr)	K_{stat} (GPa)	K_{dyn} (GPa)	V_p (km/s)	V_s (km/s)	V_p/V_s	G_{dyn} (GPa)	σ_{dyn}
5.	0.72	7.08	10.86	3.640	2.595	1.40	17.14	-0.017
10.	1.41	7.44	12.09	3.778	2.674	1.41	18.22	-0.002
20.	2.55	10.71	16.18	4.177	2.887	1.45	21.29	0.043
40.	3.91	17.35	26.09	4.844	3.155	1.54	25.48	0.132
75.	5.60	22.29	32.79	5.229	3.306	1.58	28.05	0.167
125.	7.66	24.68	36.07	5.390	3.359	1.60	29.05	0.183
125.	7.61	27.43	36.07	5.390	3.359	1.60	29.05	0.183
75.	5.81	24.23	34.83	5.333	3.341	1.60	28.66	0.177
40.	4.23	19.72	32.23	5.194	3.285	1.58	27.64	0.167
20.	3.11	14.18	25.72	4.842	3.168	1.53	25.65	0.126
10.	2.23	9.14	18.41	4.374	2.989	1.46	22.81	0.062
5.	1.65	5.81	14.05	4.017	2.823	1.42	20.32	0.012

7074

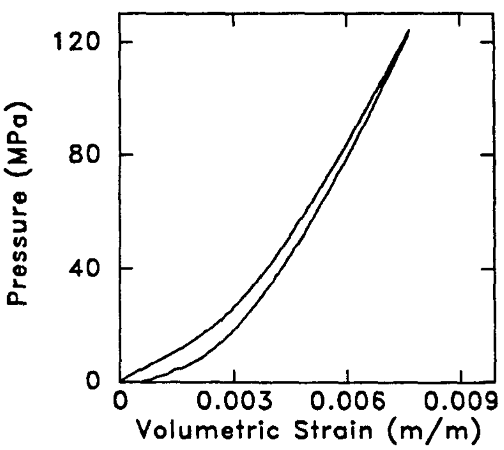
Pressure (MPa)
120
80
40
0
0
0.003
0.006
0.009
Volumetric Strain (m/m)

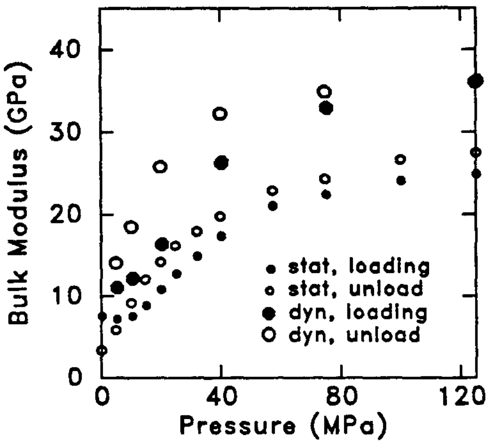
Bulk Modulus (GPa)
40
30
20
10
0
0
40
80
120
Pressure (MPa)
• stat, loading
∘ stat, unload
● dyn, loading
○ dyn, unload

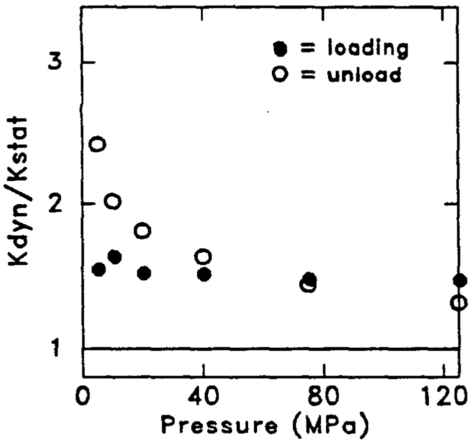
Kdyn/Kstat
3
2
1
0
40
80
120
Pressure (MPa)
● = loading
○ = unload

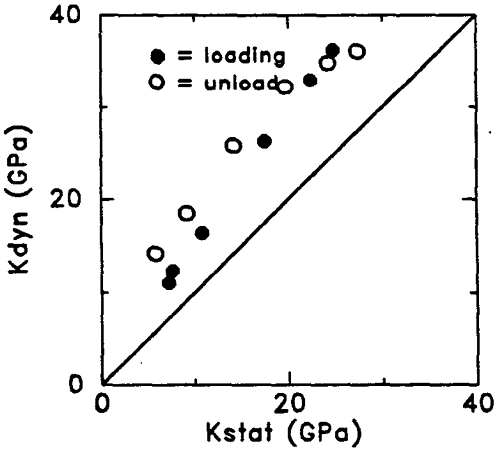
Kdyn (GPa)
40
20
0
0
20
40
Kstat (GPa)
● = loading
○ = unload

Depth (feet) = 7077.0
Length (cm) = 3.81
Grain density (g/cm^3) = 2.56
Porosity (%) = 10.1

Petrographic data:
framework clay= 1.0
matrix clay = 10.5
ankerite = 1.5
dolomite = 2.0

Strain, Static Bulk Moduli, and Dry Velocities

P_c (MPa)	ϵ_{vol} (mstr)	K_{stat} (GPa)	K_{dyn} (GPa)	V_p (km/s)	V_s (km/s)	V_p/V_s	G_{dyn} (GPa)	σ_{dyn}
5.	1.19	4.86	10.23	3.231	2.135	1.51	10.69	0.112
10.	2.10	5.90	11.91	3.497	2.317	1.51	12.61	0.109
20.	3.46	9.07	14.59	3.856	2.550	1.51	15.31	0.111
40.	5.08	13.99	18.71	4.234	2.739	1.55	17.71	0.140
75.	7.33	16.67	20.05	4.398	2.857	1.54	19.35	0.135
125.	10.06	17.50	20.71	4.470	2.908	1.54	20.13	0.133
125.	10.08	20.51	20.72	4.469	2.908	1.54	20.13	0.133
75.	7.67	18.12	20.03	4.407	2.869	1.54	19.53	0.132
40.	5.54	15.21	19.12	4.300	2.793	1.54	18.43	0.135
20.	4.12	11.08	16.27	4.022	2.638	1.52	16.41	0.123
10.	3.09	7.30	14.53	3.841	2.537	1.51	15.15	0.113
5.	2.31	4.99	12.11	3.552	2.366	1.50	13.16	0.101

7077

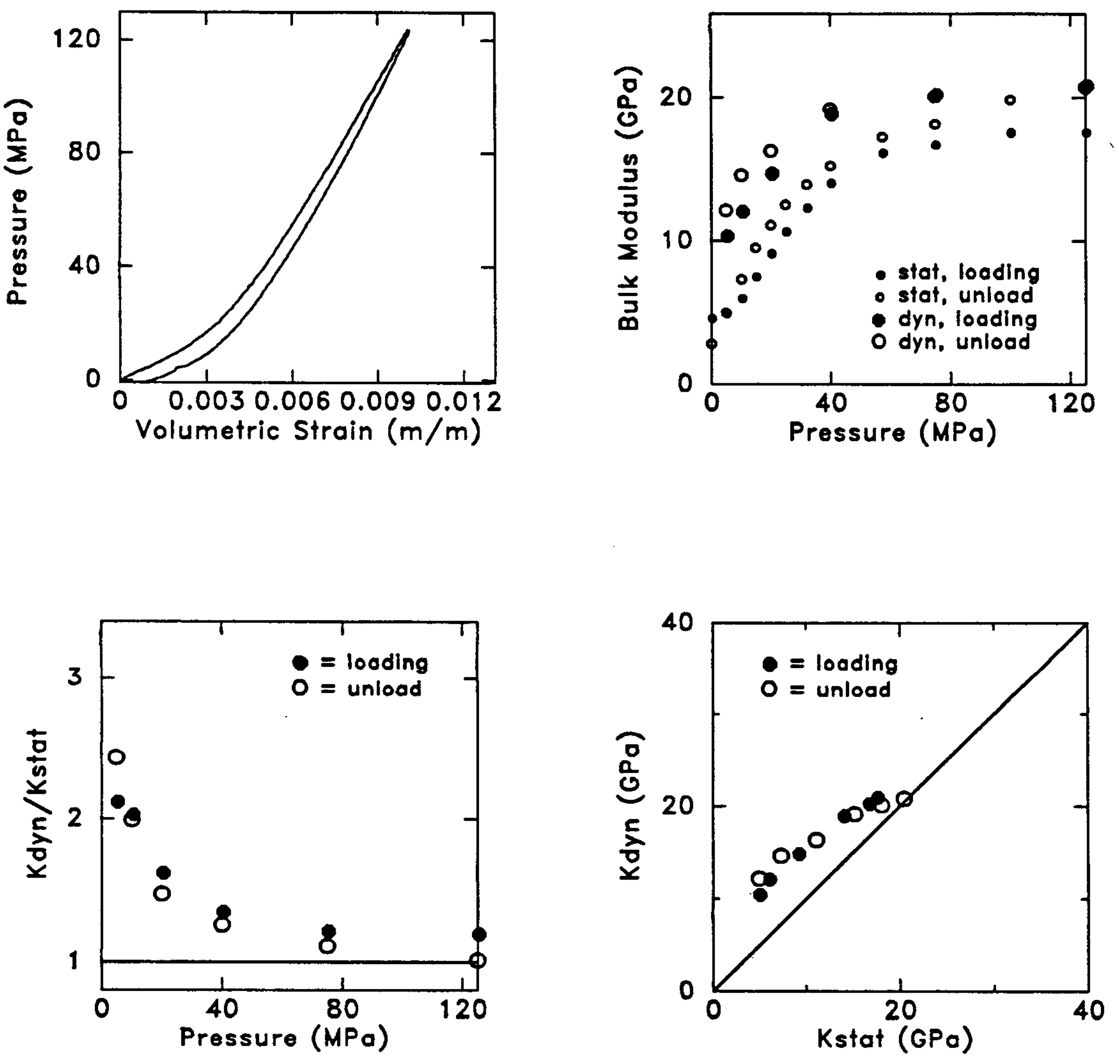
Pressure (MPa)
0
40
80
120
0
0.003
0.006
0.009
0.012
Volumetric Strain (m/m)
Bulk Modulus (GPa)
0
10
20
0
40
80
120
Pressure (MPa)
• stat, loading
∘ stat, unload
● dyn, loading
○ dyn, unload
Kdyn/Kstat
1
2
3
0
40
80
120
Pressure (MPa)
● = loading
○ = unload
Kdyn (GPa)
0
20
40
0
20
40
Kstat (GPa)
● = loading
○ = unload

Depth (feet) = 7096.0
Length (cm) = 3.47
Grain density (g/cm^3) = 2.63
Porosity (%) = 8.1

Petrographic data:
framework clay= 7.6
matrix clay = 2.4
ankerite = 0.0
dolomite = 0.0

Strain, Static Bulk Moduli, and Dry Velocities

P_c (MPa)	ϵ_{vol} (mstr)	K_{stat} (GPa)	K_{dyn} (GPa)	V_p (km/s)	V_s (km/s)	V_p/V_s	G_{dyn} (GPa)	σ_{dyn}
5.	0.68	8.23	17.45	4.112	2.697	1.52	17.61	0.122
10.	1.26	9.48	19.63	4.316	2.810	1.54	19.13	0.132
20.	2.17	12.38	22.40	4.606	2.998	1.54	21.81	0.132
40.	3.51	17.26	25.41	4.915	3.206	1.53	25.00	0.130
75.	5.23	22.42	26.92	5.042	3.285	1.53	26.32	0.131
125.	7.18	26.22	28.03	5.119	3.326	1.54	27.07	0.135
125.	7.17	27.57	28.03	5.119	3.326	1.54	27.07	0.135
75.	5.35	24.87	27.25	5.072	3.304	1.54	26.63	0.131
40.	3.82	20.30	26.31	4.985	3.245	1.54	25.62	0.132
20.	2.73	14.41	24.31	4.803	3.130	1.53	23.80	0.131
10.	1.91	10.30	21.66	4.547	2.968	1.53	21.37	0.129
5.	1.40	8.25	19.47	4.327	2.831	1.53	19.42	0.126

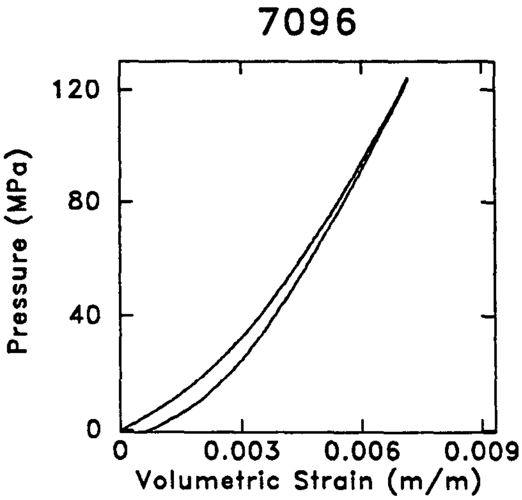
7096
Pressure (MPa)
120
80
40
0
0
0.003
0.006
0.009
Volumetric Strain (m/m)

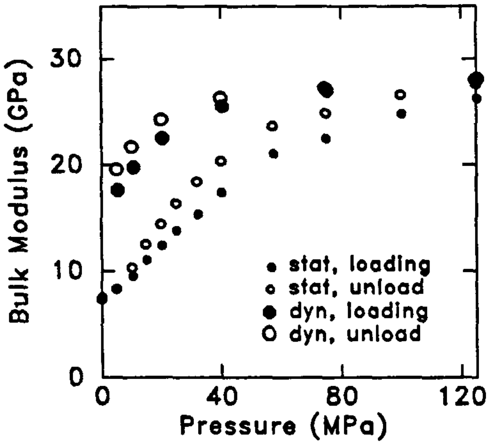
Bulk Modulus (GPa)
30
20
10
0
0
40
80
120
Pressure (MPa)
● stat, loading
○ stat, unload
● dyn, loading
○ dyn, unload

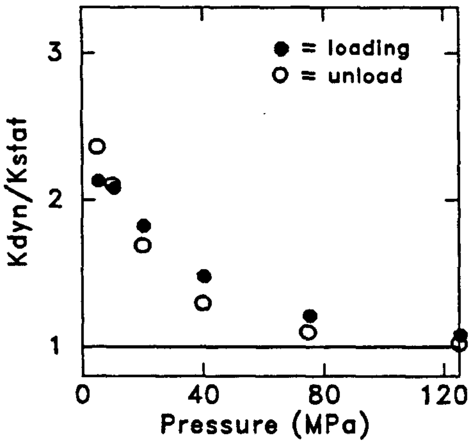
Kdyn/Kstat
3
2
1
0
40
80
120
Pressure (MPa)
● = loading
○ = unload

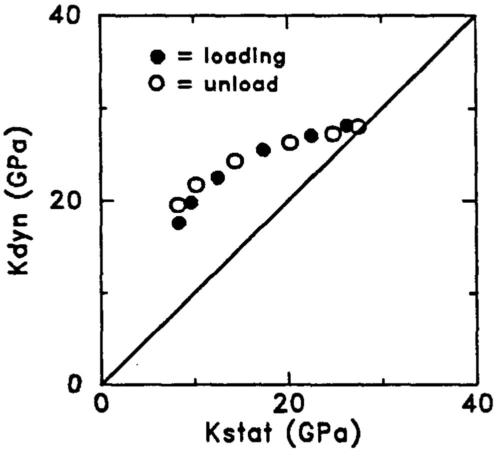
Kdyn (GPa)
40
20
0
0
20
40
Kstat (GPa)
● = loading
○ = unload

Depth (feet) = 8189.0
Length (cm) = 3.45
Grain density (g/cm^3) = 2.64
Porosity (%) = 6.8

Petrographic data:
framework clay= 4.0
matrix clay = 3.0
ankerite = 0.0
dolomite = 0.0

Strain, Static Bulk Moduli, and Dry Velocities

P_c (MPa)	ϵ_{vol} (mstr)	K_{stat} (GPa)	K_{dyn} (GPa)	V_p (km/s)	V_s (km/s)	V_p/V_s	G_{dyn} (GPa)	σ_{dyn}
5.	0.53	9.43	11.99	3.798	2.673	1.42	17.47	0.009
10.	1.09	10.20	14.11	4.018	2.791	1.44	19.06	0.034
20.	1.92	13.52	18.64	4.452	3.027	1.47	22.46	0.070
40.	3.05	20.55	24.80	4.967	3.306	1.50	26.84	0.102
75.	4.46	26.61	25.99	5.152	3.462	1.49	29.50	0.088
125.	6.24	27.93	26.79	5.209	3.494	1.49	30.12	0.091
125.	6.21	28.09	26.79	5.209	3.494	1.49	30.13	0.091
75.	4.44	26.39	26.18	5.160	3.462	1.49	29.50	0.091
40.	3.05	21.93	25.62	5.070	3.384	1.50	28.12	0.098
20.	1.96	15.08	22.92	4.766	3.166	1.51	24.57	0.105
10.	1.22	11.13	17.33	4.320	2.948	1.47	21.28	0.064
5.	0.74	10.13	14.13	4.014	2.785	1.44	18.97	0.036

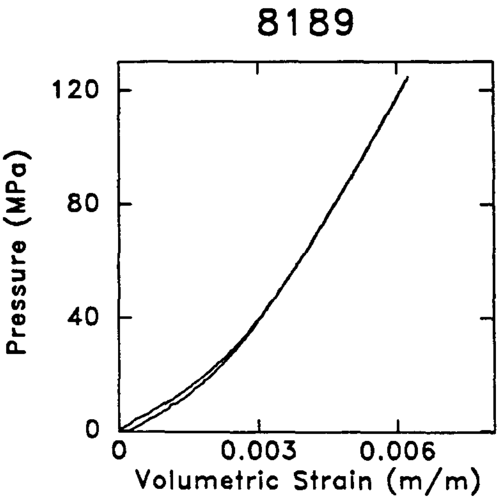
8189
Pressure (MPa)
120
80
40
0
0
0.003
0.006
Volumetric Strain (m/m)

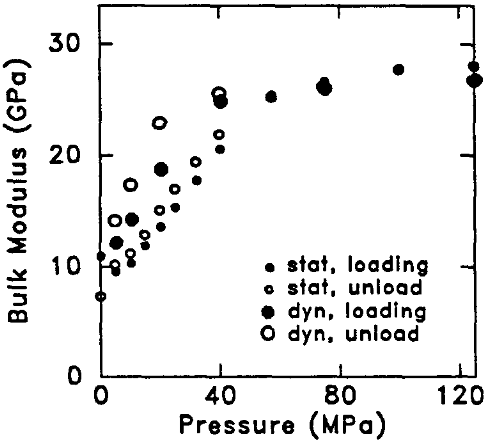
Bulk Modulus (GPa)
30
20
10
0
0
40
80
120
Pressure (MPa)
● stat, loading
○ stat, unload
● dyn, loading
○ dyn, unload

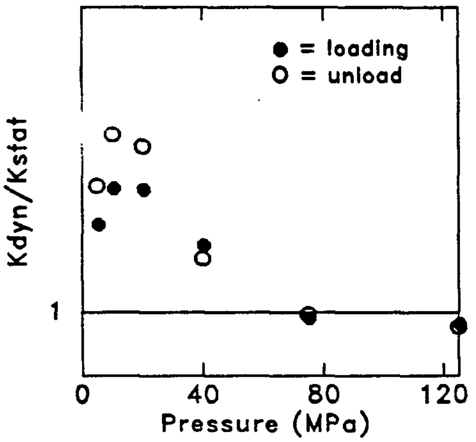
Kdyn/Kstat
1
0
40
80
120
Pressure (MPa)
● = loading
○ = unload

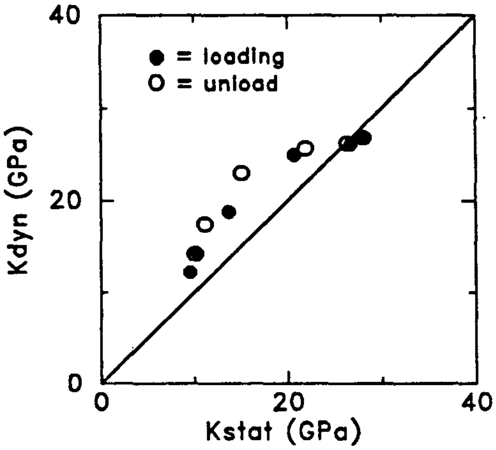
Kdyn (GPa)
40
20
0
0
20
40
Kstat (GPa)
● = loading
○ = unload

Depth (feet) = 8195.0
Length (cm) = 3.13
Grain density (g/cm^3) = 2.67
Porosity (%) = 7.1

Petrographic data:
framework clay= 6.0
matrix clay = 20.0
ankerite = 0.0
dolomite = 0.0

Strain, Static Bulk Moduli, and Dry Velocities

P_c (MPa)	ϵ_{vol} (mstr)	K_{stat} (GPa)	K_{dyn} (GPa)	V_p (km/s)	V_s (km/s)	V_p/V_s	G_{dyn} (GPa)	σ_{dyn}
5.	0.91	5.95	7.17	3.019	2.169	1.39	11.88	-0.034
10.	1.72	6.64	8.32	3.214	2.297	1.40	13.34	-0.023
20.	3.01	8.85	11.21	3.583	2.511	1.43	15.97	0.017
40.	4.78	13.21	16.48	4.083	2.764	1.48	19.40	0.077
75.	7.02	17.31	22.08	4.485	2.931	1.53	21.91	0.127
125.	9.54	18.80	24.78	4.668	3.013	1.55	23.22	0.143
125.	9.48	23.08	24.79	4.667	3.012	1.55	23.24	0.143
75.	7.40	19.33	23.08	4.557	2.964	1.54	22.42	0.133
40.	5.38	14.66	19.41	4.307	2.862	1.51	20.83	0.105
20.	3.81	10.29	14.39	3.918	2.694	1.45	18.41	0.051
10.	2.70	7.31	10.38	3.547	2.522	1.41	16.10	-0.011
5.	1.91	5.50	8.65	3.312	2.380	1.39	14.31	-0.033

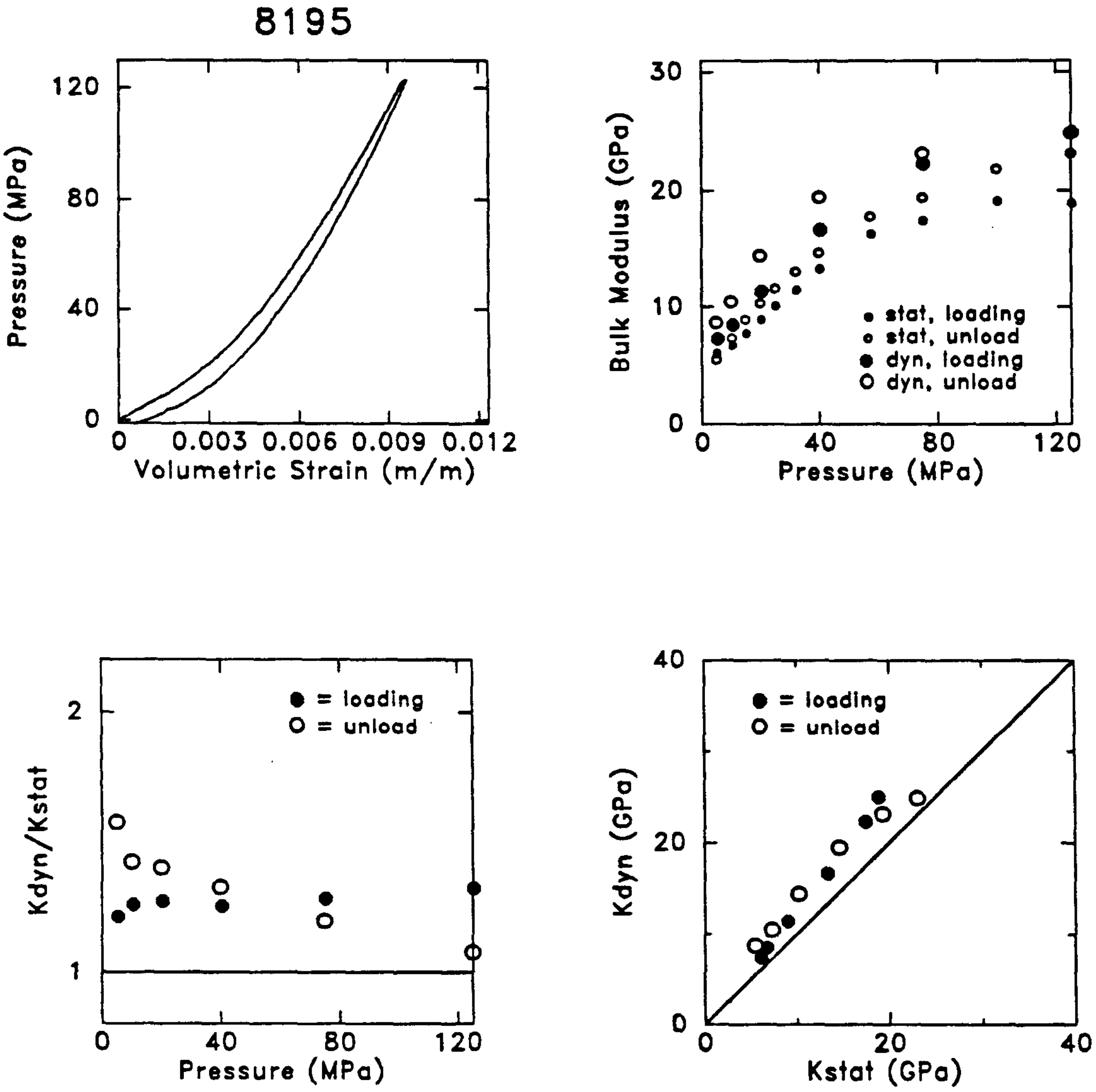
8195
Pressure (MPa)
120
80
40
0
0 0.003 0.006 0.009 0.012
Volumetric Strain (m/m)
Bulk Modulus (GPa)
30
20
10
0
0 40 80 120
Pressure (MPa)
● stat, loading
○ stat, unload
● dyn, loading
○ dyn, unload
Kdyn/Kstat
2
1
0 40 80 120
Pressure (MPa)
● = loading
○ = unload
Kdyn (GPa)
40
20
0
0 20 40
Kstat (GPa)
● = loading
○ = unload

Depth (feet) = 8227.0
Length (cm) = 3.78
Grain density (g/cm^3) = 2.70
Porosity (%) = 5.6

Petrographic data:
framework clay= 0.4
matrix clay = 54.8
ankerite = 3.6
dolomite = 6.4

Strain, Static Bulk Moduli, and Dry Velocities

P_c (MPa)	ϵ_{vol} (mstr)	K_{stat} (GPa)	K_{dyn} (GPa)	V_p (km/s)	V_s (km/s)	V_p/V_s	G_{dyn} (GPa)	σ_{dyn}
5.	0.43	11.42	13.92	4.146	2.970	1.40	22.59	-0.027
10.	0.93	9.86	15.12	4.252	3.023	1.41	23.43	-0.011
20.	1.96	10.13	18.16	4.504	3.148	1.43	25.44	0.023
40.	3.60	15.98	24.06	4.921	3.339	1.47	28.70	0.073
75.	5.16	26.85	27.48	5.168	3.471	1.49	31.09	0.089
125.	6.73	33.12	29.53	5.279	3.513	1.50	31.92	0.103
125.	6.68	35.21	29.53	5.279	3.513	1.50	31.93	0.103
75.	5.29	30.97	28.06	5.204	3.487	1.49	31.38	0.093
40.	4.08	23.76	25.98	5.065	3.417	1.48	30.08	0.082
20.	3.01	13.58	22.30	4.805	3.289	1.46	27.82	0.059
10.	2.12	8.73	18.30	4.509	3.148	1.43	25.45	0.025
5.	1.49	6.95	15.78	4.305	3.047	1.41	23.83	-0.002

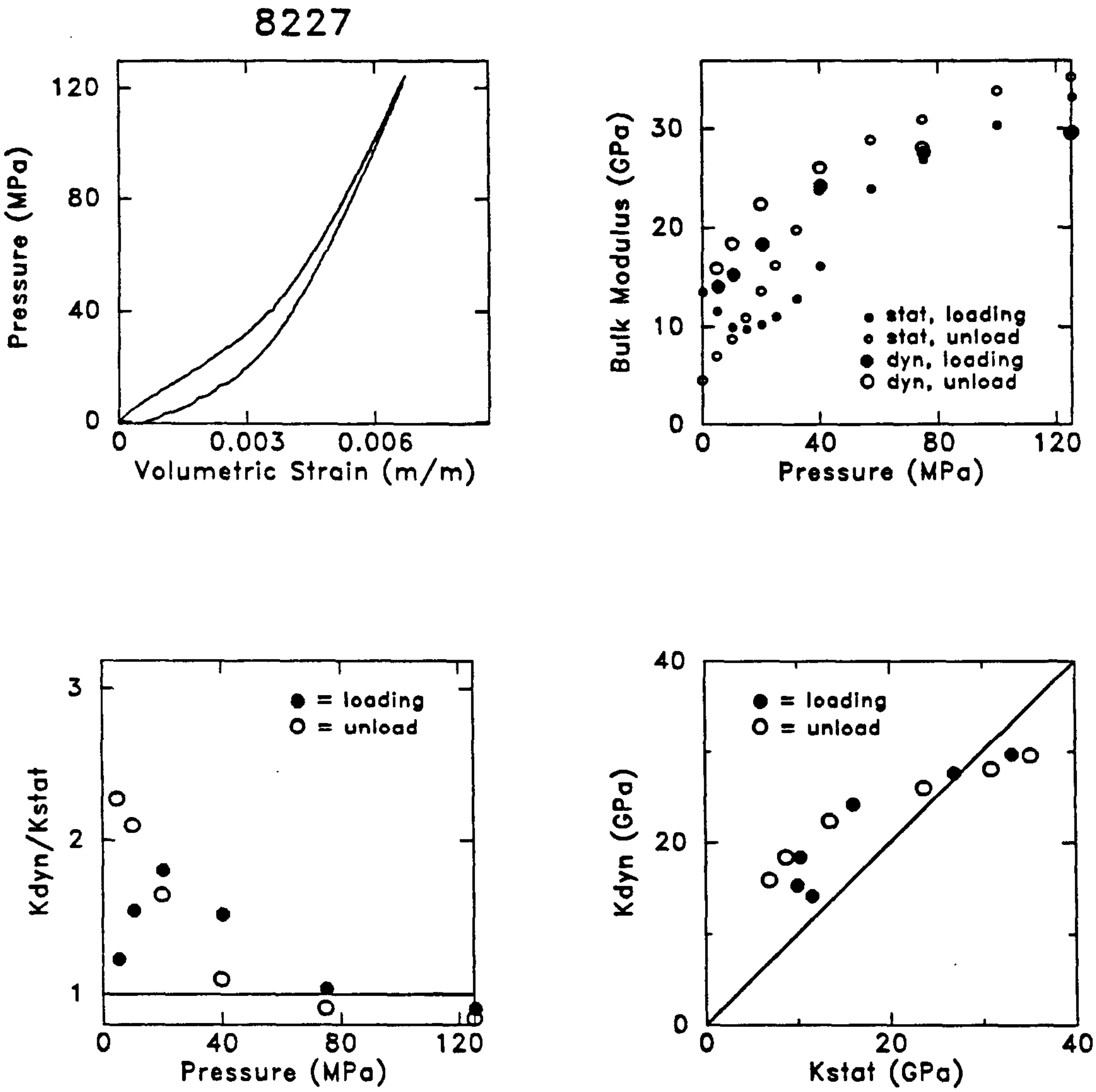
8227
Pressure (MPa)
120
80
40
0
0
0.003
0.006
Volumetric Strain (m/m)
Bulk Modulus (GPa)
30
20
10
0
0
40
80
120
Pressure (MPa)
• stat, loading
∘ stat, unload
● dyn, loading
○ dyn, unload
Kdyn/Kstat
3
2
1
0
40
80
120
Pressure (MPa)
● = loading
○ = unload
Kdyn (GPa)
40
20
0
0
20
40
Kstat (GPa)
● = loading
○ = unload

Depth (feet) = 8246.0
Length (cm) = 3.64
Grain density (g/cm^3) = 2.64
Porosity (%) = 14.4

Petrographic data:
framework clay= 2.0
matrix clay = 0.0
ankerite = 0.0
dolomite = 0.0

Strain, Static Bulk Moduli, and Dry Velocities

P_c (MPa)	ϵ_{vol} (mstr)	K_{stat} (GPa)	K_{dyn} (GPa)	V_p (km/s)	V_s (km/s)	V_p/V_s	G_{dyn} (GPa)	σ_{dyn}
5.	1.06	5.53	17.17	4.094	2.634	1.55	15.86	0.147
10.	1.85	6.91	18.18	4.241	2.744	1.55	17.24	0.140
20.	2.97	10.39	19.45	4.425	2.885	1.53	19.07	0.130
40.	4.45	16.86	20.95	4.623	3.031	1.53	21.11	0.123
75.	6.15	22.59	21.67	4.723	3.111	1.52	22.30	0.117
125.	8.26	22.79	22.30	4.774	3.140	1.52	22.80	0.119
125.	8.12	24.13	22.30	4.774	3.140	1.52	22.80	0.119
75.	6.17	22.11	21.75	4.730	3.114	1.52	22.34	0.117
40.	4.47	18.60	21.11	4.652	3.057	1.52	21.47	0.120
20.	3.22	12.28	20.14	4.507	2.940	1.53	19.83	0.129
10.	2.29	7.80	18.95	4.342	2.816	1.54	18.16	0.137
5.	1.56	5.54	17.97	4.193	2.700	1.55	16.68	0.146

8246

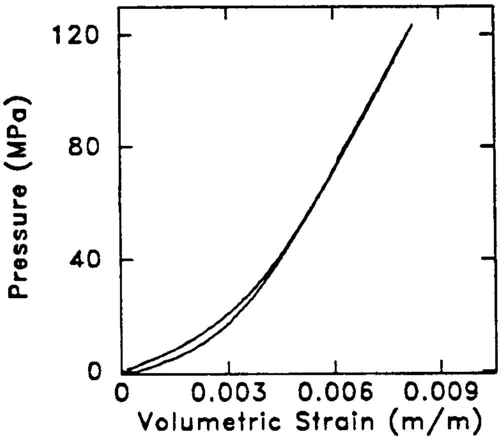
Pressure (MPa)
120
80
40
0
0
0.003
0.006
0.009
Volumetric Strain (m/m)

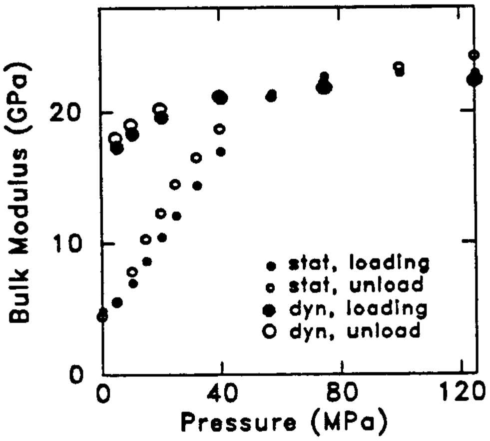
Bulk Modulus (GPa)
20
10
0
0
40
80
120
Pressure (MPa)
• stat, loading
∘ stat, unload
● dyn, loading
○ dyn, unload

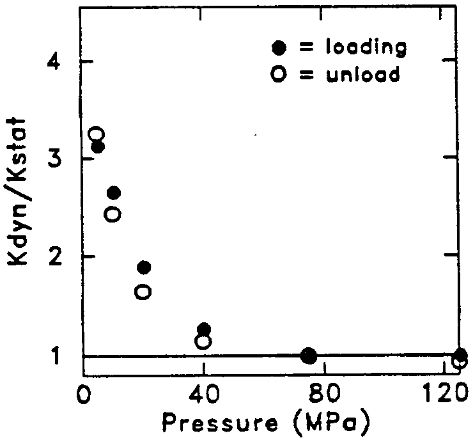
Kdyn/Kstat
4
3
2
1
0
40
80
120
Pressure (MPa)
● = loading
○ = unload

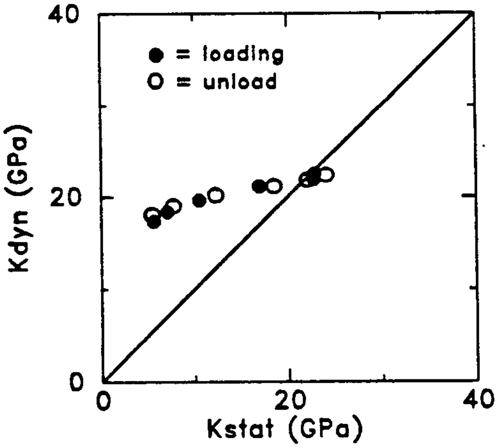
Kdyn (GPa)
40
20
0
0
20
40
Kstat (GPa)
● = loading
○ = unload

Depth (feet) = 8368.0
Length (cm) = 3.47
Grain density (g/cm^3) = 2.65
Porosity (%) = 3.9

Petrographic data:
framework clay= 0.0
matrix clay = 6.0
ankerite = 0.0
dolomite = 0.0

Strain, Static Bulk Moduli, and Dry Velocities

P_c (MPa)	ϵ_{vol} (mstr)	K_{stat} (GPa)	K_{dyn} (GPa)	V_p (km/s)	V_s (km/s)	V_p/V_s	G_{dyn} (GPa)	σ_{dyn}
5.	0.61	8.93	11.99	3.749	2.647	1.42	17.86	0.002
10.	1.12	9.78	12.99	3.891	2.745	1.42	19.22	0.005
20.	2.03	12.31	17.63	4.268	2.912	1.47	21.66	0.064
40.	3.39	17.69	26.41	4.821	3.114	1.55	24.82	0.142
75.	5.00	24.74	30.78	5.097	3.239	1.57	26.93	0.161
125.	6.70	29.00	33.89	5.263	3.301	1.59	28.04	0.176
125.	6.71	31.39	33.89	5.263	3.301	1.59	28.05	0.176
75.	5.11	27.41	32.25	5.181	3.273	1.58	27.50	0.168
40.	3.65	21.04	29.55	5.017	3.197	1.57	26.18	0.158
20.	2.57	14.40	25.01	4.727	3.069	1.54	24.08	0.136
10.	1.77	9.58	18.14	4.300	2.923	1.47	21.81	0.071
5.	1.22	8.14	14.23	3.999	2.794	1.43	19.91	0.023

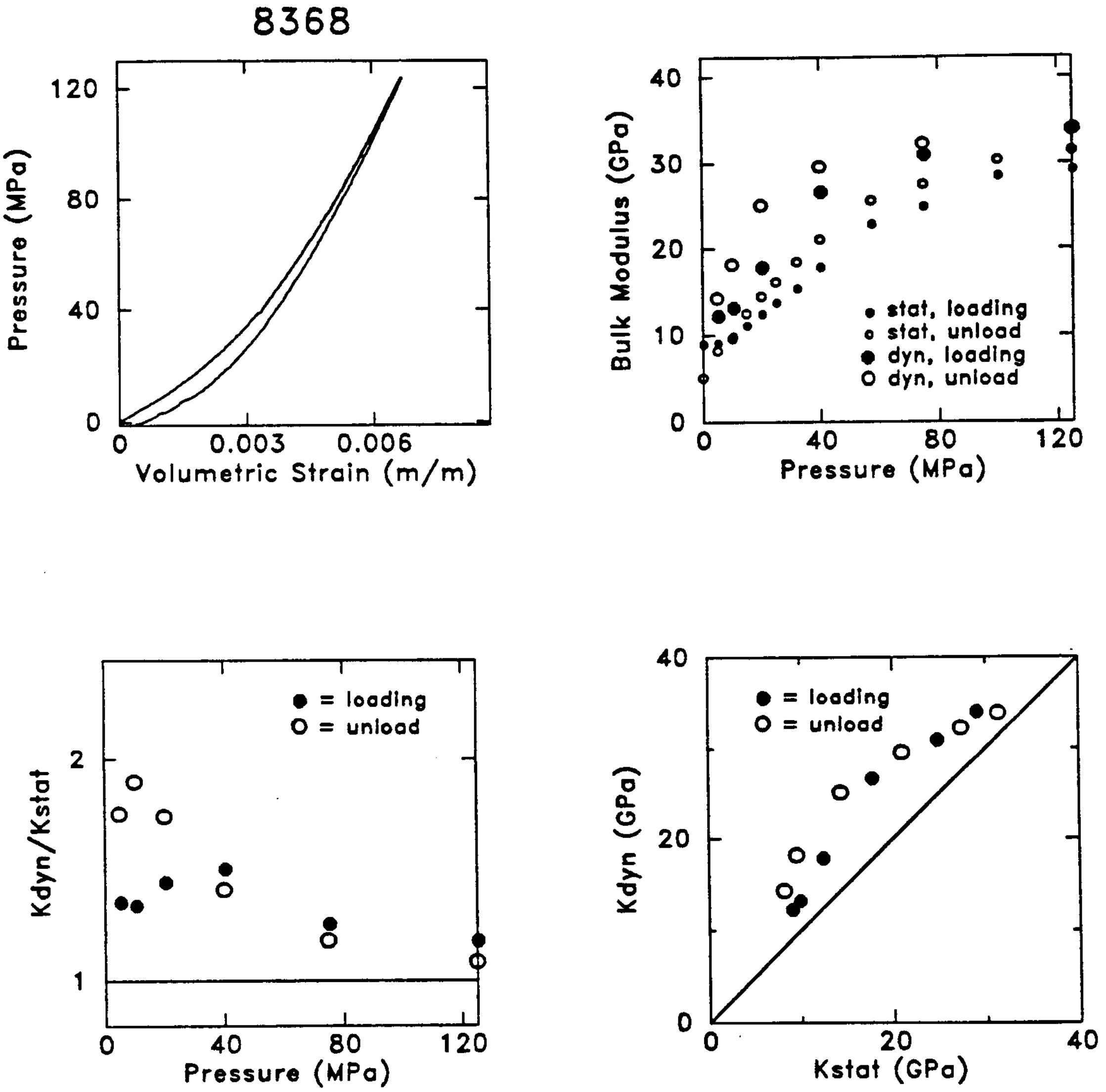
8368
Pressure (MPa)
120
80
40
0
0
0.003
0.006
Volumetric Strain (m/m)
Bulk Modulus (GPa)
40
30
20
10
0
0
40
80
120
Pressure (MPa)
● stat, loading
○ stat, unload
● dyn, loading
○ dyn, unload
Kdyn/Kstat
2
1
0
40
80
120
Pressure (MPa)
● = loading
○ = unload
Kdyn (GPa)
40
20
0
0
20
40
Kstat (GPa)
● = loading
○ = unload

Depth (feet) = 8382.0
Length (cm) = 3.73
Grain density (g/cm^3) = 2.64
Porosity (%) = 8.0

Petrographic data:
framework clay= 7.0
matrix clay = 3.0
ankerite = 0.0
dolomite = 0.0

Strain, Static Bulk Moduli, and Dry Velocities

P_c (MPa)	ϵ_{vol} (mstr)	K_{stat} (GPa)	K_{dyn} (GPa)	V_p (km/s)	V_s (km/s)	V_p/V_s	G_{dyn} (GPa)	σ_{dyn}
5.	0.93	5.17	7.13	3.093	2.245	1.38	12.63	-0.057
10.	1.92	5.71	9.97	3.381	2.364	1.43	14.01	0.022
20.	3.43	7.64	12.43	3.759	2.623	1.43	17.26	0.026
40.	5.45	12.70	17.67	4.341	2.976	1.46	22.24	0.057
75.	7.43	20.30	23.61	4.810	3.211	1.50	25.92	0.098
125.	9.50	26.07	26.24	4.985	3.287	1.52	27.17	0.115
125.	9.50	26.19	26.20	5.000	3.298	1.52	27.12	0.115
75.	7.49	22.55	24.16	4.876	3.249	1.50	26.29	0.101
40.	5.69	15.45	19.93	4.559	3.095	1.47	23.83	0.073
20.	4.03	8.63	13.82	4.024	2.824	1.42	19.83	0.015
10.	2.58	5.24	11.22	3.638	2.558	1.42	16.25	0.012
5.	1.49	3.72	9.16	3.349	2.376	1.41	14.01	-0.006

8382

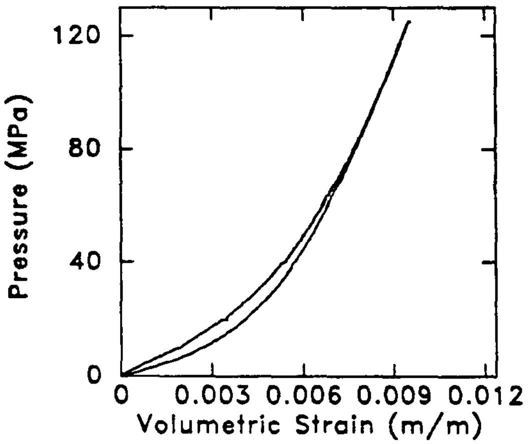
Pressure (MPa)
120
80
40
0
0
0.003
0.006
0.009
0.012
Volumetric Strain (m/m)

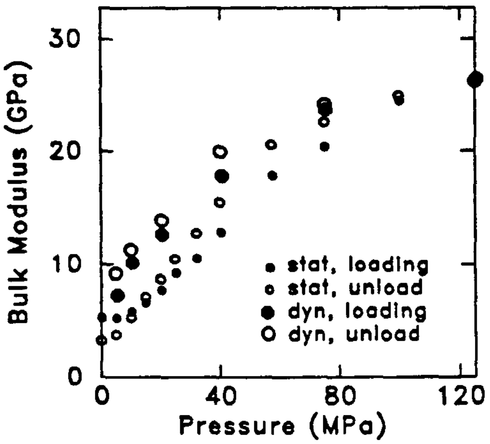
Bulk Modulus (GPa)
30
20
10
0
• stat, loading
∘ stat, unload
● dyn, loading
○ dyn, unload
0
40
80
120
Pressure (MPa)

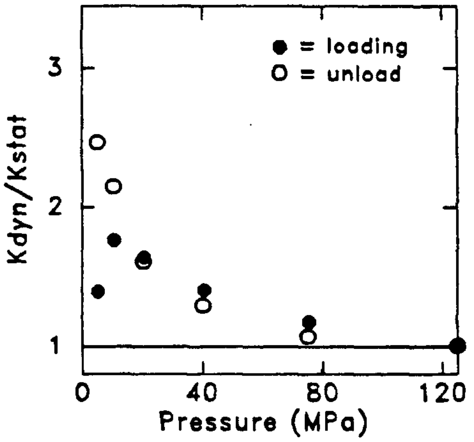
Kdyn/Kstat
3
2
1
● = loading
○ = unload
0
40
80
120
Pressure (MPa)

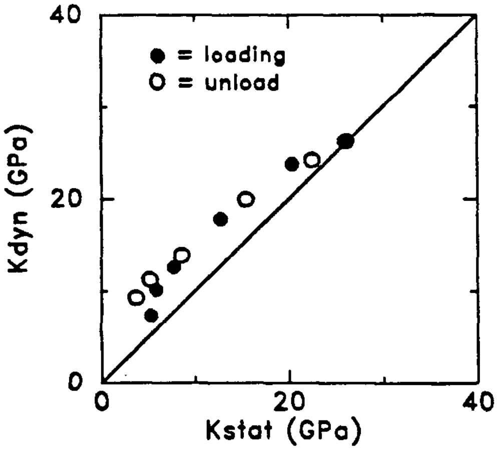
Kdyn (GPa)
40
20
0
● = loading
○ = unload
0
20
40
Kstat (GPa)

Depth (feet) = 8385.0
Length (cm) = 3.82
Grain density (g/cm^3) = 2.64
Porosity (%) = 5.4

Petrographic data:
framework clay= 2.0
matrix clay = 3.0
ankerite = 1.0
dolomite = 0.0

Strain, Static Bulk Moduli, and Dry Velocities

P_c (MPa)	ϵ_{vol} (mstr)	K_{stat} (GPa)	K_{dyn} (GPa)	V_p (km/s)	V_s (km/s)	V_p/V_s	G_{dyn} (GPa)	σ_{dyn}
5.	0.45	9.26	13.48	3.714	2.527	1.47	16.30	0.069
10.	1.07	9.86	15.63	3.996	2.717	1.47	18.85	0.070
20.	2.01	12.16	19.69	4.445	3.006	1.48	23.09	0.079
40.	3.26	19.82	24.37	4.923	3.321	1.48	28.21	0.082
75.	4.65	28.56	26.55	5.158	3.489	1.48	31.17	0.078
125.	6.24	33.61	27.31	5.242	3.551	1.48	32.28	0.076
125.	6.22	33.59	27.29	5.253	3.558	1.48	32.25	0.076
75.	4.64	30.92	26.78	5.196	3.515	1.48	31.44	0.078
40.	3.40	23.95	25.23	5.038	3.405	1.48	29.47	0.080
20.	2.39	14.08	22.42	4.731	3.189	1.48	25.83	0.084
10.	1.55	9.61	19.15	4.372	2.946	1.48	22.04	0.084
5.	1.00	7.36	14.87	3.995	2.753	1.45	19.23	0.048

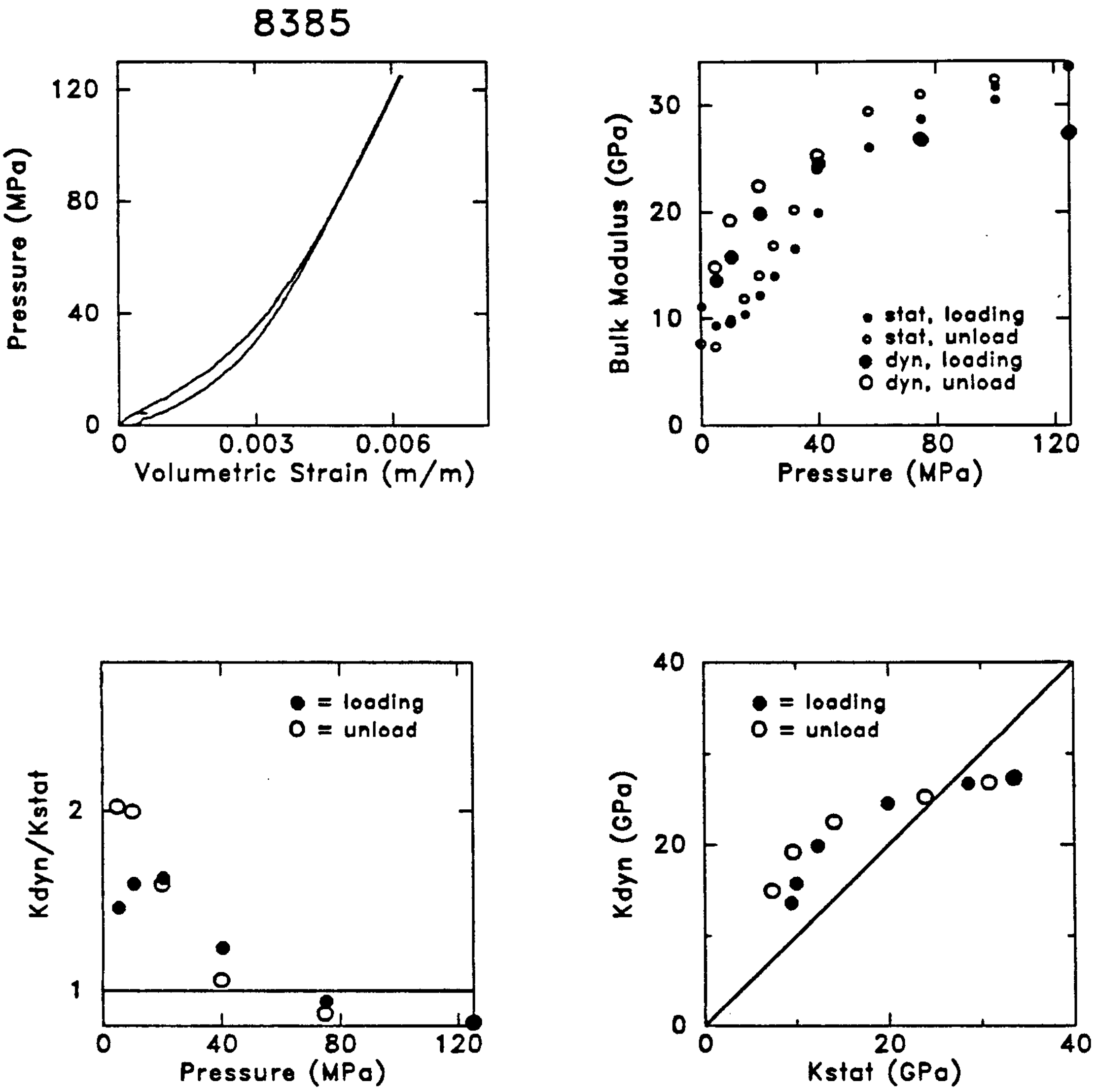

8385

Pressure (MPa)
120
80
40
0
0
0.003
0.006
Volumetric Strain (m/m)
Bulk Modulus (GPa)
30
20
10
0
0
40
80
120
Pressure (MPa)
• stat, loading
∘ stat, unload
● dyn, loading
○ dyn, unload
Kdyn/Kstat
● = loading
○ = unload
2
1
0
40
80
120
Pressure (MPa)
Kdyn (GPa)
40
20
0
● = loading
○ = unload
0
20
40
Kstat (GPa)

Depth (feet) = 8628.0
Length (cm) = 4.43
Grain density (g/cm^3) = 2.63
Porosity (%) = 10.5

Petrographic data:
framework clay= 6.4
matrix clay = 1.2
ankerite = 0.0
dolomite = 0.4

Strain, Static Bulk Moduli, and Dry Velocities

P_c (MPa)	ϵ_{vol} (mstr)	K_{stat} (GPa)	K_{dyn} (GPa)	V_p (km/s)	V_s (km/s)	V_p/V_s	G_{dyn} (GPa)	σ_{dyn}
5.	0.83	7.27	15.79	3.755	2.360	1.59	13.16	0.174
10.	1.44	9.08	16.01	3.880	2.493	1.56	14.71	0.148
20.	2.39	12.82	18.16	4.147	2.675	1.55	16.96	0.144
40.	3.50	20.62	20.79	4.401	2.822	1.56	18.91	0.151
75.	5.15	21.92	21.51	4.529	2.934	1.54	20.51	0.138
125.	7.42	21.69	22.30	4.606	2.986	1.54	21.31	0.138
125.	7.42	22.70	22.30	4.606	2.986	1.54	21.31	0.138
75.	5.29	21.77	21.50	4.538	2.946	1.54	20.67	0.136
40.	3.60	19.96	21.00	4.445	2.862	1.55	19.46	0.146
20.	2.48	16.43	19.51	4.292	2.765	1.55	18.12	0.145
10.	1.84	11.84	18.00	4.117	2.648	1.55	16.61	0.147
5.	1.33	7.95	16.26	3.907	2.509	1.56	14.89	0.149

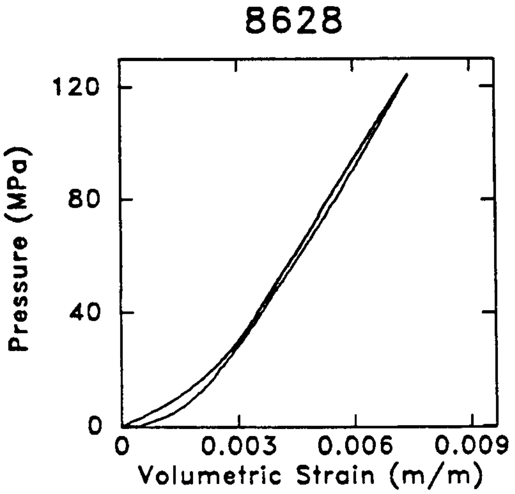
8628
Pressure (MPa)
120
80
40
0
0
0.003
0.006
0.009
Volumetric Strain (m/m)

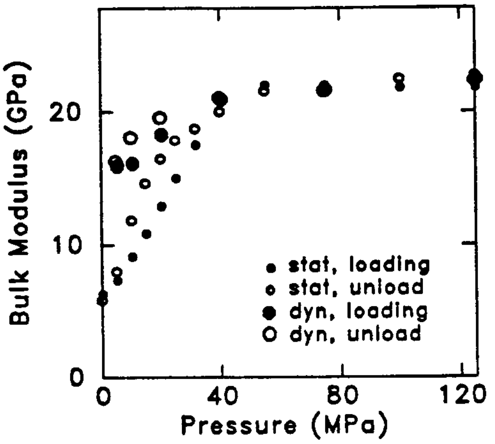
Bulk Modulus (GPa)
20
10
0
0
40
80
120
Pressure (MPa)
• stat, loading
∘ stat, unload
● dyn, loading
O dyn, unload

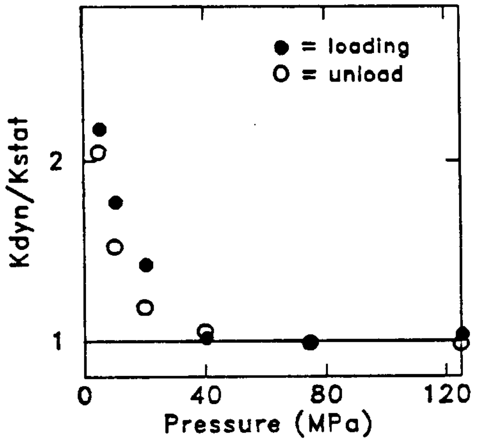
● = loading
O = unload
Kdyn/Kstat
2
1
0
40
80
120
Pressure (MPa)

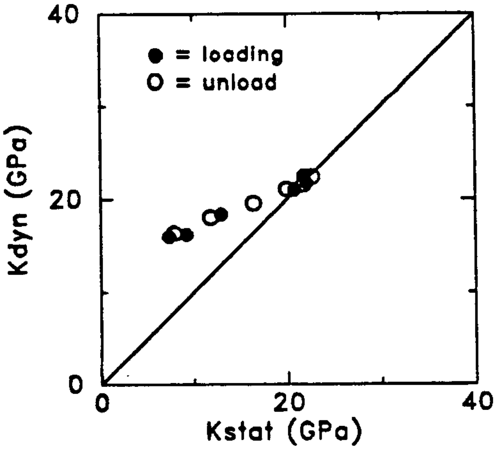
● = loading
O = unload
Kdyn (GPa)
40
20
0
0
20
40
Kstat (GPa)

Depth (feet) = 8634.0
Length (cm) = 4.47
Grain density (g/cm^3) = 2.64
Porosity (%) = 0.8

Petrographic data:
framework clay= 0.0
matrix clay = 0.0
ankerite = 9.6
dolomite = 36.4

Strain, Static Bulk Moduli, and Dry Velocities

P_c (MPa)	ϵ_{vol} (mstr)	K_{stat} (GPa)	K_{dyn} (GPa)	V_p (km/s)	V_s (km/s)	V_p/V_s	G_{dyn} (GPa)	σ_{dyn}
5.	0.36	16.54	28.14	4.696	2.920	1.61	22.43	0.185
10.	0.63	19.17	29.71	4.746	2.904	1.63	22.20	0.201
20.	1.13	20.72	30.36	4.811	2.953	1.63	22.98	0.198
40.	2.06	22.76	31.68	4.913	3.017	1.63	24.03	0.197
75.	3.55	25.44	33.09	5.011	3.075	1.63	25.02	0.198
125.	5.29	29.30	34.74	5.111	3.125	1.64	25.88	0.202
125.	5.24	32.44	34.76	5.110	3.124	1.64	25.90	0.202
75.	3.76	28.50	33.60	5.051	3.100	1.63	25.44	0.198
40.	2.44	24.03	32.43	4.973	3.056	1.63	24.66	0.197
20.	1.57	20.20	31.17	4.884	3.004	1.63	23.80	0.196
10.	1.05	16.70	30.41	4.812	2.951	1.63	22.95	0.198
5.	0.74	16.46	29.83	4.751	2.904	1.64	22.21	0.202

8634

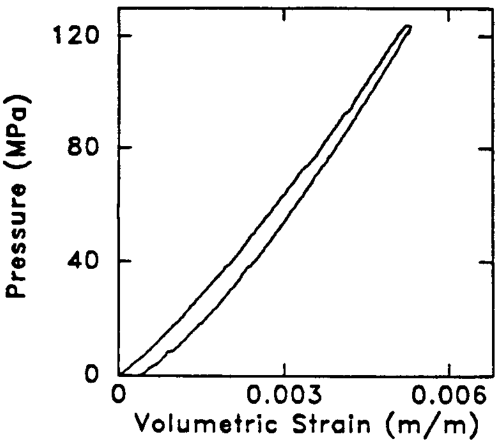
Pressure (MPa)
120
80
40
0
0
0.003
0.006
Volumetric Strain (m/m)

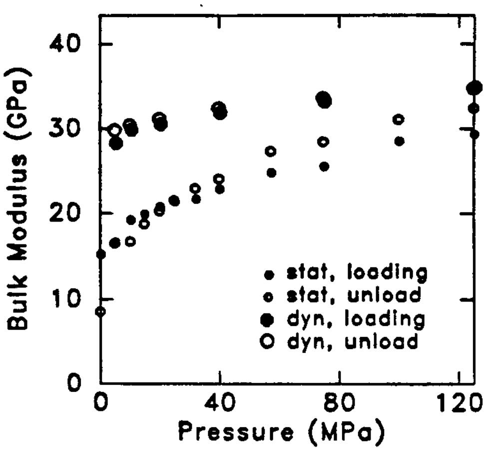
Bulk Modulus (GPa)
40
30
20
10
0
0
40
80
120
Pressure (MPa)
● stat, loading
○ stat, unload
● dyn, loading
○ dyn, unload

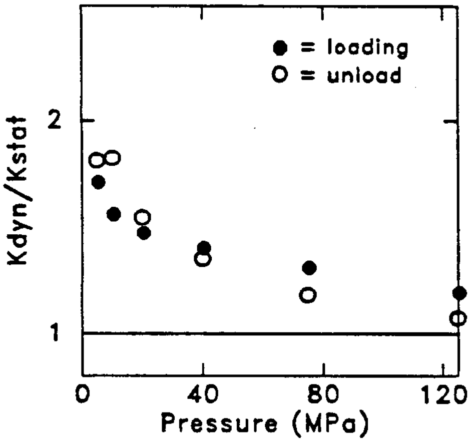
Kdyn/Kstat
2
1
0
40
80
120
Pressure (MPa)
● = loading
○ = unload

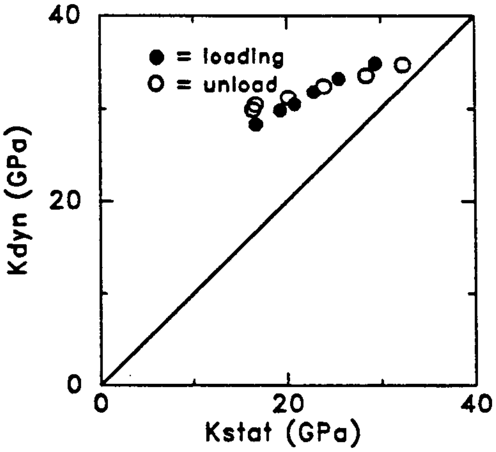
Kdyn (GPa)
40
20
0
0
20
40
Kstat (GPa)
● = loading
○ = unload

Depth (feet) = 8642.0
Length (cm) = 4.34
Grain density (g/cm^3) = 2.65
Porosity (%) = 3.6

Petrographic data:
framework clay= 0.4
matrix clay = 0.0
ankerite = 0.8
dolomite = 0.4

Strain, Static Bulk Moduli, and Dry Velocities

P_c (MPa)	ϵ_{vol} (mstr)	K_{stat} (GPa)	K_{dyn} (GPa)	V_p (km/s)	V_s (km/s)	V_p/V_s	G_{dyn} (GPa)	σ_{dyn}
5.	0.40	13.20	17.62	4.334	2.987	1.45	22.82	0.048
10.	0.76	14.70	18.92	4.458	3.060	1.46	23.97	0.055
20.	1.41	16.80	22.06	4.750	3.235	1.47	26.82	0.067
40.	2.41	23.54	26.85	5.179	3.503	1.48	31.49	0.078
75.	3.59	34.55	30.68	5.484	3.689	1.49	34.98	0.087
125.	4.83	38.92	32.77	5.603	3.742	1.50	36.05	0.098
125.	4.76	38.89	32.77	5.603	3.742	1.50	36.05	0.098
75.	3.62	36.05	31.14	5.512	3.701	1.49	35.21	0.089
40.	2.57	28.32	27.73	5.279	3.578	1.48	32.84	0.075
20.	1.72	19.55	23.67	4.933	3.365	1.47	29.02	0.065
10.	1.13	14.60	21.02	4.659	3.181	1.46	25.90	0.063
5.	0.79	11.10	18.95	4.458	3.058	1.46	23.93	0.056

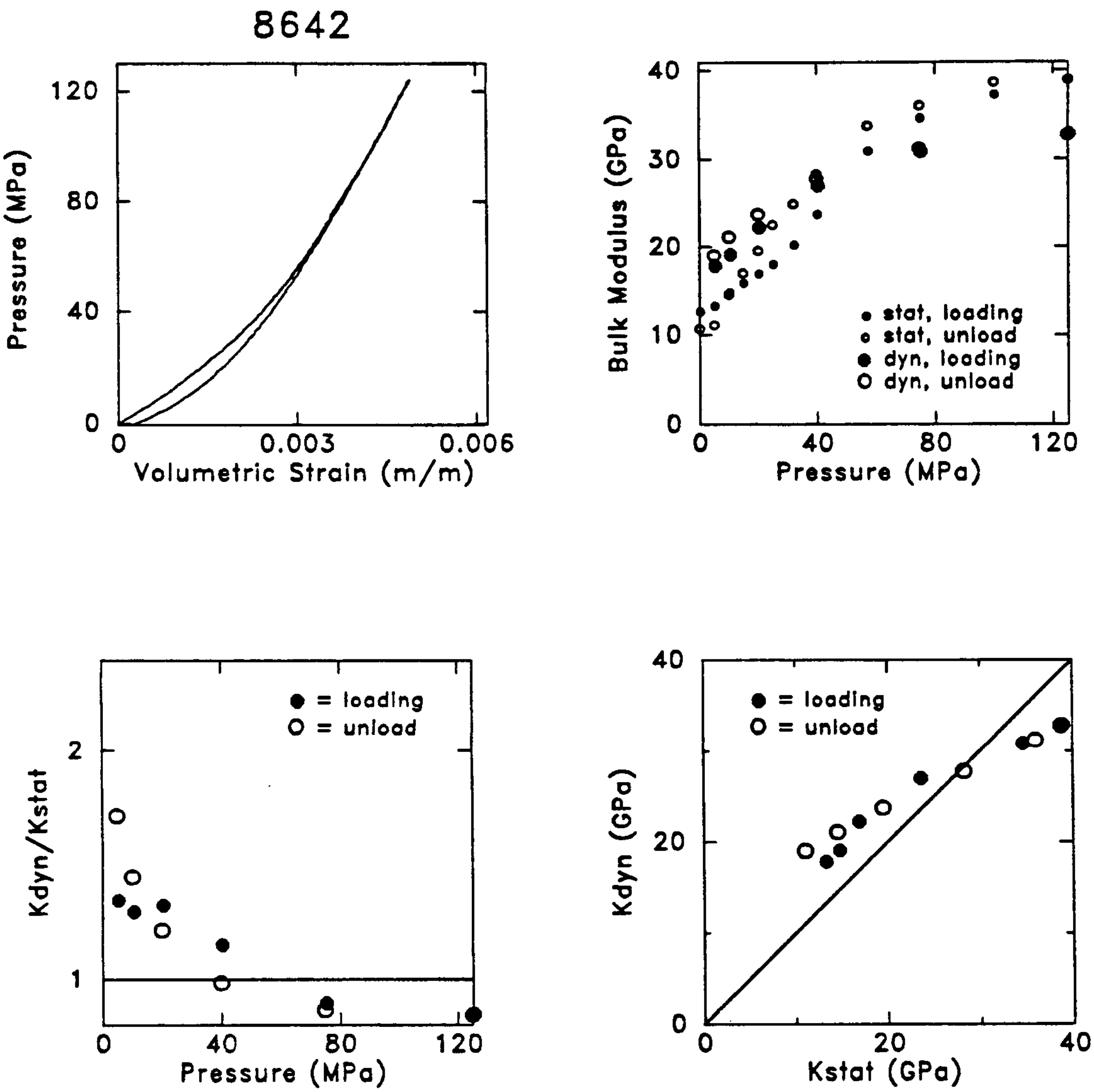
8642
Pressure (MPa)
120
80
40
0
0
0.003
0.006
Volumetric Strain (m/m)
Bulk Modulus (GPa)
40
30
20
10
0
0
40
80
120
Pressure (MPa)
● stat, loading
○ stat, unload
● dyn, loading
○ dyn, unload
Kdyn/Kstat
2
1
0
40
80
120
Pressure (MPa)
● = loading
○ = unload
Kdyn (GPa)
40
20
0
0
20
40
Kstat (GPa)
● = loading
○ = unload

Depth (feet) = 8666.0
Length (cm) = 4.36
Grain density (g/cm^3) = 2.68
Porosity (%) = 4.5

Petrographic data:
framework clay= 0.0
matrix clay = 3.0
ankerite = 19.0
dolomite = 0.0

Strain, Static Bulk Moduli, and Dry Velocities

P_c (MPa)	ϵ_{vol} (mstr)	K_{stat} (GPa)	K_{dyn} (GPa)	V_p (km/s)	V_s (km/s)	V_p/V_s	G_{dyn} (GPa)	σ_{dyn}
5.	0.66	7.62	15.74	3.829	2.532	1.51	16.49	0.112
12.	1.22	8.24	19.99	4.194	2.714	1.55	18.97	0.140
20.	2.50	10.88	22.67	4.436	2.857	1.55	21.05	0.145
40.	4.00	15.51	26.35	4.764	3.061	1.56	24.20	0.148
75.	5.83	21.93	28.51	4.982	3.218	1.55	26.79	0.142
125.	7.97	25.85	30.51	5.119	3.287	1.56	27.94	0.149
125.	7.87	27.59	30.48	5.137	3.299	1.56	27.92	0.149
75.	6.04	25.28	29.13	5.055	3.262	1.55	27.26	0.143
40.	4.50	20.20	27.25	4.917	3.185	1.54	25.96	0.138
20.	3.44	15.46	25.07	4.725	3.064	1.54	23.99	0.137
10.	2.71	10.78	22.41	4.488	2.919	1.54	21.77	0.133
4.	2.12	8.20	19.27	4.217	2.770	1.52	19.58	0.120

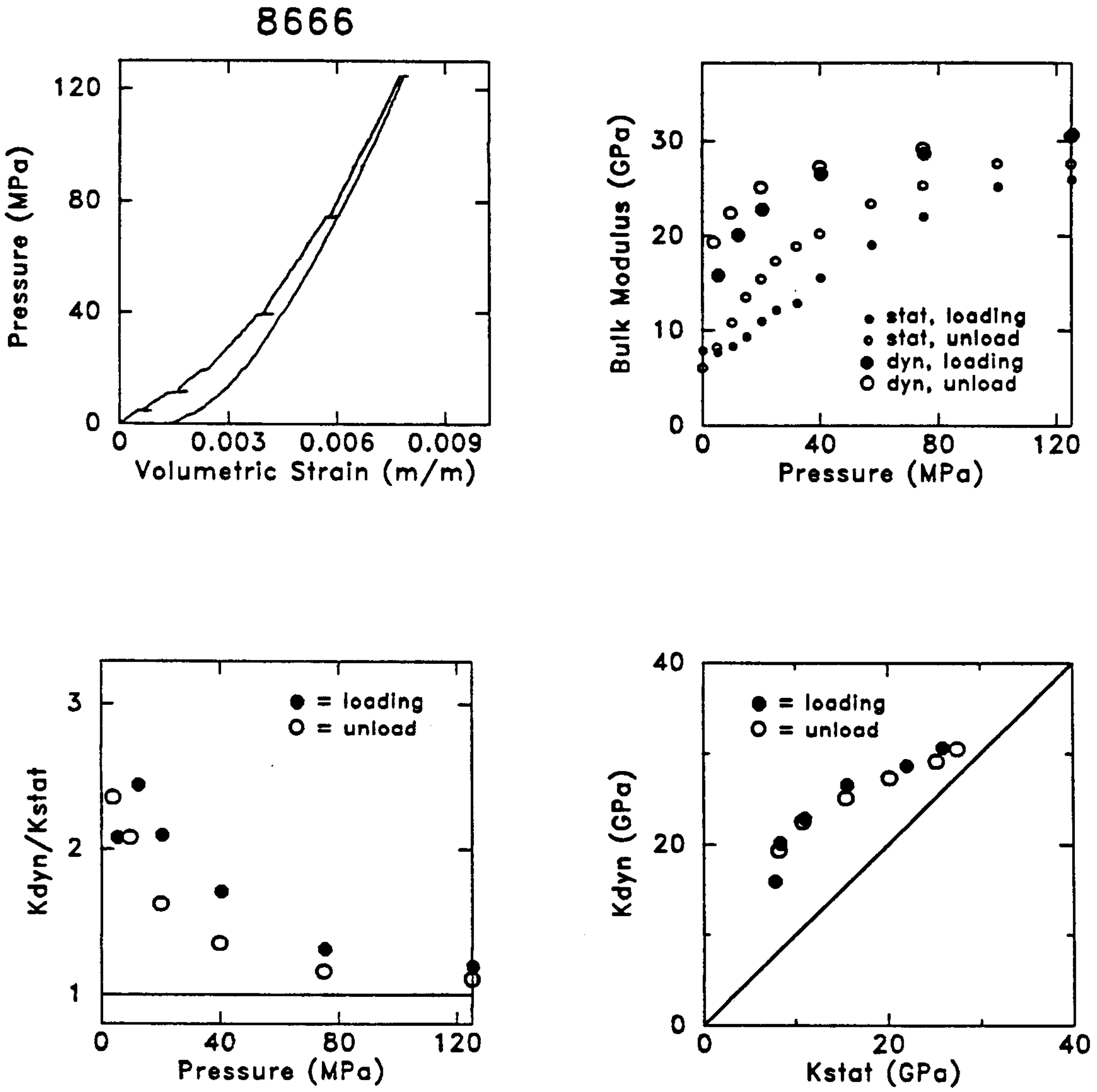
8666
Pressure (MPa)
0
40
80
120
Volumetric Strain (m/m)
0
0.003
0.006
0.009
Bulk Modulus (GPa)
0
10
20
30
Pressure (MPa)
0
40
80
120
● stat, loading
○ stat, unload
● dyn, loading
○ dyn, unload
Kdyn/Kstat
1
2
3
Pressure (MPa)
0
40
80
120
● = loading
○ = unload
Kdyn (GPa)
0
20
40
Kstat (GPa)
0
20
40
● = loading
○ = unload

Depth (feet) = 8672.0
Length (cm) = 4.30
Grain density (g/cm^3) = 2.66
Porosity (%) = 2.0

Petrographic data:
framework clay= 2.0
matrix clay = 0.0
ankerite = 1.2
dolomite = 0.4

Strain, Static Bulk Moduli, and Dry Velocities

P_c (MPa)	ϵ_{vol} (mstr)	K_{stat} (GPa)	K_{dyn} (GPa)	V_p (km/s)	V_s (km/s)	V_p/V_s	G_{dyn} (GPa)	σ_{dyn}
5.	0.76	7.21	12.49	3.684	2.566	1.44	17.17	0.029
10.	1.44	7.64	13.47	3.821	2.661	1.44	18.48	0.029
20.	2.58	10.05	15.35	4.042	2.802	1.44	20.53	0.038
40.	4.16	15.54	20.00	4.407	2.974	1.48	23.19	0.082
75.	5.88	24.00	24.14	4.720	3.134	1.51	25.83	0.106
125.	7.65	27.20	27.99	4.956	3.233	1.53	27.54	0.130
125.	7.58	30.17	28.01	4.955	3.233	1.53	27.56	0.130
75.	5.99	25.32	25.90	4.837	3.187	1.52	26.72	0.116
40.	4.46	18.74	22.36	4.610	3.089	1.49	25.03	0.092
20.	3.20	11.81	19.29	4.339	2.931	1.48	22.49	0.080
10.	2.23	7.70	16.18	4.085	2.806	1.46	20.58	0.053
5.	1.40	6.08	14.22	3.883	2.688	1.44	18.86	0.040

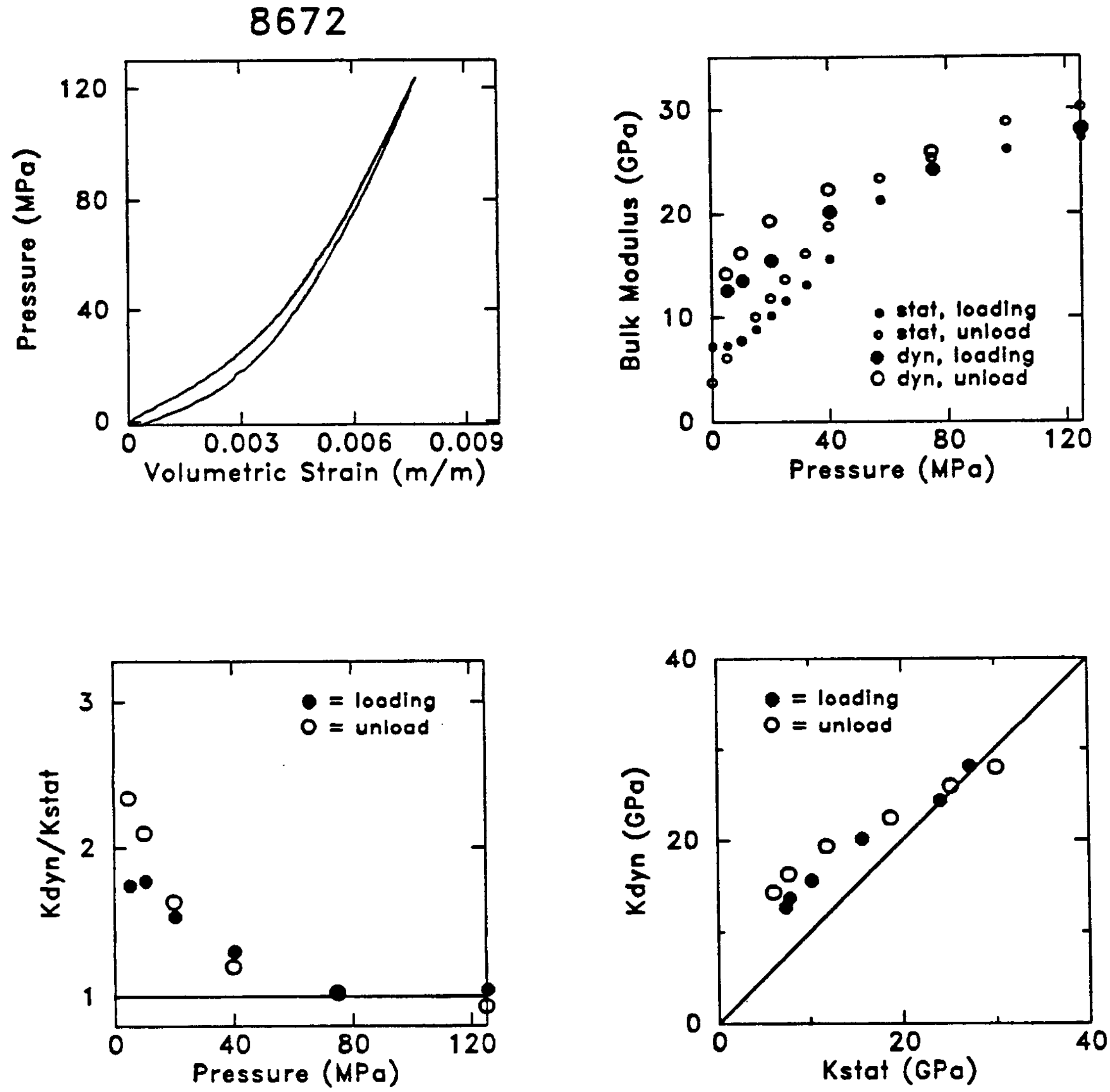
8672
Pressure (MPa)
120
80
40
0
0
0.003
0.006
0.009
Volumetric Strain (m/m)
Bulk Modulus (GPa)
30
20
10
0
0
40
80
120
Pressure (MPa)
• stat, loading
∘ stat, unload
● dyn, loading
○ dyn, unload
Kdyn/Kstat
3
2
1
0
40
80
120
Pressure (MPa)
● = loading
○ = unload
Kdyn (GPa)
40
20
0
0
20
40
Kstat (GPa)
● = loading
○ = unload

Depth (feet) = 8674.0
Length (cm) = 4.48
Grain density (g/cm^3) = 2.70
Porosity (%) = 1.0

Petrographic data:
framework clay= 12.4
matrix clay = 3.2
ankerite = 2.8
dolomite = 18.4

Strain, Static Bulk Moduli, and Dry Velocities

P_c (MPa)	ϵ_{vol} (mstr)	K_{stat} (GPa)	K_{dyn} (GPa)	V_p (km/s)	V_s (km/s)	V_p/V_s	G_{dyn} (GPa)	σ_{dyn}
5.	0.22	26.51	39.68	5.308	3.166	1.68	26.84	0.224
10.	0.39	29.24	39.98	5.334	3.186	1.67	27.19	0.223
20.	0.70	34.30	42.57	5.451	3.220	1.69	27.79	0.232
40.	1.20	40.78	44.17	5.573	3.308	1.68	29.35	0.228
75.	2.04	42.54	46.00	5.651	3.331	1.70	29.78	0.234
125.	3.20	41.98	49.53	5.790	3.363	1.72	30.38	0.245
125.	3.20	44.27	49.42	5.804	3.371	1.72	30.30	0.245
75.	2.10	44.15	47.72	5.737	3.354	1.71	29.98	0.240
40.	1.29	42.77	46.05	5.657	3.321	1.70	29.37	0.237
20.	0.79	38.04	44.36	5.573	3.285	1.70	28.73	0.234
10.	0.50	33.56	42.89	5.491	3.244	1.69	28.00	0.232
5.	0.37	30.26	40.70	5.386	3.206	1.68	27.33	0.226

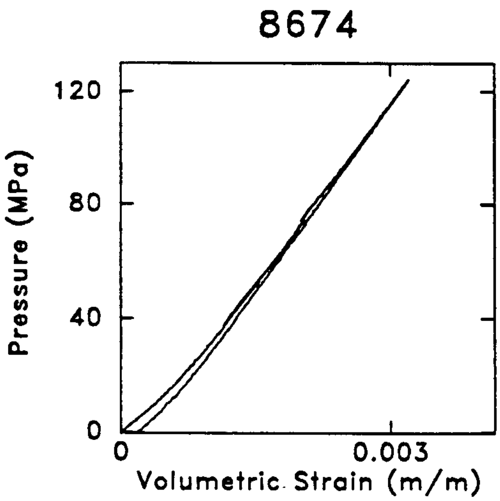
8674
Pressure (MPa)
120
80
40
0
0
0.003
Volumetric Strain (m/m)

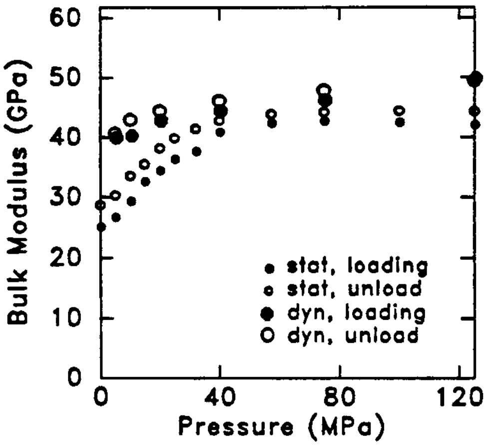
Bulk Modulus (GPa)
60
50
40
30
20
10
0
● stat, loading
○ stat, unload
● dyn, loading
○ dyn, unload
0
40
80
120
Pressure (MPa)

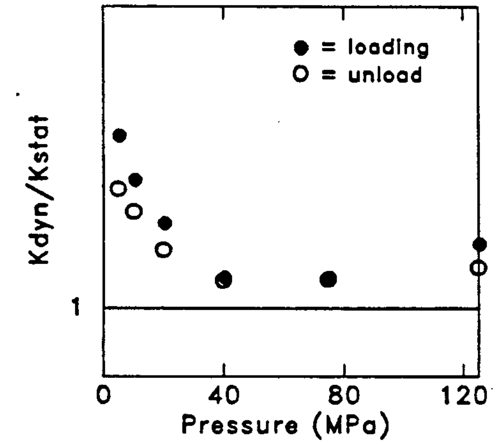
● = loading
○ = unload
Kdyn/Kstat
1
0
40
80
120
Pressure (MPa)

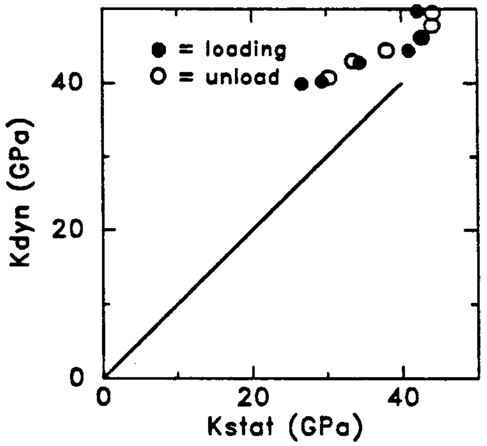
● = loading
○ = unload
Kdyn (GPa)
40
20
0
0
20
40
Kstat (GPa)

Depth (feet) = 8675.0
Length (cm) = 4.43
Grain density (g/cm^3) = 2.66
Porosity (%) = 2.0

Petrographic data:
framework clay= 0.0
matrix clay = 56.0
ankerite = 2.0
dolomite = 0.0

Strain, Static Bulk Moduli, and Dry Velocities

P_c (MPa)	ϵ_{vol} (mstr)	K_{stat} (GPa)	K_{dyn} (GPa)	V_p (km/s)	V_s (km/s)	V_p/V_s	G_{dyn} (GPa)	σ_{dyn}
5.	0.36	15.46	23.66	4.580	2.996	1.53	23.57	0.126
10.	0.69	16.49	25.06	4.642	3.001	1.55	23.68	0.141
20.	1.25	18.06	26.38	4.714	3.025	1.56	24.08	0.150
40.	2.28	20.60	28.60	4.829	3.059	1.58	24.67	0.165
75.	3.94	22.59	30.61	4.946	3.110	1.59	25.58	0.173
125.	5.89	23.87	32.66	5.048	3.144	1.61	26.25	0.183
125.	5.91	28.14	32.67	5.048	3.144	1.61	26.25	0.183
75.	4.17	24.72	31.11	4.973	3.120	1.59	25.77	0.175
40.	2.63	20.81	29.66	4.892	3.086	1.59	25.14	0.170
20.	1.61	16.48	28.00	4.801	3.052	1.57	24.53	0.161
10.	0.95	13.07	26.21	4.715	3.034	1.55	24.21	0.147
5.	0.55	13.30	25.11	4.656	3.016	1.54	23.91	0.139

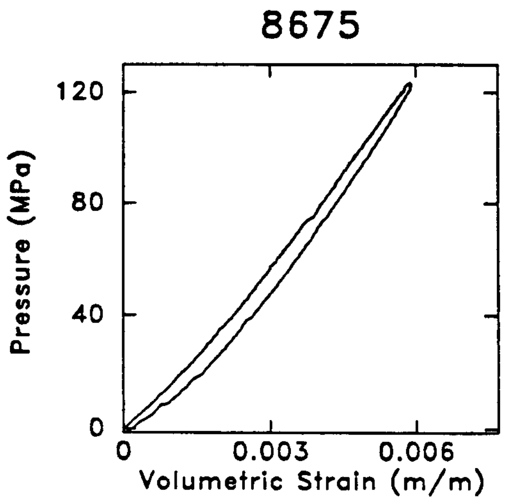
8675
Pressure (MPa)
120
80
40
0
0
0.003
0.006
Volumetric Strain (m/m)

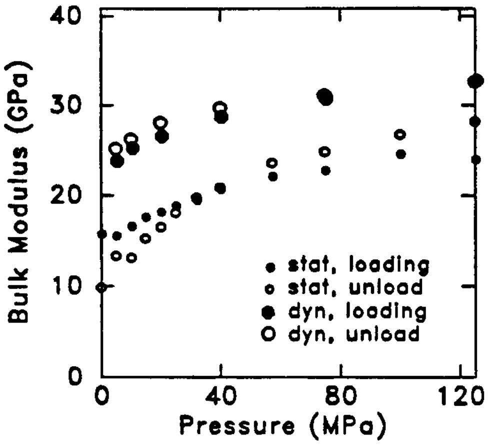
Bulk Modulus (GPa)
40
30
20
10
0
0
40
80
120
Pressure (MPa)
• stat, loading
∘ stat, unload
● dyn, loading
○ dyn, unload

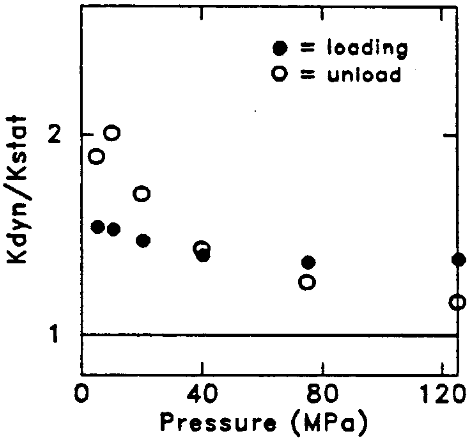
Kdyn/Kstat
2
1
0
40
80
120
Pressure (MPa)
● = loading
○ = unload

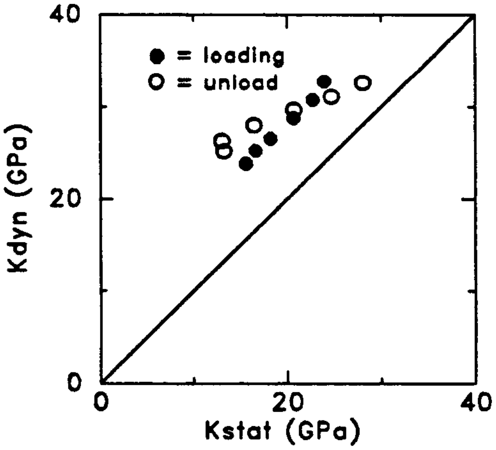
Kdyn (GPa)
40
20
0
0
20
40
Kstat (GPa)
● = loading
○ = unload

Depth (feet) = 9170.0
Length (cm) = 3.70
Grain density (g/cm^3) = 2.68
Porosity (%) = 1.1

Petrographic data:
framework clay= 0.0
matrix clay = 43.0
ankerite = 30.0
dolomite = 0.0

Strain, Static Bulk Moduli, and Dry Velocities

P_c (MPa)	ϵ_{vol} (mstr)	K_{stat} (GPa)	K_{dyn} (GPa)	V_p (km/s)	V_s (km/s)	V_p/V_s	G_{dyn} (GPa)	σ_{dyn}
5.	0.25	20.97	25.10	4.538	2.912	1.56	22.91	0.150
10.	0.47	20.18	25.64	4.566	2.919	1.56	23.02	0.154
20.	0.97	20.10	26.79	4.635	2.947	1.57	23.47	0.161
40.	1.95	21.43	28.58	4.737	2.984	1.59	24.10	0.171
75.	3.49	23.74	31.48	4.894	3.041	1.61	25.05	0.186
125.	5.37	28.02	34.68	5.055	3.095	1.63	25.98	0.200
125.	5.35	29.71	34.56	5.073	3.106	1.63	25.89	0.200
75.	3.63	26.13	32.80	4.994	3.084	1.62	25.46	0.192
40.	2.17	21.36	30.60	4.883	3.048	1.60	24.80	0.181
20.	1.18	18.37	28.78	4.777	3.004	1.59	24.05	0.173
10.	0.61	15.95	27.23	4.693	2.975	1.58	23.58	0.164
5.	0.30	16.77	26.39	4.646	2.959	1.57	23.32	0.159

9170

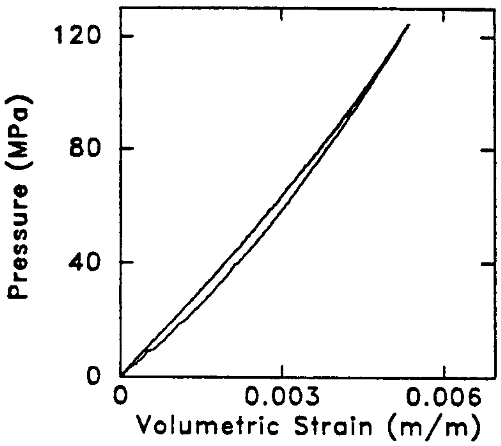
Pressure (MPa)
120
80
40
0
0
0.003
0.006
Volumetric Strain (m/m)

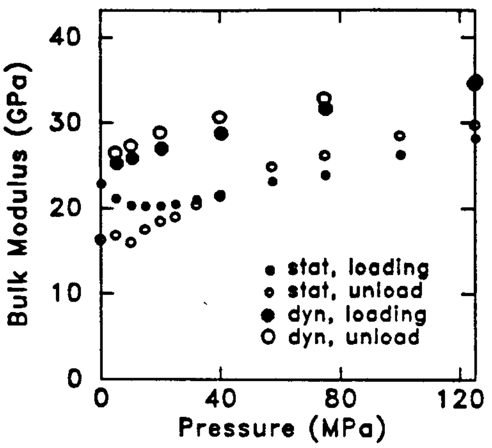
Bulk Modulus (GPa)
40
30
20
10
0
0
40
80
120
Pressure (MPa)
• stat, loading
∘ stat, unload
● dyn, loading
○ dyn, unload

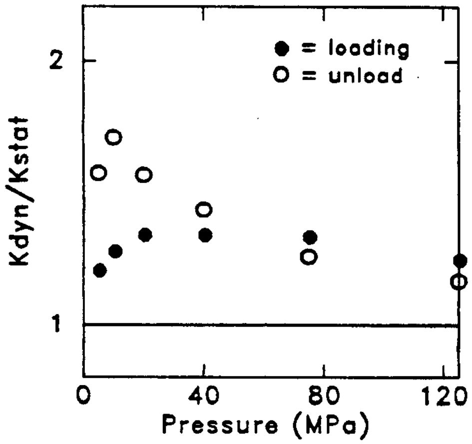
Kdyn/Kstat
2
1
0
40
80
120
Pressure (MPa)
● = loading
○ = unload

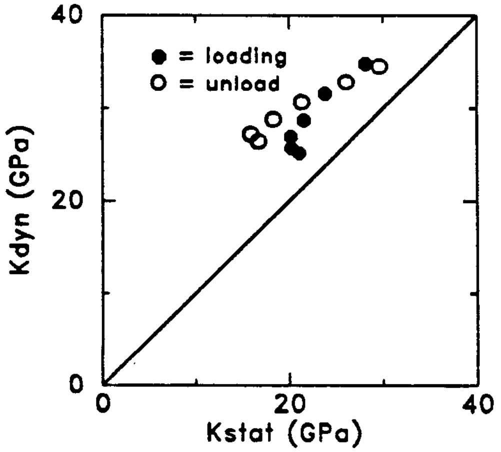
Kdyn (GPa)
40
20
0
0
20
40
Kstat (GPa)
● = loading
○ = unload

Depth (feet) = 9665.0
Length (cm) = 3.98
Grain density (g/cm^3) = 2.65
Porosity (%) = 11.8

Petrographic data:
framework clay= 10.0
matrix clay = 0.0
ankerite = 6.0
dolomite = 0.0

Strain, Dry Velocities, and Static Bulk Moduli

P_c (MPa)	ϵ_{vol} (mstr)	K_{stat} (GPa)	K_{dyn} (GPa)	V_p (km/s)	V_s (km/s)	V_p/V_s	G_{dyn} (GPa)	σ_{dyn}
5.	0.95	6.24	5.61	2.771	1.992	1.39	9.33	-0.035
10.	1.70	7.41	7.48	3.037	2.129	1.43	10.67	0.017
20.	2.83	9.62	10.33	3.428	2.351	1.46	13.03	0.056
40.	4.42	14.44	13.08	3.809	2.594	1.47	15.91	0.067
75.	6.50	18.30	17.09	4.180	2.775	1.51	18.26	0.106
125.	9.07	19.22	19.90	4.392	2.864	1.53	19.53	0.130
125.	9.03	20.28	19.90	4.392	2.864	1.53	19.53	0.130
75.	6.60	18.24	18.13	4.256	2.802	1.52	18.63	0.117
40.	4.51	14.67	14.27	3.945	2.673	1.48	16.89	0.076
20.	2.99	10.72	10.77	3.576	2.483	1.44	14.54	0.035
10.	1.87	8.02	8.98	3.304	2.308	1.43	12.54	0.023
5.	1.21	6.32	7.81	3.109	2.181	1.43	11.19	0.015

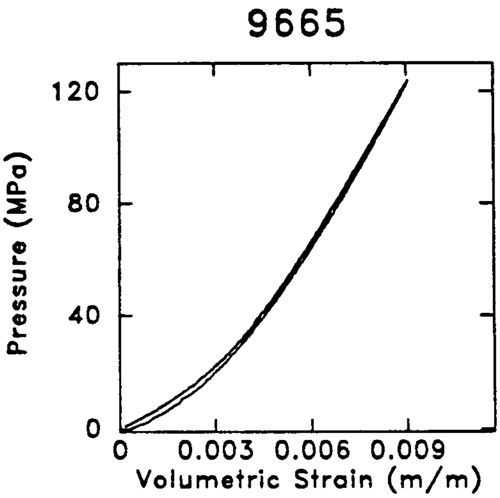
9665
Pressure (MPa)
120
80
40
0
0
0.003
0.006
0.009
Volumetric Strain (m/m)

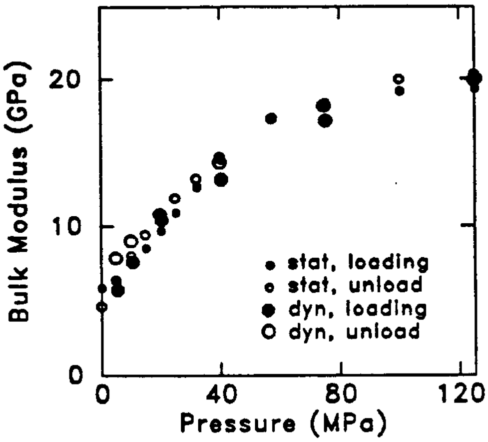
Bulk Modulus (GPa)
20
10
0
0
40
80
120
Pressure (MPa)
• stat, loading
∘ stat, unload
● dyn, loading
O dyn, unload

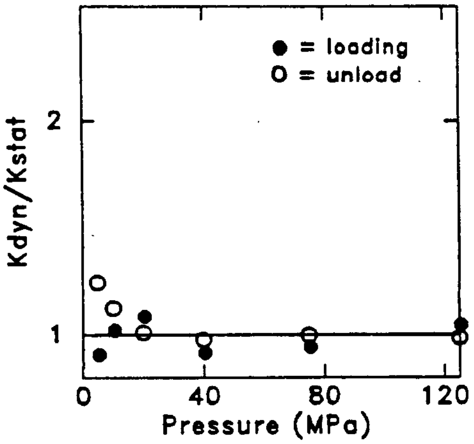
Kdyn/Kstat
2
1
0
40
80
120
Pressure (MPa)
● = loading
O = unload

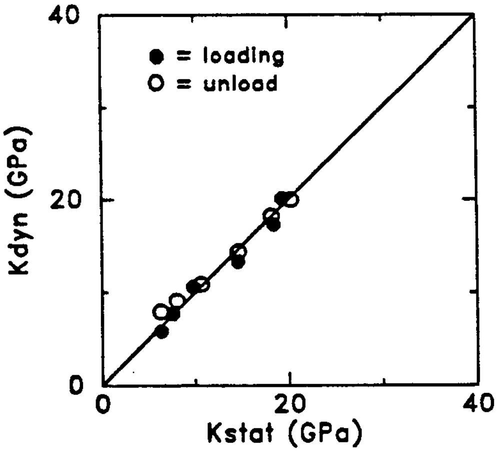
Kdyn (GPa)
40
20
0
0
20
40
Kstat (GPa)
● = loading
O = unload

Depth (feet) = 9666.0
Length (cm) = 3.99
Grain density (g/cm^3) = 2.69
Porosity (%) = 5.3

Petrographic data:
framework clay= 0.0
matrix clay = 0.0
ankerite = 50.0
dolomite = 0.0

Strain, Static Bulk Moduli, and Dry Velocities

P_c (MPa)	ϵ_{vol} (mstr)	K_{stat} (GPa)	K_{dyn} (GPa)	V_p (km/s)	V_s (km/s)	V_p/V_s	G_{dyn} (GPa)	σ_{dyn}
5.	0.60	9.65	10.90	3.653	2.614	1.40	17.58	-0.025
10.	1.09	10.14	12.35	3.759	2.646	1.42	18.03	0.009
20.	1.97	12.14	14.78	3.967	2.740	1.45	19.35	0.044
40.	3.47	15.53	20.21	4.363	2.901	1.50	21.76	0.104
75.	5.39	20.30	25.58	4.724	3.056	1.55	24.23	0.140
110.	6.89	22.65	28.73	4.889	3.104	1.57	25.05	0.162
110.	6.91	29.31	28.74	4.889	3.104	1.57	25.05	0.162
75.	5.70	26.60	26.86	4.804	3.089	1.55	24.77	0.147
40.	4.26	20.74	23.38	4.589	3.003	1.53	23.35	0.125
20.	3.10	14.71	19.63	4.328	2.890	1.50	21.58	0.098
10.	2.42	9.97	15.22	4.019	2.774	1.45	19.86	0.045
5.	1.81	8.16	12.93	3.842	2.703	1.42	18.84	0.010

9666

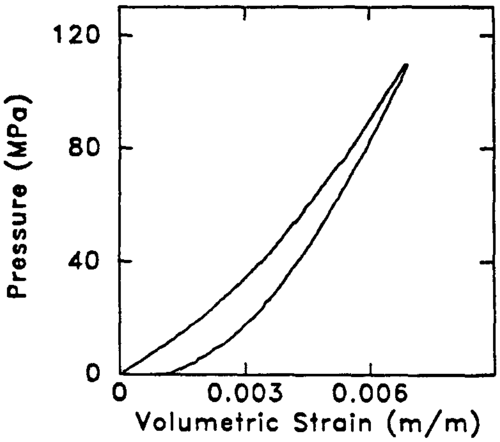
Pressure (MPa)
120
80
40
0
0
0.003
0.006
Volumetric Strain (m/m)

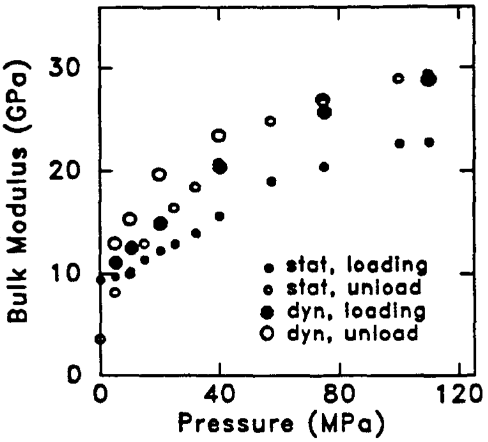
Bulk Modulus (GPa)
30
20
10
0
0
40
80
120
Pressure (MPa)
• stat, loading
∘ stat, unload
● dyn, loading
○ dyn, unload

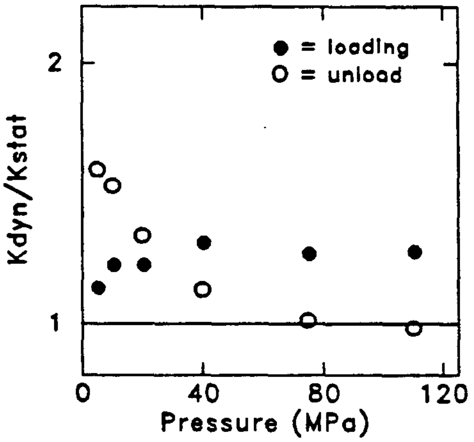
Kdyn/Kstat
2
1
0
40
80
120
Pressure (MPa)
● = loading
○ = unload

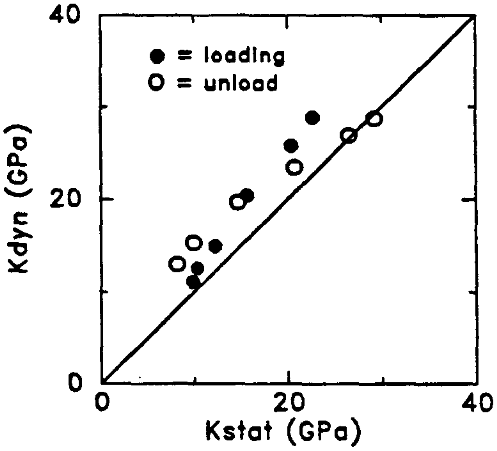
Kdyn (GPa)
40
20
0
0
20
40
Kstat (GPa)
● = loading
○ = unload

Depth (feet) = 9733.0
Length (cm) = 3.95
Grain density (g/cm^3) = 2.66
Porosity (%) = 3.1

Petrographic data:
framework clay= 6.0
matrix clay = 9.0
ankerite = 14.0
dolomite = 0.0

Strain, Static Bulk Moduli, and Dry Velocities

P_c (MPa)	ϵ_{vol} (mstr)	K_{stat} (GPa)	K_{dyn} (GPa)	V_p (km/s)	V_s (km/s)	V_p/V_s	G_{dyn} (GPa)	σ_{dyn}
5.	0.92	5.84	3.57	2.905	2.307	1.26	14.19	-0.355
10.	1.73	5.99	4.87	3.052	2.370	1.29	14.97	-0.260
20.	3.31	7.08	7.81	3.367	2.511	1.34	16.82	-0.127
40.	5.70	10.05	13.39	3.864	2.727	1.42	19.87	0.004
75.	8.36	15.80	20.41	4.360	2.922	1.49	22.84	0.092
125.	10.85	19.29	25.80	4.682	3.037	1.54	24.71	0.137
125.	10.79	24.76	25.69	4.702	3.050	1.54	24.61	0.137
75.	8.93	21.04	22.73	4.530	2.990	1.51	23.63	0.114
40.	7.01	14.50	17.49	4.196	2.869	1.46	21.73	0.061
20.	5.37	9.13	11.63	3.767	2.708	1.39	19.33	-0.035
10.	4.08	6.05	8.09	3.435	2.558	1.34	17.24	-0.123
5.	3.16	4.58	5.81	3.200	2.455	1.30	15.87	-0.215

9733

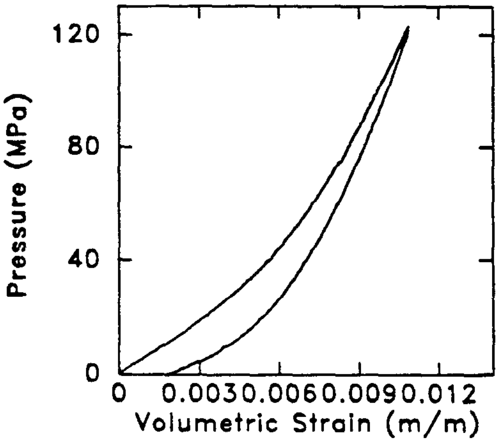
Pressure (MPa)
120
80
40
0
0
0.003
0.006
0.009
0.012
Volumetric Strain (m/m)

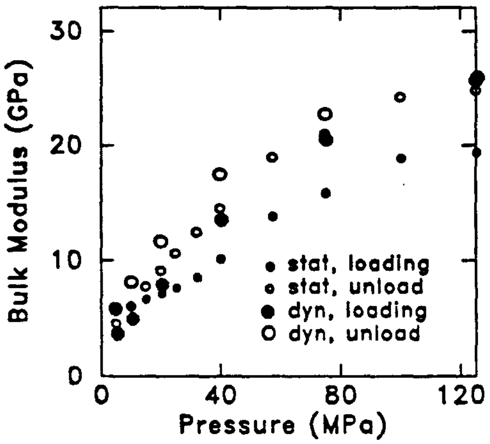
Bulk Modulus (GPa)
30
20
10
0
0
40
80
120
Pressure (MPa)
● stat, loading
○ stat, unload
● dyn, loading
○ dyn, unload

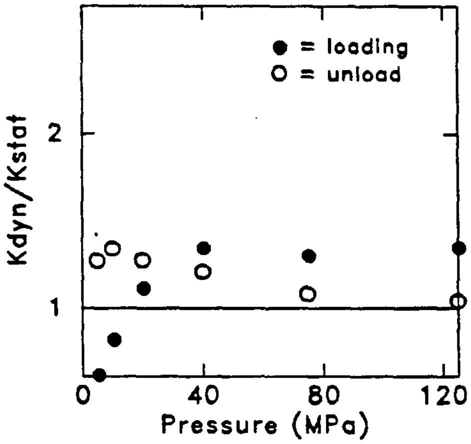
Kdyn/Kstat
2
1
0
40
80
120
Pressure (MPa)
● = loading
○ = unload

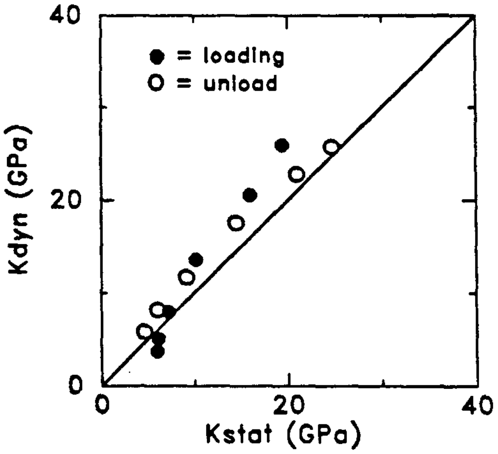
Kdyn (GPa)
40
20
0
0
20
40
Kstat (GPa)
● = loading
○ = unload

Depth (feet) = 9747.0
Length (cm) = 4.13
Grain density (g/cm^3) = 2.67
Porosity (%) = 4.1

Petrographic data:
framework clay= 11.0
matrix clay = 8.0
ankerite = 69.0
dolomite = 1.0

Strain, Static Bulk Moduli, and Dry Velocities

P_c (MPa)	ϵ_{vol} (mstr)	K_{stat} (GPa)	K_{dyn} (GPa)	V_p (km/s)	V_s (km/s)	V_p/V_s	G_{dyn} (GPa)	σ_{dyn}
5.	0.81	6.05	9.36	3.429	2.482	1.38	16.25	-0.050
10.	1.65	6.47	11.30	3.604	2.556	1.41	17.25	-0.006
20.	3.04	7.80	13.47	3.859	2.710	1.42	19.40	0.014
40.	5.21	11.22	19.18	4.326	2.932	1.48	22.74	0.075
75.	7.64	17.34	25.60	4.759	3.121	1.53	25.80	0.123
125.	9.84	22.65	29.68	5.002	3.221	1.55	27.51	0.146
125.	9.80	26.33	29.53	5.029	3.238	1.55	27.37	0.146
75.	7.98	21.79	25.62	4.819	3.169	1.52	26.18	0.119
40.	6.11	15.39	21.84	4.557	3.046	1.50	24.16	0.096
20.	4.57	9.84	16.80	4.205	2.901	1.45	21.89	0.046
10.	3.43	6.72	13.19	3.899	2.756	1.41	19.74	0.001
5.	2.56	5.12	11.35	3.706	2.650	1.40	18.24	-0.023

9747

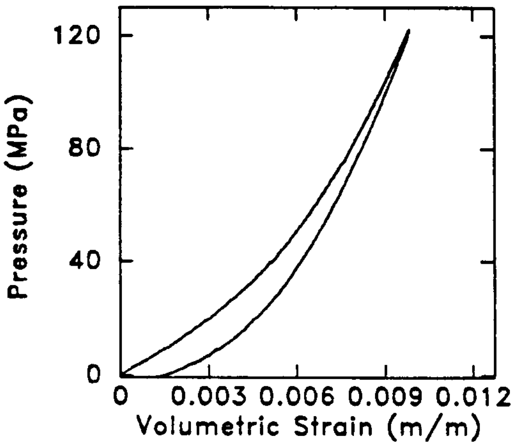
Pressure (MPa)
120
80
40
0
0
0.003
0.006
0.009
0.012
Volumetric Strain (m/m)

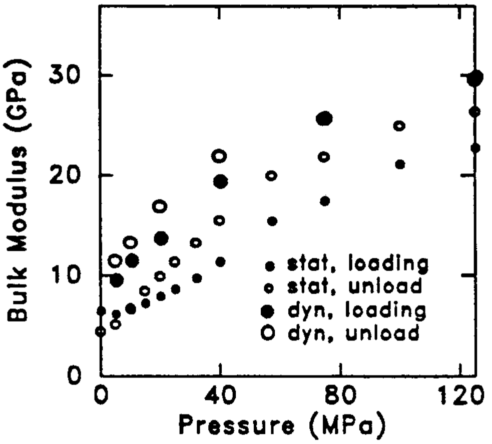
Bulk Modulus (GPa)
30
20
10
0
0
40
80
120
Pressure (MPa)
● stat, loading
○ stat, unload
● dyn, loading
O dyn, unload

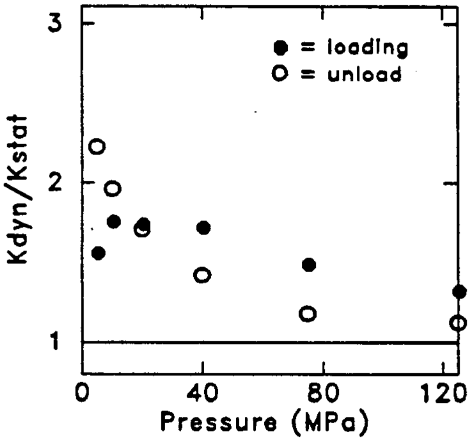
Kdyn/Kstat
3
2
1
0
40
80
120
Pressure (MPa)
● = loading
O = unload

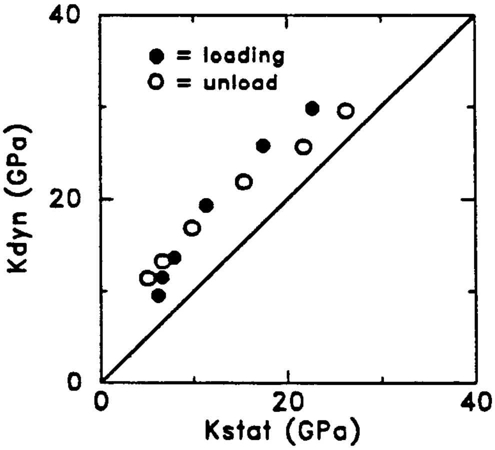
Kdyn (GPa)
40
20
0
0
20
40
Kstat (GPa)
● = loading
O = unload

Depth (feet) = 9750.0
Length (cm) = 3.16
Grain density (g/cm^3) = 2.65
Porosity (%) = 3.8

Petrographic data:
framework clay= 0.0
matrix clay = 0.0
ankerite = 2.0
dolomite = 0.8

Strain, Static Bulk Moduli, and Dry Velocities

P_c (MPa)	ϵ_{vol} (mstr)	K_{stat} (GPa)	K_{dyn} (GPa)	V_p (km/s)	V_s (km/s)	V_p/V_s	G_{dyn} (GPa)	σ_{dyn}
5.	0.48	12.83	12.72	3.970	2.841	1.40	20.53	-0.025
10.	0.83	16.94	15.10	4.207	2.971	1.42	22.47	0.003
20.	1.29	23.38	19.57	4.618	3.199	1.44	26.06	0.039
40.	2.00	29.69	27.41	5.181	3.474	1.49	30.78	0.092
75.	3.16	30.98	31.30	5.440	3.606	1.51	33.21	0.108
125.	4.62	33.23	32.89	5.521	3.636	1.52	33.84	0.117
125.	4.62	32.77	32.89	5.521	3.636	1.52	33.84	0.117
75.	3.12	30.12	31.62	5.459	3.614	1.51	33.36	0.110
40.	1.92	26.96	29.09	5.303	3.541	1.50	31.96	0.098
20.	1.13	23.77	24.08	4.943	3.351	1.47	28.60	0.075
10.	0.66	18.28	17.98	4.501	3.146	1.43	25.18	0.023
5.	0.38	14.10	15.94	4.253	2.978	1.43	22.55	0.019

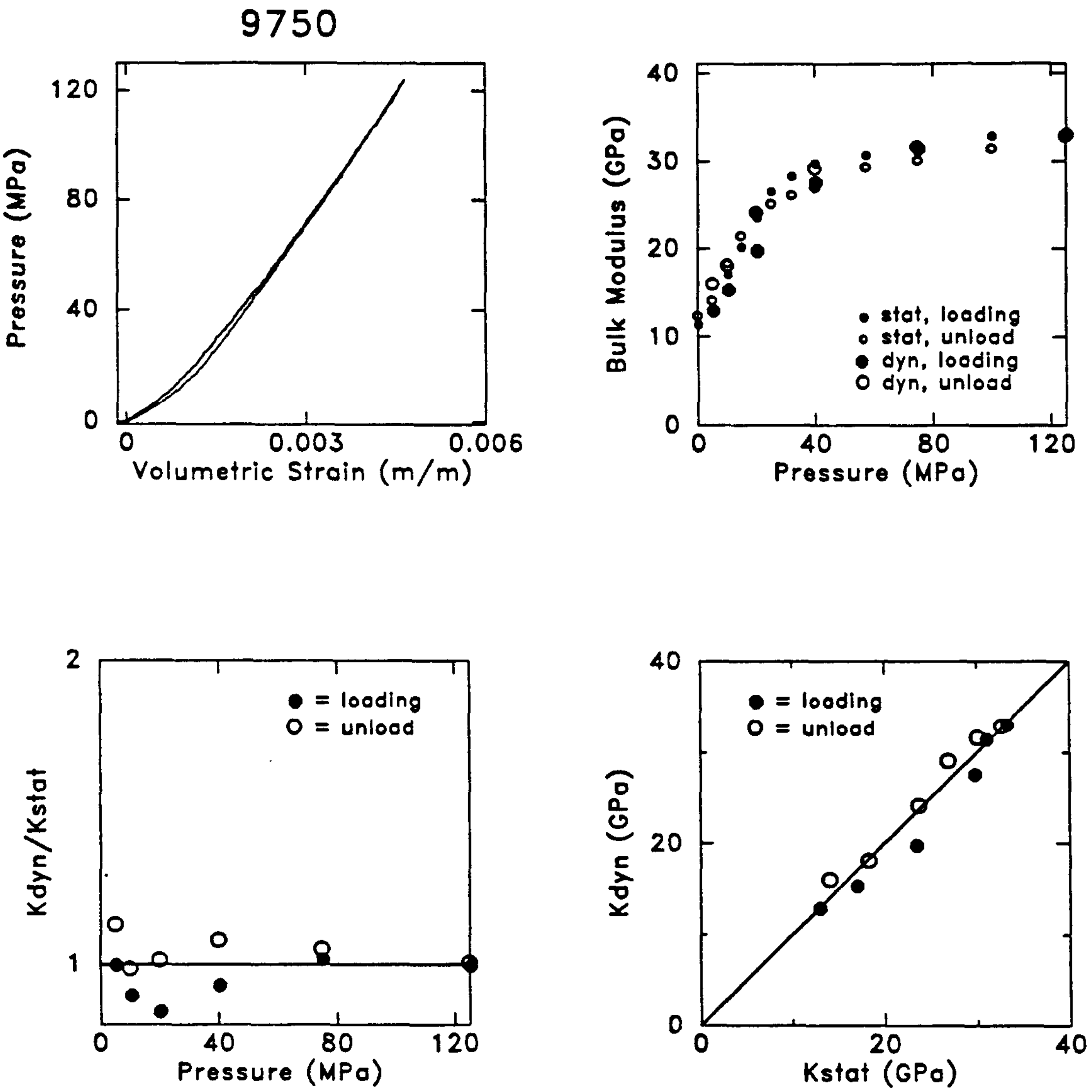
9750
Pressure (MPa)
120
80
40
0
0
0.003
0.006
Volumetric Strain (m/m)
Bulk Modulus (GPa)
40
30
20
10
0
0
40
80
120
Pressure (MPa)
● stat, loading
○ stat, unload
● dyn, loading
○ dyn, unload
Kdyn/Kstat
2
1
0
40
80
120
Pressure (MPa)
● = loading
○ = unload
Kdyn (GPa)
40
20
0
0
20
40
Kstat (GPa)
● = loading
○ = unload

Depth (feet) = 9753.0
Length (cm) = 3.82
Grain density (g/cm^3) = 2.66
Porosity (%) = 4.5

Petrographic data:
framework clay= 0.8
matrix clay = 0.0
ankerite = 3.2
dolomite = 15.2

Strain, Static Bulk Moduli, and Dry Velocities

P_c (MPa)	ϵ_{vol} (mstr)	K_{stat} (GPa)	K_{dyn} (GPa)	V_p (km/s)	V_s (km/s)	V_p/V_s	G_{dyn} (GPa)	σ_{dyn}
5.	0.28	10.09	11.44	3.815	2.748	1.39	19.28	-0.040
10.	0.78	10.38	13.74	4.049	2.874	1.41	21.10	-0.008
20.	1.72	12.94	17.52	4.393	3.055	1.44	23.88	0.032
40.	2.85	20.72	24.67	4.924	3.311	1.49	28.10	0.087
75.	4.18	31.62	30.08	5.269	3.470	1.52	30.91	0.117
125.	5.56	33.56	31.97	5.394	3.536	1.53	32.17	0.123
125.	5.50	34.98	31.97	5.394	3.536	1.53	32.17	0.123
75.	4.13	32.74	30.82	5.314	3.489	1.52	31.25	0.121
40.	2.91	23.29	27.24	5.082	3.376	1.51	29.20	0.105
20.	1.88	14.23	21.03	4.661	3.183	1.46	25.91	0.063
10.	1.01	9.24	15.89	4.247	2.977	1.43	22.64	0.017
5.	0.36	8.16	13.13	3.982	2.834	1.41	20.50	-0.013

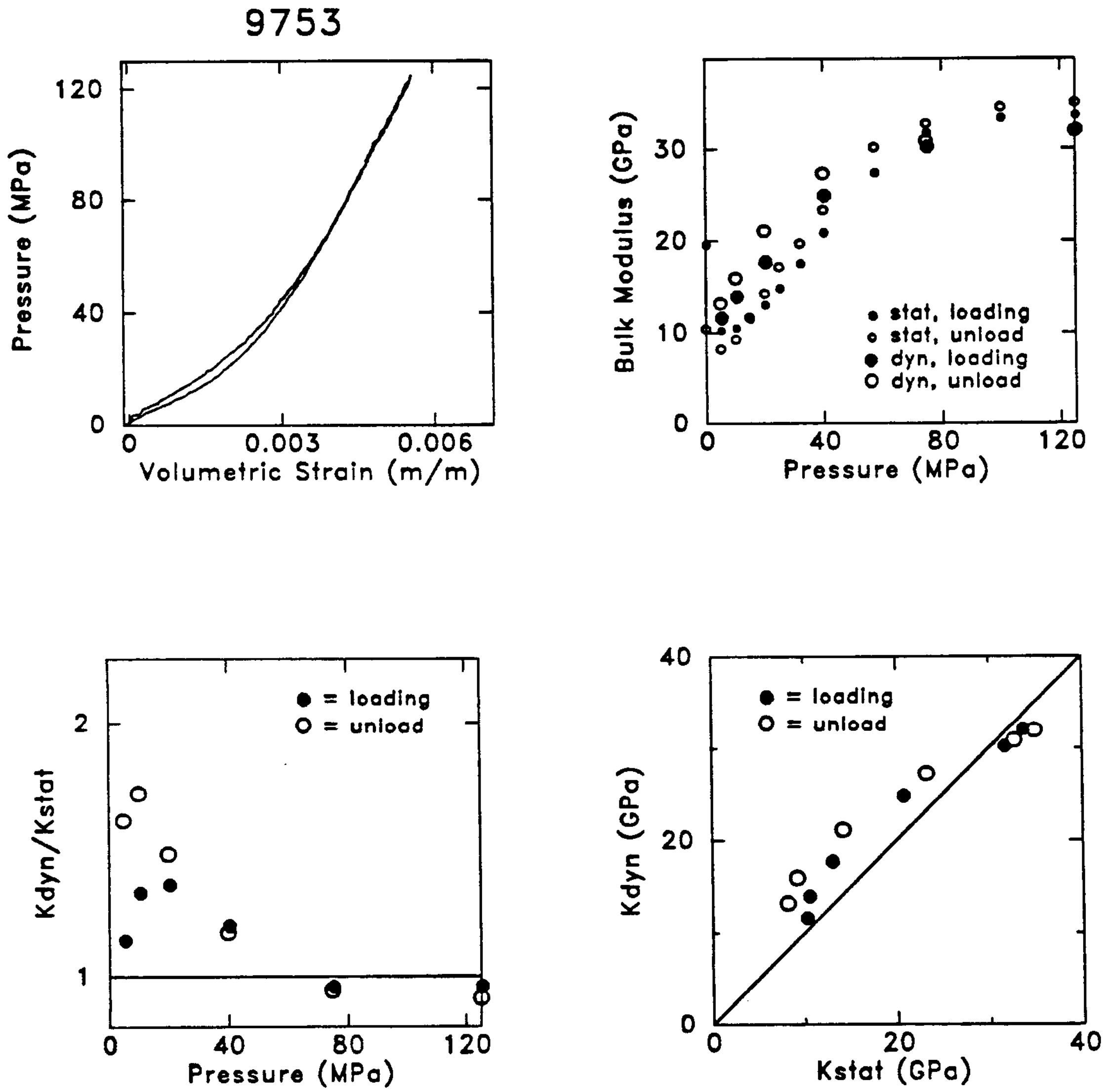
9753
Pressure (MPa)
120
80
40
0
0
0.003
0.006
Volumetric Strain (m/m)
Bulk Modulus (GPa)
30
20
10
0
0
40
80
120
Pressure (MPa)
• stat, loading
∘ stat, unload
● dyn, loading
○ dyn, unload
Kdyn/Kstat
2
1
0
40
80
120
Pressure (MPa)
● = loading
○ = unload
Kdyn (GPa)
40
20
0
0
20
40
Kstat (GPa)
● = loading
○ = unload

Depth (feet) = 9754.0
Length (cm) = 3.68
Grain density (g/cm^3) = 2.68
Porosity (%) = 7.0

Petrographic data:
framework clay= 6.0
matrix clay = 0.0
ankerite = 11.0
dolomite = 0.0

Strain, Static Bulk Moduli, and Dry Velocities

P_c (MPa)	ϵ_{vol} (mstr)	K_{stat} (GPa)	K_{dyn} (GPa)	V_p (km/s)	V_s (km/s)	V_p/V_s	G_{dyn} (GPa)	σ_{dyn}
5.	0.69	6.67	8.44	3.264	2.343	1.39	13.90	-0.032
10.	1.48	6.86	9.37	3.423	2.452	1.40	15.23	-0.027
20.	2.60	8.55	12.16	3.784	2.672	1.42	18.09	0.003
40.	4.34	11.99	18.90	4.383	2.969	1.48	22.36	0.076
75.	6.05	23.97	24.64	4.829	3.195	1.51	25.92	0.111
125.	7.94	26.06	27.13	5.021	3.302	1.52	27.72	0.119
125.	8.01	26.79	27.05	5.038	3.313	1.52	27.63	0.119
75.	6.15	25.65	25.29	4.910	3.246	1.51	26.48	0.112
40.	4.42	15.55	20.77	4.573	3.080	1.49	23.81	0.085
20.	3.23	9.91	15.17	4.094	2.835	1.44	20.16	0.040
10.	2.12	6.89	11.52	3.713	2.626	1.41	17.29	0.000
5.	1.47	4.56	8.93	3.428	2.478	1.38	15.40	-0.048

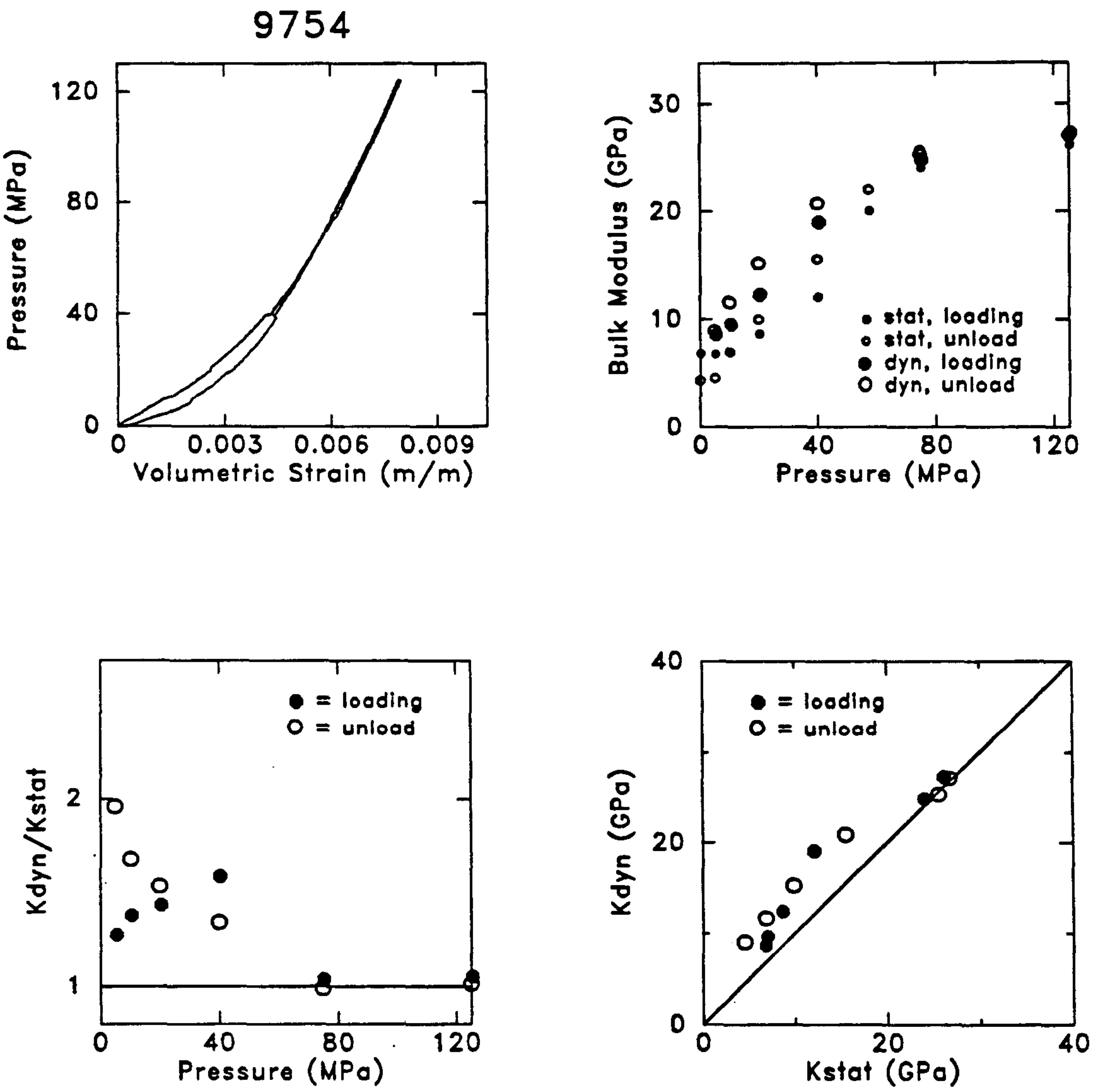
9754
Pressure (MPa)
120
80
40
0
0
0.003
0.006
0.009
Volumetric Strain (m/m)
Bulk Modulus (GPa)
30
20
10
0
0
40
80
120
Pressure (MPa)
• stat, loading
∘ stat, unload
● dyn, loading
O dyn, unload
Kdyn/Kstat
2
1
0
40
80
120
Pressure (MPa)
● = loading
O = unload
Kdyn (GPa)
40
20
0
0
20
40
Kstat (GPa)
● = loading
O = unload

Depth (feet) = 9756.0
Length (cm) = 4.07
Grain density (g/cm^3) = 2.65
Porosity (%) = 6.2

Petrographic data:
framework clay= 10.0
matrix clay = 0.0
ankerite = 2.0
dolomite = 0.0

Strain, Static Bulk Moduli, and Dry Velocities

P_c (MPa)	ϵ_{vol} (mstr)	K_{stat} (GPa)	K_{dyn} (GPa)	V_p (km/s)	V_s (km/s)	V_p/V_s	G_{dyn} (GPa)	σ_{dyn}
5.	0.60	9.34	12.70	3.796	2.643	1.44	17.40	0.030
10.	1.09	9.92	13.82	3.923	2.718	1.44	18.42	0.039
20.	1.99	12.00	15.91	4.175	2.880	1.45	20.72	0.046
40.	3.38	17.37	21.74	4.686	3.155	1.49	24.92	0.085
75.	5.02	24.79	26.10	5.057	3.374	1.50	28.58	0.099
125.	6.71	29.36	28.19	5.202	3.449	1.51	29.93	0.108
125.	6.75	31.50	28.19	5.201	3.449	1.51	29.94	0.108
75.	5.17	28.50	26.73	5.114	3.411	1.50	29.21	0.099
40.	3.83	22.28	23.68	4.870	3.271	1.49	26.81	0.089
20.	2.75	14.89	19.45	4.482	3.039	1.48	23.09	0.075
10.	2.04	10.50	15.57	4.146	2.866	1.45	20.52	0.042
5.	1.46	7.87	13.99	3.969	2.758	1.44	18.98	0.033

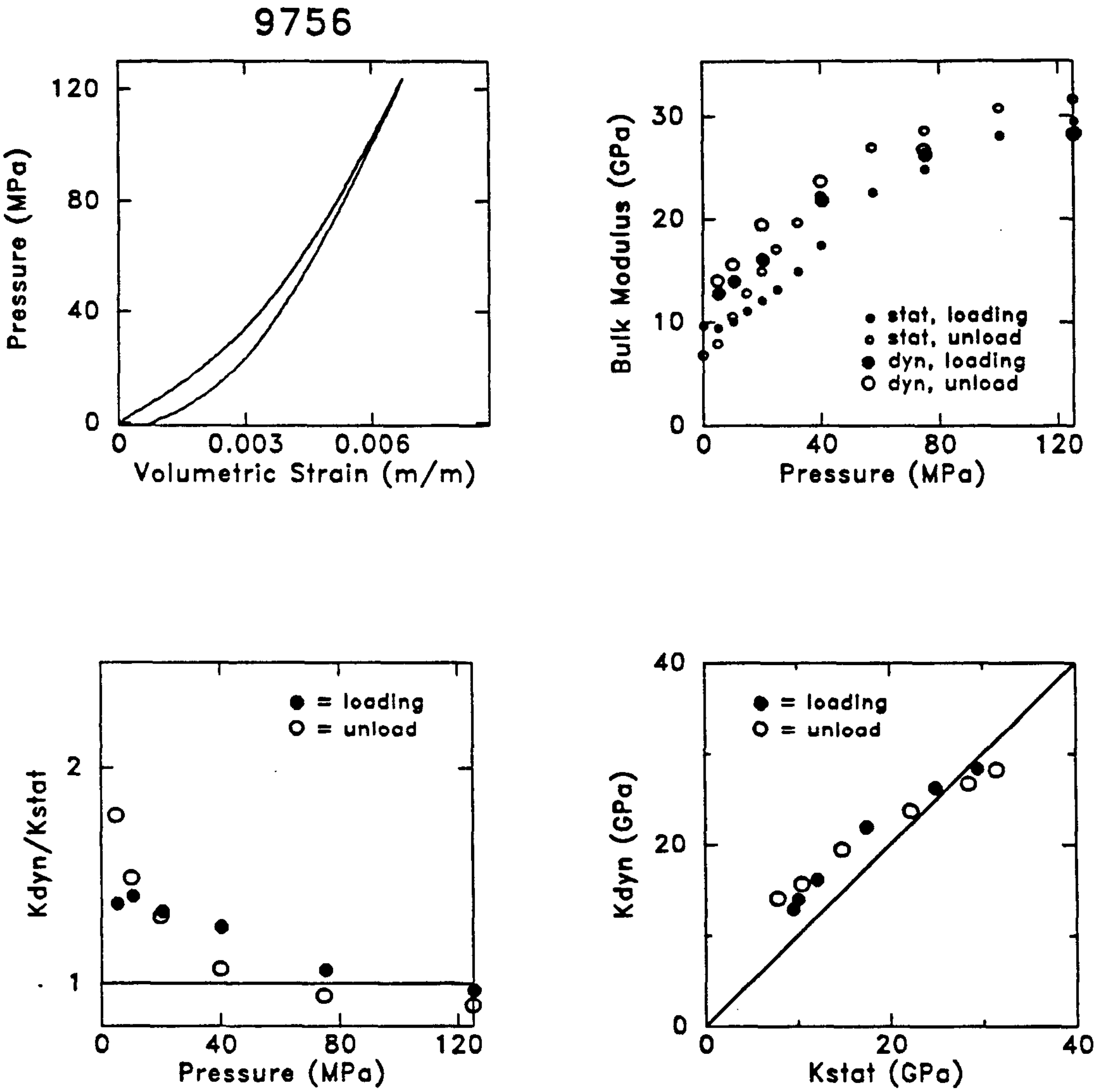
9756
Pressure (MPa)
120
80
40
0
0
0.003
0.006
Volumetric Strain (m/m)
Bulk Modulus (GPa)
30
20
10
0
0
40
80
120
Pressure (MPa)
● stat, loading
○ stat, unload
● dyn, loading
O dyn, unload
Kdyn/Kstat
2
1
0
40
80
120
Pressure (MPa)
● = loading
O = unload
Kdyn (GPa)
40
20
0
0
20
40
Kstat (GPa)
● = loading
O = unload

Depth (feet) = 9763.0
Length (cm) = 3.75
Grain density (g/cm^3) = 2.66
Porosity (%) = 3.5

Petrographic data:
framework clay= 1.0
matrix clay = 19.0
ankerite = 13.0
dolomite = 0.0

Strain, Static Bulk Moduli, and Dry Velocities

P_c (MPa)	ϵ_{vol} (mstr)	K_{stat} (GPa)	K_{dyn} (GPa)	V_p (km/s)	V_s (km/s)	V_p/V_s	G_{dyn} (GPa)	σ_{dyn}
5.	0.57	8.87	9.88	3.568	2.581	1.38	17.08	-0.049
10.	1.17	8.70	10.87	3.673	2.634	1.39	17.81	-0.030
20.	2.26	9.77	12.91	3.884	2.747	1.41	19.40	-0.001
40.	4.16	12.20	18.26	4.304	2.929	1.47	22.13	0.068
75.	6.39	18.51	23.96	4.708	3.111	1.51	25.05	0.112
125.	8.58	23.48	28.37	4.965	3.209	1.55	26.75	0.141
125.	8.60	29.97	28.37	4.965	3.209	1.55	26.76	0.141
75.	6.85	24.56	25.84	4.829	3.163	1.53	25.92	0.124
40.	5.25	17.79	21.73	4.565	3.053	1.50	24.07	0.096
20.	3.92	11.91	16.77	4.219	2.910	1.45	21.83	0.046
10.	2.93	8.03	13.48	3.953	2.792	1.42	20.06	0.002
5.	2.25	6.80	11.64	3.775	2.700	1.40	18.75	-0.024

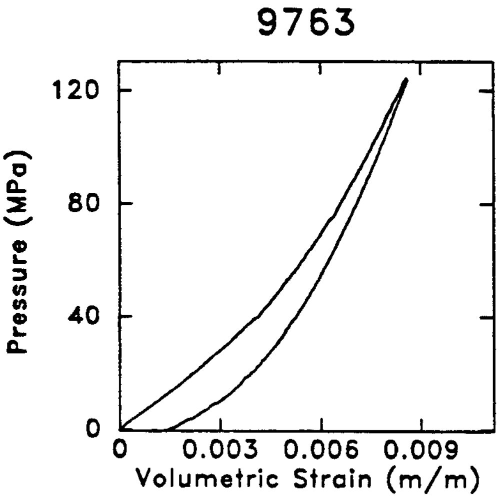
9763
Pressure (MPa)
120
80
40
0
0
0.003
0.006
0.009
Volumetric Strain (m/m)

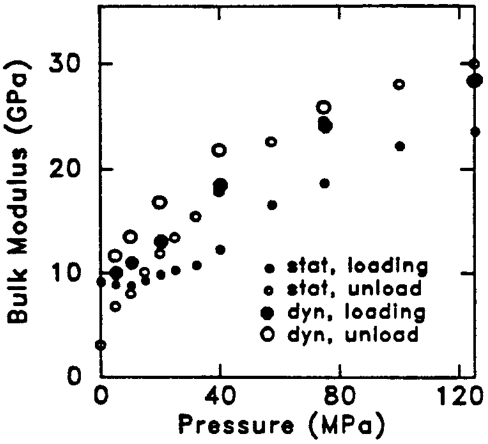
Bulk Modulus (GPa)
30
20
10
0
0
40
80
120
Pressure (MPa)
• stat, loading
∘ stat, unload
● dyn, loading
○ dyn, unload

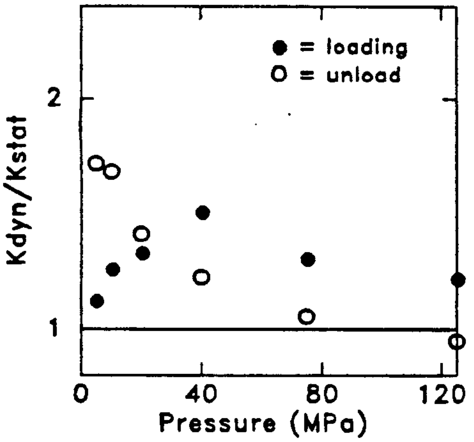
Kdyn/Kstat
2
1
0
40
80
120
Pressure (MPa)
● = loading
○ = unload

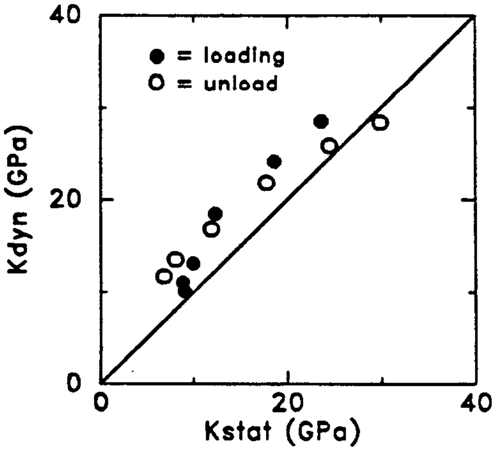
Kdyn (GPa)
40
20
0
0
20
40
Kstat (GPa)
● = loading
○ = unload

Depth (feet) = 9898.0
Length (cm) = 4.73
Grain density (g/cm^3) = 2.70
Porosity (%) = 1.6

Petrographic data:
framework clay= 0.0
matrix clay = 41.5
ankerite = 0.0
dolomite = 0.0

Strain, Static Bulk Moduli, and Dry Velocities

P_c (MPa)	ϵ_{vol} (mstr)	K_{stat} (GPa)	K_{dyn} (GPa)	V_p (km/s)	V_s (km/s)	V_p/V_s	G_{dyn} (GPa)	σ_{dyn}
5.	0.12	27.35	29.84	4.962	3.182	1.56	27.15	0.151
10.	0.32	23.74	30.45	4.993	3.192	1.56	27.34	0.154
20.	0.75	24.28	31.48	5.056	3.222	1.57	27.87	0.158
40.	1.56	25.54	33.73	5.174	3.267	1.58	28.70	0.169
75.	2.85	28.17	35.74	5.295	3.329	1.59	29.86	0.173
125.	4.47	31.19	38.08	5.412	3.376	1.60	30.80	0.181
125.	4.42	35.38	38.08	5.412	3.376	1.60	30.80	0.181
75.	3.03	30.58	36.27	5.324	3.343	1.59	30.12	0.175
40.	1.80	25.44	34.43	5.219	3.291	1.59	29.15	0.170
20.	0.92	21.73	32.42	5.110	3.246	1.57	28.30	0.162
10.	0.47	19.44	31.25	5.041	3.213	1.57	27.72	0.158
5.	0.23	22.21	30.34	4.993	3.197	1.56	27.42	0.153

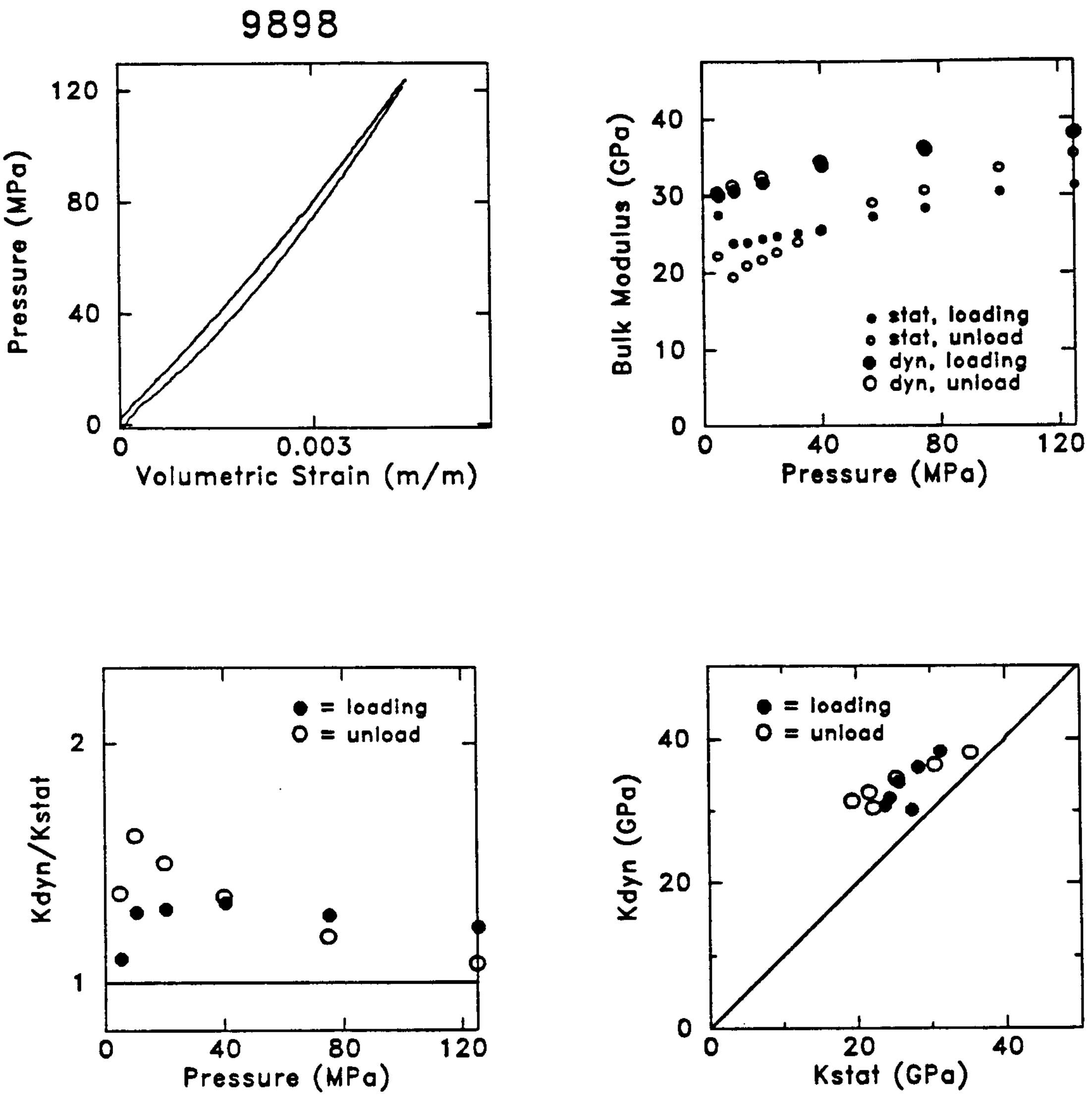
9898
Pressure (MPa)
120
80
40
0
0
0.003
Volumetric Strain (m/m)
Bulk Modulus (GPa)
40
30
20
10
0
0
40
80
120
Pressure (MPa)
● stat, loading
○ stat, unload
● dyn, loading
○ dyn, unload
Kdyn/Kstat
2
1
0
40
80
120
Pressure (MPa)
● = loading
○ = unload
Kdyn (GPa)
40
20
0
0
20
40
Kstat (GPa)
● = loading
○ = unload

Depth (feet) = 9975.0
Length (cm) = 3.81
Grain density (g/cm^3) = 2.67
Porosity (%) = 3.0

Petrographic data:
framework clay= 2.0
matrix clay = 0.0
ankerite = 0.0
dolomite = 0.0

Strain, Static Bulk Moduli, and Dry Velocities

P_c (MPa)	ϵ_{vol} (mstr)	K_{stat} (GPa)	K_{dyn} (GPa)	V_p (km/s)	V_s (km/s)	V_p/V_s	G_{dyn} (GPa)	σ_{dyn}
5.	0.47	12.70	18.30	4.449	3.072	1.45	23.94	0.044
10.	0.82	14.58	19.64	4.555	3.124	1.46	24.78	0.056
20.	1.43	17.84	22.32	4.771	3.238	1.47	26.63	0.073
40.	2.38	24.46	26.75	5.161	3.478	1.48	30.79	0.084
75.	3.59	31.57	32.10	5.520	3.662	1.51	34.21	0.107
125.	5.01	34.72	34.44	5.663	3.735	1.52	35.65	0.115
125.	5.01	35.86	34.44	5.663	3.735	1.52	35.66	0.115
75.	3.64	33.11	33.23	5.585	3.691	1.51	34.74	0.112
40.	2.50	27.19	29.54	5.350	3.572	1.50	32.49	0.098
20.	1.68	19.79	25.16	5.022	3.390	1.48	29.22	0.081
10.	1.09	15.00	22.24	4.766	3.235	1.47	26.58	0.073
5.	0.70	12.43	20.75	4.627	3.151	1.47	25.19	0.068

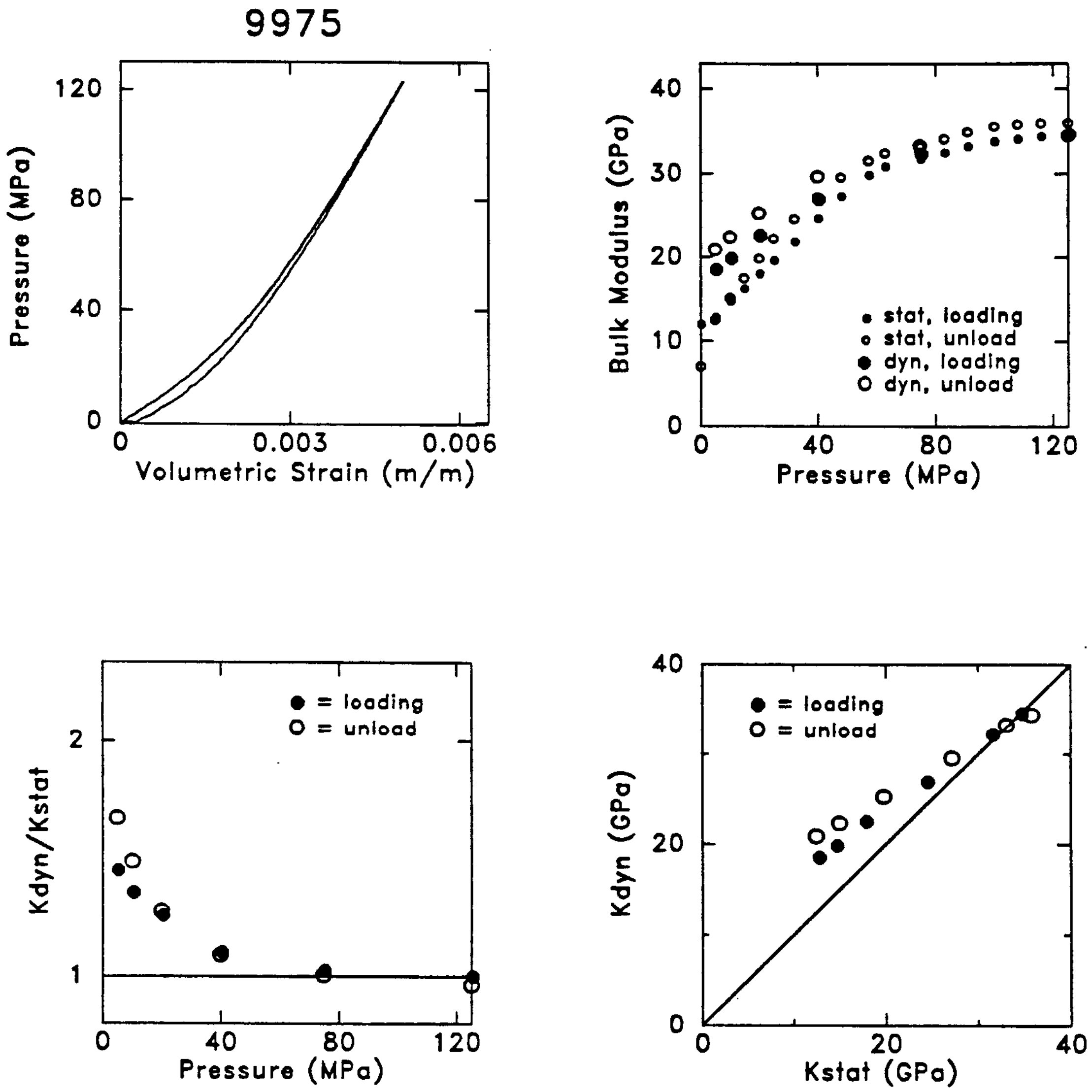
9975
Pressure (MPa)
120
80
40
0
0
0.003
0.006
Volumetric Strain (m/m)
Bulk Modulus (GPa)
40
30
20
10
0
0
40
80
120
Pressure (MPa)
● stat, loading
○ stat, unload
● dyn, loading
○ dyn, unload
Kdyn/Kstat
2
1
0
40
80
120
Pressure (MPa)
● = loading
○ = unload
Kdyn (GPa)
40
20
0
0
20
40
Kstat (GPa)
● = loading
○ = unload